



# Controlling and Protecting Coherent Quantum States

Svend Krøjer Møller

PhD Thesis

Copenhagen, November 2023

Advisor :

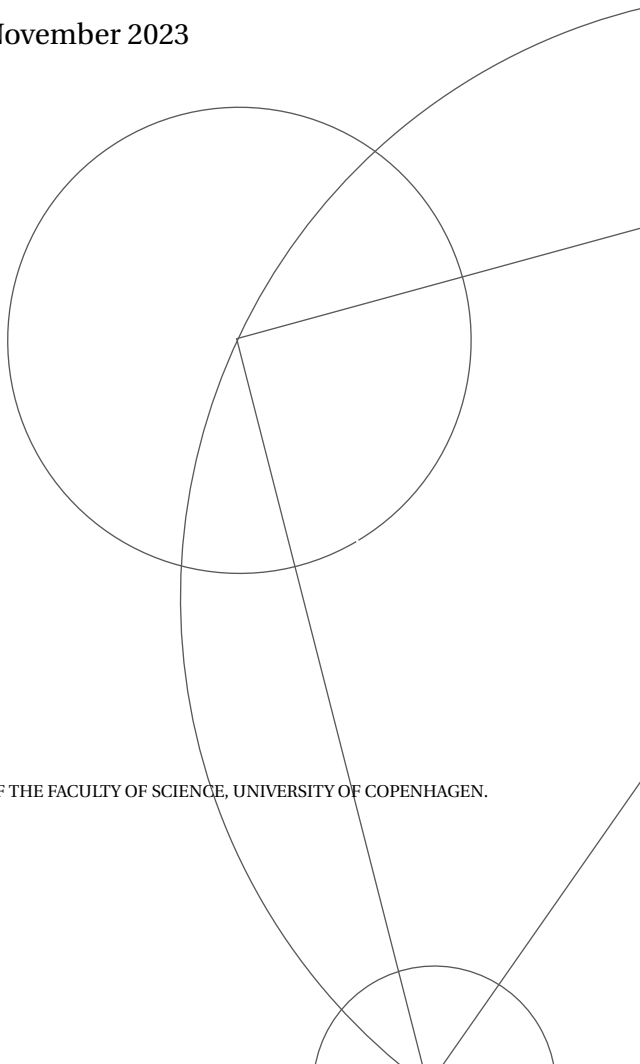
Prof. Karsten Flensberg

Assessment committee :

Prof. Jens Paaske

Prof. Reinhold Egger

Prof. Anton Frisk Kockum





Center for  
Quantum  
Devices



**European Research Council**

Established by the European Commission

## **Controlling and Protecting Coherent Quantum States**

Svend Krøjer Møller

PhD Thesis

Copenhagen, November 2023

© 2023 - Svend Krøjer Møller

All rights reserved.

### **Citation (APA):**

Krøjer, S. (2023). *Controlling and Protecting Coherent Quantum States*. Niels Bohr Institute, Faculty of Science, University of Copenhagen.

ISBN: XXX-XX-XXXX-XX-X

Revised: November 30, 2023

## Abstract

Qubits protected against noise have long coherence times and can be used as basic components in quantum computers. This thesis studies two distinct superconductor-based qubit platforms that realize noise-protection in different ways.

The first part of the thesis is concerned with Majorana zero modes that are non-Abelian anyons predicted to exist at the boundary of certain topological superconductors. Symmetries of the topological superconductor protect Majorana zero modes from decoherence and allow for non-local encoding of quantum information which is insensitive to local noise. We study a Majorana system where single electron charge-transfer between external quantum dots and the Majorana system realizes a universal gate set. We study non-idealities of the charge-transfer operations and propose a minimal experiment that can demonstrate Majorana non-Abelian properties.

The second part of the thesis is concerned with superconducting qubits based on conventional superconductors. These qubits are micrometer-sized superconducting circuits that are sensitive to the electromagnetic environment. Despite inherent noise sensitivity, superconducting qubits are promising as a platform to realize large-scale quantum computers. We study two ways superconducting qubits can be engineered to reduce noise sensitivity.

First, we consider a flux qubit that is protected against relaxation by separating its quantum states in different potential wells. We devise a universal gate scheme that momentarily reduces the level of protection to partially hybridize the qubit states, enabling direct-drive microwave gates. We also consider a readout scheme that preserves protection by reading out via an auxiliary qubit mode.

Second, we consider protection against flux noise which can be achieved using superinductors. We consider a junction array superinductor comprised of quartons that exhibits a quartic energy-phase relation, effectively increasing the inductance. We study non-idealities in the quarton array and compare it to conventional junction array superinductors. We use the quarton array superinductor as the inductive elements in the  $0 - \pi$  qubit, the bifluxon qubit, and the Blochonium qubit and numerically evaluate dephasing times due to flux noise. Finally, we discuss the experimental requirements needed to achieve protection against flux noise in superconducting qubits based on quarton array superinductors.

---

## Sammenfatning

Kvantebits beskyttet mod støj har lange kohærenstider og kan blive brugt som elementære komponenter i kvantecomputere. Denne afhandling studerer to distinkte superlederbaserede kvantebitplatforme, som realiserer støjbeskyttelse på to forskellige måder.

Den første del af afhandlingen omhandler Majoranatilstande, som er ikke-Abelske anyoner, forudsagt til at eksistere på randen af særlige topologiske superledere. Symmetrier i den topologiske superleder beskytter Majoranatilstandene fra dekohærens og tillader en ikke-lokal indkodning af kvanteinformation, der er insensitiv til lokal støj. Vi studerer et Majoranasystem, hvor ladningsudveksling af enkelte elektroner mellem kvanteprikker og Majoranasystemet realiserer et universelt sæt af kvantelogik. Vi studerer ikke-ideelle faktorer i ladningsudvekslingsprocesserne og foreslår et minimalt eksperiment, der kan eftervise ikke-Abelske egenskaber af Majoranatilstande.

Den anden del af afhandlingen omhandler superledende kvantebits baseret på konventionelle superledere. Disse kvantebits er superledende kredsløb i mikrometerstørrelse, som er sensitive til det elektromagnetiske miljø. Trods intrinsisk støjsensitivitet er superledende kvantebits lovende som platform til at realisere kvantecomputere på stor skala. Vi studerer to måder, hvorpå superledende kvantebits kan designes til at reducere støjsensitivitet.

Først betragter vi en fluxkvantebit, som er beskyttet mod henfald ved at separere dets kvantetilstande i forskellige kvantebrønde. Vi udtænker en fremgangsmåde for et universelt sæt af kvantelogik, der momentant reducerer graden af beskyttelse for delvist at hybridisere kvantebittilstandene hvorved mikrobølgekvantelogik, der drives direkte, muliggøres. Vi overvejer også en fremgangsmåde til udlæsning, der bevarer beskyttelse ved at læse ud gennem en hjælpe-kvantebittilstand.

Dernæst overvejer vi beskyttelse mod fluxstøj, som kan opnås ved at bruge superinduktorer. Vi overvejer en superinduktor bestående af en kvartronrække, der fremviser en kvartisk energi-fase relation og som effektivt øger induktansen. Vi studerer ikke-ideelle faktorer i kvartronrækken og sammenligner med konventionelle superinduktorer bestående af en række af Josephson-forbindelser. Vi bruger superinduktoren bestående af kvartronrækker som de induktive elementer i  $0 - \pi$  kvantebitten, bifluxon-kvantebitten og Blochonium-kvantebitten og evaluerer numerisk affasningstiden fra fluxstøj. Til slut diskuterer vi de nødvendige eksperimentelle krav for at opnå beskyttelse mod fluxstøj i superledende kvantebits baseret på superinduktorer bestående af kvartronrækker.



---

## Acknowledgments

I am grateful to countless people that I have encountered throughout my PhD and prior education. I mention the ones I have worked with most closely.

Rubén Seoane Souto helped and guided me in the early stages of my PhD and before that during my Master's. Because of him, I have been more confident in my research projects and paper writing later on.

Max Geier and Jens Schulenburg included me in projects that were far beyond my capabilities. Because of them, I learned many inspiring things. One of the important lessons is that I do not know a lot.

Anders Enevold Dahl and Kasper Sanggild Christensen represent all the office mates and co-workers at CMT, QDev and NQCP who participated in making hard work into fun work. Especially memorable are trips to PhD schools with wine and meetings with basser.

The students who signed up for the course I lectured. You made it as challenging and enjoyable as one can hope it to be.

Frederik Ravn Klausen and Andreas Juul Bay-Smidt provided valuable inputs to the thesis when it was most needed. Sometimes, small adjustments make the biggest differences.

Alexandre Blais and everyone associated with Institut Quantique gave me a new home for a short while. During my stay, I gained tremendously both academically and socially. Importantly, it was settled that cod is more appropriate than salmon in fish'n'chips. I am sorry to say that I do still not speak French Québécois.

Morten Kjaergaard who has acted as a second supervisor since his return to Copenhagen and perhaps sometimes as “Onkel Morten” as KF once referred to you. Pivotal to my academic pursuit, Morten taught me what is up with superconducting qubits, GIFs and far beyond. If not for Morten, I would never have aspired to work in a lab.

Karsten Flensberg whom I extend my warm and sincere appreciation to. Karsten participated in all of the above and his mentorship extends well beyond just academia. His most succinct pieces of wisdom count ““No” is also an answer”, “Computers love to compute” and, defining of his character, “If others can, then so can I”.

Svend Krøjer Møller  
Copenhagen, November 2023

---

# Contents

<b>Contents</b>	<b>iv</b>
<b>Preface</b>	<b>v</b>
<b>I Introduction</b>	<b>1</b>
<b>1 Coherent quantum systems</b>	<b>3</b>
<b>2 Majorana qubits</b>	<b>11</b>
<b>3 Superconducting qubits</b>	<b>21</b>
3.1 Circuit quantization . . . . .	23
3.2 Decoherence and noise-protection . . . . .	30
<b>4 Introduction to Project A</b>	<b>37</b>
<b>5 Introduction to Project B</b>	<b>43</b>
<b>6 Introduction to Project C</b>	<b>47</b>
<b>Bibliography</b>	<b>57</b>
<b>II Projects</b>	<b>75</b>
<b>A Demonstrating Majorana non-Abelian properties using fast adiabatic charge transfer</b>	<b>77</b>
<b>B Fast universal control of a flux qubit via exponentially tunable wave-function overlap</b>	<b>95</b>
<b>C Towards deep protection of qubits using realistic quarton array superinductors</b>	<b>109</b>

---

## Preface

Theoretical modeling, physical discoveries and technological developments are intimately linked. Today, it can sometimes be taken for granted that theoretical findings can motivate and predict experimental results. Then, once a physical mechanism or effect is adequately tested, a technology can be developed and commercialized. Yet, earlier in scientific history, this reasoning was reversed. Technological advancements urged theories to be created.

The first commercialization (or invention<sup>1</sup>) of the steam engine is due to Thomas Savory and Thomas Newcomen who in 1698 and 1712 each introduced an industrially viable steam engine [7]. Later, during the second half of the 18th century, James Watt improved the steam engine design extensively, leading to the widespread transition to mechanical power during the Industrial Revolution [8]. The successes of the steam engine inspired, among others, Sadi Carnot to study the efficiency of thermodynamic processes and his contemplations birthed the important concept of a “Carnot cycle”<sup>2</sup> in 1824 [9]. Thermodynamics was later put on a solid theoretical foundation by Rudolf Clausius and William Thomson<sup>3</sup> during the middle of the 19th century through the introduction of concepts such as entropy and the second law of thermodynamics [9]. This leaves about a 100 year gap between the commercialization of the steam engine and our modern theoretical description of its underpinning physics. Nevertheless, theoretical physics quickly caught up.

The end of the 19th century also saw its major technological invention. Thomas Edison famously commercialized the incandescent light bulb in the early 1880s and electricity slowly took over as an energy resource [10, 11]. In this case, however, the development of the light bulb was essentially parallel to the study of the theory of electrodynamics. Incandescence from a wire heated by electric current was first demonstrated as early as 1761 by Ebenezer Kinnersley [12] and was under intense development starting in the early 19th hundred with experiments inspired by Humphry Davy in 1802 [10]. Simultaneously, famous experiments by Coulomb (1787), Ørsted (1820), Ampère (1820) and Faraday<sup>4</sup> (1821/31) settled empirical laws of electromagnetism: the force law of electrical charges and the correspondence between magnetic fields and currents [9]. Within a decade of Edison’s light bulb, these efforts culminated in 1873 with James Clerk Maxwell’s

---

<sup>1</sup>It is hard to pinpoint the exact invention of the steam engine as numerous attempts to use steam as a mechanical resource has appeared throughout history. A rudimentary steam engine, “aelopile”, was described by the ancient Greek mathematician and engineer Heron of Alexandria in the 1st century.

<sup>2</sup>The Carnot cycle is the thermodynamic cycle with the theoretically highest efficiency.

<sup>3</sup>Whom you never know if you should refer to as Lord Kelvin or not.

<sup>4</sup>Incidentally, Faraday started his career by getting hired as an assistant by Humphry Davy. He was a replacement for an assistant who got into a fistfight and was subsequently dismissed.

comprehensive work “A Treatise on Electricity and Magnetism” which unified the classical theory of electrodynamics [13].

A more recent scientific breakthrough is the light-emitting diode (LED). Commonplace in today’s households, white LEDs emitting light across the entire visible spectrum were only commercialized after the fabrication advancements made by Shuji Nakamura, Hiroshi Amano and Isamu Akasaki, enabling efficient blue LEDs<sup>5</sup> [14–16]. The band-gap engineering of semiconductors, relevant to achieve the emission of blue light [15, 16], can be understood from theories developed fifty years before the commercialization of white LEDs. Felix Bloch was one of the first to study “band states” and his 1929 theorem is a crucial tool for understanding the formation of bands in crystalline solids [17–19]. In the following period, the study of band structure emerged as a rapidly developing field [18–20]. Among the successes in the description of the band structure in semiconductors is the powerful  $k \cdot p$  perturbation theory associated with the work of Evan Kane, Joaquin Luttinger and Walther Kohn around 1955 [20–23]. In the 20th century, the elementary theories of physics had at large overtaken the ever-improving technologies.

Scientific shifts, as remarkable as the one taking place during the previous centuries, are certainly gradual and a few examples might not be representative of all of physics and technology. However, if a specific point in time can be assigned to the turn-over from “observations first” to “calculations first”, 1832 is arguably the year. Here, William Rowan Hamilton likely provided the first prediction of an unknown physical phenomenon based on mathematical inference [24]. The effect he described is relatively obscure<sup>6</sup>, but marks a profound change in the relationship between theory and experiment in the evolution of science.

In light of the incredible successes of theories, experiments and technologies, we may think about which phenomena in Nature that are described by theory but not yet promoted into technological application. While such considerations may be lengthy, let us dwell on one particular property in the century-old theory of quantum mechanics; quantum coherence. Quantum coherence is the ability of a system to remain “quantum-mechanical”, despite the influence of its surroundings. In such a coherent system, the quantum properties of superposition and entanglement can potentially be a useful resource [25]. The earliest proposal in this direction is due to Richard Feynman who conjectured<sup>7</sup> in 1982 that a well-controlled coherent quantum system might be able to efficiently simulate another quantum system of interest [27].<sup>8</sup> More generally, coherent quantum properties can be used in universal quantum information processing, expanding the realm of computing [29]. Here, (the physical representation of) information is deliberately manipulated according to the principles of quantum mechanics. How, when and why such a scheme might be useful as a technology is currently under fundamental exploration [29, 30]. This thesis aims to provide a conceptual introduction and study of some of the relevant questions regarding quantum coherence in its application to quantum computation.

---

<sup>5</sup>Awarding them the 2014 Nobel Prize in physics.

<sup>6</sup>Hamiltons phenomenon is known as “conical refraction” and occurs when an incident beam of light refracts along one of the optical axes of a biaxial crystal [24].

<sup>7</sup>In 1996, Feynman’s conjecture was proved correct by Seth Lloyd [26].

<sup>8</sup>Interestingly, quantum systems were first considered as a mean to perform classical computation, see Paul Benioffs seminal 1980 work [28] on the possibility of encoding a Turing machine in a quantum system.

---

## Outline

This thesis is concerned with several topics related to protection and operations of coherent quantum systems. The thesis introduces relevant concepts before discussing the research results included in this work.

- Chapter 1 introduces basic concepts in quantum computing.
- Chapter 2 introduces Majorana zero modes.
- Chapter 3 introduces superconducting qubits.
- Chapter 4 introduces Project A [P1].
- Chapter 5 introduces Project B [P2].
- Chapter 6 introduces Project C [P3].

## Publications and author contributions

This thesis is based on the work leading to the papers listed below. Before each paper, a summary and discussion is given that introduces the work.

A *Demonstrating Majorana non-abelian exchange using fast adiabatic charge-transfer*

**Svend Krøjer**, Rubén Seoane Souto and Karsten Flensberg

[Physical Review B](#), Vol. 105, No. 4 (January 2022) p. 045425, Ref. [P1].

I was the primary contributor to scientific investigation, image preparation, and paper writing.

B *Fast universal control of a flux qubit via exponentially tunable wave-function overlap*

**Svend Krøjer**, Anders Enevold Dahl, Kasper Sangild Christensen, Morten Kjaergaard and Karsten Flensberg

[ArXiv](#), [arXiv:2303.01102 \[quant-ph\]](#) (March 2023), Ref. [P2].

I contributed substantially to the scientific investigation, numerical results, and paper writing.

C *Towards deep protection of qubits using realistic quarton array superinductors*

**Svend Krøjer**, Alexandre Blais, Morten Kjaergaard and Karsten Flensberg

In preparation, Ref. [P3]

I was the primary contributor to scientific investigation, image preparation, and paper writing.

### Work not included in the thesis

During the PhD-project, I made minor contributions to the design of the following works, which are *not* included in the thesis:

D *Detecting Majorana modes by readout of poisoning-induced parity flips*

Jens Schulenburg, **Svend Krøjer**, Michele Burrello, Martin Leijnse and Karsten Flensberg  
[Physical Review B](#), Vol. 107, No. 12 (March 2023) p. L121401, Ref. [P4].

E *Non-Abelian holonomy of Majorana zero modes coupled to a chaotic quantum dot*

Max Geier, **Svend Krøjer**, Felix von Oppen, Charles M. Marcus, Karsten Flensberg and Piet W. Brouwer  
[ArXiv](#), arXiv:2304.06754 [cond-mat.mes-hall] (April 2023), Ref. [P5].

In addition to research work and teaching duties, I also created, lectured and held exercise classes in a 7.5 ECTS course titled “*Superconducting qubits in architectures for quantum computing*” which was offered in the spring of 2023 at the University of Copenhagen.

## **Part I**

# **Introduction**





---

## Coherent quantum systems

This chapter motivates the study of highly coherent quantum systems in the context of quantum computing. We will see how elementary notions in quantum mechanics naturally lead to concepts such as qubits and universal gate sets. While this introduction is based on several classic textbooks [29, 31–33], we try to provide a more conceptual perspective on the well-established field of quantum computing which we do not claim to be exhaustive. We assume the reader has some knowledge of quantum mechanics, linear algebra and group theory.

For the purpose of this introduction, we decide that we want to control all relevant aspects of a physical quantum system. After all, being able to change, rearrange and manipulate objects in the classical world can be quite useful. Initially, several relevant questions concerning this effort are likely to surface: What is a coherent quantum system? How can a coherent quantum system be controlled? What is being manipulated when a quantum system is operated? When do we achieve complete or “universal” control of a quantum system? Answering such questions requires an understanding of how quantum systems are described in the first place. We therefore begin this section with a brief introduction to basic concepts in quantum mechanics.

## Quantum systems

In much the same way your position in space can be described by a vector of coordinates, a physical quantum system is mathematically characterized by quantum states. Like the position vector, a quantum state also lives in a vector space called the Hilbert space. The quantum states represent the energy levels of the system and these are often discrete, or as the terminology goes, “quantized”. When the total energy in the system is low, the low-energy states of the system are occupied. Exciting the system from a low-energy state to a high-energy state typically results in the system returning to a low-energy configuration by relaxing the high-energy state to a lower-energy state. The quantum system is unavoidably coupled to its surroundings and it can shed the excess energy to this environment. The characteristic time of such a relaxation process is one way of quantifying the coherence of the quantum system. Thus, systems with short relaxation times are not very coherent. Ordinarily, the higher the energy of an excitation, the faster it relaxes. For this reason, it appears to be reasonable to consider systems with only a few energy levels, or at least to consider only the low-energy states of a larger system. As we discuss later, small quantum systems combine very efficiently such that the size of the Hilbert space (the number of total quantum states) quickly gets large. It is therefore not restrictive to start by considering small quantum systems.

## Introducing the two-level system

The two-level system (TLS) is the smallest quantum system we can consider. We denote its two energy states by  $|0\rangle$  and  $|1\rangle$  such that the energy of  $|0\rangle$  is assumed smaller than the energy of  $|1\rangle$ . At a given point in time, a general state  $|\psi\rangle$  (i.e. configuration) of a TLS is a superposition of  $|0\rangle$  and  $|1\rangle$  and can be parameterized by real numbers  $(a, b, \lambda, \phi)$ ,

$$|\psi\rangle = e^{i\lambda} \left( a|0\rangle + b e^{i\phi} |1\rangle \right). \quad (1.1)$$

For a TLS on its own, the global phase  $\lambda$ , does not carry any physical meaning. Further, the quantum state needs to be normalized, meaning that its inner product equals unity  $\langle\psi|\psi\rangle = a^2 + b^2 = 1$ , and this condition relates the weights  $b = \sqrt{1 - a^2}$ . The number of free parameters describing the state of the TLS is therefore two: one parameter quantifies the phase between  $|0\rangle$  and  $|1\rangle$ , and

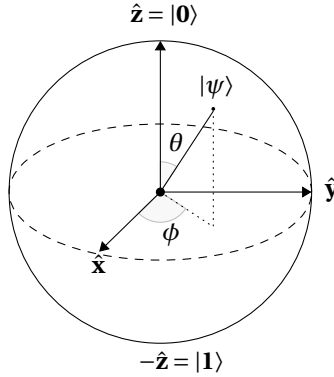


Fig. 1.1: The Bloch sphere representation of a quantum state. The parameterization in Eq. (1.2) traces out a sphere such that every point on the sphere correspond to a quantum state. Adapted from “How to Draw a Bloch Sphere?” .

one parameter quantifies the distribution of weight on  $|0\rangle$  and  $|1\rangle$ . We wish to emphasize that the superposition of quantum states is a feature not found in classical physics and it is one of the essential resources in coherent quantum systems.

The weights  $a, b$  and the relative phase  $\phi$  are also relevant in the description of decoherence. The relaxation of a higher-energy state  $|1\rangle$  to a lower-energy state  $|0\rangle$  can be thought of as changing the state  $|\psi\rangle$  by reducing the weight  $b$  and increasing  $a$ . Another decoherence channel is dephasing, which acts to randomly offset  $\phi$  by a small amount. While this description of decoherence is superficial, it can sometimes be useful to picture decoherence as a process that unpredictably changes the quantum state. We discuss decoherence in more precise terms in chapter 3 and we will for now assume that our quantum systems remain perfectly coherent.

## Operating the two-level system

The quantum state  $|\psi\rangle$  can also be visualized as a point on the sphere, see Fig. 1.1. The unit “length” of a quantum state can be thought of as the radius of the sphere and its two free parameters are equivalent to longitude ( $\phi$ ) and latitude ( $\theta$ ) coordinates. This representation is known as the Bloch sphere representation of a quantum state and it recasts Eq. (1.1) to

$$|\psi\rangle = \cos(\theta/2)|0\rangle + e^{i\phi}\sin(\theta/2)|1\rangle. \quad (1.2)$$

The Bloch sphere is especially useful when considering transformations of states. An operation that changes the state  $|\psi\rangle$  to another state  $|\psi'\rangle$  corresponds to a rotation of  $|\psi\rangle$  on the Bloch sphere. Said differently, all possible operations that can change the configuration of a TLS are described by all possible rotations on the Bloch sphere. Using this mathematical formulation of how to operate TLSs, we can connect it to the quantum dynamics which we hope to be able to control.

In the Schrödinger picture of quantum mechanics, the time-evolution of a quantum state is given by a unitary operator  $U$ , updating the state  $U|\psi\rangle = |\psi'\rangle$ . Since we are considering states living in a two-dimensional Hilbert space where global phases do not carry meaning, we are interested in

special unitary matrices of dimension two,  $U \in \text{SU}(2)$ .<sup>1</sup> These matrices are essentially equivalent to rotations on the Bloch sphere.<sup>2</sup> To better understand how unitaries relate to rotations on the Bloch sphere, we consider the generators of  $\text{SU}(2)$ -matrices, the Pauli matrices,

$$\sigma_x = \begin{pmatrix} 0 & 1 \\ 1 & 0 \end{pmatrix}, \quad \sigma_y = \begin{pmatrix} 0 & -i \\ i & 0 \end{pmatrix}, \quad \sigma_z = \begin{pmatrix} 1 & 0 \\ 0 & -1 \end{pmatrix}. \quad (1.3)$$

In this basis, we may identify  $|0\rangle = (1, 0)^T$  and  $|1\rangle = (0, 1)^T$ . A rotation on the Bloch sphere around a unit vector  $\mathbf{n} = (n_x, n_y, n_z)$  by angle  $\alpha$ , can be realized via a unitary transformation,

$$U = e^{-i\alpha(\mathbf{n}\cdot\boldsymbol{\sigma})/2} = \cos(\alpha/2) - i(\mathbf{n}\cdot\boldsymbol{\sigma})\sin(\alpha/2), \quad (1.4)$$

where  $\boldsymbol{\sigma} = (\sigma_x, \sigma_y, \sigma_z)^T$  is a vector of Pauli matrices. In this way, the Pauli matrices can help parameterize, or “generate”, the  $\text{SU}(2)$ -matrices. As a simple example, a transformation that flips the states according to  $|0\rangle \rightarrow |1\rangle$ ,  $|1\rangle \rightarrow |0\rangle$  can be accomplished by  $U = e^{i\pi\sigma_x/2}$  and corresponds to a rotation around the  $x$ -axis by angle  $\pi$ .<sup>3</sup>

The prescription in Eq. (1.4) can be compared to the direct expression of the time-evolution operator due to the Schrödinger equation,

$$U = e^{-iHt}, \quad (1.5)$$

here assuming the Hamiltonian  $H$  to be time-independent for simplicity. The Hamiltonian is a Hermitian matrix describing the energy of a quantum system and as Eq. (1.5) shows, it is also responsible for the time-evolution of the system. For our TLS, the Hamiltonian is two-dimensional and it turns out that all  $2 \times 2$  (traceless<sup>4</sup>) Hermitian matrices are spanned by the Pauli matrices via

$$H = g_x\sigma_x + g_y\sigma_y + g_z\sigma_z, \quad (1.6)$$

where  $g_i$  are real parameters that we collect in a vector  $\mathbf{g} = (g_x, g_y, g_z)$ . By comparing Eqs. (1.5)-(1.6) to Eq. (1.4), we identify the following relations,

$$\mathbf{n} = \mathbf{g}/|\mathbf{g}|, \quad (1.7)$$

$$\alpha = 2|\mathbf{g}|t. \quad (1.8)$$

Thus, normalizing the  $\mathbf{g}$ -vector gives the rotation axis of the Bloch sphere and its length multiplied by the time  $t$  gives the rotation angle  $\alpha$ . Importantly, interacting with the TLS by varying the parameters  $\mathbf{g}$  is a coherent process that preserves the quantum mechanical behavior of the TLS.

The considerations leading to Eqs. (1.7)-(1.8) provide a direct way of relating the energy of the system, encoded in the Hamiltonian, to the change of a quantum state. While the Hamiltonian description is useful, we still need to connect it to physical systems to see how turning experimental knobs changes quantum states. In chapter 3, we consider superconducting circuits as qubits and show how the Hamiltonian can be derived in such systems.

<sup>1</sup>Some unitaries are “special” in the sense that their determinant equals one.

<sup>2</sup>To fully appreciate this correspondence, the interested reader is encouraged to look into the group theory of  $\text{SU}(2)$  and the three-dimensional rotation group  $\text{SO}(3)$ , see for example [33].

<sup>3</sup>Up to a global phase factor.

<sup>4</sup>When adding the identity  $\mathbb{1}$  to the Pauli matrices, the Hermitian matrices with non-zero trace are spanned. However, the trace of the Hamiltonian in Eq. (1.5) only gives rise to a global phase and is equivalent to a constant shift of the energy.

---

## Simplifying operations

We may consider whether all matrices in  $SU(2)$  are needed to completely control the TLS. It turns out that a subset of  $SU(2)$  is sufficient to move any state  $|\psi\rangle$  on the Bloch sphere to any other state  $|\psi'\rangle$ . For example, a rotation on the Bloch sphere around the  $z$ -axis can be decomposed as rotations around the  $x$ - and  $y$ -axes,

$$e^{-i\alpha\sigma_z/2} = e^{-i\pi\sigma_x/4} e^{-i\alpha\sigma_y/2} e^{i\pi\sigma_x/4}, \quad (1.9)$$

by virtue of the anti-commutation properties of the Pauli-matrices,  $[\sigma_x, \sigma_y] = 2i\sigma_z$ . In general, any rotation on the Bloch sphere can indeed be decomposed as rotations around two fixed axes. While significantly reducing the number of basic operations needed to achieve complete control, it still leaves a continuum of rotation angles. Remarkably, it turns out that the entirety of  $SU(2)$  can be covered by just a few elements. Or rephrased; despite the continuum of possible rotations on the Bloch sphere, a small set of rotations with fixed axes and angles are sufficient to transform any state to any other. This is the content of the Solovay-Kitaev theorem. It roughly states that if you are clever about picking rotation axes and angles, as few as two specific rotations are needed.<sup>5</sup> The small caveat, however, is that an arbitrary rotation can not be exactly decomposed. The way the Solovay-Kitaev theorem works is to approximate any rotation  $U$  by a sequence of fixed rotations. The utility of the theorem lies in the fact that even very good approximations can be accomplished by relatively short sequences of rotations.<sup>6</sup> While the time  $t$  in Eq. (1.8) is a good resource for getting any rotation angle, some quantum systems are restricted in the way they can be interacted with, resulting in few ways the states can be rotated.<sup>7</sup> Under such circumstances, the Solovay-Kitaev theorem becomes extremely useful.

## Qubit intermezzo

When talking about performing operations on TLSs, the common language is often to instead talk about applying gates on qubits (quantum bits). Using this terminology naturally gives associations to computing or information theory. To align with the literature, we will also adopt this language moving forward. The exact meaning of “qubit”,<sup>8</sup> however, can depend on context; sometimes referring to a unit of quantum information, the abstract representation of a quantum system (i.e. a TLS) or the physical quantum system itself. It is up to the reader to decide whether the quantum computing connotations are read into the word “qubit” as we continue.

To familiarize the reader with the vocabulary, we provide a quick summary of the preceding sections using this terminology: If we want to perform any kind of logic on a qubit, we need a sufficient number of gates, a so-called universal gate set.<sup>9</sup> Single-qubit gates are elements in  $SU(2)$  and can be related to the dynamics of the qubit via the qubit Hamiltonian. Applying a single-qubit gate can be pictured as rotating the qubit state on the Bloch sphere. A universal set of single

---

<sup>5</sup>A common set is the Hadamard gate  $H = \frac{1}{\sqrt{2}} \begin{pmatrix} 1 & 1 \\ 1 & -1 \end{pmatrix}$  and “magic” gate  $T = \begin{pmatrix} 1 & 0 \\ 0 & e^{i\pi/4} \end{pmatrix}$ . The phase gate  $S = T^2$  is often included but not strictly necessary, see Ref. [29] for further details.

<sup>6</sup>For a rigorous definition and expanded discussion, see Ref. [29].

<sup>7</sup>For example, this is true for Majorana zero modes as we discuss in later sections.

<sup>8</sup>Interestingly, despite the different ways “bit” and “qubit” are used, they both originated in the context of (quantum) information theory [34, 35] some years after the ideas of (quantum) computers were conceived.

<sup>9</sup>Strictly speaking, a gate set is only universal when a two-qubit gate is included, as we elaborate in the upcoming section.

qubit gates can either be a continuous subset of  $SU(2)$  or be finite, by virtue of the Solovay-Kitaev theorem.

## Combining two qubits with entanglement

Performing universal gates on a single qubit is certainly an achievement but the goal is to control a quantum system of any size. For this purpose, we imagine having two qubits at our disposal. Left disconnected, we may count the number of states and free parameters describing this two-qubit system: There are  $2 \times 2 = 4$  qubit states<sup>10</sup> and  $2 + 2 = 4$  free parameters to describe the states. Had we started with a true 4-level system, we would have counted the number of free parameters to be  $2 \times 4 - 2 = 6$ ; one complex parameter (equaling two real parameters) for each level minus the global phase parameter and the normalization condition. The two non-interacting qubits are missing two degrees of freedom and do therefore not constitute a general 4-level system.

The missing parameters correspond to states in the Hilbert space: The states formed by uncoupled qubits are referred to as product states and they form a subset of all the states in the Hilbert space. The remaining states are referred to as entangled states which can only be realized if the qubits are entangled. Entanglement is the quantum property that allows collections of qubits to emulate larger quantum systems and it requires the qubits to interact. We can also think about entanglement as a form of superposition. Where superposition often refers to superposition within a single qubit as in Eq. (1.1), superposition between qubits gives rise to entanglement. As an example, we consider the superposition of two different product states,  $\frac{1}{2}(|0\rangle \pm |1\rangle)(|0\rangle \pm |1\rangle)$ , whose superposition results in

$$\frac{1}{\sqrt{2}} \left[ \frac{1}{2} (|0\rangle + |1\rangle)(|0\rangle + |1\rangle) - \frac{1}{2} (|0\rangle - |1\rangle)(|0\rangle - |1\rangle) \right] = \frac{1}{\sqrt{2}} [|01\rangle + |10\rangle], \quad (1.10)$$

which is indeed an entangled state.<sup>11</sup> Along with superposition, entanglement is the key resource in coherent quantum systems.

In the language of gates and transformations, gates on non-interacting qubits are simply single-qubit gates acting on each of the qubits,  $U_1 \otimes U_2 \in SU(2) \otimes SU(2)$ . These are non-universal as they can not transform any two-qubit state to any other two-qubit state (never a product state to an entangled state). Instead, proper two-qubit gates living in  $SU(4) \supset SU(2) \otimes SU(2)$  are required for universality in the two-qubit setup.

As for the single-qubit gates in  $SU(2)$ , it is natural to consider the smallest subset of  $SU(4)$  that provides gate universality in the two-qubit system. In addition to the single-qubit gates, it turns out that a single entangling two-qubit gate is enough.<sup>12</sup> In this way, the two-qubit gate takes care of the generation of entanglement (or superposition between qubits) and the single-qubit gates transform the entangled state as desired.

<sup>10</sup>Labelling the qubits  $i = 1, 2$  and using the notation  $|\psi\rangle_1 \otimes |\phi\rangle_2 = |\psi\phi\rangle$ , the states are  $|00\rangle, |01\rangle, |10\rangle, |11\rangle$ .

<sup>11</sup>Here is a trick to check if a state is entangled or not: For a state  $a|00\rangle + b|01\rangle + c|10\rangle + d|11\rangle$ , if  $ad = bc$ , then it is a product state. The proof is left as an exercise.

<sup>12</sup>This is the most common way of reaching universality. It is also possible to only use a two-qubit gate with three parameters, the Barenco gate, to achieve universality.

---

## Large qubit systems

Combining two qubits worked well, what about combining  $N$  qubits to describe large quantum systems with  $2^N$  states? What additional 3-qubit gates, 4-qubit gates or  $N$ -qubit gates do we need for universality in  $SU(2^N)$ ? Perhaps surprisingly, no additional resources are required. As long as the qubits are well-connected<sup>13</sup>, a basic result in linear algebra shows that single and two-qubit gates are sufficient to decompose any gate in  $SU(2^N)$ . This is maybe not so odd considering the following setup:

Suppose two qubits  $a, c$  are connected to a third qubit  $b$ . Then, any entangled relationship between qubits  $a$  and  $b$ , and  $b$  and  $c$  can be established by universal single- and two-qubit gates. Conceivably, this can be done in a manner where qubit  $b$  mediates the interaction between qubits  $a$  and  $c$ . For example, imagine qubits  $a$  and  $b$  in a balanced superposition  $(|01\rangle_{ab} + |10\rangle_{ab})/\sqrt{2}$  and qubits  $b$  and  $c$  are in a similar superposition of  $(|10\rangle_{bc} + |01\rangle_{bc})/\sqrt{2}$ . Disregarding the mediating qubit  $b$ , we see that the state is an entangled state of qubits  $a$  and  $c$ :  $(|00\rangle_{ac} + |11\rangle_{ac})/\sqrt{2}$ .

Being able to perform universal operations on qubit systems almost achieves our initial goal of being able to completely control arbitrary quantum systems. As we uncover next, two subtle details remain before we claim full command of quantum systems.

## The final steps

Universal gates are certainly necessary, however, if the initial qubit state is unknown, gates are of little use. Therefore, some method of initializing the qubits is required. It is not important what the initial state resulting from an initialization procedure is as long as we know what it is. Then, single-qubit gates can be applied to achieve whichever state we desire.

After initialization, we can in principle calculate the behavior of the quantum system as we manipulate it by multiplying unitary matrices. The point of controlling a physical quantum system, however, is that we do not have to do these mathematical gymnastics. The quantum system is “computing” all these details for us. To access the final result of this process, we need a way of extracting information from the quantum system, i.e. measuring the qubits. This is necessarily an incoherent process that translates quantum information to classical information. Measurements of the final qubit states are the last element we need to finally achieve full control of quantum systems.

## Criteria for quantum computing

Our entire discussion of the different aspects of manipulating quantum systems is quite general and does not pertain to any particular physical realization of qubits. It turns out that such a universal description of quantum computation can be highly useful as guiding principles in designing physical quantum computers. In the year 2000, David DiVincenzo collected similar considerations in the so-called DiVincenzo criteria which succinctly describes the requirements for realizing quantum computers [36]:

1. A scalable physical system with well-characterized qubits.
2. The ability to initialize the state of the qubits to a simple fiducial state.

---

<sup>13</sup>In the sense that any qubit is connected to all qubits via other qubits.

3. Long relevant decoherence times, much longer than the gate operation time.
4. A “universal” set of quantum gates.
5. A qubit-specific measurement capability.

These criteria also take into account challenges regarding the physical realization of quantum computers, extending the theoretical considerations presented here. A few details are noteworthy: Criterion (1) refers both to entanglement as a resource for scaling quantum systems, and also to the practical difficulties in combining many qubits in the same device. Additionally, it adds the sound requirement of being able to experimentally characterize the physical qubits. Criterion (3) does not assume perfect coherence in the qubits and instead requires the coherence time should be longer than the total run-time needed in a quantum computation. Criteria (2), (4), (5) are much the same as in our discussion.

Following this introduction to concepts in quantum computing, we consider two different qubit platforms: In Chapter 2, we introduce Majorana zero modes which can be used as a basis for topological quantum computers. In Chapter 3, we introduce superconducting qubits and discuss decoherence in this platform.



---

## Majorana qubits

This chapter introduces Majorana zero modes (MZMs) and some of their exotic properties. MZMs are protected against noise and they enable certain gate operations that are also noise-protected. For these reasons, qubits based on MZMs appear to be a natural choice, however, experimental challenges prohibit reliable realization and manipulation of Majorana zero modes. This chapter is based on review articles found in Refs. [37–48].

## Majorana operators

From an algebraic perspective, Majorana zero modes are described by Majorana operators in the same way Fermions are described by Fermionic creation and annihilation operators. In fact, Majorana operators are derived from Fermionic operators as we see below. First, we introduce Fermionic creation and annihilation operators which are operators that create and remove qubit excitations. We denote the creation operator of qubit  $i$  by  $d_i^\dagger$  such that  $d_i^\dagger|0\rangle_i = |1\rangle_i$ . The Fermionic operators respect canonical anticommutation relations given by

$$\{d_i^\dagger, d_j\} = \delta_{ij}, \quad (2.1)$$

where all other anticommutators with the Fermionic operators are zero. The Fermionic operators can, for example, describe a quantum dot that can be occupied by a single electron. In this scenario, the number operator defined by  $n_i = d_i^\dagger d_i$  measures whether an electron occupies the quantum dot  $n_i|1\rangle_i = |1\rangle_i$  or not  $n_i|0\rangle_i = 0$ .

To introduce Majorana operators, we make the following consideration: Fermionic operators are complex operators which we can formally write in terms of their “real” and “imaginary” parts,

$$d_i = (\gamma_{2i-1} + i\gamma_{2i})/2, \quad (2.2)$$

$$d_i^\dagger = (\gamma_{2i-1} - i\gamma_{2i})/2, \quad (2.3)$$

where the Majorana operators are denoted by  $\gamma_j$ . The Majorana operators are “real” in the sense that  $\gamma^\dagger = \gamma$  is always satisfied. Moving forward, we will refer to Majorana operators and MZMs colloquially as Majoranas. Since the parent Fermionic operators satisfy canonical anticommutation relations, the associated Majoranas obey

$$\{\gamma_i, \gamma_j\} = 2\delta_{ij}. \quad (2.4)$$

Pairs of Majoranas can be used to measure the parity of a Fermion, also known as fusing the Majorana pair. Since  $n_i = (1 + i\gamma_{2i-1}\gamma_{2i})$ , the occupancy of a state  $n_i = 0, 1$  corresponds to reading out the parity of the Majoranas pair  $i\gamma_{2i-1}\gamma_{2i} = \pm 1$ . It turns out that it is possible to perform gate-equivalent operations by fusing different Majoranas pairs in a certain order. This procedure of achieving gate operations is known as fusion-based or “measurement only”. We refer the reader to Refs. [49–59] for literature on fusion-based operations in Majorana systems. Instead, we focus on another curious way that gate operations can be performed on Majorana qubits.

Formulating Fermionic operators in terms of Majoranas makes it possible to perform unconventional basis changes by fusing different pairs of Majoranas. As an example, we consider four Majoranas  $\gamma_1, \dots, \gamma_4$  which we can group into two qubits as qubit 1 ( $\gamma_1, \gamma_2$ ) and qubit 2 ( $\gamma_3, \gamma_4$ ) or as qubit  $\tilde{1}$  ( $\gamma_2, \gamma_3$ ) and qubit  $\tilde{2}$  ( $\gamma_1, \gamma_4$ ). The corresponding annihilation operators of these qubits are

$$d_1 = (\gamma_1 + i\gamma_2)/2, \quad d_2 = (\gamma_3 + i\gamma_4)/2, \quad (2.5)$$

$$\tilde{d}_1 = (\gamma_2 + i\gamma_3)/2, \quad \tilde{d}_2 = (\gamma_1 + i\gamma_4)/2, \quad (2.6)$$

which corresponds to a basis change of Fermionic operators given by

$$d_1 = \frac{1}{2}(\tilde{d}_2 + \tilde{d}_2^\dagger) + \frac{i}{2}(\tilde{d}_1 + \tilde{d}_1^\dagger), \quad (2.7)$$

$$d_2 = \frac{1}{2}(\tilde{d}_2 - \tilde{d}_2^\dagger) - \frac{i}{2}(\tilde{d}_1 - \tilde{d}_1^\dagger). \quad (2.8)$$

This basis change of operators results in a change of basis of qubit states which is given by<sup>1</sup>

$$|00\rangle = \frac{1}{\sqrt{2}} (|\widetilde{00}\rangle + i|\widetilde{11}\rangle), \quad (2.9)$$

$$|01\rangle = \frac{1}{\sqrt{2}} (|\widetilde{01}\rangle + i|\widetilde{10}\rangle), \quad (2.10)$$

$$|10\rangle = \frac{1}{\sqrt{2}} (|\widetilde{01}\rangle - i|\widetilde{10}\rangle), \quad (2.11)$$

$$|11\rangle = \frac{1}{\sqrt{2}} (|\widetilde{00}\rangle - i|\widetilde{11}\rangle). \quad (2.12)$$

Here, states on the left-hand side denote the qubit states of qubit 1 and 2, and the states on the right-hand side denote the qubit states of qubits  $\tilde{1}$  and  $\tilde{2}$ . As we discuss later, Majorana systems conserve the total parity and we can therefore focus our attention on, for example, the even parity sector containing the states  $|00\rangle$  and  $|11\rangle$ . In this way, the four Majoranas only encode a single qubit due to parity selection. While this is not the most efficient way of encoding qubits in a collection of Majoranas, it presents a straightforward method of performing single qubit gates as we show in the next section.

## Phase-based operations

The change of basis in Eqs. (2.9)-(2.12) makes it possible to execute gates by only controlling the relative phase between states. By defining  $|00\rangle = |0\rangle_q$  and  $|11\rangle = |1\rangle_q$  as qubit states, the relative phase can be changed by a  $z$ -axis rotation  $U_z = e^{-i\phi\sigma_z/2}$  as can be seen by letting  $U_z$  act on a generic state  $|\psi\rangle = \cos(\theta/2)|0\rangle_q + \sin(\theta/2)|1\rangle_q$ ,

$$U_z|\psi\rangle = e^{-i\phi/2}\cos(\theta/2)|0\rangle_q + e^{i\phi/2}\sin(\theta/2)|1\rangle_q. \quad (2.13)$$

The phase gate can be achieved in different ways that often rely on manipulating the geometric phase of qubit states as we discuss more in Chapter 4 and below. We can also consider performing a phase gate in the tilde basis formed by states  $|\widetilde{00}\rangle$  and  $|\widetilde{11}\rangle$ . The corresponding phase gate is given by  $\tilde{U}_z = e^{-i\phi\tilde{\sigma}_z/2}$  where  $\tilde{\sigma}_z$  is the Pauli  $Z$  operator in the tilde basis. Acting with  $\tilde{U}_z$  on the state  $|\psi\rangle$  results in

$$\tilde{U}_z|\psi\rangle = \cos\left(\frac{\theta + \phi}{2}\right)|0\rangle_q + \sin\left(\frac{\theta + \phi}{2}\right)|1\rangle_q \quad (2.14)$$

$$= U_y|\psi\rangle. \quad (2.15)$$

<sup>1</sup>A derivation of this simple result can be found in my Masters thesis, see Ref. [P6].

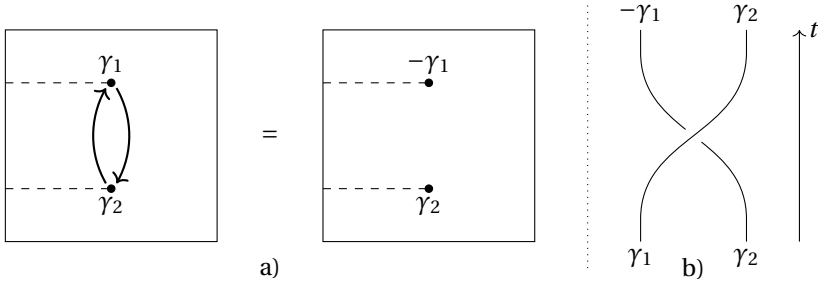


Fig. 2.1: Adapted from [P6]. a) The exchange of two Majoranas gives a sign to one of the Majorana operators. Exchange is also known as a half-braid. (b) A diagram of the half-braid where the time-axis is indicated.

Evidently, the phase gate in the tilde basis corresponds to a  $y$ -axis rotation in the qubit basis  $\tilde{U}_z = U_y = e^{-i\phi\sigma_y/2}$ . If it is possible to arbitrarily choose the rotation angle  $\phi$ , it is therefore possible to perform any rotation on the Bloch sphere with these phase gates. As a result, the continuous set of phase gates  $\{U_z, \tilde{U}_z\}$  can produce any single qubit gate. It turns out that exchanging Majoranas, so-called braiding, results in phase gates with a specific rotation as we describe in the next section.

### Non-Abelian anyons

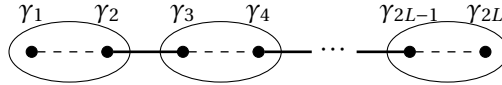
Being a constituent of a Fermionic operator, it is relevant to consider what exchange statistics Majoranas obey. The answer is that Majoranas are so-called non-Abelian anyons, a class of particles outside of ordinary Fermions or Bosons. When particles are confined in two dimensions they can circumvent the spin-statistics theorem and can achieve any phase upon exchange [60–63]. The spin-statistics theorem states that all particles in three dimensions are either Fermions (half-integer spin) or Bosons (integer spin). Upon exchange of Fermions, their combined wave function changes sign which is not the case for Bosons whose wave function remains unchanged. When anyons are exchanged, the wave function can acquire any phase  $e^{i\phi}$  that can also be matrix-valued as is the case for non-Abelian anyons. Successive exchanges of different non-Abelian anyons constitute non-commuting operations. As an example, the exchange of two Majoranas  $(\gamma_1, \gamma_2)$  results in  $\gamma_1 \rightarrow \gamma_2$  and  $\gamma_2 \rightarrow -\gamma_1$  [64], see Fig. 2.1. This operation is equivalent to the unitary  $U_{12} = e^{\frac{\pi}{4}\gamma_2\gamma_1}$  which can be rewritten as

$$U_{12} = e^{-i\frac{\pi}{4}(d_1 d_1^\dagger - d_1^\dagger d_1)} \quad (2.16)$$

$$= e^{-i\frac{\pi}{4}\sigma_z} \quad (2.17)$$

where the second equality holds when the operator acts on the  $|0\rangle_q$  and  $|1\rangle_q$  states defined in the previous section. Similarly, it follows that the exchange of Majoranas  $(\gamma_2, \gamma_3)$  results in a unitary  $U_{23} = e^{-i\pi\sigma_y/4}$  when acting on  $|0\rangle_q$  and  $|1\rangle_q$ .

Compared to the discussion in Sec. 2, we see that exchange operations exactly correspond to phase gates with fixed rotation angle  $\phi/2 = \pi/4$  and that the two exchange operations do not commute  $[U_{12}, U_{23}] = \gamma_1\gamma_3$  as expected from non-Abelian anyons. As a result, the exchange operations only give rise to a non-universal set of single qubit gates. In the context of the Solovay-Kitaev theorem, the exchange operations lack the magic gate  $T = e^{-i\frac{\pi}{8}\sigma_z}$  before the gate set is



b)

Fig. 2.2: Adapted from [P6]. A schematic of the Kitaev chain where dashed lines indicate on-site couplings  $\mu$  and solid lines indicate hopping  $t$  between neighboring cells. When the on-site coupling is small, Majoranas on the edge are approximately decoupled from the rest of the chain.

universal.<sup>2</sup> Depending on how qubits are encoded in a collection of Majoranas, two-qubit gates can either be realized via exchange operations or in a fusion-based approach, see Refs. [46, 48–51, 56, 57, 65] for further details. To achieve a universal gate set using Majoranas, it is therefore necessary to perform an operation that is not based on braiding or measurements. In Chapter 4, we study such a universal gate scheme that goes beyond real space braiding. In the next section, we consider how localized Majoranas can appear in physical systems.

## The Kitaev chain

Fermionic operators can describe the presence of an electron on a single site or in a given orbital. In this setting, the Majorana description of Fermionic operators is not physically motivated and it does not make sense to treat Majoranas as individual entities. We therefore seek to physically separate Majoranas to address them individually. To do so, we consider a long chain of  $L$  sites where each site can host a single electron described by a Fermionic operator  $d_i^\dagger = (\gamma_{2i-1} - i\gamma_{2i})/2$ , see Fig. 2.2. We can decouple and separate Majoranas at the ends of the chain by coupling adjacent Majoranas  $\gamma_{2i}$  and  $\gamma_{2i+1}$  as indicated with black lines in Fig. 2.2. The chain physically separate Majoranas  $\gamma_1$  and  $\gamma_{2L}$  at its ends but this feature appears to be sensitive to additional couplings. To address this potential issue, we introduce small couplings between Majoranas  $\gamma_{2i-1}$  and  $\gamma_{2i}$  as indicated by dashed lines in Fig. 2.2. We analyze the influence of the small coupling by considering the system Hamiltonian given by

$$H = -i\frac{\mu}{2} \sum_j^L \gamma_{2j-1} \gamma_{2j} + it \sum_j^{L-1} \gamma_{2j} \gamma_{2j+1}, \quad (2.18)$$

where  $\mu$  is the small on-site coupling and  $t$  is the tunnel coupling between neighboring sites<sup>3</sup>. For  $\mu = 0$ , the boundary Majoranas  $\gamma_1$  and  $\gamma_{2L}$  decouple from the Hamiltonian  $[\gamma_{1/2L}, H] = 0$  and together they form a non-local electronic state described by  $d^\dagger = (\gamma_1 - i\gamma_{2L})/2$ .

In the presence of small, non-zero  $\mu$ , we can attempt to find approximately decoupled Majorana modes  $\gamma_a$  and  $\gamma_b$  that commute with the Hamiltonian and reduce to  $\gamma_{a/b} \rightarrow \gamma_{1/2L}$  in the limit  $\mu = 0$ . To construct these decoupled modes, we consider commutators between Majoranas and the

<sup>2</sup>The Hadamard gate can be decomposed as  $H = U_{12}U_{23}U_{12}$ .

<sup>3</sup>Majorana coupling terms require a factor of  $i$  to ensure Hermiticity of the Hamiltonian

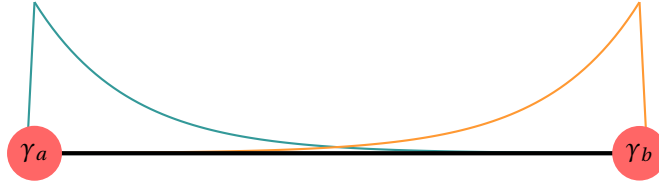


Fig. 2.3: Schematic of exponentially localized Majoranas at the ends of a Kitaev chain. The small overlap of the wave functions around the middle of the chain gives rise to an exponentially small splitting of the energy of the Fermion formed by the  $\gamma_a$  and  $\gamma_b$ .

Hamiltonian,

$$[\gamma_1, H] = -i\mu\gamma_2, \quad (2.19)$$

$$[\gamma_3, H] = -i2t\gamma_2 - i\mu\gamma_4, \quad (2.20)$$

$$[\gamma_{2j-1}, H] = -i2t\gamma_{2j-2} - i\mu\gamma_{2j}, \quad (2.21)$$

$$[\gamma_{2j+1}, H] = -i2t\gamma_{2j} - i\mu\gamma_{2j+2}. \quad (2.22)$$

Here, we observe that an appropriate linear combination of  $\gamma_{2j-1}$  and  $\gamma_{2j+1}$  can cancel the  $\gamma_{2j}$  contribution in the commutator. For example,

$$\left[\gamma_1 - \frac{\mu}{2t}\gamma_3, H\right] = \frac{i\mu^2}{2t}\gamma_4, \quad (2.23)$$

which cancels the  $\gamma_2$  contribution and leaves a  $\gamma_4$  contribution that is smaller by a factor  $\mu/2t$  compared to Eq. (2.19). We can keep canceling such terms in the commutator until we run out of Majoranas in the chain. The resulting Majorana operator is

$$\gamma_a = \sum_j^L \left(\frac{-\mu}{2t}\right)^{j-1} \gamma_{2j-1}, \quad (2.24)$$

where

$$[\gamma_a, H] = -2it \left(\frac{-\mu}{2t}\right)^L \gamma_{2L}. \quad (2.25)$$

We have successfully identified a Majorana operator<sup>4</sup>  $\gamma_a^\dagger = \gamma_a$  whose commutator with the Hamiltonian is exponentially close to zero when the chain is long  $L \gg 1$  and the on-site coupling is small  $\mu < 2t$ . As can be seen from Eq. (2.24), the Majorana mode  $\gamma_a$  is also exponentially localized near the left end of the chain, see Fig. 2.3 for an illustration. At the right end of the chain, an analogous Majorana operator can be found  $\gamma_b = \sum_{j=L}^1 \left(\frac{-\mu}{2t}\right)^{L-j} \gamma_{2j}$  that anticommutes with the Majorana at the left end  $\{\gamma_a, \gamma_b\} = 0$ . Together, this Majorana pair forms a non-local Fermionic operator  $b^\dagger = (\gamma_a - i\gamma_b)/2$  whose constituent Majoranas are physically separated and can be addressed individually as desired.

By rewriting the Hamiltonian in Eq. (2.18) using the Fermionic operators  $d_i^\dagger$ , we obtain a model that is easier to interpret,

$$H = -\mu \sum_j^L (d_j^\dagger d_j - 1/2) - t \sum_j^{L-1} (d_j^\dagger d_{j+1} + \text{H.c.}) + \Delta \sum_j^{L-1} (d_j d_{j+1} + \text{H.c.}). \quad (2.26)$$

<sup>4</sup>The Majorana operator can be normalized to satisfy  $\tilde{\gamma}_a^2 = 1$  via  $\tilde{\gamma}_a = \sqrt{1 - \mu/2t} \cdot \gamma_a$ .

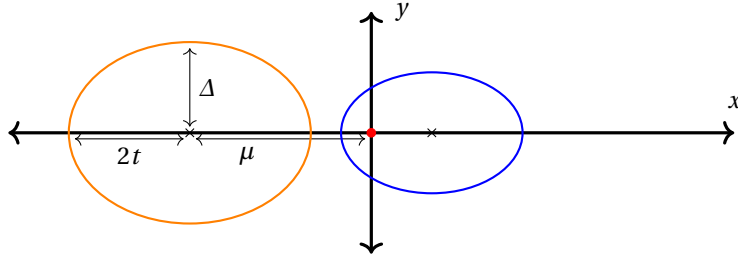


Fig. 2.4: Adapted from [P6]. The energy dispersion of the Kitaev chain is represented as a vector  $v = (\mu + 2t \cos(k), \Delta \sin(k))^T$  where the momentum  $k$  runs from  $-\pi$  to  $\pi$ . When  $|\mu| < 2t$ , the trace of the vector (blue) winds around the origin, resulting in a winding number of  $+1$ . When  $|\mu| > 2t$ , the trace (orange) does not wind around the origin and the winding number is zero. The two cases correspond to two distinct topological phases which are separated by a topological phase transition at  $|\mu| = 2t$  where the trace crosses the origin.

This model is known as the Kitaev chain [66] and it generalizes the example in Eq. (2.18). In Eq. (2.26), we identify  $\mu$  as the on-site energy,  $t$  as the strength of tunnel coupling between neighboring sites and  $\Delta$  as a superconducting pairing strength. In our example, we considered the special case where the superconducting gap equals the tunneling strength  $\Delta = t$ .<sup>5</sup> The Kitaev chain describes a one-dimensional, spinless  $p$ -wave superconductor in a tight-binding model. “Spinless” refers to the fact that spin is not involved. The electrons described by the Fermionic operators do carry spin but if a large magnetic field is applied, there will be a large energy cost involved in flipping a spin. For this reason, the Kitaev chain can be thought of as describing low-energy electrons constrained by a large magnetic field such that their spins are fixed. In this way, the magnetic field breaks time reversal symmetry which turns out to be an important ingredient to the formation of Majoranas as we discuss further below. A “ $p$ -wave” superconductor is a superconductor where Cooper pairs are formed between electrons with the same spin orientation as opposed to conventional  $s$ -wave superconductors which pairs spins of opposite orientation.<sup>6</sup>

The superconducting pairing  $\Delta$  results in a symmetry between particles and holes such that a hole state with energy  $-E$  has a mirrored particle state with energy  $E$ . Since Majoranas “are their own antiparticles” in the sense that  $\gamma^\dagger = \gamma$ , it forces Majoranas to always have zero energy. Particle-hole symmetry also conserves parity and leads to a degeneracy between even and odd parity sectors. Together with the breaking of time-reversal symmetry, these symmetry properties have profound consequences for the Kitaev chain. It turns out that the emergence of Majoranas in the Kitaev chain is a “topological” feature that is determined by the symmetries (or lack thereof) [44, 68]. As we saw in our proto-Kitaev chain example, exponentially localized Majoranas are present at the end of the chain when  $\mu < 2t$ . It turns out that a topological phase transition occurs at the point  $\mu = 2t$  that separates the topologically trivial phase ( $\mu > 2t$ ) from the topological phase ( $\mu < 2t$ ). In a topological phase transition, a gap closes and reopens, changing a so-called topological invariant that can be associated with each phase. Focusing on the Kitaev chain, its energy dispersion can be

<sup>5</sup>The general situation  $\Delta \neq t$  gives rise to a coupling term  $i(\Delta - t)/2 \sum_j^{L-1} \gamma_{2j-1} \gamma_{2j+2}$  in Eq. (2.18) and replaces  $t \rightarrow (\Delta + t)/2$  in the other coupling term.

<sup>6</sup>For this reason,  $p$ -wave superconductors are said to have a triplet pairing. Further, the orbital angular momentum of a  $p$ -wave type Cooper pair has eigenvalue  $m = 1$  [67].

found by Fourier transforming to  $k$ -space, resulting in

$$E(k) = \pm \sqrt{[\mu + 2t \cos(k)]^2 + \Delta^2 \sin^2(k)}. \quad (2.27)$$

At  $k = 0, \pi$ , the energy gap closes at exactly  $\mu = \pm 2t$  and the system undergoes a topological phase transition. The energy can be described as a vector  $E(k) = \pm |v(k)|$  where  $v = (\mu + 2t \cos(k), \Delta \sin(k))^T$  to uncover the topological invariant associated with the topological phase. In Fig. 2.4, we show traces of the vector  $v$  when  $k$  runs from  $-\pi$  to  $\pi$ . The trace of the vector forms an ellipse which encloses the origin in the topological regime  $|\mu| < 2t$ . In this case, the vector winds around the origin corresponding to a topological invariant that is the winding number, taking the value +1 (blue ellipse). The trivial phase corresponds to a situation where the ellipse (orange) does not enclose the origin and its winding number is therefore zero. An important property of localized Majoranas in this regard is that they are formed in the topological phase transition. As long as the Kitaev chain is in its topological regime, two Majoranas are well-separated and pinned to zero energy. Additionally, since the Fermion they form is non-local, any local perturbation is unable to change its parity. For these reasons, it is expected that qubits based on Majoranas can have exceptionally long coherence times.

The topological properties of the Kitaev chain are generic to systems that share the same symmetry properties (particle-hole symmetry and breaking of time-reversal). More generally, topological systems can be described by Altland-Zirnbauer symmetry classes [68–70] which is a framework that relates symmetries and the number of spatial dimensions to topological invariants and edge modes. This means that as long as a one-dimensional system exhibits the same symmetries as the Kitaev chain, Majoranas appear at the ends of this system in its topological phase. This is an instance of the so-called bulk-boundary correspondence that relates the topological phase in the bulk to localized modes on the edge. It turns out that no materials found in Nature exhibit  $p$ -wave superconductivity in the way described by the Kitaev chain. Instead, superconducting-semiconducting heterostructures can in principle be engineered to possess the same symmetry properties and be tuned to its topological phase to produce Majorana edge modes. In the next section, we present a brief discussion about experimental results in such systems that attempt to realize topological phases and Majoranas.

## Experiments

Super-semi heterostructures are flexible systems that provide the necessary ingredients to realize Majoranas. A one-dimensional semiconducting wire (e.g. InSb, InAs) can be electrostatically gated to control its chemical potential. As discussed in previous sections, the ability to control the on-site energy in the Kitaev chain is necessary to tune into the topological regime. Further, by (partially) covering the semiconducting wire with a superconductor (e.g. Al, NbTiN), superconductivity can be induced in the wire via the proximity effect. The superconducting gap, however, is reduced when a large magnetic field is introduced to polarize the spin direction and break time reversal. Another challenge is that the superconducting pairing appears to be required to be  $p$ -wave. As realized by Lutchyn et al. [71] and Oreg et al. [72] in 2010, this issue can be reconciled by spin-orbit interaction in the semiconducting wire. Spin-orbit interaction can arise from asymmetry in the device (Rashba type) or from asymmetry in the crystal lattice (Dresselhaus type) [73] and gives rise to a spin-chirality of electrons propagating in different directions along the wire. When the spin-orbit coupling is perpendicular to the external magnetic field, it allows for conventional



---

singlet pairing  $s$ -wave superconductivity to coexist with a relatively large magnetic field. In this way, superconductivity can be induced in a semiconducting wire while subject to a spin-polarizing magnetic field, effectively realizing a Kitaev chain. By appropriately tuning the chemical potential of the semiconducting wire the resulting super-semi heterostructure can in principle be tuned to the topological regime where Majoranas can be experimentally investigated. There exist other proposals for realizing Majoranas that utilize two-dimensional topological insulators [74, 75], magnetic insulators [76, 77], half-metals [78, 79], magnetic impurities [80], two-dimensional electron gases [81] and superconducting phase control [82]. Among the numerous proposals, the proximitized semiconductor nanowire is the most studied experimentally.

Several experiments show results that are in agreement with the realization of Majoranas. Among these results are the measurement of zero-bias peaks [83–88], the fractional Josephson effect [89], long parity lifetimes [90] and separation of bound states [91, 92]. Despite the immense effort and many experimental signatures of Majoranas, there have been no experiments that provide direct evidence for the topological nature of Majoranas that is based on fusion or braiding. Conclusive experiments that show Majorana physics are challenging to perform since disorder plays an important role in mesoscopic devices. One of the challenges in disordered wires is that disorder can break up the topological phase in segments, necessitating nanowires to not be too long in experiments (e.g. longer than a  $\sim 1 \mu\text{m}$  [91]). This is problematic as short wires partially fuse Majoranas and split the degeneracy. An arguably more profound aspect of disorder is that disorder-induced subgap states of non-topological origin (e.g. Andreev bound states) can mimic Majorana behavior [93, 94]. In principle, conspiring Andreev bound states can reproduce Majorana signatures that can be challenging to completely rule out in experiments. To address this issue, a topological gap protocol has been developed [95] which is comprised of different conductance measurements that together can provide a strong signature of Majoranas. Recently, an experiment [96] claims to have succeeded in satisfying the topological gap protocol, showing promising signatures before fusion or braiding-based experiments develop.



---

## Superconducting qubits

In this chapter, we introduce superconducting circuits as described in the framework of circuit quantum electrodynamics (cQED).<sup>1</sup> Several excellent resources cover this topic thoroughly [97–105] and we do not attempt to provide an exhaustive review of this field. Instead, we focus on selected parts relevant to the pertinent thesis and contextualize aspects related to circuit quantization, decoherence and noise protection. We base this chapter on the mentioned literature in Refs. [97–105].

## From device to Hamiltonian

Superconducting qubits are microscale superconducting circuits that typically consist of capacitors, inductors and Josephson junctions. Similar to classical circuit theory, these components are modeled as lumped elements with given capacitances, inductances and Josephson energies. The Josephson junction is an element that is unique to superconducting circuits and is formed when the superconducting wire (e.g. Al, Ta) is interrupted by a non-superconducting material. Josephson junctions are most commonly fabricated as superconductor-insulator-superconductor junctions where the insulating layer is an oxide formed at the interface of the superconductors. As predicted by Brian Josephson in 1962 [106], such superconducting junctions exhibit interesting current-phase and energy-phase relations. When the superconducting phase difference across the junction is  $\phi$ , the corresponding energy-phase relation is  $E_J(1 - \cos(\phi))$ , where  $E_J$  is referred to as the Josephson energy. It turns out that this simple relation has profound consequences for the ability to control qubits based on superconducting circuits. In this chapter, we uncover some of the interesting features of Josephson junctions.

When faced with a superconducting qubit in practice, the goal in cQED, or more specifically circuit quantization, is to obtain a quantum Hamiltonian description of the qubit. Below, we present a short overview of the standard recipe in circuit quantization. The starting point is the lumped-element circuit diagram of the superconducting device, see Fig. 3.1. The components (capacitors, inductors, junctions) connect superconducting islands which are represented by nodes in the diagram. Curiously, the starting point is a classical rather than a quantum mechanical description of the lumped-element model. While conventional superconductors can be described by a microscopic quantum theory, i.e. BCS theory, the emergence of a coherent superconducting state leads to a good macroscopic description of the superconducting islands in terms of the superconducting phase  $\phi$  and the number of Cooper pairs  $n$ . By initially treating the phase and charge variables as classical degrees of freedom, a Lagrangian description of the superconducting circuit can be obtained where each of the circuit elements contributes with energy terms in the Lagrangian. Then, via a Legendre transformation, the Hamiltonian can be constructed from the Lagrangian as is well-known from analytical mechanics. The variables  $\phi$  and  $n$  can finally be promoted to quantum operators with a canonical commutator relation. This recipe is incredibly useful as a method for going from a physical device to a quantum Hamiltonian description. Considering the discussion in Chapter 1, the Hamiltonian can further be related to the notions of qubits and gates. In practice, when employing the recipe presented here, several subtleties can arise. In the following part, we develop the circuit quantization recipe as we introduce different superconducting circuits.

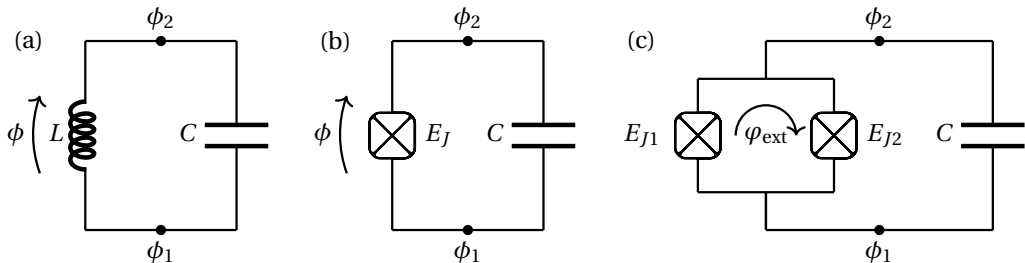


Fig. 3.1: Example circuit diagrams consisting of capacitors ( $C$ ), inductors ( $L$ ) and Josephson junctions ( $E_J$ ). (a) The  $LC$ -oscillator with phase difference  $\phi = \phi_2 - \phi_1$  between the two superconducting islands (nodes). (b) Same as (a) but with the inductor replaced by a Josephson junction to realize an anharmonic oscillator. (c) Same as (a) and (b) but the inductive element is replaced by a SQUID. The SQUID is threaded by a (reduced) flux  $\varphi_{\text{ext}} = 2\pi\Phi/\Phi_0$  which tunes the effective Josephson energy of the SQUID.

### 3.1 Circuit quantization

#### The $LC$ -oscillator

We may start with a simple example from classical electrodynamics, the  $LC$ -oscillator as shown in Fig. 3.1(a). Using the circuit quantization recipe, we are required to write down the Lagrangian. To construct the Lagrangian, we are interested in the energy stored in the capacitor ( $C$ ) and the inductor ( $L$ ),

$$U_C = \frac{Q^2}{2C} = \frac{1}{2}CV^2, \quad (3.1)$$

$$U_L = \frac{1}{2}LI^2 = \frac{\Phi^2}{2L}. \quad (3.2)$$

The energy in the capacitor can equally well be expressed in terms of the displaced charge  $Q$  or the voltage drop  $V$  across the capacitor. Similarly, the energy in the inductor can be written either using the current  $I$  through the inductor or the magnetic flux  $\Phi$  induced by the current. The current is related to the displaced charge via  $I = \dot{Q}$  and the voltage is related to the flux via Faraday's law  $V = -\dot{\Phi}$ . It is therefore possible to give two equivalent formulations of the Lagrangian,

$$\mathcal{L}(Q, \dot{Q}) = \frac{1}{2}L\dot{Q}^2 - \frac{Q^2}{2C}, \quad (3.3)$$

$$\mathcal{L}(\Phi, \dot{\Phi}) = \frac{1}{2}C\dot{\Phi}^2 - \frac{\Phi^2}{2L}. \quad (3.4)$$

In the two descriptions of the Lagrangian, the capacitive and inductive energy interchange role as kinetic and potential energy. Sometimes, students of superconducting circuits have a better intuition of charges and currents than fluxes and voltages. Nevertheless, it is customary to use the flux description<sup>2</sup> despite potentially leading to confusion. This choice is made since it is more

<sup>1</sup>Sometimes referred to as (circuit-based) cavity quantum electrodynamics [97, 98].

<sup>2</sup>See Ref. [107] for the dual description in terms of charges.

convenient to let the Josephson energy-phase relation correspond to potential energy rather than kinetic energy.

Having picked the flux formulation of the Lagrangian, we may perform a Legendre transformation to uncover the Hamiltonian. First, we identify the conjugate variable to  $\Phi$ ,

$$\frac{\partial \mathcal{L}(\Phi, \dot{\Phi})}{\partial \dot{\Phi}} = C\dot{\Phi} = Q. \quad (3.5)$$

It turns out that the conjugate variable is simply the charge  $Q$ . This result should not be too surprising when considering the symmetry between Eqs. (3.3) and (3.4). We complete the Legendre transformation and obtain the Hamiltonian,

$$H(\Phi, Q) = \dot{\Phi}Q - \mathcal{L} = \frac{Q^2}{2C} + \frac{\Phi^2}{2L}. \quad (3.6)$$

This is the familiar Hamiltonian of a harmonic oscillator using variables  $Q$  and  $\Phi$  in place of momentum and position. For a more general circuit, the conjugate charges are not necessarily as simple as the one found in Eq. (3.5). In this case, the capacitive term can be expressed as  $U_C = \boldsymbol{\Phi}^T \mathbf{C} \boldsymbol{\Phi} / 2$  where  $\boldsymbol{\Phi}$  is a vector of fluxes and  $\mathbf{C}$  is the capacitance matrix. By diagonalizing the capacitance matrix, the conjugate charges are straightforward to compute.

We continue by quantizing the coordinates  $Q \rightarrow \hat{Q}$  and  $\Phi \rightarrow \hat{\Phi}$  according to the canonical commutator relation,  $[\hat{\Phi}, \hat{Q}] = i\hbar$ . It is customary to work in reduced variables and we therefore define the Cooper pair number operator  $\hat{n} = \hat{Q}/2e$  and the reduced flux  $\hat{\phi} = 2\pi\hat{\Phi}/\Phi_0$  such that their commutator becomes  $[\hat{\phi}, \hat{n}] = i$ . The reduced flux is also referred to as a phase and  $\Phi_0 = h/2e$  is the magnetic flux quantum with  $h$  being Planck's constant and  $e$  the electron charge. Using the reduced operators, the Hamiltonian becomes

$$H(\phi, n) = 4E_C \hat{n}^2 + \frac{1}{2} E_L \hat{\phi}^2. \quad (3.7)$$

In this formulation of the Hamiltonian, we introduce the charging energy  $E_C = e^2/2C$  and the inductive energy  $E_L = (\Phi_0/2\pi)^2/L$ .

Having derived the Hamiltonian, we consider the energy levels of the system and discuss its utility as a qubit. The energy levels of the harmonic  $LC$ -oscillator are given by  $E_n = \hbar\omega(n + 1/2)$  where  $\omega = \sqrt{8E_C E_L}/\hbar$  is the oscillating frequency. The energy difference between neighboring levels is the same for all levels,  $E_{n+1} - E_n = \hbar\omega$ . It is therefore not possible to single out two levels that can act as qubit states since we need something that is not purely harmonic to separate the transition energies. Josephson junctions provide the necessary anharmonicity to the system and also introduce other curious features as we elaborated in the next section.

Before moving on, it is important to mention that it is possible to encode a qubit in a harmonic oscillator by other means. In a Bosonic code, the qubit states are carefully constructed from a superposition of Fock states. In this way, quantum information is redundantly encoded in several energy levels. The redundancy is cleverly used to effectively increase the coherence of the resulting qubit through error correction. The fascinating topic of Bosonic codes is outside the scope of this thesis and we refer the reader to Refs. [105, 108–111] instead.

### The junction-based oscillator

To introduce anharmonicity, we can replace the inductor in the  $LC$ -oscillator with a Josephson junction and derive the corresponding Hamiltonian in an analogous fashion, see Fig. 3.1(b). While

doing so, we develop the circuit quantization recipe a little further and shed light on the important physics exhibited by Josephson junctions.

Using the flux description, we begin by labeling the nodes of the circuit (the superconducting islands) by  $j = 1, 2$  and assign node fluxes  $\Phi_j$  to each of the nodes. This is the starting point of the “method of nodes” as this recipe is called. We now have two flux variables, but the system only has one degree of freedom. This can be seen by considering the sum of node fluxes in the system  $\Phi_\Sigma = \Phi_1 + \Phi_2$ : The node flux is related to the node charge through  $\Phi_j = LI_j = L\dot{Q}_j$ , so for the summed quantities,  $\Phi_\Sigma \propto \dot{Q}_\Sigma = 0$ , we find that the sum  $\Phi_\Sigma$  is non-dynamical due to the conservation of charge. We are therefore left with a single degree of freedom,  $\Phi = \Phi_1 - \Phi_2$ .

In general, the method of nodes introduces one flux variable more than the degrees of freedom in the system. If no node in the system is grounded, then the sum of node fluxes will be zero due to charge conservation as described above. If one or more nodes are grounded, the associated voltage on the grounded nodes is zero. According to Faraday’s law, zero voltage implies  $\dot{\Phi}_{\text{ground}} = 0$ . Thus, the node flux on the grounded node is non-dynamical and its constant value may be taken to be zero too,  $\Phi_{\text{ground}} = 0$ . In this way, the method of nodes handily finds the degrees of freedom in the system. As previously mentioned, in more general circuits it is desirable to find the eigenmodes of the capacitance matrix and this is also a practical way of determining the degrees of freedom.

Moving on with the capacitor-junction circuit, we may write down the Lagrangian using the junction energy-phase relation  $E_J [1 - \cos(\phi)]$ , perform the Legendre transformation, quantize the variables and arrive at the quantum Hamiltonian [112],

$$H = 4E_C \hat{n}^2 + E_J (1 - \cos(\hat{\phi})), \quad (3.8)$$

$$= 4E_C \sum_n n^2 |n\rangle \langle n| + E_J \left( 1 - \frac{1}{2} \sum_n |n\rangle \langle n+1| + |n+1\rangle \langle n| \right). \quad (3.9)$$

In the second line, we write the Hamiltonian in Dirac notation using the charge states  $|n\rangle$ . Important to this example is that the Josephson junction only admits for tunneling of single Cooper pairs.<sup>3</sup> Consequently, the eigenvalues of the charge operator are discrete  $n = \dots, -1, 0, 1, \dots$ . Comparing expressions for the Hamiltonians in Eqs. (3.8) and (3.9), we notice that the transfer of single Cooper pairs is related to the periodicity of the phase  $\phi$ . The periodicity of the Hamiltonian implies that we can not quantize the charge and flux variables according to  $[\hat{\phi}, \hat{n}] = i$ . Instead, we must respect the periodicity and work with operators  $\exp(\pm i\hat{\phi})$ . The analogous commutator relation for the periodic variable is given by  $[\exp(-i\hat{\phi}), \hat{n}] = \exp(-i\hat{\phi})$ . The slight reformulation of the commutator rarely plays an important role when working with the operators. However, getting the right periodicity of  $\hat{\phi}$  and the true discretization of  $\hat{n}$  can be tricky. For example, it is not immediately obvious how the charge value  $n$  relates to the node charges on the superconducting islands  $n_j$ . By considering the transfer of a single Cooper pair from island 1 to island 2, we see that the corresponding charges  $n_j$  changes according to  $n_1 \rightarrow n_1 - 1$  and  $n_2 \rightarrow n_2 + 1$ , implying  $n = (n_1 - n_2)/2$  such that  $n \rightarrow n - 1$  when a single Cooper pair tunnels. We can also verify this result by evaluating the commutator,

$$\left[ e^{-i(\hat{\phi}_1 - \hat{\phi}_2)}, \frac{\hat{n}_1 - \hat{n}_2}{2} \right] = e^{-i(\hat{\phi}_1 - \hat{\phi}_2)} \quad (3.10)$$

and see that it agrees with the canonical commutator relation only when the factor of 1/2 is included in the charge operator. In general, care should be taken when changing the basis by rotating or

<sup>3</sup>In practice, small higher-order tunneling processes slightly augments the energy-phase relation [113], see Ref. [114] for a recent experimental investigation of this phenomena.

scaling the phase and charge operators to ensure that the commutator relation and the charge discretization imposed by the Josephson junctions are satisfied.

### Offset charges

There is an additional consideration relevant to the junction-based oscillator. A discrete charge system is sensitive to the local electric potential  $V_{\text{env}}$ . The energy due to the presence of a local electric field is  $2e\hat{n}V_{\text{env}}$  and can be included in the Hamiltonian in Eq. (3.8) by completing the square with  $4E_C\hat{n}^2$ . The result is to simply make the substitution  $\hat{n} \rightarrow \hat{n} - n_{\text{offset}}$  which leads to

$$H = 4E_C(\hat{n} - n_{\text{offset}})^2 + E_J(1 - \cos(\hat{\phi})), \quad (3.11)$$

where the charge offset is given by  $n_{\text{offset}} = -V_{\text{env}}C/2e$ . This situation can be compared to the  $LC$ -oscillator, where the charge operator can always take a continuous value  $n$  such that the charging energy  $4E_C(n - n_{\text{offset}})$  is minimized. The continuous charge can therefore absorb the offset charge,  $\hat{n}_{\text{cont}} \rightarrow \hat{n}_{\text{cont}} - n_{\text{offset}} = \hat{n}'_{\text{cont}}$ . The same trick can not be used in a discrete charge system and it is therefore sensitive to fluctuations in the electric potential produced by the environment.

To better understand the effect of fluctuations in the offset charge, we consider two standard limits of the system. The first scenario is  $E_C > E_J$  which we refer to as the light regime. Associating the charge operator  $\hat{n}$  with momentum, the capacitance plays the role of a mass of the  $\phi$ -mode. In the small capacitance/mass regime  $E_C > E_J$ , the  $\phi$ -mode becomes light. In this regime, the physics of the device is determined mostly by the charging energy and the charge number becomes a good quantum number. The system also becomes sensitive to offset charges as it directly determines the energy associated with a given charge state. Such a device is called a Cooper-pair box and despite its sensitivity to offset charges, it functions well as a qubit due to its large anharmonicity: the Cooper pair box energy levels are approximately given by  $E_n \approx 4E_C(n - n_{\text{offset}})^2$ , showing a large degree of anharmonicity as defined by  $\alpha = (E_1 - E_0) - (E_2 - E_1) \approx -8E_C$ . The choice  $E_J/E_C < 1$  is therefore also referred to as the Cooper-pair box regime. In 1999, the Cooper-pair box was the first superconducting qubit device to exhibit coherent Rabi oscillations [115]. The coherence time of the qubit was relatively short, being on the nanosecond scale, but demonstrated the exciting possibility of controlling coherent superconducting devices based on Josephson junctions.

Next, we consider the limit  $E_J \gg E_C$ , referred to as the heavy mode regime or the transmon limit. In this regime, the states spread across several charge numbers,  $\langle \hat{n}^2 \rangle \propto \sqrt{E_J/E_C} \gg 1$ , and are less sensitive to fluctuations in the charge offset as a result. In fact, the sensitivity to  $n_{\text{offset}}$  is exponentially suppressed in  $\sqrt{E_J/E_C}$ . The trade-off, however, is the decreased anharmonicity between the ground and excited state. As the charge delocalizes, the conjugate phase localizes,  $\langle \hat{\phi}^2 \rangle \propto \sqrt{E_C/E_J} \ll 1$ , to the minimum of the cosine potential. Here, the cosine potential is approximately quadratic and the dynamics are approximately described by a harmonic oscillator. However, the anharmonicity only decreases linearly in  $\sqrt{E_C/E_J}$  and it becomes advantageous to choose  $E_J/E_C \sim 50$  which is the typical operating regime. In this limit, the qubit is referred to as a transmon. The transmon was first proposed in Ref. [112] and was soon after realized experimentally [116]. The coherence time of the transmon was found to be above one microsecond, about three orders of magnitude improvements compared to the original Cooper-pair box experiment [115]. Subsequently, the transmon has been the superconducting qubit of choice in many applications and today's state-of-the-art transmons show coherence times close to the millisecond scale [117–119].



## External fluxes

To achieve more control over the transmon, the single Josephson junction is sometimes replaced by an asymmetric SQUID (superconducting quantum interference device), realizing a “tunable transmon” [112], see Fig. 3.1(c). The SQUID consists of two junctions ( $E_{J1}, E_{J2}$ ) in parallel and forms a loop where magnetic flux can be threaded through. By adjusting the  $B$ -field in this loop, the effective Josephson energy of the SQUID can be controlled. This design introduces a sensitivity to flux noise, leading to decoherence of the qubit. In Chapter 6, we study other qubits that are exponentially insensitive to flux noise, analogous to the way the transmon is exponentially insensitive to charge noise.

The presence of an external flux brings up the question of how to include this parameter in a circuit Hamiltonian. In classical circuits, Kirchoff’s voltage law takes care of (time-dependent) external  $B$ -fields and we may use the same here. In the language of phases, Kirchoff’s voltage law states that the sum of phase differences around a loop and the reduced external flux  $\phi_{\text{ext}} = 2\pi\Phi_{\text{ext}}/\Phi_0$  should sum to zero,

$$\sum_{\text{loop}} \phi_{\text{diff},i} + \varphi_{\text{ext}} = 0. \quad (3.12)$$

Considering the SQUID, we see that the phase drop across the two junctions can not be  $\phi$  and  $-\phi$  as they sum to zero. Instead, the phase drops should account for the external magnetic field. We can allocate the external flux in either of the two junctions or split it in some ratio,  $\phi \rightarrow \phi - (1+a)\varphi_{\text{ext}}/2$  and  $-\phi \rightarrow -\phi - (1-a)\varphi_{\text{ext}}/2$ , such that they sum to  $-\varphi_{\text{ext}}$ . In general, a spanning tree can be used to allocate the flux as discussed in Ref. [100].

Having allocated the flux, we can implement the SQUID in a tunable transmon whose corresponding Hamiltonian becomes

$$H = 4E_C(\hat{n} - n_{\text{offset}})^2 + E_{J1} \cos(\hat{\phi} - (1+a)\varphi_{\text{ext}}) - E_{J2} \cos(\hat{\phi} + (1-a)\varphi_{\text{ext}}/2), \quad (3.13)$$

$$= 4E_C(\hat{n} - n_{\text{offset}})^2 - E_{J,\text{eff}}(\varphi_{\text{ext}}) \cos(\hat{\phi} - \phi_0 - a\varphi_{\text{ext}}/2), \quad (3.14)$$

where we define the flux-tunable effective Josephson energy

$$E_{J,\text{ext}} = (E_{J1} + E_{J2}) \cos(\varphi_{\text{ext}}/2) \sqrt{1 + \tan^2 \phi_0} \quad (3.15)$$

and the phase shift  $\tan \phi_0 = \frac{E_{J2} - E_{J1}}{E_{J2} + E_{J1}} \tan(\varphi_{\text{ext}}/2)$ . The flux allocation can always be chosen through the parameter  $a$  such that the minimum of the cosine potential is at  $\phi = 0$ . This is a reasonable choice as it reflects that the current across the SQUID  $I = I_C \sin(\phi)$  is zero without additional flux bias.

Since the tunable transmon is a superconducting circuit with only junctions as inductive elements, we need to respect the periodicity of the phase. In this setting, Kirchoff’s voltage law gets translated to the “fluxoid quantization condition” [120, 121] which implies that the sum of phases and external flux in Eq. (3.12) instead equates to zero modulo  $2\pi$ . With these final considerations, we may summarize the circuit quantization recipe:

1. Assign (reduced) fluxes to all  $N$  nodes of the circuit
2. Assign zero flux to the ground node or the sum of all nodes
3. Allocate external flux according to Kirchoff’s law/fluxoid quantization

4. Write up the Lagrangian, preferably in terms of the eigenmodes of the capacitance matrix
5. Compute the Hamiltonian via a Legendre transformation
6. Quantize the variables, taking into account phase periodicity
7. Include offset charges if charges are discrete

This recipe works well under most circumstances<sup>4</sup> and can be used to derive the Hamiltonian of other superconducting qubits. We mention other relevant superconducting qubits (persistent current flux qubit,  $C$ -shunt flux qubit, fluxonium, the  $0 - \pi$  qubit, bifluxon and Blochonium) in Chapters 5 and 6. In the next section, we take a short detour that investigates the relationship between discrete and continuous charge in superconducting circuits.

### Going from discrete to continuous charge

As discussed, phase periodicity and charge discretization lead to qualitatively different behavior in the transmon compared to the  $LC$ -oscillator. There is not a universally correct description of charge and phase in the sense that it is not more or less “natural” for the phase/charge to be periodic/discrete than to be non-compact/continuous. We discuss in more detail how the two phase/charge regimes can be connected in this section and refer the interested reader to Ref. [99] for further discussion.

We can understand the relationship between discrete/continuous charge and compact/non-compact phase through the following example: By constructing an inductor from a chain of  $N$  Josephson junctions, we can interpolate between discrete and continuous charge, see Fig. 3.2. It turns out that junction arrays are a very useful way of fabricating large inductors in practice [124, 125] as we discuss in Chapter 6. In this example, each junction has Josephson energy  $E_J$  and charging energy  $E_C$ . Before we start, we focus on a single junction labeled by  $i$  and make some general considerations. First, we denote the phase drop across this junction by  $\phi_i$ . When  $E_J/E_C \gg 1$ , the  $\hat{\phi}_i$ -mode is heavy and localized near the minimum of the cosine potential  $\phi_i \approx 0$  and we do not need to consider phase-slips where  $\phi_i$  jumps by  $2\pi$  since the tunneling amplitude is exponentially suppressed in  $\sqrt{E_J/E_C}$ . Additionally, the energy of exciting the  $\hat{\phi}_i$ -mode,  $\omega_i = \sqrt{8E_J E_C}/\hbar$ , is required to be large such that the array of Josephson junctions acts like a true inductor in a low-energy description. In agreement with these requirements, we later take the limit  $E_J, N \rightarrow \infty$  while keeping  $E_C$  fixed such that  $E_J/E_C \rightarrow \infty$  and  $\omega_i \rightarrow \infty$ .

We can now consider the junction array in the phase basis to see how the phase becomes non-compact. Consider the energy of the array,

$$V = \sum_i E_J (1 - \cos(\hat{\phi}_i)). \quad (3.16)$$

Since we are working in the semi-classical regime  $E_J/E_C \gg 1$ , we may use an energy minimization argument or Kirchoff’s current law to find that the total phase drop  $\phi = \sum_i \phi_i$  is distributed evenly between the  $N$  identical junctions,  $\phi_i = \phi/N$ . We refer to the substitution  $\hat{\phi}_i \rightarrow \hat{\phi}/N$  as the

<sup>4</sup>Some situations require further attention when going from a classical to a quantum description as studied in Refs. [122, 123].

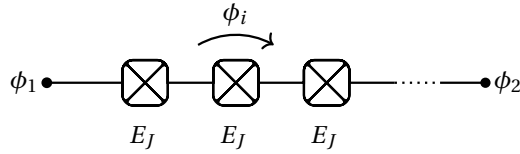


Fig. 3.2: A Josephson junction array that mimics an inductor. The phase drop across the array  $\phi = \phi_2 - \phi_1$  can be distributed to the  $N$  junctions such that the phase drop across each junction is  $\phi_i = \phi/N$ .

“distributed phase approximation” (DPA) and applying it to Eq. (3.16) while expanding in  $\hat{\phi}/N$  results in

$$V = NE_J \left( \frac{1}{2} (\hat{\phi}/N)^2 - \frac{1}{24} (\hat{\phi}/N)^4 + \dots \right). \quad (3.17)$$

By taking the limit  $E_J, N \rightarrow \infty$  while keeping  $E_J/N = E_L$  fixed, we get

$$V = \frac{1}{2} E_L \hat{\phi}^2. \quad (3.18)$$

This is exactly the energy of an inductor with inductive energy  $E_L = (\Phi_0/2\pi)^2/L$ . We also see that the domain of the phase  $\hat{\phi}$  has extended to  $(-\infty, \infty)$ . It appears that a mathematical trick, the distributed phase approximation, is responsible for this result, but the DPA has a sound physical interpretation: Once the phase drop across the array is above  $2\pi$ , it is energetically favorable for one of the junctions to slip by  $2\pi$ . However, the probability for one of the junctions to tunnel from the minima at  $\phi_i = 0$  to  $\phi_i = 2\pi$  is exponentially suppressed in the large ratio  $\sqrt{E_J/E_C} \rightarrow \infty$ . Despite the prospect of minimizing energy, the tunneling event is forbidden by the semi-classical limit  $E_J/E_C \rightarrow \infty$  and the array can support large fluctuations in  $\hat{\phi}$ .

We can also see how the charge operator becomes continuous by transforming to the charge basis. Instead of expanding Eq. (3.17) in  $\hat{\phi}/N$ , we rewrite the cosine term in Dirac notation using

$$\cos(\hat{\phi}/N) = \int_{-N\pi}^{N\pi} d\phi \cos(\phi/N) |\phi\rangle \langle \phi|, \quad (3.19)$$

giving the potential energy of the array,

$$V = NE_J \left( 1 - \int_{-N\pi}^{N\pi} d\phi \cos(\phi/N) |\phi\rangle \langle \phi| \right). \quad (3.20)$$

At the moment, we do not know exactly what the charge basis states  $|n\rangle$  are. We only know that they form a complete set of basis states and are related to the phase basis states  $|\phi\rangle$  via

$$\langle n|\phi\rangle = \frac{1}{\sqrt{2\pi}} e^{-in\phi}. \quad (3.21)$$

Using this relation while inserting identities  $\sum_n |n\rangle \langle n|$  in Eq. (3.20), we obtain the energy of the array in charge basis,

$$V = NE_J \left[ 1 - \left( \sum_{n,m} \frac{1}{2} \delta_{n-m, \frac{1}{N}} |n\rangle \langle m| + \text{H.c.} \right) \right]. \quad (3.22)$$

The Kronecker  $\delta$  tells us that the charge can jump in fractional steps  $1/N$  across the junction array. In the limit  $N \rightarrow \infty$ , the step-size is infinitesimal and the charge value becomes continuous. Rewriting Eq. (3.22) and taking the limit  $E_J, N \rightarrow \infty$ , we arrive at

$$V = \frac{1}{2} E_L \sum_n |n\rangle \frac{\langle n+1/N| - 2\langle n| + \langle n-1/N|}{-1/N^2} \rightarrow \frac{1}{2} E_L \int dn |n\rangle i^2 \frac{\partial^2}{\partial n^2} \langle n|. \quad (3.23)$$

Comparing this result to Eq. (3.18), we identify  $\phi = i\partial/\partial n$  as expected from conjugate variables. In light of these calculations, we directly see the relationship between compact/discrete and non-compact/continuous phase/charge and how the continuous charge can be seen as a limit of tunneling of fractionalized charges. This interpretation is not completely physical and is not the same as the notion of fractional charges in topologically non-trivial systems. Instead, the continuous charge should be thought of as the displacement of electrons relative to the ion lattice.

Having obtained a basic understanding of superconducting qubits, we discuss their decoherence properties next. Moving forward to the next part, we drop the hat on operators to ease the notation.

### 3.2 Decoherence and noise-protection

We introduced decoherence (relaxation and dephasing) on a conceptual level in Chapter 1 and we now turn to a more quantitative description of noise in superconducting qubits. We also discuss strategies to minimize the impact of noise on the qubit states which leads to the notion of noise protection. Decoherence and noise protection play an important role in the work contained in this thesis as detailed in Chapters 5 and 6. This part collects some of the results found in Refs. [102, 112, 126–131] and we begin by considering various relevant sources of noise.

#### Noise

Noise in superconducting qubits are random fluctuations in quantities that couple to the qubit.<sup>5</sup> Examples of noise sources  $\lambda(t)$  are the offset charge  $n_{\text{offset}}$  or the external flux  $\varphi_{\text{ext}}$ . Any parameter that enters in the Hamiltonian is a potential source of noise that can lead to qubit decoherence. The noisy parameter can be expressed as the sum of its mean value  $\lambda_0$  and its fluctuating part  $\delta\lambda(t)$ ,  $\lambda(t) = \lambda_0 + \delta\lambda(t)$ . The noise source can further be characterized by its power spectral density (PSD)

$$S(\omega) = \int_{-\infty}^{\infty} dt \langle \lambda(t)\lambda(0) \rangle e^{-i\omega t}, \quad (3.24)$$

which describes the amplitude of noise at a given frequency  $\omega$  and is computed as the Fourier transform of the autocorrelation function  $\langle \lambda(t)\lambda(0) \rangle$ .<sup>6</sup> Most noise sources have a quasi-universal noise spectrum that is encoded in the PSD. Since the noise background is somewhat expected, it is possible to engineer qubits that are insensitive to the most dominant sources of noise. As already mentioned, the transmon is an example of this approach to increase qubit coherence and we discuss general ways qubits can be made insensitive to noise in Secs. 3.2 and 3.2.

Flux and charge noise are common sources of noise in superconducting qubits. The origin of charge noise is typically assigned to fluctuating charges present in material interfaces or in the

---

<sup>5</sup>Specifically, we talk about stochastic noise as opposed to systematic noise.

<sup>6</sup>This result is known as the Wiener-Khinchin theorem.

substrate. Similarly, flux noise is often assigned to fluctuating spins that reside in the thin oxide covering the superconducting circuit. These noise sources are often well-described by  $1/f$ -type noise, meaning that the noise amplitude scales with the inverse frequency. The PSD of  $1/f$  noise is

$$S(\omega) = A_\lambda^2 \frac{2\pi \text{ Hz}}{|\omega|}, \quad (3.25)$$

where  $A_\lambda$  is the general noise amplitude of the noise source  $\lambda$ . The experimentally found flux and charge noise amplitudes are typically around

$$A_\Phi \sim 10^{-5} - 10^{-6} \Phi_0 / \sqrt{\text{Hz}}, \quad (3.26)$$

$$A_Q \sim 10^{-3} - 10^{-4} e / \sqrt{\text{Hz}}. \quad (3.27)$$

In experiments, charge noise is the dominating noise source compared to flux noise as seen by its relatively large noise amplitude. This fact also explains part of the success of the transmon: The qubit's sensitivity to the limiting noise source is exponentially suppressed. Only after reducing the sensitivity to charge noise, flux noise becomes a limiting noise channel.

Some mechanisms of decoherence due to charge noise are described by Ohmic noise rather than  $1/f$  noise. Ohmic noise depends linearly on the frequency as can be seen from the associated PSD,

$$S(\omega) = B_Q^2 \frac{|\omega|}{2\pi \text{ GHz}} \quad (3.28)$$

where the noise amplitude  $B_Q$  depends on the experimental realization to a larger degree than the  $1/f$  noise amplitudes  $A_\lambda$ . In Ref. [126], the Ohmic charge noise amplitude is found to be around  $B_Q \sim 5 \cdot 10^{-9} e / \sqrt{\text{GHz}}$ . Ohmic charge noise can also be modeled as bulk dielectric loss, see for example Refs. [128, 131, 132]

There exist other relevant sources of noise worth mentioning [130]. Quasiparticles in the superconductor can tunnel across Josephson junctions and this mechanism can lead to relaxation and dephasing. Especially, in certain parameter regimes for the fluxonium qubit, relaxation due to quasiparticles is a limiting decoherence channel [131]. Ohmic flux noise, also modeled as inductive loss, is analogous to Ohmic charge noise/dielectric loss. This noise source is believed to be less significant compared to dielectric loss but it can be hard to distinguish between the two since they share the same PSD [126]. Fluctuations in the tunneling region of Josephson junctions can effectively be modeled as fluctuations in the Josephson energy. This source of noise is referred to as  $1/f$  critical current noise and due to its low noise amplitude  $A_I \sim 10^{-7} 2\pi E_J / \Phi_0 \sqrt{\text{Hz}}$ , it is typically not a limiting coherence channel [127]. Additional sources of noise are also introduced when a qubit is coupled to a readout resonator: The qubit dissipates energy into the readout resonator which leads to (Purcell enhanced) relaxation [102]. Further, if there are residual photons in the resonator, temporal fluctuations in the photon number induce dephasing of the qubit [127, 133]. In addition to randomly fluctuating TLSs, the presence of coherent TLSs can also lead to relaxation, especially when the qubit frequency is tuned and accidentally becomes resonant with a coherent TLS [130]. On much longer time scales  $\sim 10$ s, high-energy cosmic rays are believed to create ‘‘catastrophic’’ events where correlated errors involving several qubits across a chip occur [134].

## Relaxation

Relaxation is the process where a quantum system loses energy to the environment and thereby changes its quantum state.<sup>7</sup> Relaxation is necessarily incoherent as energy is transferred to the environment where it can not be retrieved to reverse the process. The rate at which a quantum system, described by a Hamiltonian  $H$ , relaxes due to a noise source  $\lambda$  is given by Fermi's golden rule,

$$\Gamma_1 = \frac{1}{\hbar^2} \left| \left\langle 0 \left| \frac{\partial H}{\partial \lambda} \right| 1 \right\rangle \right|^2 S(\omega_q), \quad (3.29)$$

where the relaxation time is given by  $T_1 = 1/\Gamma_1$ . The relaxation rate can be interpreted in the following way: The matrix element  $\langle 0 | \partial H / \partial \lambda | 1 \rangle$  describes the qubit's sensitivity to the noise source  $\lambda$  by quantifying how strongly the noise source couples the qubit states. On the other hand, the PSD describes the noise environment by quantifying the frequency distribution of noise. The PSD is evaluated at the qubit frequency  $\omega_q$  since noise at the qubit frequency induces a transition from the excited state to the ground state. Typically, the qubit frequency is larger than the temperature  $\hbar\omega_q \gg k_B T$  such that the reverse process where the qubit absorbs energy from the environment is suppressed.<sup>8</sup>

Since qubits are only sensitive to noise near their qubit frequency, it is possible to engineer qubits such that their frequencies lie in a range where the noise is small amplitude. One strategy is to engineer the qubit frequency such that it lies in the cross-over regime between  $1/f$  and Ohmic noise as investigated in Ref. [126]. In experiments, however, a qubit's frequency is restricted by several practical considerations, limiting the range of reasonable qubit frequencies. Some of these relevant considerations include: the frequency of readout resonators with the possibility of multiplexing readout, frequency matching in two-qubit gates, frequency crowding, cross-talk and compatibility with high-frequency drive lines. Except for near-degenerate qubits, qubit frequencies often lie in the 1 – 5 GHz range given the experimental constraints.

Another strategy for suppressing relaxation is to consider the matrix element  $\langle 0 | \partial H / \partial \lambda | 1 \rangle$  which can, in principle, be made arbitrarily small [135]. For qubit wave functions with disjoint support, the matrix element  $\langle 0 | \partial H / \partial \lambda | 1 \rangle$  vanishes for common noise sources. The support of a wave function  $\langle \phi | \Psi \rangle$  of a state  $|\Psi\rangle$  is the range of  $\phi$  where the value of the wave function is nonzero. Disjoint support of the qubit states implies that the product of the qubit wave functions  $\langle 0 | \phi \rangle \langle \phi | 1 \rangle$  is zero for all values of  $\phi$ . The product of the disjoint wave functions remains at zero when an operator  $\phi^k$  or  $n^k$  is inserted between them,

$$\left\langle 0 \left| \frac{\partial H}{\partial \lambda} \right| 1 \right\rangle = \int d\phi \langle 0 | \phi \rangle \frac{\partial H(n, \phi)}{\partial \lambda} \langle \phi | 1 \rangle = 0 \quad (3.30)$$

for  $\partial H / \partial \lambda \propto \phi^k, n^k$ .<sup>9</sup> The relevant noise sources usually take the form  $\partial H / \partial \lambda \propto \phi, n$ .

In qubits, disjoint support of the wave functions is not exact due to the evanescent part of the wave functions. Localized wave functions feature exponential tails which are determined by the confining potential. Qubit wave functions that are separated in different quantum wells

<sup>7</sup>This notion of relaxation is also referred to as longitudinal relaxation [102, 130] or depolarization [127]. Relaxation and dephasing together is sometimes referred to as transverse relaxation but more often the term decoherence is used.

<sup>8</sup>Superconducting qubits are placed in cryostats which can cool to around  $T \sim 15\text{mK} = 0.3125 \hbar k_B^{-1} \text{GHz}$  [102].

<sup>9</sup>In principle, a noise source that shifts the qubit wave functions by a large amount can circumvent this general approach to reduce relaxation. For example, if  $\partial H / \partial \lambda \propto e^{-in\phi_0}$ , one of the wave functions can be displaced by an amount  $\phi_0$  to make it overlap with the other wave function, however, none of the common noise sources take this form.

only overlap at these tails. This overlap, and consequently the matrix element  $\langle 0|\partial H/\partial\lambda|1\rangle$ , is exponentially suppressed in the height and the width of the barrier separating the two wells. With this approach, experiments using (heavy) fluxonium and the  $0 - \pi$  qubit have demonstrated relaxation times beyond 1 ms [132, 136–138]. In other proof-of-principle experiments with a  $\cos(2\phi)$  qubit [139] and a bifluxon qubit [140], the level of protection against relaxation can be controlled, showing an order of magnitude increase in relaxation time when operating in the protected regime.

An inevitable trade-off when making a qubit insensitive to noise is that it also becomes more insensitive to deliberate manipulation. Drive lines interact with the qubit in much the same way as noise does, for example, a microwave drive can control the offset charge which can be used to excite the qubit from the ground to the excited state. This direct way of performing gates is, however, not optional for a qubit where the matrix element between the qubit states is near zero. In the protected regime, states outside of the qubit subspace can be used as a resource to perform gates. If a higher-lying state  $|n\rangle$  couples to both of the qubit states,  $\langle 0|\partial H/\partial\lambda|n\rangle \neq 0$  and  $\langle 1|\partial H/\partial\lambda|n\rangle \neq 0$ , then a transition between the qubit states can be achieved by first going to the higher-lying state. This method is occasionally referred to as “multi-level excursion” and several states are sometimes required to perform gates as is the case for the  $0 - \pi$  qubit, see for example Refs. [138, 141, 142]. In Chapter 5, we study another way of making gates on a qubit that has a tunable level of protection as an alternative to using high-energy states. When attempting to engineer qubits with long relaxation times, it is important to also take into account what the expected gate times will be. The ratio of the decoherence time and the gate time is therefore a good measure of the quality of a qubit system.

A long relaxation time is only one aspect of highly coherent qubits. In the next section, we discuss dephasing which plays an equally important role in qubit decoherence.

## Dephasing

Dephasing of a qubit is the result of noise that leads to fluctuations in the qubit frequency. The time-dependent qubit frequency can, in the presence of noise, be described as  $\omega(t) = \omega_q + \delta\omega(t)$  where  $\omega_q$  is the qubit frequency without noise and  $\delta\omega(t)$  is noise-induced random fluctuations. To better understand dephasing as a mechanism of decoherence, we consider a time-evolving qubit state in the frame that rotates with the qubit frequency. Our example state is

$$|\Psi(t)\rangle = \frac{1}{\sqrt{2}}(|0\rangle + e^{i\int_0^t \delta\omega(\tau) d\tau} |1\rangle). \quad (3.31)$$

As time goes on and  $\delta\omega(t)$  fluctuates, the relative phase between the qubit states changes in a way that is reminiscent of a random walk in one dimension. In a random walk, the average distance traveled away from the origin increases at a certain rate. In the same way, we may ask at what rate does the average of  $e^{i\int_0^t \delta\omega(\tau) d\tau}$  dephase the qubit? This question can be posed in terms of the noisy parameter  $\lambda(t) = \lambda_0 + \delta\lambda(t)$  by relating it to fluctuations in the qubit frequency. First, the Hamiltonian is expanded around the mean value  $\lambda_0$  of the noisy parameter,

$$H(\lambda(t)) - H(\lambda_0) = \frac{\partial H}{\partial \lambda} \delta\lambda(t) + \dots \quad (3.32)$$

The resulting fluctuations of the qubit frequency is given by

$$\delta\omega(t) = \frac{\delta\lambda(t)}{\hbar} \left[ \left\langle 1 \left| \frac{\partial H}{\partial \lambda} \right| 1 \right\rangle - \left\langle 0 \left| \frac{\partial H}{\partial \lambda} \right| 0 \right\rangle \right] = \delta\lambda(t) \frac{\partial\omega_q}{\partial\lambda}, \quad (3.33)$$

to first order in the noise  $\delta\lambda(t)$  and where the derivatives are evaluated at  $\lambda_0$ . The relative phase between the qubit states in Eq. (3.31) can now be expressed in terms of the noisy parameter,  $e^{i\partial\omega/\partial\lambda\int_0^t d\tau\delta\lambda(\tau)}$ . The corresponding dephasing rate due to the average of this phase depends on the PSD of the noise. Most noise sources that induce dephasing (i.e. charge and flux noise) are described by  $1/f$ -noise in which case the dephasing rate takes the form<sup>10</sup>

$$\Gamma_\varphi = \sqrt{2A_\lambda^2 \left(\frac{\partial\omega}{\partial\lambda}\right)^2 |\ln(\omega_{\text{ir}} t_0)| + 2A_\lambda^4 \left(\frac{\partial^2\omega}{\partial\lambda^2}\right)^2 [\ln^2(\omega_{\text{ir}} t_0) + \ln^2(\omega_{\text{uv}}/\omega_{\text{ir}})]}, \quad (3.34)$$

where the second-order contribution in  $\delta\lambda(t)$  is also included. Using this expression for the dephasing rate, the dephasing time  $T_\varphi = 1/\Gamma_\varphi$  can be computed. The PSD of  $1/f$  noise gives rise to logarithmic divergences which necessitates the introduction of infrared and ultraviolet cutoffs  $\omega_{\text{ir/uv}}$  and the time of the experiment  $t_0$ . The dephasing rate depends very weakly on these values and estimates suffice. We can estimate the experiment time  $t_0$  as the expected coherence time of the qubit. Low-frequency noise with a frequency much lower than the coherence time of the qubit can be considered systematic noise during an experiment and the infrared cutoff can be estimated according to  $\omega_{\text{ir}} \ll 1/t_0$ . The ultraviolet cutoff can, for example, be estimated as the frequency where the dominant noise source crosses over from  $1/f$  noise to Ohmic noise. The cross-over frequency is in the range 1 – 10GHz but depends on the experiment, see for example Ref. [126].

There exist two main strategies to reduce dephasing. The first is to operate the qubit at a so-called “sweet spot” where the first derivative of the qubit frequency vanishes  $\partial\omega/\partial\lambda = 0$ . This approach cancels the leading order contribution in Eq. (3.34) and increases the dephasing time of the qubit significantly. Using this strategy, an early experiment by Vion et al.[144] increased the dephasing time of the Cooper pair box by almost three orders of magnitude, reaching close to 1  $\mu\text{s}$ .

It is also possible to exponentially suppress  $\partial\omega/\partial\lambda$  for all  $\lambda$ , reaching what is sometimes referred to as the “sweet-spot-everywhere” regime. As before, we will refer to exponential insensitivity of this kind as protection. As previously mentioned, the transmon achieves protection against charge noise in the limit  $E_J/E_C \gg 1$  where the qubit states are localized near the minimum of the cosine potential. In this regime, tunneling between wells where the phase slips by  $2\pi$  is exponentially suppressed. These tunneling events can be related to charge noise dephasing by performing a unitary transform of the Hamiltonian in Eq. (3.11) with unitary  $U = e^{in_{\text{offset}}\phi}$ . This transformation effectively removes the offset charge  $n_{\text{offset}}$  from the Hamiltonian and attaches it to the qubit state  $|\tilde{\psi}\rangle = e^{in_{\text{offset}}\phi} |\psi\rangle$ . Thus, when a tunneling event occurs, the state acquires a phase  $e^{i2\pi n_{\text{offset}}}$  that leads to dephasing in the presence of fluctuating offset charges. Exponential suppression of the tunneling rate thereby leads to an exponential insensitivity to random fluctuations in  $n_{\text{offset}}$ . As we explore in Chapter 6, the sensitivity to flux noise can be achieved in the opposite regime  $E_J \sim E_C$ ,  $E_L \ll E_C$ , where charge is localized and phase fluctuations are large.

Using the expressions for the relaxation rate in Eq. (3.29) and the dephasing rate in Eq. (3.34), we can evaluate the decoherence time

$$T_2 = \left( \frac{\Gamma_1}{2} + \Gamma_\varphi \right)^{-1}, \quad (3.35)$$

which quantifies the total decoherence experienced by a qubit. The decoherence time can be computed by numerically evaluating the energy spectrum and matrix elements, for example, using

<sup>10</sup>A derivation of this result can be found in Ref. [127]. See also Ref. [143] for an alternative treatment.



dedicated packages such as those found in Refs. [145–147]. The computation of decoherence times is very useful to characterize superconducting qubits in experiments and to design novel qubits where coherence properties are engineered. The work discussed in Chapters 5 and 6 heavily relies on numerical evaluation of decoherence times and tests aspects of noise-protected qubits as covered in this chapter.



---

## Introduction to Project A

---

Parts of this chapter have been published in S. Krøjer, R. Seoane Souto, and K. Flensberg. “Demonstrating Majorana non-Abelian properties using fast adiabatic charge transfer”. In: *Phys. Rev. B* 105 (4 Jan. 2022), p. 045425. DOI: [10.1103/PhysRevB.105.045425](https://doi.org/10.1103/PhysRevB.105.045425). URL: <https://link.aps.org/doi/10.1103/PhysRevB.105.045425> and been included in my Master’s thesis S. Krøjer. *Demonstrating the Non-Abelian Nature of Majoranas*. 2020.

## Overview

This chapter introduces the work in Project A [P2] which is co-authored with Rubén Seoane Souto and Karsten Flensberg. The majority of the work leading to the main results in Project A was carried out during my Master's thesis [P6]. I gathered these results, prepared the corresponding figures and wrote the manuscript during the PhD in collaboration with the co-authors.

The study contained in Project A is concerned with charge-transfer operations between a quantum dot and a pair of Majoranas. This process can be used to demonstrate Majorana non-Abelian properties as proposed in Ref.[148]. Such charge-transfer operations rely on adiabatically manipulating the energy level of the quantum dot to shuttle a charge between the Majorana pair and the dot. It turns out that charge-transfer operations change the state of the Majorana pair in much the same way as an exchange in real space. Charge-transfer operations are therefore referred to as parameter space braiding and can be used in place of real-space braiding operations to show non-Abelian Majorana properties. Relatively few electrostatic gates are required to control charge-transfer operations compared to proposals that rely on real space exchange of Majoranas [41, 149], implying that a charge-transfer protocol is potentially simpler to execute in experiments. Since the Majoranas are coupled to a quantum dot, they are not topologically pinned to zero energy and become sensitive to fluctuations in the energy splitting. The interaction between Majoranas and the dot, however, also results in the charge-transfer operations comprising a universal set of single qubit gates. Despite the promising outlook of providing non-Abelian evidence for the realization of Majoranas, experimental challenges have prohibited the realization of charge-transfer operations [43, 150].

## Non-ideal charge-transfer

Project A includes several non-ideal factors in the description of charge-transfer operations that are generally present in experiments. Specifically, we consider systematic offsets in gates and external fluxes, see Fig. 4.1 for a device schematic. Here, a quantum dot (green, labeled  $D1$ ) is tunnel coupled to two MZMs (red, labeled  $M1, M2$  and described by operators  $\gamma_1, \gamma_2$ ) with coupling strengths  $w_1$  and  $w_2$ . The tunnel couplings and the energy level of the dot (denoted by  $\varepsilon_1$ ) are controlled by electrostatic gates. The relative phase between the tunnel couplings  $w_1, w_2$  can effectively be controlled by the external flux denoted by  $\Phi_1$ . The quantum dot is assumed to be spin-polarized by a large external magnetic field that is unrelated to  $\Phi_1$  such that the dot can be described by a single electronic state. A gate is used to adjust the energy level  $\varepsilon_1$  of the dot such that a single charge occupies the dot for  $\varepsilon_1 \rightarrow -\infty$ . When the energy level is adiabatically tuned to  $\varepsilon_1 \rightarrow \infty$ , the charge is expelled from the dot and tunnels to the Majorana system, occupying the zero energy state formed by Majoranas  $M1$  and  $M2$  [148, 151]. In the ideal case, the external flux equals an integer multiple of the flux quantum resulting in a degeneracy between the even and odd parity sectors of the combined dot/Majorana system. Under these circumstances, a charge-transfer between the dot and the Majorana system can be effectively described as an operation  $U = \cos(\theta)\gamma_1 + \sin(\theta)\gamma_2$  that acts on the Majorana system [148]. The rotation angle  $\theta$  is given by  $\tan(\theta) = |w_2/w_1|$  and can be controlled by adjusting the tunnel couplings via electrostatic gates.

Outside of the ideal regime, the charge-transfer operation will be affected by offsets in external flux and electrostatic gates as studied in Project A. Here, we find that offsets in tunnel couplings do not play a significant role, however, offsets in the external flux qualitatively changes the effect of charge-transfer operations. To describe charge-transfer operations away from the flux degeneracy

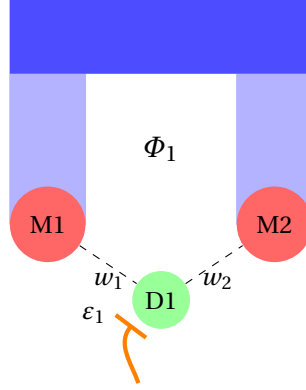


Fig. 4.1: A simple charge-transfer device adapted from [P1]. A quantum dot (green) is coupled to two Majoranas (red) via tunnel couplings  $w_1, w_2$ . The energy level  $\varepsilon_1$  of the quantum dot can be controlled by an electrostatic gate (orange). Majoranas appear at the ends of topological superconductors (light blue) which are connected via a (conventional) superconducting backbone (dark blue). A magnetic flux  $\Phi_1$  threads the loop formed by the superconducting arms and the quantum dot.

points, we consider the relative geometric and dynamical phases acquired for the even/odd parity during charge-transfer. As introduced in Chapter 2, operations on Majorana systems can be determined by the relative phase between states of different parity. Via this identification, we can describe charge-transfer operations in the non-degenerate case as an effective operation acting on the Majorana system,

$$U = \cos\left(\frac{\theta^G + \theta^D}{2}\right)\gamma_1 + \sin\left(\frac{\theta^G + \theta^D}{2}\right)\gamma_2. \quad (4.1)$$

The geometric and dynamical phases are denoted by  $\theta^G$  and  $\theta^D$  where we find

$$\tan(\theta^G) = \cos(\phi/2) \tan(2\theta) \quad (4.2)$$

with  $\phi$  being the reduced flux given by  $\phi = 2\pi\Phi_1/\Phi_0$ . The geometric phase is only slightly perturbed when the external flux is close to the flux degeneracy points  $\cos(\phi) \approx \pm 1$ . The dynamical phase, however, can lead to a substantial contribution even when the flux is very close to the degeneracy points. In the adiabatic limit, the operation time  $T$  of the charge-transfer is formally infinite and the dynamical phase also diverges in this limit (unless the flux is tuned to the degeneracy point with artificial accuracy). To mitigate the large effect due to the dynamical phase, we develop two ideas: (1) we propose a flux echo protocol that cancels dynamical phases and (2) we increase the speed of the charge-transfer process by optimizing the adiabatic trajectory. Concerning point (1), we propose a minimal protocol that demonstrates the non-Abelian nature of Majoranas using three consecutive charge-transfer operations. The non-Abelian signal corresponds to a parity measurement of a Majorana pair where the order of charge-transfer operations changes the outcome of the final measurement. If the external flux is changed by one flux quantum midway through the protocol, the dynamical phases of these operations cancel. If the echo is not perfectly executed, the residual dynamical phase can still be problematic as it reduces the visibility of the non-Abelian signal in the protocol.

## Optimizing the adiabatic trajectory

Point (2) attempts to reduce the impact of the residual dynamical phase inspired by the work in Ref. [152]. There, an adiabatic perturbation theory (APT) is developed for non-degenerate quantum systems. APT aims to quantify non-adiabatic corrections that appear when the time  $T$  of the evolution is finite, using the inverse time  $1/T$  as the perturbative expansion parameter. Specializing to the charge-transfer system, we use APT to find the optimal trajectory of the energy level  $\varepsilon_1$  by minimizing the leading order non-adiabatic contribution. In our case, it turns out that it is not sufficient to minimize the leading order contribution as APT does not guarantee that higher order terms are smaller. This can be traced back to the perturbative expansion parameter  $1/T$  not being dimensionless. We find the appropriate conditions to ensure that higher-order terms are always decreasing in magnitude and can derive the optimal trajectory of  $\varepsilon_1$  on this basis.

## Discussion

To test our analytical results, we simulate the dynamics of the charge-transfer process by numerically evaluating the time evolution due to the Schrödinger equation. For realistic parameters, we find that the charge-transfer process can be achieved in  $\sim 10$ ns using the optimal trajectory without introducing significant non-adiabatic errors. Depending on parameters, the optimal trajectory reduces the operation time by one to two orders of magnitude compared to a naive approach where the dot level energy is increased proportional to time. Regarding the visibility of the non-Abelian signal in our proposed protocol, we find that the theoretical predictions agree well with the numerical results. Further, the numerical results show that the flux echo protocol shows a clear non-Abelian signal for an appreciable range of parameters. We therefore conclude that demonstration of Majorana non-Abelian properties can be performed based on charge-transfer operations if fabrication and materials improve sufficiently in Majorana devices.

It is always relevant to consider whether subgap states of non-topological origin, e.g. Andreev bound states, can mimic the behavior of Majoranas in a given experiment. In our proposal, we believe that it is unlikely that ABSs can reproduce the non-Abelian signal. It is possible that ABSs can show a non-Abelian signal at highly fine-tuned points, however, our flux echo protocol shows that the non-Abelian signal due to Majoranas extend over a wide range of parameters. Additionally, the flux-echo is  $4\pi$ -periodic and this property is unlikely mimicked by ABSs while also showing strong non-Abelian signatures. Ultimately, the experiment signal-to-noise ratio determines how confidently a non-Abelian signal can be attributed to the presence of Majoranas and it should be supported by a thorough analysis of the ABS scenario and relevant disorder models.

Our results show that charge-transfer operations are robust against systematic offsets in experimental parameters, however, several other factors can reduce the visibility of the non-Abelian signature. For example, a non-zero temperature and electric fluctuations in gates can reduce the non-Abelian signal, if they are not much smaller than the tunnel couplings. Poisoning from quasiparticles will also interfere with the non-Abelian signal and it is typically required that the timescale of the experiment is shorter than the timescale of quasiparticle poisoning. Another benefit of the optimal adiabatic trajectory is that the effect of these non-ideal processes is diminished when the experiment time is reduced. Further work that elucidates the role played by temperature, gate fluctuations, etc. will provide interesting insights into the requirements that a potential experiment would need to fulfill. Another perspective is to consider shortcuts to adiabaticity as a way of further reducing the experiment time, see for example Refs. [153, 154].

---

A recent experiment [155] shows a promising direction for non-Abelian signatures based on charge-transfer. The experiment realizes a minimal two-site Kitaev chain that can be tuned to a sweet spot where “poor man’s” Majoranas appear [155–157]. These sweet-spot Majoranas are not topologically protected but can in principle show the same non-Abelian effects as topological Majoranas. It is an exciting possibility that charge-transfer operations, or other braiding-like protocols, can be used to test the non-Abelian properties of poor man’s Majoranas in minimal Kitaev chains or other suitable devices [157, 158].





---

## Introduction to Project B

---

Parts of this chapter have been submitted in S. Krøjer et al. *Fast universal control of a flux qubit via exponentially tunable wave-function overlap*. 2023. arXiv: [2303.01102](https://arxiv.org/abs/2303.01102) [quant-ph].

## Overview

This chapter introduces the work in Project B [P2] which is co-authored with Anders Enevold Dahl, Kasper Sangild Christensen, Morten Kjaergaard and Karsten Flensberg. I contributed to all parts of this work and led the simulations of the single and two-qubit gates. I wrote the introduction and sections concerning single and two-qubit gates with input and comments from the co-authors. I provided inputs to the remaining parts of the manuscript.

The study contained in Project B is concerned with a  $T_1$ -protected flux qubit variation and discusses its coherence properties, readout and single and two-qubit gates. The flux qubit is a type of superconducting qubit where the qubit mode is a heavy flux mode. Often, flux qubits are realized in the regime  $E_J > E_C$ ,  $E_L > E_C$  [103, 104, 159]. The persistent current flux qubit (PCFQ) is the first flux qubit design and consists of three large junctions connected in a loop [160, 161]. The qubit states of the PCFQ correspond to counter-propagating circulating currents that are induced when the qubit is biased near half flux quantum. The circulating current states, referred to as fluxon states, have opposite magnetic dipole moments, making their energy sensitive to fluctuations in the external magnetic field. A later notable variation of the flux qubit attempts to reduce the sensitivity to flux noise: the capacitively shunted flux qubit (CSFQ) operates in a slightly different parameter regime where the qubit states are the ground and excited state of a plasma mode [126]. The relative flux noise insensitivity of the CSFQ combined with significant advancements in fabrication increased this flux qubit's coherence time to  $T_1 \sim 50 \mu\text{s}$ .

As discussed in Chapter 3, qubits that are protected against relaxation can be challenging to perform gates on. For this reason, higher-lying states outside of the computational subspace are sometimes used during gate operations. An issue with this approach is that the higher-lying states can be significantly less coherent and thus limit the gate fidelity. That being said, recent experiments with fluxonium qubits show that the second excited state in this qubit is highly coherent [132] and can be used to assist two-qubit gates with exceptionally high fidelity  $F \approx 99.9\%$  [162]. In other qubits, for example the  $0 - \pi$  qubit, states beyond the second excited state are required to perform single and two-qubit gates [138, 141, 163]. For such qubits, it is relevant to consider alternative gate schemes that do not involve short-lived high-energy states.

## The double-shunted flux qubit

In Project A, we study a flux qubit variation which we refer to as the double-shunted flux qubit (DSFQ), see Fig. 5.1(a) for a device schematic. This flux qubit design is similar to the PCFQ, however, instead of using large Josephson junctions to reach a large ratio of  $E_J/E_C$ , we make use of smaller junctions and two large capacitive shunts. This choice enables more design flexibility as the size of the junction and the corresponding Josephson energy does not determine the  $E_J/E_C$  ratio. The DSFQ suffers from the same flux noise sensitivity as the PCFQ but enjoys protection against relaxation when  $E_J/E_C \gg 1$ , see Fig. 5.1(b, c). We use the design flexibility to add a feature to the DSFQ that complements its  $T_1$ -protection: one of the Josephson junctions is a nanowire junction. The Josephson energy of a nanowire junction can be controlled by electrostatic gates and has been demonstrated in experiments with gatemons and  $\cos(2\phi)$  qubits [139, 164–168]. In the DSFQ, the Josephson energy of the nanowire junction directly controls the potential barrier separating the fluxon states, see Fig. 5.1(c). This means that the hybridization between the qubit states can be directly adjusted via the gated nanowire junction.

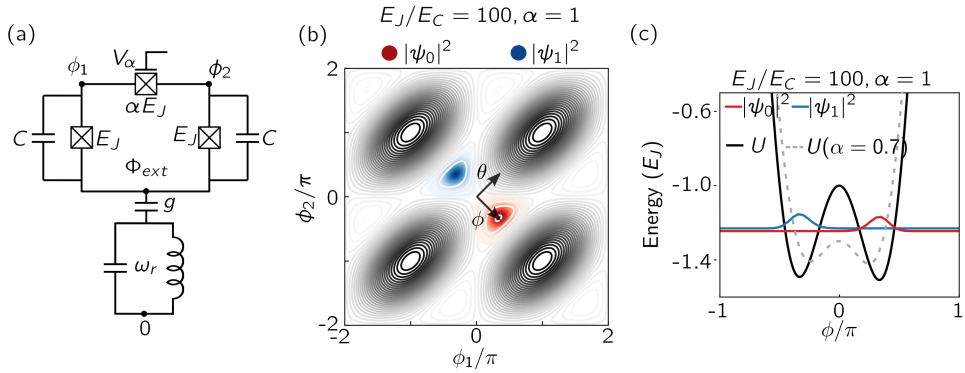


Fig. 5.1: Adapted from [P2]. (a) The DSFQ coupled to a readout resonator. The top junction is a nanowire junction whose Josephson energy  $\alpha E_J$  can be controlled via a gate voltage  $V_\alpha$ . (b) Potential landscape of the DSFQ where  $\phi = \phi_1 - \phi_2$  and  $\theta = \phi_1 + \phi_2$ . The ground state (red) and excited state (blue) are separated in respective wells. (c) Cut of the potential along  $\theta = 0$ . The potential barrier separating the two wells can be decreased by decreasing  $\alpha$ . The flux bias is  $\Phi_{\text{ext}} = 0.997 \times \Phi_0/2$ .

## Gates

The DSFQ is a relatively simple qubit platform where a novel gate scheme can be studied experimentally: To perform gates, we propose to momentarily decrease the potential barrier to hybridize the fluxon states, allowing for conventional direct-drive microwave gates. For gates based on multi-level excursions, it can be challenging to simultaneously engineer the properties of several high-energy states to improve the gate fidelity. In the gate scheme presented in Project B, the nanowire junction provides in situ control of the states that participate in gate operations, leading to more flexibility when optimizing gates.

Our numerical results show that proof-of-principle single qubit gates can be performed in this gate scheme and are compatible with standard  $IQ$ -mixing. Despite requiring a near-adiabatic control of the nanowire Josephson energy to lower the potential barrier, coherent errors are small and the gates are relatively fast. Including the near-adiabatic control, we find that single qubit gates can be performed in  $\sim 25\text{ns}$  with a  $T_1$ -limited fidelity of  $\sim 99\%$ . The coherent errors are around one order of magnitude less than errors due to relaxation during the gate.

We also propose to lower the potential barrier in order to execute two-qubit gates on capacitively coupled DSFQs. In this gate scheme, we only lower the potential barrier and do not apply a microwave drive. When the frequencies of coupled qubits are similar ( $\Delta\omega \sim 1\text{GHz}$ ), lowering the barrier can induce a swap of excitations between the qubits. In this case, the control of the potential barrier is near-adiabatic for all transitions except  $|01\rangle \leftrightarrow |10\rangle$ . This interaction results in a  $\sqrt{i\text{SWAP}}$  gate which can be executed in  $\sim 32\text{ns}$  with a  $T_1$ -limited fidelity of  $\sim 99.7\%$ . Again, the coherent errors are found to be about one order of magnitude less than the errors due to relaxation during the gate. It is a surprising result that the two-qubit gate fidelity is greater than the single qubit gate fidelity. It suggests that single qubit gates can be significantly optimized by reducing the time spent where the barrier is lowered.

## Readout

The DSFQ consists of two modes: a  $\phi$  mode, describing the qubit states as counter-propagating currents, and an auxiliary plasma mode that is in its ground state, see Fig. 5.1(b). We denote the auxiliary mode by  $\theta$ . To measure the state of the DSFQ, we capacitively couple a readout resonator to the  $\theta$  mode and read out in the dispersive regime, see Fig. 5.1(a). When the flux bias is near half flux quantum, the  $\theta$  mode does not contain information about the qubit state. To read out the qubit, the flux is adjusted away from a half flux quantum. In this case, the transition frequencies of the  $\theta$  mode are shifted by a small amount that depends on the state of the qubit. When the frequency of the readout resonator is close to a transition frequency of the  $\theta$  mode, the resonator frequency is shifted via the dispersive interaction. Since the transition frequency of the  $\theta$  mode depends on the qubit state, the dispersive shift of the readout resonator also depends on the qubit state. In this way, the auxiliary  $\theta$  mode can be used to mediate the interaction between the qubit mode  $\phi$  and the readout resonator.

There are several benefits of reading out through the  $\theta$  mode rather than the  $\phi$  mode. The qubit can not decay into the readout resonator since the  $\theta$  mode is in its ground state regardless of the qubit state. Said differently, the matrix element with the charge operator  $\langle 1|n_\theta|0\rangle$  vanishes due to even/odd selection rules of the  $\theta$  mode. Additionally, the qubit remains in the protected regime throughout the readout process, resulting in long relaxation times. Assuming a measurement time of  $1\mu\text{s}$ , we find the  $T_1$ -limited readout fidelity to be  $\sim 99.8\%$ .

## Discussion

The DSFQ is a platform where several interesting features can be experimentally explored. These features, variable-protection gates and readout via an auxiliary mode can potentially be relevant for other qubit designs which future work can elucidate. While variable-protection gates are only relevant for protected qubits, the idea of reading out through an auxiliary mode to prevent qubit relaxation can potentially be applied to a wider range of qubit designs.

State-of-the-art large-scale qubit systems are a highly competitive area where the transmon has paved the way for several remarkable experiments that demonstrate the capabilities of quantum computers [169–173]. The emergence of fluxonium as a flexible and capable qubit platform has further increased the competition [128, 131, 132, 136, 137, 162, 174, 175]. In this context, the DSFQ struggles with sensitivity to flux noise and a comparatively high dephasing rate through this channel. An additional concern regarding the DSFQ is the potential challenges in using nanowire junctions, for example, increased fabrication complexity and loss mechanisms in the mesoscopic junction. On the other hand, basing the DSFQ on a nanowire junction gives the opportunity to better characterize and improve this technology.

---

## Introduction to Project C

---

Parts of this chapter is contained in the unpublished work S. Krøjer et al. “Towards deep protection of qubits using realistic quarton array superinductors”. In: *preparation* (Nov. 2023).

## Overview

This chapter introduces the work in Project C [P3] which is co-authored with Alexandre Blais, Morten Kjaergaard and Karsten Flensberg. I led the scientific investigation, contributed substantially to the preparation of figures and wrote the manuscript with guidance, inputs and comments from the co-authors. This project was planned to be completed and submitted before the thesis deadline, however, we realized shortly before the deadline that one of the derivations in Project C ought to be revisited. Due to time constraints, these changes have not been included in the version of Project C that is part of this thesis. Below, we discuss what relevant changes should be made and how they change the main results presented in Project C.

The study contained in Project C is concerned with large superinductors and their role in protecting qubits against dephasing from flux noise. As introduced in Chapter 3, a large ratio  $E_J/E_C$  can be used to exponentially reduce sensitivity to charge noise. In this regime, quantum fluctuations in the charge mode are large and as a result, the qubit frequency becomes insensitive to small fluctuations in the offset charge. Superconducting qubits can be made insensitive to flux noise in an analogous fashion [127, 129, 140, 141, 159, 176–179]. In the limit of small inductive energy and large charging energy,  $E_L \ll E_C$ , quantum fluctuations in phase are large and the qubit becomes insensitive to flux noise. Since the charge operator can take continuous values in circuits with inductors, the superinductor is a very useful element that helps suppress sensitivity to both flux and charge noise. Satisfying the requirement  $E_L \ll E_C$  in practice, however, poses a fundamental experimental challenge since the self-impedance of inductive elements is limited by self-capacitance or parasitic capacitances to ground [124, 125, 180]. Superinductors are commonly based on Josephson junction arrays [124, 128, 132, 136, 137, 162, 174, 175] as described in Chapter 3. Here, conventional fabrication methods give rise to parasitic capacitances to ground that limit the number of junctions in the array to be around  $\sim 300$ , resulting in  $E_L > 0.1$  GHz [137]. While the experimentally realized inductive energies are small, they still need to be reduced by one to two orders of magnitude to fully protect superconducting qubits against flux noise [127, 129, 138, 140, 141]

## Quarton array superinductors

To improve superinductors based on junction arrays, we consider an array of quartons. In this context, the quarton can be described as an asymmetric interference device similar to the SQUID. The SQUID and the quarton, however, differ in one important aspect: one of the interferometer arms in the quarton consists of an array of junctions rather than a single junction [126, 181], see Fig. 6.1(a). To avoid confusion with the array of quartons, we refer to the array of junctions within the quarton as the subarray. The subarray plays an important role since its energy-phase relation is different from that of a single junction. If there are  $N_s$  junctions with Josephson energy  $\gamma N_s E_{JA}$  in the subarray, the energy-phase relation is approximately given by

$$V_{\text{subarray}} = -\gamma N_s^2 E_{JA} \cos(\phi_i / N_s). \quad (6.1)$$

where  $\phi_i$  is the phase drop across the  $i$ th quarton in the quarton array whose total phase drop is  $\sum_i \phi_i = \phi$ . The subarray energy-phase relation can be compared to the single junction energy-phase relation  $-E_{JA} \cos(\phi_i)$ . The difference between the two energy-phase relations means that interference effects can be used to cancel select energy terms. Specifically, when a quarton is biased by a half flux quantum  $\varphi_{\text{ext}} = \pi$  while  $\gamma = 1$ , we cancel the leading order energy term which

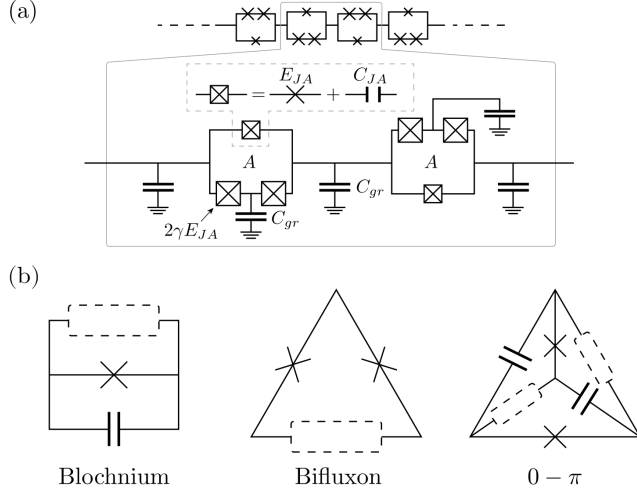


Fig. 6.1: Adapted from [P3]. (a) A quarton array superinductor with  $N_s = 2$  junctions in the quarton subarrays. (b) Circuit diagram of Blochnium, bifluxon and the  $0 - \pi$  qubit. The empty dashed boxes indicate where large inductive elements are placed. In the main text, we consider using quarton array superinductors as the inductive elements in the three qubits.

is quadratic in phase,

$$V_{\text{quarton}} = -E_{JA} \cos(\phi_i - \varphi_{\text{ext}}) - \gamma N_s^2 E_{JA} \cos(\phi_i / N_s) \quad (6.2)$$

$$\xrightarrow{\varphi_{\text{ext}} = \pi} (\gamma - 1) \frac{E_{JA}}{2} \phi_i^2 + \left(1 - \frac{\gamma}{N_s^2}\right) \frac{E_{JA}}{24} \phi_i^4 + \dots \quad (6.3)$$

Using the quarton energy-phase relation, we can obtain the energy-phase relation of the quarton array superinductor (QASI): When identical quartons are connected in series, the distributed phase approximation can be used across the QASI as described in Chapter 3. We denote the number of quartons by  $N_q$  and sum the energy contributions from all quartons. The resulting energy-phase relation of the QASI is,

$$V_{\text{QASI}} = (\gamma - 1) \frac{E_{JA}}{2N_q} \phi^2 + \left(1 - \frac{\gamma}{N_s^2}\right) \frac{E_{JA}}{24N_q^3} \phi^4 \quad (6.4)$$

where we identify the inductive energy as  $E_L = (\gamma - 1)E_{JA}/N_q$ . Canceling the quadratic term by choosing the value  $\gamma = 1$ , i.e. reducing  $E_L$ , effectively increases the inductance of the array. The cancellation of energy terms in Eq. (6.2) is not unique to the quarton and can be realized in any superconducting interferometer where the interferometer arms have different energy-phase relations [182]. The idea of tuning the non-linearity in junction arrays was first explored in Ref. [183] and has recently been considered as a way of increasing the anharmonicity of the Blochnium qubit [184]. In Project C, we use the QASI as inductive elements in the  $0 - \pi$  qubit [127, 129, 138, 141, 176, 177], the bifluxon qubit [140] and the Blochnium qubit [159, 178], see Fig. 6.1(b). We study the decoherence properties of the mentioned qubits and assess the experimental requirements in realizing superinductor-based protection against flux noise.

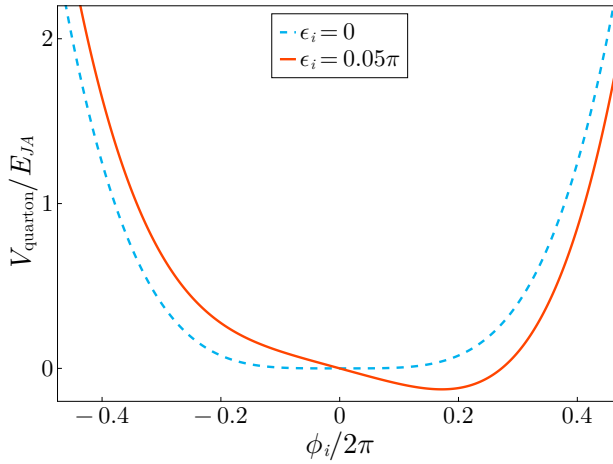


Fig. 6.2: The quarton energy-phase relation in the ideal case  $\epsilon_i = 0$  (blue, dashed line) and the disordered case  $\epsilon_i = 0.05\pi$  (red, solid line).

## Disorder

When fabricating QASIs, variations in Josephson energies, area of the quarton loops, etc. will impact the energy-phase relation of individual quartons and the array as a whole. We refer to these variations as disorder. In project C, we consider disorder in loop areas and Josephson junctions but focus on disorder in the quarton loop areas here. As we show, variations in loop areas lead to asymmetries in the quarton energy-phase relation which was not taken into account in Project C.

When disordered quartons are biased by a uniform magnetic field variations in loop areas result in variations in flux biases of individual quartons. We therefore consider the generic example where the quartons are biased by a flux that is slightly offset from half flux quantum  $\varphi_{\text{ext}} = \pi - \epsilon_i$ . Specializing to the case  $N_s = 2$ ,  $\gamma = 1$ , the quarton energy-phase relation in Eq. (6.2) becomes

$$\frac{V_{\text{quarton}}}{E_{JA}} = -\epsilon_i \phi_i + \frac{1}{32} \phi_i^4 \quad (6.5)$$

to leading order in  $\epsilon$  and  $\phi_i$ . This expression for the quarton energy-phase relation is a simplified version of the energy-phase relation presented in Project C. We will use this simple example to discuss challenges that arise when disorder is taken into account. In project C, we sum the contributions in Eq. (6.5) from all  $N_q$  quartons in the array and use the distributed phase approximation  $\phi_i = \phi/N_q$  to arrive at an expression for the QASI energy-phase relation,

$$\frac{V_{\text{QASI}}}{E_{JA}} = -\frac{\sum_i \epsilon_i}{N_q} \phi + \frac{1}{32 N_q^3} \phi^4. \quad (6.6)$$

However, the distributed phase approximation relies on all quartons to be identical which is not the case when we introduce disorder. Below, we discuss how to properly take disorder into account and compare this new result to Eq. (6.6).

In Fig. 6.2, we show the energy-phase relation of a disordered quarton in Eq. (6.5) when  $\epsilon_i = 0$  (blue, dashed line) and  $\epsilon_i = 0.05\pi$  (red, solid line). The flux offset  $\epsilon_i = 0.05\pi$  is about an order of



magnitude larger than what is expected from variations in loop areas [185, 186] and is chosen to make it easier to see the effect of area variation in Fig. 6.2. In the disordered case, we observe two important effects due to area variation: (1) the potential minimum shifts away from  $\phi_i = 0$  and (2) the potential is asymmetric around the minimum. Neither of these effects are taken into account when the distributed phase approximation is made to obtain Eq. (6.6) in Project C.

We start by considering point (1): the minimum of the quarton potential shifts relatively far away from  $\phi_i = 0$ , by an amount  $\sigma_i$  which we find to be

$$\sigma_i = \text{sign}(\epsilon_i) \cdot 2|\epsilon_i|^{1/3}. \quad (6.7)$$

Even for small offsets  $\epsilon_i$ , the shift of the minimum is significant due to the small exponent of  $1/3$ . This shift can not be physically observed since it depends on the choice of flux allocation in Eq. (6.2), see the discussion in Chapter 3 concerning the tunable transmon below Eq. (3.13). As a consequence, the linear term in the QASI energy-phase relation given in Eq. (6.6) is also not observable (e.g. as a non-zero current when  $\phi = 0$ ). To better describe the quarton, we therefore expand its potential around the minimum  $\sigma_i$ . We define  $\tilde{\phi}_i = \phi_i - \sigma_i$  and rewrite Eq. (6.5),

$$\frac{V_{\text{quarton}}}{E_{JA}} = -\epsilon_i \sigma_i + \frac{3\sigma_i^2}{16} \tilde{\phi}_i^2 + \frac{\sigma_i}{8} \tilde{\phi}_i^3 + \frac{1}{32} \tilde{\phi}_i^4. \quad (6.8)$$

Using this energy-phase relation, we can sum the contributions from all quartons in the array and consider if the distributed phase approximation is reasonable. This brings us to point (2): each quarton experiences a different shift  $\sigma_i$  which leads to different asymmetries encoded in the cubic term in Eq. (6.8). Considering that the distributed phase approximation is a way of minimizing the classical energy in arrays with identical elements, it is not obvious that this approximation holds for disordered quartons that show a large degree of asymmetry.

To explore when the DPA is a good approximation, we consider a simplified model of disorder where area variations result in  $N_q/2$  quartons that are biased by  $\varphi_{\text{ext}} = \pi - \epsilon$  and  $N_q/2$  quartons that are biased by  $\varphi_{\text{ext}} = \pi + \epsilon$ . We refer to these quartons as ( $\mp$ ) respectively. We may now consider three different applications of the DPA: (I) Apply the DPA directly to Eq. (6.5). This approach is equivalent to Project C and does not take the shift  $\sigma$  or the asymmetry into account. (II) Take into account the shift of the minima and apply the DPA to Eq. (6.8) (not taking into account the asymmetry). (III) Pair up all ( $-$ ) quartons with a ( $+$ ) quarton and minimize the classical energy of a single pair. Then apply the DPA across all pairs. Approach (III) effectively minimizes the classical energy across the array since all pairs of ( $\mp$ ) quartons are identical in the simplified model of disorder. The energy-phase relation of the QASI is straightforward to write down using approaches (I) and (II) while (III) is detailed below. The results are

$$(I) : \frac{V_{\text{QASI}}^{(I)}}{E_{JA}} = \frac{1}{32N_q^3} \phi^4, \quad (6.9)$$

$$(II) : \frac{V_{\text{QASI}}^{(II)}}{E_{JA}} = -\epsilon\sigma N_q + \frac{3\sigma^2}{16N_q} \phi^2 + \frac{1}{32N_q^3} \phi^4, \quad (6.10)$$

$$(III) : \frac{V_{\text{QASI}}^{(III)}}{E_{JA}} = -\epsilon\sigma N_q + \frac{1}{2} \sum_{\mp} \frac{3\sigma^2}{16N_q} (\phi \mp \eta)^2 \pm \frac{\sigma}{8N_q^2} (\phi \mp \eta)^3 + \frac{1}{32N_q^3} (\phi \mp \eta)^4, \quad (6.11)$$

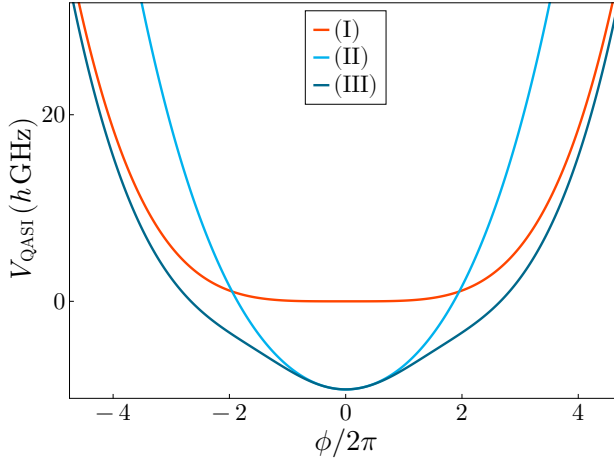


Fig. 6.3: The QASI energy-relation for the three approaches in Eqs. (6.9)-(6.11). The parameters used are  $E_{JA} = 40 \text{ h GHz}$ ,  $N_q = 30$ ,  $\epsilon = 0.005\pi$ .

where  $\eta$  is an internal mode that can be determined by minimizing the energy  $\partial V_{\text{QASI}}^{(III)}/\partial\eta = 0$ , giving the result

$$\eta = N_q\sigma + 2|\phi| \sinh \left[ \frac{1}{3} \log \left( \frac{\sqrt{(N_q\sigma)^6 + 4\phi^6} - (N_q\sigma)^3}{2|\phi|^3} \right) \right] \quad (6.12)$$

To derive the result from approach (III), we consider a pair of ( $\mp$ ) quartons where the total phase drop across the two quartons are  $2\phi/N_q$  following the DPA. We assume the phase drop across the ( $\mp$ ) quarton is  $\phi/N_q \mp \eta/N_q$  where  $\eta$  is the internal mode that can be found by minimizing the classical energy. Summing the energy contributions from the quarton pairs, we recover Eq. (6.11).

In Fig. 6.3, we show the QASI energy-phase relation for the three approaches resulting in Eqs. (6.9)-(6.11). We use values consistent with Project C,  $E_{JA} = 40 \text{ h GHz}$ ,  $N_q = 30$ ,  $\epsilon = 0.005\pi$ . Interestingly, we observe that approaches (I) and (II) agree with (III) in different limits. When  $\phi \approx 0$ , approach (II) agrees with (III) since the quadratic term in  $\phi$  dominates over the cubic term such that the asymmetry between ( $\mp$ ) quartons is small in this regime. For large  $\phi$ , the quartic term in  $\phi$  dominates and the ( $\mp$ ) quartons are not affected by the asymmetry near the potential minima and as a result approach (I) agrees with (III). In the intermediate regime, only approach (III) gives a faithful representation of the QASI energy-phase relation since it minimizes the classical energy with respect to the internal modes of the array. Since approach (I) cancels the quadratic contribution in  $\phi$ , it overestimates the inductance of the QASI compared to (III). Ideally, approach (III) should be developed further and implemented in Project C to properly account for disordered quartons. In its place, the simple approach (II) can be used as an approximation that underestimates the inductance. In practice, approach (II) is likely more fruitful to use due to its relative simplicity.

## Flux noise

In project C, we study dephasing due to noise in the flux that threads the quarton loops. In light of the results of the previous section, we here discuss how to best treat this flux noise.

When considering flux noise in general, the so-called irrotational basis should be used [122, 187]. The irrotational basis corresponds to the choice of flux allocation that ensures that the time-dependent external flux  $\varphi_{\text{ext}}$  is not present in the Hamiltonian. For a single quarton where  $\gamma = 1$  and  $N_s = 2$ , the proper choice of flux allocation following Ref. [122] results in

$$V_{\text{quarton}} = -E_{JA} \cos(\phi_i^{\text{ir}} - \varphi_{\text{ext}}/2) - 4E_{JA} \cos(\phi_i^{\text{ir}}/2 + \varphi_{\text{ext}}/4), \quad (6.13)$$

assuming the Josephson capacitances are  $C_J$  and  $\gamma N_s C_J$  for the single and subarray junctions respectively. The flux allocation leading to the irrotational basis can be related to the basis used in Eq. (6.2) via  $\phi_i^{\text{ir}} = \phi_i - \varphi_{\text{ext}}/2$ . We assume the external flux is  $\varphi_{\text{ext}} = \pi - \epsilon_i - \delta\epsilon_i(t)$  where  $\delta\epsilon_i(t)$  are time-dependent fluctuations in the flux. Using Eq. (6.13), we can compute the leading order noise term due to fluctuations in the flux,

$$\frac{\partial V_{\text{quarton}}}{\partial \delta\epsilon_i(t)} \delta\epsilon_i(t) = -4E_{JA} \sin(\phi_i/4) \cos^3(\phi_i/4) \delta\epsilon_i(t) \quad (6.14)$$

$$\approx -E_{JA} \phi_i \delta\epsilon_i(t). \quad (6.15)$$

Here, shifted back after the differentiation wrt.  $\delta\epsilon(t)$  to the basis used in the previous section  $\phi_i$ . Following approach (I), the result in Eq. (6.15) is summed across all quartons and the DPA is applied, giving the result

$$\frac{\delta V_{\text{QASI}}^{(I)}}{E_{JA}} = -\frac{\sum_i \delta\epsilon_i(t)}{N_q} \phi. \quad (6.16)$$

Assuming the local flux fluctuations  $\delta\epsilon_i(t)$  to be independently and identically distributed, we can replace the sum by  $\sum_i \delta\epsilon_i(t) = \sqrt{N_q} \delta\epsilon(t)$ . This is done in Project C to compute the dephasing rate due to local flux noise in the array as described in Chapter 3 and following Ref. [127].

Concerning approaches (II) and (III), we need to consider if the internal modes of the quarton array are fast enough to adapt to flux fluctuations. If the internal modes are slow compared to fluctuations in  $\delta\epsilon(t)$ , then the shifts of the minima  $\sigma_i$  and the internal mode  $\eta$  can be assumed to be fixed in time. In this case, Eq. (6.15) can be used to compute flux noise dephasing times in approaches (II) and (III). However, flux fluctuations are small and typically follow a  $1/f$ -type noise spectrum where low frequencies dominate. At the same time, the internal modes are high-frequency modes  $\sim 10$  GHz, implying that it is reasonable to assume that the internal modes can instantaneously accommodate flux fluctuations. Fast internal modes can in this case significantly modify the QASI's response to local flux noise. In an ultra-simplified noise model where all ( $\mp$ ) quartons in approach (II) and (III) experience the same noise  $\varphi_{\text{ext}} = \pi \mp \epsilon \mp \delta\epsilon(t)$ , the flux noise simply updates the shift  $\sigma$  and the internal mode  $\eta$  through  $\epsilon \rightarrow \epsilon + \delta\epsilon(t)$ , see Eqs. (6.7) and (6.12). The effect of flux noise in this simple model is to “wiggle” existing parameters, maintaining the symmetry of the energy-phase relation. In a more realistic noise model, it is possible that  $\delta\epsilon(t)$  couples to new terms that introduce an asymmetry in the energy-phase relations in Eqs. (6.10)-(6.11). This could, for example, be a term proportional to  $\delta\epsilon(t)\phi^3$  in Eq. (6.10). Importantly, a term proportional to  $\delta\epsilon(t)\phi$  can never appear as approach (II) and (III) ensure that the minimum of the energy-phase relation is at  $\phi = 0$ . Compared to approach (I), where flux noise enters as  $\delta\epsilon(t)\phi$ , there

is a qualitative difference in how flux noise couples to phase depending on whether the internal modes of the array are fast or slow compared to the flux noise. While the energy minimization in approaches (II) and (III) is complicated by flux noise and its effect on the shifts of the minima and the internal modes, it is relevant to continue to develop this approach to apply it in Project C. In the next section, we discuss how the main results in Project C change in light of the considerations of this chapter.

## Discussion

In Project C, we study dephasing due to  $1/f$  flux noise in the  $0 - \pi$  qubit, bifluxon and Blochonium where their inductive elements are QASIs. In addition to flux noise in the quarton array, there is also flux noise in the qubit loops which is typically a significant dephasing channel. Common to the three qubits, however, we find that sensitivity to flux noise in the quarton array is typically increased by two to three orders of magnitude compared to flux noise in the qubit loop. Since approach (III) suggests that the inductance is smaller than quoted in Project C, the qubits are likely more sensitive to flux noise in the qubit loop, reducing dephasing times due to this noise source.

On the other hand, the sensitivity to local flux noise in the quarton array is likely to be reduced since fast internal modes in the quarton array can adapt to fluctuations in flux. The leading order noise term in Eq. (6.16),  $\delta\epsilon(t)\phi/\sqrt{N_q}$ , is a relatively large term compared to the energy-phase relations in Eqs. (6.9)-(6.11) since it is only reduced by a factor  $1/\sqrt{N_q}$ . This is in part responsible for the large sensitivity to flux noise in the quarton array quoted in Project C. When flux noise couples to higher powers of phase as in approaches (II) and (III), the terms are reduced by equally higher powers of  $1/N_q$ . For example, if flux noise couples to a cubic phase term, the noise term will presumably be proportional to  $[\sqrt{N_q}\delta\epsilon(t)] \cdot [\phi^3/N_q^3]$  in the simplest case. While speculative, it is therefore possible that fast internal modes in the array have a significant impact that substantially reduces the sensitivity to flux noise in the quarton array. As a consequence, we believe that a more accurate description of the QASI following approaches (II) and (III) will decrease the sensitivity to the limiting noise channel in Project C. For this reason, the experimental requirements to reach protection against flux noise can potentially be relaxed somewhat.

As a penultimate remark, we mention that we also consider photon shot-noise dephasing due to the spurious  $\zeta$  mode in the QASI-based  $0 - \pi$  qubit. We study an interaction between the  $\zeta$  mode and the qubit mode  $\phi$  that is due to the quartic term in the QASI energy-phase relation obtained from approach (I). In Project C, we find that dephasing due to shot-noise is about as detrimental as flux noise in the quarton array. Turning to approach (III), it is hard to assess what the  $\zeta$ - $\phi$  interaction will be given the non-trivial energy-phase relation in Eq. (6.11). Provided that approach (II) is a good approximation, it is relatively straightforward to treat the interaction between the  $\zeta$  and  $\phi$  mode. Since the energy-phase relation in Eq. (6.10) is approximately quadratic in phase, it follows that the  $\zeta$ - $\phi$  interaction is similar to the dispersive interaction found in the conventional  $0 - \pi$  qubit [127, 141]. Shot-noise dephasing in the conventional  $0 - \pi$  qubit is a second-order process of the dispersive interaction while the interaction considered in Project C contributes at first order. It is therefore possible that the  $\zeta$ - $\phi$  interaction obtained from approach (II) is less significant than the one obtained from (I) in Project C. We therefore speculate that shot-noise dephasing due to the spurious  $\zeta$  mode is overestimated in Project C and that approach (II) gives a more accurate result that also relaxes the experimental requirements to protect the  $0 - \pi$  qubit against shot-noise dephasing.

---

To conclude, we consider the results found in Project C in the light of the considerations presented in this chapter. Flux noise protected superconducting qubits based on QASIs can achieve significantly higher ratios of  $E_C/E_L$  due to the cancellation of the quadratic phase term. In principle, this mechanism lowers the experimental requirement to realize the protected regime  $E_C/E_L \gg 1$ . However, QASIs also introduce flux noise in the array that results in dephasing times which are orders of magnitude shorter compared to existing decoherence channels. Despite this significant drawback, Project C finds that the increased inductance of the QASI outweighs the high sensitivity to flux noise in the array when compared to conventional junction array superinductors. Given the new results provided in this chapter, it appears that the approximations used to describe the disordered QASI in Project C are not sufficiently accurate. We speculate that using a better description of the disordered QASI leads to a decreased sensitivity to array flux noise since internal modes of the array can accommodate the randomly fluctuating fluxes. For these reasons, the QASI is an interesting platform for realizing very large inductance elements that may lower the experimental requirements to realize flux noise protected superconducting qubits.



---

## Bibliography

- [P1] S. Krøjer, R. Seoane Souto, and K. Flensberg. “Demonstrating Majorana non-Abelian properties using fast adiabatic charge transfer”. In: *Phys. Rev. B* 105 (4 Jan. 2022), p. 045425. DOI: [10.1103/PhysRevB.105.045425](https://doi.org/10.1103/PhysRevB.105.045425). URL: <https://link.aps.org/doi/10.1103/PhysRevB.105.045425>.
- [P2] S. Krøjer, A. E. Dahl, K. S. Christensen, M. Kjaergaard, and K. Flensberg. *Fast universal control of a flux qubit via exponentially tunable wave-function overlap*. 2023. arXiv: [2303.01102](https://arxiv.org/abs/2303.01102) [quant-ph].
- [P3] S. Krøjer, A. Blais, M. Kjaergaard, and K. Flensberg. “Towards deep protection of qubits using realistic qurton array superinductors”. In: *preparation* (Nov. 2023).
- [P4] J. Schulenburg, S. Krøjer, M. Burrello, M. Leijnse, and K. Flensberg. “Detecting Majorana modes by readout of poisoning-induced parity flips”. In: *Phys. Rev. B* 107 (12 Mar. 2023), p. L121401. DOI: [10.1103/PhysRevB.107.L121401](https://doi.org/10.1103/PhysRevB.107.L121401). URL: <https://link.aps.org/doi/10.1103/PhysRevB.107.L121401>.
- [P5] M. Geier, S. Krøjer, F. von Oppen, C. M. Marcus, K. Flensberg, and P. W. Brouwer. *Non-Abelian holonomy of Majorana zero modes coupled to a chaotic quantum dot*. 2023. arXiv: [2304.06754](https://arxiv.org/abs/2304.06754) [cond-mat.mes-hall].
- [P6] S. Krøjer. *Demonstrating the Non-Abelian Nature of Majoranas*. 2020.
- [7] T. E. of Encyclopaedia Britannica. *Steam engine*. <https://www.britannica.com/technology/steam-engine>. Sept. 2023.
- [8] J. Watt. *James Watt on the steam engine*. <https://www.britannica.com/topic/James-Watt-on-the-steam-engine-2215552>. Accessed Nov. 2023.
- [9] O. Nathan and H. Smith. *Den Harmoniske Begejstring (eng.: The Harmonic Inspiration)*. Gyldendal, 1999.
- [10] L. Davis. *Fleet Fire*. Arcade Publishing, 2003.
- [11] E. E. Burns. *The Story of Great Inventions*. Harper & Brothers Publishers, 1910.
- [12] B. C. Blake-Coleman. *Copper Wire and Electrical Conductors: The Shaping of a Technology*. Harwood Academic Publishers, 1992.
- [13] J. C. Maxwell. *A Treatise on Electricity and Magnetism*. Oxford University Press, 1873.

- [14] T. R. S. A. of Sciences. *The Nobel Prize in Physics 2014*. <https://www.nobelprize.org/prizes/physics/2014/summary/>. Oct. 2014.
- [15] S. P. Shuji Nakamura and G. Fasol. *The Blue Laser Diode*. Springer, 2000.
- [16] E. F. Schubert. *Light-Emitting Diodes*. Cambridge University Press, 2012.
- [17] F. Bloch. “Über die Quantenmechanik der Elektronen in Kristallgittern”. In: *Zeitschrift für Physik* 52.7 (July 1929), pp. 555–600. ISSN: 0044-3328. DOI: [10.1007/BF01339455](https://doi.org/10.1007/BF01339455). URL: <https://doi.org/10.1007/BF01339455>.
- [18] J. J. Quinn and K.-S. Yi. *Solid State Physics*. Springer, 2009.
- [19] S. M. Girvin and K. Yang. *Modern Condensed Matter Physics*. Cambridge University Press, 2019.
- [20] P. Y. Yu and M. Cardona. *Fundamentals of Semiconductors, 4th Ed.* Springer, 2010.
- [21] J. M. Luttinger and W. Kohn. “Motion of Electrons and Holes in Perturbed Periodic Fields”. In: *Phys. Rev.* 97 (4 Feb. 1955), pp. 869–883. DOI: [10.1103/PhysRev.97.869](https://doi.org/10.1103/PhysRev.97.869). URL: <https://link.aps.org/doi/10.1103/PhysRev.97.869>.
- [22] E. Kane. “Energy band structure in p-type germanium and silicon”. In: *Journal of Physics and Chemistry of Solids* 1.1 (1956), pp. 82–99. ISSN: 0022-3697. DOI: [https://doi.org/10.1016/0022-3697\(56\)90014-2](https://doi.org/10.1016/0022-3697(56)90014-2). URL: <https://www.sciencedirect.com/science/article/pii/0022369756900142>.
- [23] E. O. Kane. “Band structure of indium antimonide”. In: *Journal of Physics and Chemistry of Solids* 1.4 (1957), pp. 249–261. ISSN: 0022-3697. DOI: [https://doi.org/10.1016/0022-3697\(57\)90013-6](https://doi.org/10.1016/0022-3697(57)90013-6). URL: <https://www.sciencedirect.com/science/article/pii/0022369757900136>.
- [24] M. Berry and M. Jeffrey. “Chapter 2 Conical diffraction: Hamilton’s diabolical point at the heart of crystal optics”. In: ed. by E. Wolf. Vol. 50. *Progress in Optics*. Elsevier, 2007, pp. 13–50. DOI: [https://doi.org/10.1016/S0079-6638\(07\)50002-8](https://doi.org/10.1016/S0079-6638(07)50002-8). URL: <https://www.sciencedirect.com/science/article/pii/S0079663807500028>.
- [25] A. Streltsov, G. Adesso, and M. B. Plenio. “Colloquium: Quantum coherence as a resource”. In: *Rev. Mod. Phys.* 89 (4 Oct. 2017), p. 041003. DOI: [10.1103/RevModPhys.89.041003](https://doi.org/10.1103/RevModPhys.89.041003). URL: <https://link.aps.org/doi/10.1103/RevModPhys.89.041003>.
- [26] S. Lloyd. “Universal Quantum Simulators”. In: *Science* 273.5278 (1996), pp. 1073–1078. DOI: [10.1126/science.273.5278.1073](https://doi.org/10.1126/science.273.5278.1073). eprint: <https://www.science.org/doi/pdf/10.1126/science.273.5278.1073>. URL: <https://www.science.org/doi/abs/10.1126/science.273.5278.1073>.
- [27] R. P. Feynman. “Simulating physics with computers”. In: *International Journal of Theoretical Physics* 21.6 (June 1982), pp. 467–488. ISSN: 1572-9575. DOI: [10.1007/BF02650179](https://doi.org/10.1007/BF02650179). URL: <https://doi.org/10.1007/BF02650179>.
- [28] P. Benioff. “The computer as a physical system: A microscopic quantum mechanical Hamiltonian model of computers as represented by Turing machines”. In: *Journal of Statistical Physics* 22.5 (May 1980), pp. 563–591. ISSN: 1572-9613. DOI: [10.1007/BF01011339](https://doi.org/10.1007/BF01011339). URL: <https://doi.org/10.1007/BF01011339>.



- [29] M. A. Nielsen and I. L. Chuang. *Quantum Computation and Quantum Information: 10th Anniversary Edition*. Cambridge University Press, 2010. DOI: [10.1017/CB09780511976667](https://doi.org/10.1017/CB09780511976667).
- [30] E. R. MacQuarrie, C. Simon, S. Simmons, and E. Maine. “The emerging commercial landscape of quantum computing”. In: *Nature Reviews Physics* 2.11 (Nov. 2020), pp. 596–598. ISSN: 2522-5820. DOI: [10.1038/s42254-020-00247-5](https://doi.org/10.1038/s42254-020-00247-5). URL: <https://doi.org/10.1038/s42254-020-00247-5>.
- [31] D. J. Griffiths and D. F. Schroeter. *Introduction to Quantum Mechanics*. 3rd ed. Cambridge University Press, 2018. DOI: [10.1017/9781316995433](https://doi.org/10.1017/9781316995433).
- [32] J. J. Sakurai and J. Napolitano. *Modern Quantum Mechanics*. 2nd ed. Cambridge University Press, 2017. DOI: [10.1017/9781108499996](https://doi.org/10.1017/9781108499996).
- [33] A. Zee. *Group Theory in a Nutshell for Physicists*. USA: Princeton University Press, Mar. 2016. ISBN: 978-1-4008-8118-5, 978-0-691-16269-0.
- [34] C. E. Shannon. “A Mathematical Theory of Communication”. In: *The Bell System Technical Journal* 27 (1948), pp. 379–423. URL: <http://plan9.bell-labs.com/cm/ms/what/shannonday/shannon1948.pdf> (visited on 04/22/2003).
- [35] B. Schumacher. “Quantum coding”. In: *Phys. Rev. A* 51 (4 Apr. 1995), pp. 2738–2747. DOI: [10.1103/PhysRevA.51.2738](https://doi.org/10.1103/PhysRevA.51.2738). URL: <https://link.aps.org/doi/10.1103/PhysRevA.51.2738>.
- [36] D. P. DiVincenzo. “The Physical Implementation of Quantum Computation”. In: *Fortschritte der Physik* 48.9-11 (2000), pp. 771–783. DOI: [https://doi.org/10.1002/1521-3978\(200009\)48:9/11<771::AID-PROP771>3.0.CO;2-E](https://doi.org/10.1002/1521-3978(200009)48:9/11<771::AID-PROP771>3.0.CO;2-E). eprint: <https://onlinelibrary.wiley.com/doi/pdf/10.1002/1521-3978%28200009%2948%3A9/11%3C771%3A%3AAID-PROP771%3E3.0.CO%3B2-E>. URL: <https://onlinelibrary.wiley.com/doi/abs/10.1002/1521-3978%28200009%2948%3A9/11%3C771%3A%3AAID-PROP771%3E3.0.CO%3B2-E>.
- [37] M. Leijnse and K. Flensberg. “Introduction to topological superconductivity and Majorana fermions”. In: *Semicond. Sci. Technol.* 27.12 (Dec. 2012), p. 124003. ISSN: 0268-1242. DOI: [10.1088/0268-1242/27/12/124003](https://doi.org/10.1088/0268-1242/27/12/124003). URL: <http://stacks.iop.org/0268-1242/27/i=12/a=124003?key=crossref.24c8187eaf71ff4bca950d5184462df5>.
- [38] C. Nayak, S. H. Simon, A. Stern, M. Freedman, and S. Das Sarma. “Non-Abelian anyons and topological quantum computation”. In: *Rev. Mod. Phys.* 80.3 (2008), p. 1083. DOI: [10.1103/RevModPhys.80.1083](https://doi.org/10.1103/RevModPhys.80.1083).
- [39] R. Aguado. In: *La Rivista del Nuovo Cimento* 40 (2017), p. 523. DOI: [10.1393/ncr/i2017-10141-9](https://doi.org/10.1393/ncr/i2017-10141-9).
- [40] C. W. J. Beenakker. “Search for non-Abelian Majorana braiding statistics in superconductors”. In: *SciPost Phys. Lect. Notes* (2020), p. 15. DOI: [10.21468/SciPostPhysLectNotes.15](https://doi.org/10.21468/SciPostPhysLectNotes.15). URL: <https://scipost.org/10.21468/SciPostPhysLectNotes.15>.
- [41] J. Alicea, Y. Oreg, G. Refael, F. von Oppen, and M. P. A. Fisher. “Non-Abelian statistics and topological quantum information processing in 1D wire networks”. In: *Nat. Phys.* 7.5 (Feb. 2011), pp. 412–417. ISSN: 1745-2473. DOI: [10.1038/nphys1915](https://doi.org/10.1038/nphys1915).

- [42] J. Alicea. “New directions in the pursuit of Majorana fermions in solid state systems.” In: *Rep. Prog. Phys.* 75 (2012), p. 076501. DOI: [10.1088/0034-4885/75/7/076501](https://doi.org/10.1088/0034-4885/75/7/076501). URL: <http://www.ncbi.nlm.nih.gov/pubmed/22790778>.
- [43] K. Flensberg, F. von Oppen, and A. Stern. “Engineered platforms for topological superconductivity and Majorana zero modes”. In: *Nature Reviews Materials* 6.10 (Oct. 2021), pp. 944–958. ISSN: 2058-8437. DOI: [10.1038/s41578-021-00336-6](https://doi.org/10.1038/s41578-021-00336-6). URL: <https://doi.org/10.1038/s41578-021-00336-6>.
- [44] A. Kitaev and C. Laumann. *Topological phases and quantum computation*. 2009. arXiv: 0904.2771 [cond-mat.mes-hall].
- [45] R. Moessner and J. E. Moore. “Topological Quantum Computation via Non-Abelian Statistics”. In: *Topological Phases of Matter*. Cambridge University Press, 2021, pp. 285–315. DOI: [10.1017/9781316226308.010](https://doi.org/10.1017/9781316226308.010).
- [46] S. D. Sarma, M. Freedman, and C. Nayak. “Majorana zero modes and topological quantum computation”. In: *npj Quantum Information* 1.1 (Oct. 2015), p. 15001. ISSN: 2056-6387. DOI: [10.1038/npjqi.2015.1](https://doi.org/10.1038/npjqi.2015.1). URL: <https://doi.org/10.1038/npjqi.2015.1>.
- [47] K. Laubscher and J. Klinovaja. “Majorana bound states in semiconducting nanostructures”. In: *Journal of Applied Physics* 130.8 (Aug. 2021), p. 081101. ISSN: 0021-8979. DOI: [10.1063/5.0055997](https://doi.org/10.1063/5.0055997). eprint: [https://pubs.aip.org/aip/jap/article-pdf/doi/10.1063/5.0055997/15267235/081101\\_1\\_online.pdf](https://pubs.aip.org/aip/jap/article-pdf/doi/10.1063/5.0055997/15267235/081101_1_online.pdf). URL: <https://doi.org/10.1063/5.0055997>.
- [48] P. Marra. “Majorana nanowires for topological quantum computation”. In: *Journal of Applied Physics* 132.23 (Dec. 2022), p. 231101. ISSN: 0021-8979. DOI: [10.1063/5.0102999](https://doi.org/10.1063/5.0102999). eprint: [https://pubs.aip.org/aip/jap/article-pdf/doi/10.1063/5.0102999/16519324/231101\\_1\\_online.pdf](https://pubs.aip.org/aip/jap/article-pdf/doi/10.1063/5.0102999/16519324/231101_1_online.pdf). URL: <https://doi.org/10.1063/5.0102999>.
- [49] S. B. Bravyi and A. Y. Kitaev. “Fermionic Quantum Computation”. In: *Annals of Physics* 298.1 (May 2002), pp. 210–226. DOI: [10.1006/aphy.2002.6254](https://doi.org/10.1006/aphy.2002.6254). URL: <http://linkinghub.elsevier.com/retrieve/doi/10.1006/aphy.2002.6254>.
- [50] J. Sau, S. Tewari, and S. Das Sarma. “Universal quantum computation in a semiconductor quantum wire network”. In: *Phys. Rev. A* 82.5 (Nov. 2010), p. 052322. ISSN: 1050-2947. DOI: [10.1103/PhysRevA.82.052322](https://doi.org/10.1103/PhysRevA.82.052322). URL: <http://link.aps.org/doi/10.1103/PhysRevA.82.052322>.
- [51] O. Zilberberg, B. Braunecker, and D. Loss. “Controlled-NOT gate for multiparticle qubits and topological quantum computation based on parity measurements”. In: *Phys. Rev. A* 77 (1 Jan. 2008), p. 012327. DOI: [10.1103/PhysRevA.77.012327](https://doi.org/10.1103/PhysRevA.77.012327). URL: <https://link.aps.org/doi/10.1103/PhysRevA.77.012327>.
- [52] P. Bonderson, M. Freedman, and C. Nayak. “Measurement-Only Topological Quantum Computation”. In: *Phys. Rev. Lett.* 101.1 (June 2008), p. 010501. ISSN: 0031-9007. DOI: [10.1103/PhysRevLett.101.010501](https://doi.org/10.1103/PhysRevLett.101.010501). URL: <http://link.aps.org/doi/10.1103/PhysRevLett.101.010501>.
- [53] P. Bonderson. “Measurement-only topological quantum computation via tunable interactions”. In: *Phys. Rev. B* 87 (3 Jan. 2013), p. 035113. DOI: [10.1103/PhysRevB.87.035113](https://doi.org/10.1103/PhysRevB.87.035113). URL: <https://link.aps.org/doi/10.1103/PhysRevB.87.035113>.

- [54] D. Aasen, M. Hell, R. V. Mishmash, A. Higginbotham, J. Danon, M. Leijnse, T. S. Jespersen, J. A. Folk, C. M. Marcus, K. Flensberg, and J. Alicea. “Milestones Toward Majorana-Based Quantum Computing”. In: *Phys. Rev. X* 6.3 (Aug. 2016), p. 031016. ISSN: 2160-3308. DOI: [10.1103/PhysRevX.6.031016](https://doi.org/10.1103/PhysRevX.6.031016). URL: <http://journals.aps.org/prx/abstract/10.1103/PhysRevX.6.031016>.
- [55] S. Vijay and L. Fu. “Teleportation-based quantum information processing with Majorana zero modes”. In: *Phys. Rev. B* 94 (23 Dec. 2016), p. 235446. DOI: [10.1103/PhysRevB.94.235446](https://doi.org/10.1103/PhysRevB.94.235446). URL: <https://link.aps.org/doi/10.1103/PhysRevB.94.235446>.
- [56] S. Plugge, A. Rasmussen, R. Egger, and K. Flensberg. “Majorana box qubits”. In: *New Journal of Physics* 19 (2017), p. 012001. DOI: [10.1088/1367-2630/aa54e1](https://doi.org/10.1088/1367-2630/aa54e1).
- [57] T. Karzig, C. Knapp, R. M. Lutchyn, P. Bonderson, M. B. Hastings, C. Nayak, J. Alicea, K. Flensberg, S. Plugge, Y. Oreg, C. M. Marcus, and M. H. Freedman. “Scalable designs for quasiparticle-poisoning-protected topological quantum computation with Majorana zero modes”. In: *Phys. Rev. B* 95 (2017), p. 235305. DOI: [10.1103/PhysRevB.95.235305](https://doi.org/10.1103/PhysRevB.95.235305).
- [58] T. Karzig, Y. Oreg, G. Refael, and M. H. Freedman. “Robust Majorana magic gates via measurements”. In: *Phys. Rev. B* 99 (14 Apr. 2019), p. 144521. DOI: [10.1103/PhysRevB.99.144521](https://doi.org/10.1103/PhysRevB.99.144521). URL: <https://link.aps.org/doi/10.1103/PhysRevB.99.144521>.
- [59] R. S. Souto and M. Leijnse. “Fusion rules in a Majorana single-charge transistor”. In: *SciPost Phys.* 12 (2022), p. 161. DOI: [10.21468/SciPostPhys.12.5.161](https://doi.org/10.21468/SciPostPhys.12.5.161). URL: <https://scipost.org/10.21468/SciPostPhys.12.5.161>.
- [60] J. M. Leinaas and J. Myrheim. “On the theory of identical particles”. In: *Il Nuovo Cimento B (1971-1996)* 37.1 (Jan. 1977), pp. 1–23. ISSN: 1826-9877. DOI: [10.1007/BF02727953](https://doi.org/10.1007/BF02727953). URL: <https://doi.org/10.1007/BF02727953>.
- [61] G. A. Goldin, R. Menikoff, and D. H. Sharp. “Particle statistics from induced representations of a local current group”. In: *Journal of Mathematical Physics* 21.4 (July 1980), pp. 650–664. ISSN: 0022-2488. DOI: [10.1063/1.524510](https://doi.org/10.1063/1.524510). eprint: [https://pubs.aip.org/aip/jmp/article-pdf/21/4/650/8151401/650\\_1\\_online.pdf](https://pubs.aip.org/aip/jmp/article-pdf/21/4/650/8151401/650_1_online.pdf). URL: <https://doi.org/10.1063/1.524510>.
- [62] F. Wilczek. “Magnetic Flux, Angular Momentum, and Statistics”. In: *Phys. Rev. Lett.* 48 (17 Apr. 1982), pp. 1144–1146. DOI: [10.1103/PhysRevLett.48.1144](https://doi.org/10.1103/PhysRevLett.48.1144). URL: <https://link.aps.org/doi/10.1103/PhysRevLett.48.1144>.
- [63] F. Wilczek. “Quantum Mechanics of Fractional-Spin Particles”. In: *Phys. Rev. Lett.* 49 (14 Oct. 1982), pp. 957–959. DOI: [10.1103/PhysRevLett.49.957](https://doi.org/10.1103/PhysRevLett.49.957). URL: <https://link.aps.org/doi/10.1103/PhysRevLett.49.957>.
- [64] D. A. Ivanov. “Non-Abelian Statistics of Half-Quantum Vortices in p-Wave Superconductors”. In: *Phys. Rev. Lett.* 86.2 (Jan. 2001), pp. 268–271. ISSN: 0031-9007. DOI: [10.1103/PhysRevLett.86.268](https://doi.org/10.1103/PhysRevLett.86.268).
- [65] A. Y. Kitaev. “Fault-tolerant quantum computation by anyons”. In: *Annals of Physics* 303.1 (2003), pp. 2–30. DOI: [10.1016/S0003-4916\(02\)00018-0](https://doi.org/10.1016/S0003-4916(02)00018-0).
- [66] A. Y. Kitaev. “Unpaired Majorana fermions in quantum wires”. In: *Phys. Usp.* 44.10S (Oct. 2001), p. 131. DOI: [10.1070/1063-7869/44/10S/S29](https://doi.org/10.1070/1063-7869/44/10S/S29).

- [67] A. Mackenzie and Y. Maeno. “p-wave superconductivity”. In: *Physica B: Condensed Matter* 280.1 (2000), pp. 148–153. ISSN: 0921-4526. DOI: [https://doi.org/10.1016/S0921-4526\(99\)01546-X](https://doi.org/10.1016/S0921-4526(99)01546-X). URL: <https://www.sciencedirect.com/science/article/pii/S092145269901546X>.
- [68] A. Altland and M. R. Zirnbauer. “Nonstandard symmetry classes in mesoscopic normal-superconducting hybrid structures”. In: *Phys. Rev. B* 55 (2 Jan. 1997), pp. 1142–1161. DOI: [10.1103/PhysRevB.55.1142](https://doi.org/10.1103/PhysRevB.55.1142). URL: <https://link.aps.org/doi/10.1103/PhysRevB.55.1142>.
- [69] A. Kitaev. “Periodic table for topological insulators and superconductors”. In: *AIP Conference Proceedings* 1134.1 (May 2009), pp. 22–30. ISSN: 0094-243X. DOI: [10.1063/1.3149495](https://doi.org/10.1063/1.3149495). eprint: [https://pubs.aip.org/aip/acp/article-pdf/1134/1/22/11584243/22/\\_1\online.pdf](https://pubs.aip.org/aip/acp/article-pdf/1134/1/22/11584243/22/_1\online.pdf). URL: <https://doi.org/10.1063/1.3149495>.
- [70] C.-K. Chiu, J. C. Y. Teo, A. P. Schnyder, and S. Ryu. “Classification of topological quantum matter with symmetries”. In: *Rev. Mod. Phys.* 88 (3 Aug. 2016), p. 035005. DOI: [10.1103/RevModPhys.88.035005](https://doi.org/10.1103/RevModPhys.88.035005). URL: <https://link.aps.org/doi/10.1103/RevModPhys.88.035005>.
- [71] R. M. Lutchyn, J. D. Sau, and S. Das Sarma. “Majorana Fermions and a Topological Phase Transition in Semiconductor-Superconductor Heterostructures”. In: *Phys. Rev. Lett.* 105 (7 Aug. 2010), p. 077001. DOI: [10.1103/PhysRevLett.105.077001](https://doi.org/10.1103/PhysRevLett.105.077001).
- [72] Y. Oreg, G. Refael, and F. von Oppen. “Helical Liquids and Majorana Bound States in Quantum Wires”. In: *Phys. Rev. Lett.* 105.17 (Oct. 2010), p. 177002. ISSN: 0031-9007. DOI: [10.1103/PhysRevLett.105.177002](https://doi.org/10.1103/PhysRevLett.105.177002).
- [73] A. Manchon, H. C. Koo, J. Nitta, S. M. Frolov, and R. A. Duine. “New perspectives for Rashba spin-orbit coupling”. In: *Nature Materials* 14.9 (Sept. 2015), pp. 871–882. ISSN: 1476-4660. DOI: [10.1038/nmat4360](https://doi.org/10.1038/nmat4360). URL: <https://doi.org/10.1038/nmat4360>.
- [74] L. Fu and C. L. Kane. “Superconducting Proximity Effect and Majorana Fermions at the Surface of a Topological Insulator”. In: *Phys. Rev. Lett.* 100.9 (2008), p. 096407. DOI: [10.1103/PhysRevLett.100.096407](https://doi.org/10.1103/PhysRevLett.100.096407).
- [75] M. Z. Hasan and C. L. Kane. “Colloquium: Topological insulators”. In: *Reviews of Modern Physics* 82.4 (Nov. 2010), pp. 3045–3067. ISSN: 0034-6861. DOI: [10.1103/RevModPhys.82.3045](https://doi.org/10.1103/RevModPhys.82.3045). URL: <http://link.aps.org/doi/10.1103/RevModPhys.82.3045>.
- [76] J. D. Sau, R. M. Lutchyn, S. Tewari, and S. Das Sarma. “Generic New Platform for Topological Quantum Computation Using Semiconductor Heterostructures”. In: *Phys. Rev. Lett.* 104 (4 Jan. 2010), p. 040502. DOI: [10.1103/PhysRevLett.104.040502](https://doi.org/10.1103/PhysRevLett.104.040502). URL: <https://link.aps.org/doi/10.1103/PhysRevLett.104.040502>.
- [77] A. Maiani, R. Seoane Souto, M. Leijnse, and K. Flensberg. “Topological superconductivity in semiconductor–superconductor–magnetic-insulator heterostructures”. In: *Phys. Rev. B* 103 (10 Mar. 2021), p. 104508. DOI: [10.1103/PhysRevB.103.104508](https://doi.org/10.1103/PhysRevB.103.104508). URL: <https://link.aps.org/doi/10.1103/PhysRevB.103.104508>.
- [78] S. B. Chung, H. J. Zhang, X. L. Qi, and S. C. Zhang. “Topological superconducting phase and Majorana fermions in half-metal/superconductor heterostructures”. In: *Phys. Rev. B* 84 (2011), pp. 1–4. DOI: [10.1103/PhysRevB.84.060510](https://doi.org/10.1103/PhysRevB.84.060510).

- [79] M. Duckheim and P. Brouwer. “Andreev reflection from noncentrosymmetric superconductors and Majorana bound-state generation in half-metallic ferromagnets”. In: *Phys. Rev. B* 83.5 (Feb. 2011), p. 054513. ISSN: 1098-0121. DOI: [10.1103/PhysRevB.83.054513](https://doi.org/10.1103/PhysRevB.83.054513).
- [80] S. Nadj-Perge, I. K. Drozdov, J. Li, H. Chen, S. Jeon, J. Seo, A. H. MacDonald, B. A. Bernevig, and A. Yazdani. “Observation of Majorana fermions in ferromagnetic atomic chains on a superconductor”. In: *Science* 346.6209 (2014), pp. 602–607. DOI: [10.1126/science.1259327](https://doi.org/10.1126/science.1259327). eprint: <https://www.science.org/doi/pdf/10.1126/science.1259327>. URL: <https://www.science.org/doi/abs/10.1126/science.1259327>.
- [81] M. Hell, M. Leijnse, and K. Flensberg. “Two-Dimensional Platform for Networks of Majorana Bound States”. In: *Phys. Rev. Lett.* 118 (2017), p. 107701. DOI: [10.1103/PhysRevLett.118.107701](https://doi.org/10.1103/PhysRevLett.118.107701).
- [82] O. Lesser, Y. Oreg, and A. Stern. “One-dimensional topological superconductivity based entirely on phase control”. In: *Phys. Rev. B* 106 (24 Dec. 2022), p. L241405. DOI: [10.1103/PhysRevB.106.L241405](https://doi.org/10.1103/PhysRevB.106.L241405). URL: <https://link.aps.org/doi/10.1103/PhysRevB.106.L241405>.
- [83] V. Mourik, K. Zuo, S. M. Frolov, S. R. Plissard, E. P. A. M. Bakkers, and L. P. Kouwenhoven. “Signatures of Majorana fermions in hybrid superconductor-semiconductor nanowire devices.” In: *Science* 336 (2012), p. 1003. DOI: [10.1126/science.1222360](https://doi.org/10.1126/science.1222360).
- [84] M. T. Deng, C. L. Yu, G. Y. Huang, M. Larsson, P. Caroff, and H. Q. Xu. “Anomalous Zero-Bias Conductance Peak in a Nb–InSb Nanowire–Nb Hybrid Device”. In: *Nano Lett.* 12.12 (Dec. 2012), pp. 6414–6419. ISSN: 1530-6984. DOI: [10.1021/nl303758w](https://doi.org/10.1021/nl303758w). URL: <http://pubs.acs.org/doi/abs/10.1021/nl303758w>.
- [85] M. T. Deng, S. Vaitiek, E. B. Hansen, J. Danon, M. Leijnse, K. Flensberg, P. Krogstrup, and C. M. Marcus. “Majorana bound state in a coupled quantum-dot hybrid-nanowire system”. In: *Science* 354 (2016), p. 1557. DOI: [10.1126/science.aaf3961](https://doi.org/10.1126/science.aaf3961).
- [86] F. Nichele, A. C. C. Drachmann, A. M. Whiticar, E. C. T. O’Farrell, H. J. Suominen, A. Fornieri, T. Wang, G. C. Gardner, C. Thomas, A. T. Hatke, P. Krogstrup, M. J. Manfra, K. Flensberg, and C. M. Marcus. “Scaling of Majorana Zero-Bias Conductance Peaks”. In: *Phys. Rev. Lett.* 119 (2017), p. 136803. DOI: [10.1103/PhysRevLett.119.136803](https://doi.org/10.1103/PhysRevLett.119.136803).
- [87] H. J. Suominen, M. Kjaergaard, A. R. Hamilton, J. Shabani, C. J. Palmstrøm, C. M. Marcus, and F. Nichele. “Zero-Energy Modes from Coalescing Andreev States in a Two-Dimensional Semiconductor-Superconductor Hybrid Platform”. In: *Phys. Rev. Lett.* 119 (2017), p. 176805. DOI: [10.1103/PhysRevLett.119.176805](https://doi.org/10.1103/PhysRevLett.119.176805).
- [88] S. Vaitiekėnas, G. W. Winkler, B. van Heck, T. Karzig, M. T. Deng, K. Flensberg, L. I. Glazman, C. Nayak, P. Krogstrup, R. M. Lutchyn, and C. M. Marcus. “Flux-induced topological superconductivity in full-shell nanowires”. In: *Science* 367 (2020), p. 1442. DOI: [10.1126/science.aav3392](https://doi.org/10.1126/science.aav3392).
- [89] L. P. Rokhinson, X. Liu, and J. K. Furdyna. “The fractional a.c. Josephson effect in a semiconductor–superconductor nanowire as a signature of Majorana particles”. In: *Nature Physics* 8.11 (Nov. 2012), pp. 795–799. ISSN: 1745-2481. DOI: [10.1038/nphys2429](https://doi.org/10.1038/nphys2429). URL: <https://doi.org/10.1038/nphys2429>.

- [90] A. P. Higginbotham, S. M. Albrecht, G. Kiršanskas, W. Chang, F. Kuemmeth, P. Krogstrup, T. S. Jespersen, J. Nygård, K. Flensberg, and C. M. Marcus. “Parity lifetime of bound states in a proximitized semiconductor nanowire”. In: *Nat. Phys.* 11 (2015), p. 107. DOI: [10.1038/nphys3461](https://doi.org/10.1038/nphys3461). URL: <http://www.nature.com/doi/10.1038/nphys3461>.
- [91] S. M. Albrecht, A. P. Higginbotham, M. Madsen, F. Kuemmeth, T. S. Jespersen, J. Nygård, P. Krogstrup, and C. M. Marcus. “Exponential Protection of Zero Modes in Majorana Islands”. In: *Nature* 531 (2016), p. 206. DOI: [10.1038/nature17162](https://doi.org/10.1038/nature17162).
- [92] M. T. Deng, S. Vaitiekėnas, E. Prada, P. San-Jose, J. Nygård, P. Krogstrup, R. Aguado, and C. M. Marcus. “Nonlocality of Majorana modes in hybrid nanowires”. In: *Phys. Rev. B* 98 (2018), p. 085125. DOI: [10.1103/PhysRevB.98.085125](https://doi.org/10.1103/PhysRevB.98.085125).
- [93] H. Pan and S. Das Sarma. “Disorder effects on Majorana zero modes: Kitaev chain versus semiconductor nanowire”. In: *Phys. Rev. B* 103 (22 June 2021), p. 224505. DOI: [10.1103/PhysRevB.103.224505](https://doi.org/10.1103/PhysRevB.103.224505). URL: <https://link.aps.org/doi/10.1103/PhysRevB.103.224505>.
- [94] S. Das Sarma and H. Pan. “Disorder-induced zero-bias peaks in Majorana nanowires”. In: *Phys. Rev. B* 103 (19 May 2021), p. 195158. DOI: [10.1103/PhysRevB.103.195158](https://doi.org/10.1103/PhysRevB.103.195158). URL: <https://link.aps.org/doi/10.1103/PhysRevB.103.195158>.
- [95] D. I. Pikulin, B. van Heck, T. Karzig, E. A. Martinez, B. Nijholt, T. Laeven, G. W. Winkler, J. D. Watson, S. Heedt, M. Temurhan, V. Svidenko, R. M. Lutchyn, M. Thomas, G. de Lange, L. Casparis, and C. Nayak. *Protocol to identify a topological superconducting phase in a three-terminal device*. 2021. arXiv: [2103.12217](https://arxiv.org/abs/2103.12217) [[cond-mat.mes-hall](https://arxiv.org/abs/2103.12217)].
- [96] M. Aghaee et al. “InAs-Al hybrid devices passing the topological gap protocol”. In: *Phys. Rev. B* 107 (24 June 2023), p. 245423. DOI: [10.1103/PhysRevB.107.245423](https://doi.org/10.1103/PhysRevB.107.245423). URL: <https://link.aps.org/doi/10.1103/PhysRevB.107.245423>.
- [97] A. Blais, R.-S. Huang, A. Wallraff, S. M. Girvin, and R. J. Schoelkopf. “Cavity quantum electrodynamics for superconducting electrical circuits: An architecture for quantum computation”. In: *Phys. Rev. A* 69 (6 June 2004), p. 062320. DOI: [10.1103/PhysRevA.69.062320](https://doi.org/10.1103/PhysRevA.69.062320). URL: <https://link.aps.org/doi/10.1103/PhysRevA.69.062320>.
- [98] S. Girvin, R. -S. Huang, A. Blais, A. Wallraff, and R. Schoelkopf. “Course 16 - Prospects for Strong Cavity Quantum Electrodynamics with Superconducting Circuits”. In: *Quantum Entanglement and Information Processing*. Ed. by D. Estève, J.-M. Raimond, and J. Dalibard. Vol. 79. Les Houches. Elsevier, 2004, pp. 591–608. DOI: [https://doi.org/10.1016/S0924-8099\(03\)80040-9](https://doi.org/10.1016/S0924-8099(03)80040-9). URL: <https://www.sciencedirect.com/science/article/pii/S0924809903800409>.
- [99] M. H. Devoret. “Does Brian Josephson’s Gauge-Invariant Phase Difference Live on a Line or a Circle?” In: *Journal of Superconductivity and Novel Magnetism* 34.6 (June 2021), pp. 1633–1642. ISSN: 1557-1947. DOI: [10.1007/s10948-020-05784-9](https://doi.org/10.1007/s10948-020-05784-9). URL: <https://doi.org/10.1007/s10948-020-05784-9>.
- [100] U. Vool and M. Devoret. “Introduction to quantum electromagnetic circuits”. In: *International Journal of Circuit Theory and Applications* 45.7 (2017), pp. 897–934. DOI: <https://doi.org/10.1002/cta.2359>. eprint: <https://onlinelibrary.wiley.com/doi/pdf/10.1002/cta.2359>. URL: <https://onlinelibrary.wiley.com/doi/abs/10.1002/cta.2359>.



- [101] A. Blais, A. L. Grimsmo, S. M. Girvin, and A. Wallraff. “Circuit quantum electrodynamics”. In: *Rev. Mod. Phys.* 93 (2 May 2021), p. 025005. DOI: [10.1103/RevModPhys.93.025005](https://doi.org/10.1103/RevModPhys.93.025005). URL: <https://link.aps.org/doi/10.1103/RevModPhys.93.025005>.
- [102] P. Krantz, M. Kjaergaard, F. Yan, T. P. Orlando, S. Gustavsson, and W. D. Oliver. “A quantum engineer’s guide to superconducting qubits”. In: *Applied Physics Reviews* 6.2 (June 2019), p. 021318. ISSN: 1931-9401. DOI: [10.1063/1.5089550](https://doi.org/10.1063/1.5089550). eprint: [https://pubs.aip.org/aip/apr/article-pdf/doi/10.1063/1.5089550/16667201/021318\\_1\\_online.pdf](https://pubs.aip.org/aip/apr/article-pdf/doi/10.1063/1.5089550/16667201/021318_1_online.pdf). URL: <https://doi.org/10.1063/1.5089550>.
- [103] M. Kjaergaard, M. E. Schwartz, J. Braumüller, P. Krantz, J. I.-J. Wang, S. Gustavsson, and W. D. Oliver. “Superconducting Qubits: Current State of Play”. en. In: *Annual Review of Condensed Matter Physics* 11.1 (Mar. 2020), pp. 369–395. ISSN: 1947-5454, 1947-5462. DOI: [10.1146/annurev-conmatphys-031119-050605](https://doi.org/10.1146/annurev-conmatphys-031119-050605). URL: <https://www.annualreviews.org/doi/10.1146/annurev-conmatphys-031119-050605> (visited on 12/13/2021).
- [104] S. Rasmussen, K. Christensen, S. Pedersen, L. Kristensen, T. Bækkegaard, N. Loft, and N. Zinner. “Superconducting Circuit Companion—an Introduction with Worked Examples”. In: *PRX Quantum* 2 (4 Dec. 2021), p. 040204. DOI: [10.1103/PRXQuantum.2.040204](https://doi.org/10.1103/PRXQuantum.2.040204). URL: <https://link.aps.org/doi/10.1103/PRXQuantum.2.040204>.
- [105] A. F. Kockum, A. Soro, L. García-Álvarez, P. Vikstål, T. Douce, G. Johansson, and G. Ferrini. *Lecture notes on quantum computing*. 2023. arXiv: [2311.08445](https://arxiv.org/abs/2311.08445) [quant-ph].
- [106] B. D. Josephson. “Possible new effects in superconductive tunnelling”. en. In: *Physics Letters* 1.7 (July 1962), pp. 251–253. ISSN: 0031-9163. DOI: [10.1016/0031-9163\(62\)91369-0](https://doi.org/10.1016/0031-9163(62)91369-0). URL: <https://www.sciencedirect.com/science/article/pii/0031916362913690> (visited on 05/31/2022).
- [107] J. Ulrich and F. Hassler. “Dual approach to circuit quantization using loop charges”. In: *Phys. Rev. B* 94 (9 Sept. 2016), p. 094505. DOI: [10.1103/PhysRevB.94.094505](https://doi.org/10.1103/PhysRevB.94.094505). URL: <https://link.aps.org/doi/10.1103/PhysRevB.94.094505>.
- [108] B. M. Terhal, J. Conrad, and C. Vuillot. “Towards scalable bosonic quantum error correction”. In: *Quantum Science and Technology* 5.4 (July 2020), p. 043001. DOI: [10.1088/2058-9565/ab98a5](https://doi.org/10.1088/2058-9565/ab98a5). URL: <https://dx.doi.org/10.1088/2058-9565/ab98a5>.
- [109] W. Cai, Y. Ma, W. Wang, C.-L. Zou, and L. Sun. “Bosonic quantum error correction codes in superconducting quantum circuits”. In: *Fundamental Research* 1.1 (2021), pp. 50–67. ISSN: 2667-3258. DOI: <https://doi.org/10.1016/j.fmre.2020.12.006>. URL: <https://www.sciencedirect.com/science/article/pii/S2667325820300145>.
- [110] J. Hastrup. “Continuous-variable quantum codes for fault-tolerant quantum information processing”. English. PhD thesis. 2021.
- [111] A. J. Brady, A. Eickbusch, S. Singh, J. Wu, and Q. Zhuang. *Advances in Bosonic Quantum Error Correction with Gottesman-Kitaev-Preskill Codes: Theory, Engineering and Applications*. 2023. arXiv: [2308.02913](https://arxiv.org/abs/2308.02913) [quant-ph].
- [112] J. Koch, T. M. Yu, J. Gambetta, A. A. Houck, D. I. Schuster, J. Majer, A. Blais, M. H. Devoret, S. M. Girvin, and R. J. Schoelkopf. “Charge-insensitive qubit design derived from the Cooper pair box”. In: *Phys. Rev. A* 76 (4 Oct. 2007), p. 042319. DOI: [10.1103/PhysRevA.76.042319](https://doi.org/10.1103/PhysRevA.76.042319). URL: <https://link.aps.org/doi/10.1103/PhysRevA.76.042319>.

- [113] C. W. J. Beenakker. “Three “universal” mesoscopic Josephson effects”. In: *Transport Phenomena in Mesoscopic Systems*. Springer, 1992, pp. 235–253.
- [114] D. Willsch, D. Rieger, P. Winkel, M. Willsch, C. Dickel, J. Krause, Y. Ando, R. Lescanne, Z. Leghtas, N. T. Bronn, P. Deb, O. Lanes, Z. K. Mineev, B. Dennig, S. Geisert, S. Günzler, S. Ihssen, P. Paluch, T. Reisinger, R. Hanna, J. H. Bae, P. Schüffelgen, D. Grützmaker, L. Buimagarlarinca, C. Morari, W. Wernsdorfer, D. P. DiVincenzo, K. Michielsen, G. Catelani, and I. M. Pop. *Observation of Josephson Harmonics in Tunnel Junctions*. 2023. arXiv: [2302.09192](https://arxiv.org/abs/2302.09192) [quant-ph].
- [115] Y. Nakamura, Y. A. Pashkin, and J. S. Tsai. “Coherent control of macroscopic quantum states in a single-Cooper-pair box”. In: *Nature* 398.6730 (Apr. 1999), pp. 786–788. ISSN: 1476-4687. DOI: [10.1038/19718](https://doi.org/10.1038/19718). URL: <https://doi.org/10.1038/19718>.
- [116] J. A. Schreier, A. A. Houck, J. Koch, D. I. Schuster, B. R. Johnson, J. M. Chow, J. M. Gambetta, J. Majer, L. Frunzio, M. H. Devoret, S. M. Girvin, and R. J. Schoelkopf. “Suppressing charge noise decoherence in superconducting charge qubits”. In: *Phys. Rev. B* 77 (18 May 2008), p. 180502. DOI: [10.1103/PhysRevB.77.180502](https://doi.org/10.1103/PhysRevB.77.180502). URL: <https://link.aps.org/doi/10.1103/PhysRevB.77.180502>.
- [117] A. P. M. Place, L. V. H. Rodgers, P. Mundada, B. M. Smitham, M. Fitzpatrick, Z. Leng, A. Premkumar, J. Bryon, A. Vrajitoarea, S. Sussman, G. Cheng, T. Madhavan, H. K. Babla, X. H. Le, Y. Gang, B. Jäck, A. Gyenis, N. Yao, R. J. Cava, N. P. de Leon, and A. A. Houck. “New material platform for superconducting transmon qubits with coherence times exceeding 0.3 milliseconds”. In: *Nature Communications* 12.1 (Mar. 2021), p. 1779. ISSN: 2041-1723. DOI: [10.1038/s41467-021-22030-5](https://doi.org/10.1038/s41467-021-22030-5). URL: <https://doi.org/10.1038/s41467-021-22030-5>.
- [118] C. Wang, X. Li, H. Xu, Z. Li, J. Wang, Z. Yang, Z. Mi, X. Liang, T. Su, C. Yang, G. Wang, W. Wang, Y. Li, M. Chen, C. Li, K. Linghu, J. Han, Y. Zhang, Y. Feng, Y. Song, T. Ma, J. Zhang, R. Wang, P. Zhao, W. Liu, G. Xue, Y. Jin, and H. Yu. “Towards practical quantum computers: transmon qubit with a lifetime approaching 0.5 milliseconds”. In: *npj Quantum Information* 8.1 (Jan. 2022), p. 3. ISSN: 2056-6387. DOI: [10.1038/s41534-021-00510-2](https://doi.org/10.1038/s41534-021-00510-2). URL: <https://doi.org/10.1038/s41534-021-00510-2>.
- [119] S. Ganjam, Y. Wang, Y. Lu, A. Banerjee, C. U. Lei, L. Krayzman, K. Kisslinger, C. Zhou, R. Li, Y. Jia, M. Liu, L. Frunzio, and R. J. Schoelkopf. *Surpassing millisecond coherence times in on-chip superconducting quantum memories by optimizing materials, processes, and circuit design*. 2023. arXiv: [2308.15539](https://arxiv.org/abs/2308.15539) [quant-ph].
- [120] B. S. Deaver and W. M. Fairbank. “Experimental Evidence for Quantized Flux in Superconducting Cylinders”. In: *Phys. Rev. Lett.* 7 (2 July 1961), pp. 43–46. DOI: [10.1103/PhysRevLett.7.43](https://doi.org/10.1103/PhysRevLett.7.43). URL: <https://link.aps.org/doi/10.1103/PhysRevLett.7.43>.
- [121] R. Doll and M. Näbauer. “Experimental Proof of Magnetic Flux Quantization in a Superconducting Ring”. In: *Phys. Rev. Lett.* 7 (2 July 1961), pp. 51–52. DOI: [10.1103/PhysRevLett.7.51](https://doi.org/10.1103/PhysRevLett.7.51). URL: <https://link.aps.org/doi/10.1103/PhysRevLett.7.51>.
- [122] X. You, J. A. Sauls, and J. Koch. “Circuit quantization in the presence of time-dependent external flux”. In: 99.17, 174512 (May 2019), p. 174512. DOI: [10.1103/PhysRevB.99.174512](https://doi.org/10.1103/PhysRevB.99.174512). arXiv: [1902.04734](https://arxiv.org/abs/1902.04734) [quant-ph].



- [123] M. Rymarz and D. DiVincenzo. “Consistent Quantization of Nearly Singular Superconducting Circuits”. In: *Physical Review X* 13 (May 2023). DOI: [10.1103/PhysRevX.13.021017](https://doi.org/10.1103/PhysRevX.13.021017).
- [124] V. E. Manucharyan, J. Koch, L. I. Glazman, and M. H. Devoret. “Fluxonium: Single Cooper-Pair Circuit Free of Charge Offsets”. en. In: *Science* 326.5949 (Oct. 2009), pp. 113–116. ISSN: 0036-8075, 1095-9203. DOI: [10.1126/science.1175552](https://doi.org/10.1126/science.1175552). URL: <https://www.science.org/doi/10.1126/science.1175552> (visited on 02/17/2022).
- [125] V. E. Manucharyan. “Superinductance”. PhD thesis. Yale University, 2012.
- [126] F. Yan, S. Gustavsson, A. Kamal, J. Birenbaum, A. P. Sears, D. Hover, T. J. Gudmundsen, D. Rosenberg, G. Samach, S. Weber, J. L. Yoder, T. P. Orlando, J. Clarke, A. J. Kerman, and W. D. Oliver. “The flux qubit revisited to enhance coherence and reproducibility”. In: *Nature Communications* 7.1 (Nov. 2016), p. 12964. ISSN: 2041-1723. DOI: [10.1038/ncomms12964](https://doi.org/10.1038/ncomms12964). URL: <https://doi.org/10.1038/ncomms12964>.
- [127] P. Groszkowski, A. D. Paolo, A. L. Grimsmo, A. Blais, D. I. Schuster, A. A. Houck, and J. Koch. “Coherence properties of the 0- qubit”. In: *New Journal of Physics* 20.4 (Apr. 2018), p. 043053. DOI: [10.1088/1367-2630/aab7cd](https://doi.org/10.1088/1367-2630/aab7cd). URL: <https://dx.doi.org/10.1088/1367-2630/aab7cd>.
- [128] L. B. Nguyen, Y.-H. Lin, A. Somoroff, R. Mencia, N. Grabon, and V. E. Manucharyan. “High-Coherence Fluxonium Qubit”. In: *Phys. Rev. X* 9 (4 Nov. 2019), p. 041041. DOI: [10.1103/PhysRevX.9.041041](https://doi.org/10.1103/PhysRevX.9.041041). URL: <https://link.aps.org/doi/10.1103/PhysRevX.9.041041>.
- [129] A. Gyenis, A. Di Paolo, J. Koch, A. Blais, A. A. Houck, and D. I. Schuster. “Moving beyond the Transmon: Noise-Protected Superconducting Quantum Circuits”. In: *PRX Quantum* 2 (3 Sept. 2021), p. 030101. DOI: [10.1103/PRXQuantum.2.030101](https://doi.org/10.1103/PRXQuantum.2.030101). URL: <https://link.aps.org/doi/10.1103/PRXQuantum.2.030101>.
- [130] I. Siddiqi. “Engineering high-coherence superconducting qubits”. In: *Nature Reviews Materials* 6.10 (Oct. 2021), pp. 875–891. ISSN: 2058-8437. DOI: [10.1038/s41578-021-00370-4](https://doi.org/10.1038/s41578-021-00370-4). URL: <https://doi.org/10.1038/s41578-021-00370-4>.
- [131] L. B. Nguyen, G. Koolstra, Y. Kim, A. Morvan, T. Chistolini, S. Singh, K. N. Nesterov, C. Jünger, L. Chen, Z. Pedramrazi, B. K. Mitchell, J. M. Kreikebaum, S. Puri, D. I. Santiago, and I. Siddiqi. “Blueprint for a High-Performance Fluxonium Quantum Processor”. In: *PRX Quantum* 3 (3 Aug. 2022), p. 037001. DOI: [10.1103/PRXQuantum.3.037001](https://doi.org/10.1103/PRXQuantum.3.037001). URL: <https://link.aps.org/doi/10.1103/PRXQuantum.3.037001>.
- [132] A. Somoroff, Q. Ficheux, R. A. Mencia, H. Xiong, R. Kuzmin, and V. E. Manucharyan. “Millisecond Coherence in a Superconducting Qubit”. In: *Phys. Rev. Lett.* 130 (26 June 2023), p. 267001. DOI: [10.1103/PhysRevLett.130.267001](https://doi.org/10.1103/PhysRevLett.130.267001). URL: <https://link.aps.org/doi/10.1103/PhysRevLett.130.267001>.
- [133] P. Bertet, I. Chiorescu, G. Burkard, K. Semba, C. J. P. M. Harmans, D. P. DiVincenzo, and J. E. Mooij. “Dephasing of a Superconducting Qubit Induced by Photon Noise”. In: *Phys. Rev. Lett.* 95 (25 Dec. 2005), p. 257002. DOI: [10.1103/PhysRevLett.95.257002](https://doi.org/10.1103/PhysRevLett.95.257002). URL: <https://link.aps.org/doi/10.1103/PhysRevLett.95.257002>.

- [134] M. McEwen, L. Faoro, K. Arya, A. Dunsworth, T. Huang, S. Kim, B. Burkett, A. Fowler, F. Arute, J. C. Bardin, A. Bengtsson, A. Bilmes, B. B. Buckley, N. Bushnell, Z. Chen, R. Collins, S. Demura, A. R. Derk, C. Erickson, M. Giustina, S. D. Harrington, S. Hong, E. Jeffrey, J. Kelly, P. V. Klimov, F. Kostritsa, P. Laptev, A. Locharla, X. Mi, K. C. Miao, S. Montazeri, J. Mutus, O. Naaman, M. Neeley, C. Neill, A. Opremcak, C. Quintana, N. Redd, P. Roushan, D. Sank, K. J. Satzinger, V. Shvarts, T. White, Z. J. Yao, P. Yeh, J. Yoo, Y. Chen, V. Smelyanskiy, J. M. Martinis, H. Neven, A. Megrant, L. Ioffe, and R. Barends. “Resolving catastrophic error bursts from cosmic rays in large arrays of superconducting qubits”. In: *Nature Physics* 18.1 (Jan. 2022), pp. 107–111. ISSN: 1745-2481. DOI: [10.1038/s41567-021-01432-8](https://doi.org/10.1038/s41567-021-01432-8). URL: <https://doi.org/10.1038/s41567-021-01432-8>.
- [135] F. Hassani, M. Peruzzo, L. N. Kapoor, A. Trioni, M. Zemlicka, and J. M. Fink. “Inductively shunted transmons exhibit noise insensitive plasmon states and a fluxon decay exceeding 3 hours”. In: *Nature Communications* 14.1 (July 2023), p. 3968. ISSN: 2041-1723. DOI: [10.1038/s41467-023-39656-2](https://doi.org/10.1038/s41467-023-39656-2). URL: <https://doi.org/10.1038/s41467-023-39656-2>.
- [136] N. Earnest, S. Chakram, Y. Lu, N. Irons, R. K. Naik, N. Leung, L. Ocola, D. A. Czapslewski, B. Baker, J. Lawrence, J. Koch, and D. I. Schuster. “Realization of a  $\tilde{\nu}$  System with Metastable States of a Capacitively Shunted Fluxonium”. In: *Phys. Rev. Lett.* 120 (15 Apr. 2018), p. 150504. DOI: [10.1103/PhysRevLett.120.150504](https://link.aps.org/doi/10.1103/PhysRevLett.120.150504). URL: <https://link.aps.org/doi/10.1103/PhysRevLett.120.150504>.
- [137] H. Zhang, S. Chakram, T. Roy, N. Earnest, Y. Lu, Z. Huang, D. K. Weiss, J. Koch, and D. I. Schuster. “Universal Fast-Flux Control of a Coherent, Low-Frequency Qubit”. In: *Phys. Rev. X* 11 (1 Jan. 2021), p. 011010. DOI: [10.1103/PhysRevX.11.011010](https://link.aps.org/doi/10.1103/PhysRevX.11.011010). URL: <https://link.aps.org/doi/10.1103/PhysRevX.11.011010>.
- [138] A. Gyenis, P. S. Mundada, A. Di Paolo, T. M. Hazard, X. You, D. I. Schuster, J. Koch, A. Blais, and A. A. Houck. “Experimental Realization of a Protected Superconducting Circuit Derived from the  $0-\pi$  Qubit”. In: *PRX Quantum* 2 (1 Mar. 2021), p. 010339. DOI: [10.1103/PRXQuantum.2.010339](https://link.aps.org/doi/10.1103/PRXQuantum.2.010339). URL: <https://link.aps.org/doi/10.1103/PRXQuantum.2.010339>.
- [139] T. W. Larsen, M. E. Gershenson, L. Casparis, A. Kringhøj, N. J. Pearson, R. P. G. McNeil, F. Kuemmeth, P. Krogstrup, K. D. Petersson, and C. M. Marcus. “Parity-Protected Superconductor-Semiconductor Qubit”. In: *Phys. Rev. Lett.* 125 (5 July 2020), p. 056801. DOI: [10.1103/PhysRevLett.125.056801](https://link.aps.org/doi/10.1103/PhysRevLett.125.056801). URL: <https://link.aps.org/doi/10.1103/PhysRevLett.125.056801>.
- [140] K. Kalashnikov, W. T. Hsieh, W. Zhang, W.-S. Lu, P. Kamenov, A. Di Paolo, A. Blais, M. E. Gershenson, and M. Bell. “Bifluxon: Fluxon-Parity-Protected Superconducting Qubit”. In: *PRX Quantum* 1 (1 Sept. 2020), p. 010307. DOI: [10.1103/PRXQuantum.1.010307](https://link.aps.org/doi/10.1103/PRXQuantum.1.010307). URL: <https://link.aps.org/doi/10.1103/PRXQuantum.1.010307>.
- [141] A. D. Paolo, A. L. Grimsmo, P. Groszkowski, J. Koch, and A. Blais. “Control and coherence time enhancement of the  $0-\pi$  qubit”. In: *New Journal of Physics* 21.4 (Apr. 2019), p. 043002. DOI: [10.1088/1367-2630/ab09b0](https://dx.doi.org/10.1088/1367-2630/ab09b0). URL: <https://dx.doi.org/10.1088/1367-2630/ab09b0>.
- [142] M. Abdelhafez, B. Baker, A. Gyenis, P. Mundada, A. A. Houck, D. Schuster, and J. Koch. “Universal gates for protected superconducting qubits using optimal control”. In: *Phys. Rev. A* 101 (2 Feb. 2020), p. 022321. DOI: [10.1103/PhysRevA.101.022321](https://link.aps.org/doi/10.1103/PhysRevA.101.022321). URL: <https://link.aps.org/doi/10.1103/PhysRevA.101.022321>.

- [143] Z. Huang, X. You, U. Alyanak, A. Romanenko, A. Grassellino, and S. Zhu. “High-Order Qubit Dephasing at Sweet Spots by Non-Gaussian Fluctuators: Symmetry Breaking and Floquet Protection”. In: *Phys. Rev. Appl.* 18 (6 Dec. 2022), p. L061001. DOI: [10.1103/PhysRevApplied.18.L061001](https://doi.org/10.1103/PhysRevApplied.18.L061001). URL: <https://link.aps.org/doi/10.1103/PhysRevApplied.18.L061001>.
- [144] D. Vion, A. Aassime, A. Cottet, P. Joyez, H. Pothier, C. Urbina, D. Esteve, and M. H. Devoret. “Manipulating the Quantum State of an Electrical Circuit”. In: *Science* 296.5569 (2002), pp. 886–889. DOI: [10.1126/science.1069372](https://doi.org/10.1126/science.1069372). eprint: <https://www.science.org/doi/pdf/10.1126/science.1069372>. URL: <https://www.science.org/doi/abs/10.1126/science.1069372>.
- [145] P. Aumann, T. Menke, W. D. Oliver, and W. Lechner. “CircuitQ: An open-source toolbox for superconducting circuits”. en. In: *arXiv:2106.05342 [quant-ph]* (June 2021). arXiv: 2106.05342. URL: <http://arxiv.org/abs/2106.05342> (visited on 12/20/2021).
- [146] P. Groszkowski and J. Koch. “Scqubits: a Python package for superconducting qubits”. In: *Quantum* 5 (Nov. 2021), p. 583. ISSN: 2521-327X. DOI: [10.22331/q-2021-11-17-583](https://doi.org/10.22331/q-2021-11-17-583). URL: <https://doi.org/10.22331/q-2021-11-17-583>.
- [147] K. S. Christensen. “Designing superconducting circuits for quantum computation”. PhD thesis. Affl=Aarhus University, Natural Sciences, Department of Physics and Astronomy, Aarhus U., 2023.
- [148] K. Flensberg. “Non-Abelian Operations on Majorana Fermions via Single-Charge Control”. In: *Phys. Rev. Lett.* 106.9 (Mar. 2011), p. 090503. ISSN: 0031-9007. DOI: [10.1103/PhysRevLett.106.090503](https://doi.org/10.1103/PhysRevLett.106.090503).
- [149] B. I. Halperin, Y. Oreg, A. Stern, G. Refael, J. Alicea, and F. von Oppen. “Adiabatic manipulations of Majorana fermions in a three-dimensional network of quantum wires”. In: *Phys. Rev. B* 85.14 (Apr. 2012), p. 144501. ISSN: 1098-0121. DOI: [10.1103/PhysRevB.85.144501](https://doi.org/10.1103/PhysRevB.85.144501). URL: <http://link.aps.org/doi/10.1103/PhysRevB.85.144501>.
- [150] M. R. Lykkegaard. *Measuring Spectroscopy of Andreev Bound States in One Dimensional Superconducting Nanowires*. 2021.
- [151] R. Seoane Souto, K. Flensberg, and M. Leijnse. “Timescales for charge transfer based operations on Majorana systems”. In: *Phys. Rev. B* 101 (8 Feb. 2020), 081407(R). DOI: [10.1103/PhysRevB.101.081407](https://doi.org/10.1103/PhysRevB.101.081407). URL: <https://link.aps.org/doi/10.1103/PhysRevB.101.081407>.
- [152] G. Rigolin, G. Ortiz, and V. H. Ponce. “Beyond the quantum adiabatic approximation: Adiabatic perturbation theory”. In: *Phys. Rev. A* 78 (5 Nov. 2008), p. 052508. DOI: [10.1103/PhysRevA.78.052508](https://doi.org/10.1103/PhysRevA.78.052508). URL: <https://link.aps.org/doi/10.1103/PhysRevA.78.052508>.
- [153] T. Karzig, F. Pientka, G. Refael, and F. von Oppen. “Shortcuts to non-Abelian braiding”. In: *Phys. Rev. B* 91 (20 May 2015), p. 201102. DOI: [10.1103/PhysRevB.91.201102](https://doi.org/10.1103/PhysRevB.91.201102). URL: <https://link.aps.org/doi/10.1103/PhysRevB.91.201102>.
- [154] D. Guéry-Odelin, A. Ruschhaupt, A. Kiely, E. Torrontegui, S. Martínez-Garaot, and J. G. Muga. “Shortcuts to adiabaticity: Concepts, methods, and applications”. In: *Rev. Mod. Phys.* 91 (4 Oct. 2019), p. 045001. DOI: [10.1103/RevModPhys.91.045001](https://doi.org/10.1103/RevModPhys.91.045001). URL: <https://link.aps.org/doi/10.1103/RevModPhys.91.045001>.

- [155] T. Dvir, G. Wang, N. van Loo, C.-X. Liu, G. P. Mazur, A. Bordin, S. L. D. ten Haaf, J.-Y. Wang, D. van Driel, F. Zatelli, X. Li, F. K. Malinowski, S. Gazibegovic, G. Badawy, E. P. A. M. Bakkers, M. Wimmer, and L. P. Kouwenhoven. “Realization of a minimal Kitaev chain in coupled quantum dots”. In: *Nature* 614.7948 (Feb. 2023), pp. 445–450. ISSN: 1476-4687. DOI: [10.1038/s41586-022-05585-1](https://doi.org/10.1038/s41586-022-05585-1). URL: <https://doi.org/10.1038/s41586-022-05585-1>.
- [156] M. Leijnse and K. Flensberg. “Hybrid topological-spin qubit systems for two-qubit-spin gates”. In: *Phys. Rev. B* 86 (2012), p. 104511. DOI: [10.1103/PhysRevB.86.104511](https://doi.org/10.1103/PhysRevB.86.104511).
- [157] A. Tsintzis, R. S. Souto, K. Flensberg, J. Danon, and M. Leijnse. *Roadmap towards Majorana qubits and nonabelian physics in quantum dot-based minimal Kitaev chains*. 2023. arXiv: [2306.16289](https://arxiv.org/abs/2306.16289) [cond-mat.mes-hall].
- [158] A. Tsintzis, R. S. Souto, and M. Leijnse. “Creating and detecting poor man’s Majorana bound states in interacting quantum dots”. In: *Phys. Rev. B* 106 (20 Nov. 2022), p. L201404. DOI: [10.1103/PhysRevB.106.L201404](https://doi.org/10.1103/PhysRevB.106.L201404). URL: <https://link.aps.org/doi/10.1103/PhysRevB.106.L201404>.
- [159] M. Peruzzo, F. Hassani, G. Szep, A. Trioni, E. Redchenko, M. Žemlička, and J. M. Fink. “Geometric Superinductance Qubits: Controlling Phase Delocalization across a Single Josephson Junction”. In: *PRX Quantum* 2 (4 Nov. 2021), p. 040341. DOI: [10.1103/PRXQuantum.2.040341](https://doi.org/10.1103/PRXQuantum.2.040341). URL: <https://link.aps.org/doi/10.1103/PRXQuantum.2.040341>.
- [160] T. P. Orlando, J. E. Mooij, L. Tian, C. H. van der Wal, L. S. Levitov, S. Lloyd, and J. J. Mazo. “Superconducting persistent-current qubit”. In: *Phys. Rev. B* 60 (22 Dec. 1999), pp. 15398–15413. DOI: [10.1103/PhysRevB.60.15398](https://doi.org/10.1103/PhysRevB.60.15398). URL: <https://link.aps.org/doi/10.1103/PhysRevB.60.15398>.
- [161] J. E. Mooij, T. P. Orlando, L. Levitov, L. Tian, C. H. van der Wal, and S. Lloyd. “Josephson Persistent-Current Qubit”. en. In: *Science* 285.5430 (Aug. 1999), pp. 1036–1039. ISSN: 0036-8075, 1095-9203. DOI: [10.1126/science.285.5430.1036](https://doi.org/10.1126/science.285.5430.1036). URL: <https://www.science.org/doi/10.1126/science.285.5430.1036> (visited on 10/28/2021).
- [162] L. Ding, M. Hays, Y. Sung, B. Kannan, J. An, A. Di Paolo, A. H. Karamlou, T. M. Hazard, K. Azar, D. K. Kim, B. M. Niedzielski, A. Melville, M. E. Schwartz, J. L. Yoder, T. P. Orlando, S. Gustavsson, J. A. Grover, K. Serniak, and W. D. Oliver. “High-Fidelity, Frequency-Flexible Two-Qubit Fluxonium Gates with a Transmon Coupler”. In: *Phys. Rev. X* 13 (3 Sept. 2023), p. 031035. DOI: [10.1103/PhysRevX.13.031035](https://doi.org/10.1103/PhysRevX.13.031035). URL: <https://link.aps.org/doi/10.1103/PhysRevX.13.031035>.
- [163] M. Abdelhafez, B. Baker, A. Gyenis, P. Mundada, A. A. Houck, D. Schuster, and J. Koch. “Universal gates for protected superconducting qubits using optimal control”. en. In: *Physical Review A* 101.2 (Feb. 2020), p. 022321. ISSN: 2469-9926, 2469-9934. DOI: [10.1103/PhysRevA.101.022321](https://doi.org/10.1103/PhysRevA.101.022321). URL: <https://link.aps.org/doi/10.1103/PhysRevA.101.022321> (visited on 12/01/2021).
- [164] T. W. Larsen, K. D. Petersson, F. Kuemmeth, T. S. Jespersen, P. Krogstrup, J. Nygård, and C. M. Marcus. “Semiconductor-Nanowire-Based Superconducting Qubit”. In: *Physical Review Letters* 115.12 (Sept. 2015). Publisher: American Physical Society, p. 127001. DOI: [10.1103/PhysRevLett.115.127001](https://doi.org/10.1103/PhysRevLett.115.127001). URL: <https://link.aps.org/doi/10.1103/PhysRevLett.115.127001> (visited on 09/23/2022).

- [165] L. Casparis, T. W. Larsen, M. S. Olsen, F. Kuemmeth, P. Krogstrup, J. Nygård, K. D. Petersson, and C. M. Marcus. “Gatemon Benchmarking and Two-Qubit Operations”. In: *Phys. Rev. Lett.* 116 (15 Apr. 2016), p. 150505. DOI: [10.1103/PhysRevLett.116.150505](https://doi.org/10.1103/PhysRevLett.116.150505). URL: <https://link.aps.org/doi/10.1103/PhysRevLett.116.150505>.
- [166] L. Casparis, M. R. Connolly, M. Kjaergaard, N. J. Pearson, A. Kringhøj, T. W. Larsen, F. Kuemmeth, T. Wang, C. Thomas, S. Gronin, G. C. Gardner, M. J. Manfra, C. M. Marcus, and K. D. Petersson. “Superconducting gatemon qubit based on a proximitized two-dimensional electron gas”. In: *Nature Nanotechnology* 13.10 (Oct. 2018), pp. 915–919. ISSN: 1748-3395. DOI: [10.1038/s41565-018-0207-y](https://doi.org/10.1038/s41565-018-0207-y). URL: <https://doi.org/10.1038/s41565-018-0207-y>.
- [167] A. Hertel, M. Eichinger, L. O. Andersen, D. M. van Zanten, S. Kallatt, P. Scarlino, A. Kringhøj, J. M. Chavez-Garcia, G. C. Gardner, S. Gronin, M. J. Manfra, A. Gyenis, M. Kjaergaard, C. M. Marcus, and K. D. Petersson. “Gate-Tunable Transmon Using Selective-Area-Grown Superconductor-Semiconductor Hybrid Structures on Silicon”. In: *Phys. Rev. Appl.* 18 (3 Sept. 2022), p. 034042. DOI: [10.1103/PhysRevApplied.18.034042](https://doi.org/10.1103/PhysRevApplied.18.034042). URL: <https://link.aps.org/doi/10.1103/PhysRevApplied.18.034042>.
- [168] R. Aguado. “A perspective on semiconductor-based superconducting qubits”. In: *Applied Physics Letters* 117.24 (Dec. 2020), p. 240501. ISSN: 0003-6951. DOI: [10.1063/5.0024124](https://doi.org/10.1063/5.0024124). eprint: [https://pubs.aip.org/aip/apl/article-pdf/doi/10.1063/5.0024124/13863017/240501\\_1\\_online.pdf](https://pubs.aip.org/aip/apl/article-pdf/doi/10.1063/5.0024124/13863017/240501_1_online.pdf). URL: <https://doi.org/10.1063/5.0024124>.
- [169] F. Arute, K. Arya, R. Babbush, D. Bacon, J. C. Bardin, R. Barends, R. Biswas, S. Boixo, F. G. S. L. Brandao, D. A. Buell, B. Burkett, Y. Chen, Z. Chen, B. Chiaro, R. Collins, W. Courtney, A. Dunsworth, E. Farhi, B. Foxen, A. Fowler, C. Gidney, M. Giustina, R. Graff, K. Guerin, S. Habegger, M. P. Harrigan, M. J. Hartmann, A. Ho, M. Hoffmann, T. Huang, T. S. Humble, S. V. Isakov, E. Jeffrey, Z. Jiang, D. Kafri, K. Kechedzhi, J. Kelly, P. V. Klimov, S. Knysh, A. Korotkov, F. Kostritsa, D. Landhuis, M. Lindmark, E. Lucero, D. Lyakh, S. Mandrà, J. R. McClean, M. McEwen, A. Megrant, X. Mi, K. Michielsen, M. Mohseni, J. Mutus, O. Naaman, M. Neeley, C. Neill, M. Y. Niu, E. Ostby, A. Petukhov, J. C. Platt, C. Quintana, E. G. Rieffel, P. Roushan, N. C. Rubin, D. Sank, K. J. Satzinger, V. Smelyanskiy, K. J. Sung, M. D. Trevithick, A. Vainsencher, B. Villalonga, T. White, Z. J. Yao, P. Yeh, A. Zalcman, H. Neven, and J. M. Martinis. “Quantum supremacy using a programmable superconducting processor”. In: *Nature* 574.7779 (Oct. 2019), pp. 505–510. ISSN: 1476-4687. DOI: [10.1038/s41586-019-1666-5](https://doi.org/10.1038/s41586-019-1666-5). URL: <https://doi.org/10.1038/s41586-019-1666-5>.
- [170] Y. Zhao, Y. Ye, H.-L. Huang, Y. Zhang, D. Wu, H. Guan, Q. Zhu, Z. Wei, T. He, S. Cao, F. Chen, T.-H. Chung, H. Deng, D. Fan, M. Gong, C. Guo, S. Guo, L. Han, N. Li, S. Li, Y. Li, F. Liang, J. Lin, H. Qian, H. Rong, H. Su, L. Sun, S. Wang, Y. Wu, Y. Xu, C. Ying, J. Yu, C. Zha, K. Zhang, Y.-H. Huo, C.-Y. Lu, C.-Z. Peng, X. Zhu, and J.-W. Pan. “Realization of an Error-Correcting Surface Code with Superconducting Qubits”. In: *Phys. Rev. Lett.* 129 (3 July 2022), p. 030501. DOI: [10.1103/PhysRevLett.129.030501](https://doi.org/10.1103/PhysRevLett.129.030501). URL: <https://link.aps.org/doi/10.1103/PhysRevLett.129.030501>.
- [171] S. Krinner, N. Lacroix, A. Remm, A. Di Paolo, E. Genois, C. Leroux, C. Hellings, S. Lazar, F. Swiadek, J. Herrmann, G. J. Norris, C. K. Andersen, M. Müller, A. Blais, C. Eichler, and A. Wallraff. “Realizing repeated quantum error correction in a distance-three surface code”.

- In: *Nature* 605.7911 (May 2022), pp. 669–674. ISSN: 1476-4687. DOI: [10.1038/s41586-022-04566-8](https://doi.org/10.1038/s41586-022-04566-8). URL: <https://doi.org/10.1038/s41586-022-04566-8>.
- [172] R. Acharya et al. “Suppressing quantum errors by scaling a surface code logical qubit”. In: *Nature* 614.7949 (Feb. 2023), pp. 676–681. ISSN: 1476-4687. DOI: [10.1038/s41586-022-05434-1](https://doi.org/10.1038/s41586-022-05434-1). URL: <https://doi.org/10.1038/s41586-022-05434-1>.
- [173] T. I. Andersen et al. “Non-Abelian braiding of graph vertices in a superconducting processor”. In: *Nature* 618.7964 (June 2023), pp. 264–269. ISSN: 1476-4687. DOI: [10.1038/s41586-023-05954-4](https://doi.org/10.1038/s41586-023-05954-4). URL: <https://doi.org/10.1038/s41586-023-05954-4>.
- [174] Q. Ficheux, L. B. Nguyen, A. Somoroff, H. Xiong, K. N. Nesterov, M. G. Vavilov, and V. E. Manucharyan. “Fast Logic with Slow Qubits: Microwave-Activated Controlled-Z Gate on Low-Frequency Fluxoniums”. en. In: *Physical Review X* 11.2 (May 2021), p. 021026. ISSN: 2160-3308. DOI: [10.1103/PhysRevX.11.021026](https://link.aps.org/doi/10.1103/PhysRevX.11.021026). URL: <https://link.aps.org/doi/10.1103/PhysRevX.11.021026> (visited on 12/13/2021).
- [175] I. N. Moskalenko, I. A. Simakov, N. N. Abramov, A. A. Grigorev, D. O. Moskalev, A. A. Pishchikova, N. S. Smirnov, E. V. Zikiy, I. A. Rodionov, and I. S. Besedin. “High fidelity two-qubit gates on fluxoniums using a tunable coupler”. In: *npj Quantum Information* 8.1 (Nov. 2022), p. 130. ISSN: 2056-6387. DOI: [10.1038/s41534-022-00644-x](https://doi.org/10.1038/s41534-022-00644-x). URL: <https://doi.org/10.1038/s41534-022-00644-x>.
- [176] P. Brooks, A. Kitaev, and J. Preskill. “Protected gates for superconducting qubits”. en. In: *Physical Review A* 87.5 (May 2013). arXiv: 1302.4122, p. 052306. ISSN: 1050-2947, 1094-1622. DOI: [10.1103/PhysRevA.87.052306](http://arxiv.org/abs/1302.4122). URL: <http://arxiv.org/abs/1302.4122> (visited on 10/28/2021).
- [177] J. Dempster, B. Fu, D. G. Ferguson, D. I. Schuster, and J. Koch. “Understanding degenerate ground states of a protected quantum circuit in the presence of disorder”. en. In: *Physical Review B* 90.9 (Sept. 2014). arXiv: 1402.7310, p. 094518. ISSN: 1098-0121, 1550-235X. DOI: [10.1103/PhysRevB.90.094518](http://arxiv.org/abs/1402.7310). URL: <http://arxiv.org/abs/1402.7310> (visited on 11/25/2021).
- [178] I. V. Pechenezhskiy, R. A. Mencia, L. B. Nguyen, Y.-H. Lin, and V. E. Manucharyan. “The superconducting quasicharge qubit”. In: *Nature* 585.7825 (Sept. 2020), pp. 368–371. ISSN: 1476-4687. DOI: [10.1038/s41586-020-2687-9](https://doi.org/10.1038/s41586-020-2687-9). URL: <https://doi.org/10.1038/s41586-020-2687-9>.
- [179] A. Gyenis, A. Di Paolo, J. Koch, A. Blais, A. A. Houck, and D. I. Schuster. “Moving beyond the Transmon: Noise-Protected Superconducting Quantum Circuits”. en. In: *PRX Quantum* 2.3 (Sept. 2021), p. 030101. ISSN: 2691-3399. DOI: [10.1103/PRXQuantum.2.030101](https://link.aps.org/doi/10.1103/PRXQuantum.2.030101). URL: <https://link.aps.org/doi/10.1103/PRXQuantum.2.030101> (visited on 11/24/2021).
- [180] M. Peruzzo, A. Trioni, F. Hassani, M. Zemlicka, and J. M. Fink. “Surpassing the Resistance Quantum with a Geometric Superinductor”. In: *Phys. Rev. Appl.* 14 (4 Oct. 2020), p. 044055. DOI: [10.1103/PhysRevApplied.14.044055](https://link.aps.org/doi/10.1103/PhysRevApplied.14.044055). URL: <https://link.aps.org/doi/10.1103/PhysRevApplied.14.044055>.



- [181] F. Yan, Y. Sung, P. Krantz, A. Kamal, D. K. Kim, J. L. Yoder, T. P. Orlando, S. Gustavsson, and W. D. Oliver. “Engineering Framework for Optimizing Superconducting Qubit Designs”. en. In: *arXiv:2006.04130 [quant-ph]* (June 2020). arXiv: 2006.04130. URL: <http://arxiv.org/abs/2006.04130> (visited on 11/30/2021).
- [182] A. M. Bozkurt, J. Brookman, V. Fatemi, and A. R. Akhmerov. “Double-Fourier engineering of Josephson energy-phase relationships applied to diodes”. In: *SciPost Phys.* 15 (2023), p. 204. DOI: [10.21468/SciPostPhys.15.5.204](https://doi.org/10.21468/SciPostPhys.15.5.204). URL: <https://scipost.org/10.21468/SciPostPhys.15.5.204>.
- [183] M. T. Bell, I. A. Sadovskyy, L. B. Ioffe, A. Y. Kitaev, and M. E. Gershenson. “Quantum Superinductor with Tunable Nonlinearity”. In: *Phys. Rev. Lett.* 109 (13 Sept. 2012), p. 137003. DOI: [10.1103/PhysRevLett.109.137003](https://doi.org/10.1103/PhysRevLett.109.137003). URL: <https://link.aps.org/doi/10.1103/PhysRevLett.109.137003>.
- [184] L. Chirolli, M. Carrega, and F. Giazotto. *The quartic Blochium: an anharmonic quasicharge superconducting qubit*. 2023. arXiv: [2304.10401](https://arxiv.org/abs/2304.10401) [[cond-mat.mes-hall](https://arxiv.org/abs/2304.10401)].
- [185] A. Kou, W. C. Smith, U. Vool, R. T. Brierley, H. Meier, L. Frunzio, S. M. Girvin, L. I. Glazman, and M. H. Devoret. “Fluxonium-Based Artificial Molecule with a Tunable Magnetic Moment”. en. In: *Physical Review X* 7.3 (Aug. 2017), p. 031037. ISSN: 2160-3308. DOI: [10.1103/PhysRevX.7.031037](https://doi.org/10.1103/PhysRevX.7.031037). URL: <https://link.aps.org/doi/10.1103/PhysRevX.7.031037> (visited on 11/24/2021).
- [186] D. Gusenkova, F. Valenti, M. Spiecker, S. Günzler, P. Paluch, D. Rieger, L.-M. Pioraş-Țimbolmaş, L. P. Zârbo, N. Casali, I. Colantoni, A. Cruciani, S. Pirro, L. Cardani, A. Petrescu, W. Wernsdorfer, P. Winkel, and I. M. Pop. “Operating in a deep underground facility improves the locking of gradiometric fluxonium qubits at the sweet spots”. en. In: *Applied Physics Letters* 120.5 (Jan. 2022), p. 054001. ISSN: 0003-6951, 1077-3118. DOI: [10.1063/5.0075909](https://doi.org/10.1063/5.0075909). URL: <https://aip.scitation.org/doi/10.1063/5.0075909> (visited on 09/08/2022).
- [187] J. Bryon, D. Weiss, X. You, S. Sussman, X. Croot, Z. Huang, J. Koch, and A. A. Houck. “Time-Dependent Magnetic Flux in Devices for Circuit Quantum Electrodynamics”. In: *Phys. Rev. Appl.* 19 (3 Mar. 2023), p. 034031. DOI: [10.1103/PhysRevApplied.19.034031](https://doi.org/10.1103/PhysRevApplied.19.034031). URL: <https://link.aps.org/doi/10.1103/PhysRevApplied.19.034031>.






**Part II**

**Projects**



---

Demonstrating Majorana non-Abelian properties using fast  
adiabatic charge transfer

**Demonstrating Majorana non-Abelian properties using fast adiabatic charge transfer**Svend Krøjer<sup>1</sup>, Rubén Seoane Souto<sup>1,2</sup> and Karsten Flensberg<sup>1</sup>*Center for Quantum Devices, Niels Bohr Institute, University of Copenhagen, DK-2100 Copenhagen, Denmark*<sup>2</sup>*Division of Solid State Physics and NanoLund, Lund University, S-22100 Lund, Sweden* (Received 1 September 2021; revised 12 January 2022; accepted 14 January 2022; published 28 January 2022)

Demonstration of Majorana non-Abelian properties is a major challenge in the field of topological superconductivity. In this work, we propose a minimal device and protocol for testing non-Abelian properties using charge-transfer operations between a quantum dot and two Majorana bound states combined with reading the parity state using a second dot. We use an adiabatic perturbation theory to find fast adiabatic paths to perform operations and to account for nonadiabatic errors. We find the ideal parameter sweep and a region in parameter space that reduces the charge-transfer operation time 1–2 orders of magnitude with respect to constant velocity driving. Using realistic parameters, we estimate that the lower bound for the timescale can be reduced to  $\sim 10$  ns. Deviations from the ideal parameters lead to the accumulation of an undesired dynamical phase, affecting the outcome of the proposed protocol. We furthermore suggest to reduce the influence from the dynamical phase using a flux echo. The echo protocol is based on the  $4\pi$  periodicity of the topological state, absent for trivial bound states.

DOI: [10.1103/PhysRevB.105.045425](https://doi.org/10.1103/PhysRevB.105.045425)**I. INTRODUCTION**

The realization and verification of Majorana bound states (MBSs) have received a substantial amount of attention in the past decade [1–7]. MBSs are exotic zero-energy quasiparticle states appearing at the ends of one-dimensional topological superconductors (TSs) or in vortices of two-dimensional TSs [8–10]. MBSs exhibit non-Abelian exchange properties contrary to topologically trivial subgap states. Experimental demonstration of MBSs non-Abelian properties is one of the key goals in the field as it will probe their topological origin, distinguishing them from trivial states. An additional promising feature of MBSs is their ability to store quantum information in nonlocal fermionic degrees of freedom, becoming robust to local perturbations [3]. In this way, MBSs can encode quantum information in the degenerate ground-state manifold. Braiding operations (exchange of MBSs) can perform Clifford gates, thus implementing (nonuniversal) topological quantum computing [1].

To experimentally realize MBSs, a number of structures and devices have been proposed [13]. Hybrid semiconductor-superconductor heterostructures are widely used platforms in the attempt to realize one-dimensional spin-polarized  $p$ -wave superconductors hosting MBSs at its ends [9,10]. Recent progress on fabrication techniques has made it possible to measure signatures consistent with MBSs. Early observations include the measurement of a robust zero-bias

conductance peak [14,15]. Later experiments indicated the  $2e^2/h$ -quantization of the zero-bias peak [16]. Measurements have shown coherent transport through a Majorana island [17], exponential scaling of energy separation with length [18,19], and hybridization characteristics with quantum dot states [15,20]. Despite the mounting signatures consistent with MBSs, direct observation of their non-Abelian exchange properties remains a challenge in the field. Such demonstration could provide smoking-gun evidence for the topological origin of MBSs, while having the outlook of being a first step in implementing protected gates in Majorana qubit devices.

In practice, showing non-Abelian exchange properties through real space braiding of MBSs in T or Y junctions is expected to be a great experimental challenge as it is difficult to tune in and out of the topological regime [7,21]. For this reason, this paper instead focuses on implementing braiding-like operations of MBSs in parameter space. Following Refs. [11,12], we consider manipulating the occupation of MBSs through charge-transfer processes with a nearby quantum dot in the Coulomb-blockaded regime, see Fig. 1 for a device schematic similar to Ref. [11]. In a successful charge-transfer process, an electron is adiabatically exchanged between the gate-controlled quantum dot and the MBSs, changing the Majorana parity. An advantage of this parameter space operation is that it generalizes the real space braiding to rotations through a continuum of angles, extending the space of possible operations through braiding operations alone. The immediate downside, however, is that charge-transfer operations are not topologically protected and require accurate tuning of the parameters to achieve high fidelity.

Noncommutativity of braiding-like operations can provide evidence for the non-Abelian nature of MBSs. Concretely, we search for protocols where interchanging two charge-transfer operations influence the measured parity of the Majorana state. A protocol consists of two sequences with

*Published by the American Physical Society under the terms of the Creative Commons Attribution 4.0 International license. Further distribution of this work must maintain attribution to the author(s) and the published article's title, journal citation, and DOI. Funded by Bibsam.*

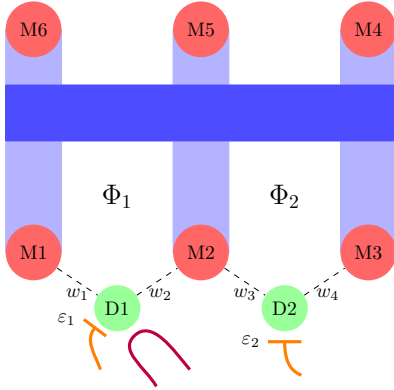


FIG. 1. Schematic of the proposed device for demonstrating MBSs non-Abelian properties. Three long TS nanowires (light blue) extend from a trivial superconducting backbone (blue). MBSs (red) form at the ends of the TSs. M1, M2, and M3 are tunnel coupled to quantum dots (green) D1 and D2 with coupling strengths  $w_i$ . The dot energies  $\varepsilon_i$  are controlled with nearby gates (orange). In our protocols, D1 is used for initialization and read out of the M1/M2 pair using a charge sensor (purple). D2 is used for charge-transfer processes involving the M2/M3 pair [11,12]. Magnetic fluxes  $\Phi_1, \Phi_2$  control the splitting between the even and odd parity states. The remaining MBSs (M4, M5, and M6) are separated from M1, M2, and M3 and do not contribute to the system dynamics.

charge-transfer operations applied in different order, testing the noncommutativity of the operations [11]. In the device shown in Fig. 1, the principal source of error is due to splitting of the ground state degeneracy with imperfect tuning of the parameters. This leads to a relative dynamical phase between the split states, reducing the visibility of the geometric phase originated from non-Abelian charge-transfer operations. As the charge-transfer process is meant to operate on long, adiabatic timescales, even a small energy splitting can lead to a substantial relative phase error, overwhelming the non-Abelian signal. This presents a trade-off between driving the system slowly enough to remain in the ground state and fast enough to avoid the effects of the splitting.

In this study, we propose an experiment for testing the non-Abelian properties of MBSs. We simplify the device and reduce the number of operations needed with respect to the original proposal in Ref. [11]. We improve the visibility of the MBSs non-Abelian signature by optimizing the adiabatic charge-transfer processes. We also design a  $4\pi$ -periodic flux echo protocol that cancels the undesired dynamical phase of subsequent operations.

Specifically, our device and protocol proposals are minimal as they require controlling a single quantum dot (D2) and one tunneling amplitude ( $w_4$ ), see Fig. 1. A second quantum dot, D1, is used to measure the parity of the nonlocal fermion formed by M1 and M2 [22–27]. We propose two variants of the protocol: with and without the echo mechanism. Both protocols, depicted in Fig. 2, require using one dot and three adiabatic charge-transfer processes. In the flux echo protocol,

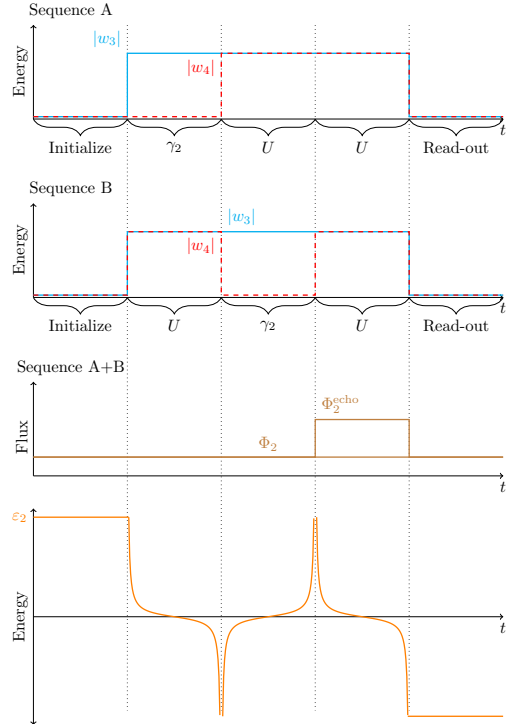


FIG. 2. Diagram of the two sequences (top and middle panels), consisting of three charge-transfer processes. In each diagram, both the protocols with and without the echo effect are depicted. (Top) Sequence A. Here,  $|w_4|$  is initially set to zero during the first charge-transfer process. For the two subsequent charge-transfer processes, it is ideally set to  $|w_4| = |w_3|$ . As indicated, the echo protocol is achieved by adjusting the magnetic field before the third charge-transfer process. (Middle) Sequence B. Here,  $|w_4|$  is instead set to zero during the second charge-transfer process, reversing the order of the first two operations. (Bottom) Level energy of D2 for both sequences.

the dynamical phase is canceled by flipping the sign of the energy splitting in between charge-transfer operations. This is accomplished by tuning the magnetic field  $\Phi_2$  to induce an additional superconducting (SC) phase difference, flipping the sign of the energy splitting between the even and odd parity ground states. We find that the echo protocol is robust to drifts in the SC phase difference and that the deviations in the additional SC phase can be as large as  $\sim 10\%$  from the ideal value,  $2\pi$ . As the flux echo relies on the  $4\pi$  periodicity of Majorana parity states, it also makes it possible to distinguish from  $2\pi$ -periodic trivial states.

To mitigate nonadiabatic and phase errors, we formulate a consistent theoretical framework for finding fast, adiabatic paths based on adiabatic perturbation theory (APT) developed in Ref. [28]. Within the framework, we find how to optimally

control the level energy of the quantum dot to minimize the dynamical phase without introducing nonadiabatic errors such as transitions to excited states. Compared to driving the system with constant (Landau-Zener) velocity, we find an adiabatic path that is one to two orders of magnitude faster than a linear sweep of D2 energy, as used in Ref. [12]. We provide numerical calculations supporting these results. Finding fast adiabatic paths is crucial for adiabatic quantum computing as discussed by previous attempts [29–32]. Specifically in the context of Majorana-based systems, the velocity of real space exchange and operations using varying tunnel couplings between MBSs has been considered [33–45]. In this work, we instead consider the nonadiabatic effects that occur when MBSs are coupled to a driven quantum dot.

## II. THEORY

We begin by reviewing the charge-transfer process following Ref. [11] and formulate the non-Abelian operations in terms of the relative geometric phase between the even and the odd parity ground states. This enables us to identify the non-Abelian operations resulting from charge-transfer processes where the ground states energy split.

Then, we review the adiabatic perturbation theory following Ref. [28] and formulate a framework for studying fast adiabatic processes, resulting in predictions for the optimal charge control.

### A. Charge-transfer process

To describe the charge-transfer process between the quantum dot D2 and the MBSs M2 and M3 (see Fig. 1), we consider the low-energy Hamiltonian [11],

$$H = \varepsilon_2 d_2^\dagger d_2 + (w_3^* d_2^\dagger - w_3 d_2) \gamma_2 + (w_4^* d_2^\dagger - w_4 d_2) \gamma_3. \quad (1)$$

The first term describes D2 with  $\varepsilon_2$  being its time-dependent energy and  $d_2$  its electron annihilation operator. The second and third terms in Eq. (1) describe the tunnel coupling to M2 and M3, with  $w_3$  and  $w_4$  being the tunneling amplitudes. Here,  $\gamma_2$  and  $\gamma_3$  are the self-adjoint Majorana operators.

Our proposed protocol is based on operating on the state of M23 using D2. The annihilation operator of the M23 fermion is defined by  $f_{23} = 1/2(\gamma_2 + i\gamma_3)$ , giving a Hilbert space of dimension four. Due to the total parity conservation, the Hamiltonian matrix corresponding to Eq. (1) is block diagonal with even and odd parity blocks given by

$$\mathcal{H}^\rho = \begin{pmatrix} 0 & w^\rho \\ (w^\rho)^* & \varepsilon_2 \end{pmatrix}, \quad (2)$$

where  $w^\rho = w_3 - \rho i w_4$ . We use the even basis ( $\rho = +$ )  $\{|0\rangle_{D2} |0\rangle_{M23}, |1\rangle_{D2} |1\rangle_{M23}\}$  and odd basis ( $\rho = -$ )  $\{|0\rangle_{D2} |1\rangle_{M23}, |1\rangle_{D2} |0\rangle_{M23}\}$ , with  $0(1)$  referring to the occupation of D2 and M23.

We parametrize the tunnel couplings as  $w_3 = w e^{i\phi/2} \cos \theta$  and  $w_4 = w \sin \theta$  where the magnetic flux  $\Phi_2$  controls the SC phase difference  $\phi = \Phi_2/(h/(2e))$ . Here,  $\theta$  controls the asymmetry on the tunnel coupling strength. The eigenenergies of the Hamiltonian matrix in Eq. (2) are

$$E_\pm^\rho = \varepsilon_2/2 \pm \sqrt{(\varepsilon_2/2)^2 + w^2(1 - \rho \sin(2\theta) \sin(\phi/2))}, \quad (3)$$

with the corresponding eigenstates

$$\psi_\pm^\rho = \frac{1}{\sqrt{(E_\pm^\rho)^2 + |w^\rho|^2}} \begin{pmatrix} w^\rho \\ E_\pm^\rho \end{pmatrix}. \quad (4)$$

The energy spectrum of the system is  $4\pi$ -periodic, and the even and the odd parity sectors are degenerate at integer values of  $\phi/(2\pi)$ .

In a successful charge-transfer process, an electron is transferred between D2 and the fermion formed by M23. This is accomplished by inverting the energy on D2 from  $\varepsilon_0$  to  $-\varepsilon_0$ , allowing the exchange of a charge. The initial and final level energies are not required to be equal in magnitude but they should be much larger than the coupling strength to D2. We assume  $\varepsilon_0 > 0$  in what follows and disregard the effect from the continuum of states by taking the limit  $\Delta_{SC} > \varepsilon_0 \gg w$ . The effect of the continuum of states above the superconducting gap  $\Delta_{SC}$  has been discussed in Ref. [12]. We further assume that the time  $T$  of the charge-transfer process is shorter than the quasiparticle poisoning timescale, yet long enough for the process to be adiabatic.

To understand the nonideal charge-transfer operations, it is helpful to consider the geometric phase acquired by the even parity ground state relative to the odd parity ground state. Since the charge-transfer process is not a loop in parameter space, the calculation of the geometric phase is slightly subtle and can be found in Appendix A. The accrued relative geometric phase between the even and odd parity ground states during a process where the dot is filled ( $\varepsilon_2 : \varepsilon_0 \rightarrow -\varepsilon_0, \varepsilon_0 > 0$ ) is

$$\theta^G = \arctan[\tan(2\theta) \cos(\phi/2)], \quad (5)$$

with corrections of order  $(w/\varepsilon_0)^2$ . The corresponding operation on the MBSs is

$$\begin{aligned} U^G &= e^{i\theta^G/2} f_{23}^\dagger + e^{-i\theta^G/2} f_{23} \\ &= \cos(\theta^G/2) \gamma_2 + \sin(\theta^G/2) \gamma_3. \end{aligned} \quad (6)$$

When the dot is filled, an electron tunnels from the superconductor to the dot. In the odd parity sector, the electron jumps from the occupied M23 fermionic state ( $d_2^\dagger f_{23}$ ). In the even sector, the M23 fermion state is vacant. In this case, a Cooper pair splits with one electron occupying the M23 state while the other tunnels to the dot ( $d_2^\dagger f_{23}^\dagger$ ). Isolating the part acting on the M23 fermion and inserting the relative geometric phase, we arrive at Eq. (6). For the reverse process, the sign of the geometric phase and the roles of even and odd sectors with regards to the tunneling are both interchanged. For this reason, Eq. (6) also holds when emptying the dot. In the ideal situation, integer  $\phi/(2\pi)$  and adiabatic dot energy sweep, our result simplifies to  $U^G = \cos \theta \gamma_2 + \sin \theta \gamma_3$ , agreeing with the original result found in Ref. [11].

It is straightforward to relate the relative phase between the even and odd ground states to a parity measurement of the fermion formed by the M12 pair using the dot D1. In the measurement basis, we define  $f_{12} = 1/2(\gamma_1 + i\gamma_2)$  and  $f_{34} = 1/2(\gamma_3 + i\gamma_4)$  with even  $\{|0\rangle_{M12} |0\rangle_{M34}, |1\rangle_{M12} |1\rangle_{M34}\}$  and odd  $\{|0\rangle_{M12} |1\rangle_{M34}, |1\rangle_{M12} |0\rangle_{M34}\}$  occupation states. We take as an example the ideal situation where  $\theta^G/2 = \theta$ . Our proposed device can only initialize the fermion M12 so we consider the initial state  $|0\rangle_{M12} |\psi\rangle_{M34}$  where

$|\psi\rangle_{M34} = \alpha |0\rangle_{M34} + \beta |1\rangle_{M34}$  is a ground state. The final state after the charge-transfer operation is found by applying  $U^G$  to the initial state,

$$U^G |0\rangle_{M12} |\psi\rangle_{M34} = i \cos \theta |1\rangle_{M12} |\psi\rangle_{M34} + \sin \theta |0\rangle_{M12} |\psi'\rangle_{M34}, \quad (7)$$

where  $|\psi'\rangle_{M34} = \alpha |1\rangle_{M34} + \beta |0\rangle_{M34}$ . Using the dot D1 to measure the occupation of the M12 fermion gives the result  $f_{12}^\dagger f_{12} = 0(1)$  with probability  $\sin^2 \theta (\cos^2 \theta)$ , which does not depend on the initial state of the M34 pair. In this way, the relative phase between the even and odd ground states could be experimentally inferred from statistics.

Away from the degeneracy point, integer  $\phi/(2\pi)$ , the even- and odd-parity ground-states also acquire a relative dynamical phase,  $\theta^D$ , affecting the outcome of the final measurement. In Sec. IID, we compute the relative dynamical phase for the charge-transfer process we consider, see Eq. (51). The relative dynamical phase, unlike its geometric counterpart, does not switch sign when reversing the charge-transfer process and its contribution accumulates with successive processes. This makes a difference in the operations on the MBSs when filling or emptying the dot. Including the relative dynamical phase to Eq. (6), the operation depends on whether the dot is emptied (–) or filled (+),

$$U = e^{i(\theta^G \mp \theta^D)/2} f_{23}^\dagger + e^{-i(\theta^G \mp \theta^D)/2} f_{23} \\ = \cos\left(\frac{\theta^G \mp \theta^D}{2}\right) \gamma_2 + \sin\left(\frac{\theta^G \mp \theta^D}{2}\right) \gamma_3. \quad (8)$$

This is the full operator acting on the ground state of the system after a charge-transfer process away from the degeneracy point. The relative geometric and dynamical phases  $\theta^G$  and  $\theta^D$  are given in Eqs. (5) and (51).

### B. Protocol

A charge-transfer operation changes the parity of the superconductor regardless of whether it is in its trivial or topological phase. It is therefore insufficient to perform only a single operation to distinguish between topologically trivial and nontrivial subgap states. To probe the non-Abelian properties associated with topologically nontrivial states, we instead test the noncommutativity of operations executed on the degenerate Majorana subspace. In our proposed experiment, we compare the resulting states after executing two sequences of operations. These sequences consist of the same set of operations ordered in different ways, see Fig. 2. The dot D1 is used to initialize and measure the occupation of the M12 Majorana pair. Applying the two sequences on the initial state  $|0\rangle_{M12} |\psi\rangle_{M34}$  give the following final states,

Sequence A:

$$U U \gamma_2 |0\rangle_{M12} |\psi\rangle_{M34} = i \cos \theta^D |1\rangle_{M12} |\psi\rangle_{M34} + \sin \theta^D |0\rangle_{M12} |\psi'\rangle_{M34}. \quad (9)$$

Sequence B:

$$U \gamma_2 U |0\rangle_{M12} |\psi\rangle_{M34} = i \cos(\theta^G + \theta^D) |1\rangle_{M12} |\psi\rangle_{M34} + \sin(\theta^G + \theta^D) |0\rangle_{M12} |\psi'\rangle_{M34}. \quad (10)$$

Here, we assume that the energy sweeps during the charge-transfer processes are adiabatic. We also take the parameters  $\theta$  and  $\phi$  to be the same for the operations  $U$ . The operation  $\gamma_2$  performs a charge-transfer process where  $w_4$  is turned off (corresponding to  $\theta = 0$ ), without inducing any relative phase between the even and odd parity sectors. The order of the first two operations in Eqs. (9) and (10) is switched between sequence A and B. Due to the noncommutativity of  $\gamma_2$  and  $U$ , each sequence has a different geometric phase. This difference can be sampled statistically by measuring the occupation of the M12 Majorana pair using the dot D1 [22]. In the final measurement, the probability of measuring the state  $|0\rangle_{M12}$  is  $\sin^2(\theta^D)$  and  $\sin^2(\theta^G + \theta^D)$  for the sequences A and B. In the ideal situation, integer  $\phi/(2\pi)$ , the relative phases simplify to  $\theta^D = 0$  and  $\theta^G = 2\theta$ . The two sequences are maximally distinguishable for  $\theta = \pi/4$ , corresponding to symmetric coupling  $w_3 = w_4$ . For these finely tuned values, the final state is  $|1\rangle_{M12}$  and  $|0\rangle_{M12}$  for the sequences A and B.

The dynamical phase,  $\theta^D$ , acquired during the operations described in Eqs. (9) and (10) can overwhelm the Majorana signature, coming from  $\theta^G$ . This effect of  $\theta^D$  can be mitigated using a mechanism similar to the spin-echo used in spin qubits [46]. In Majorana devices, parity echo or flux echo have been proposed to increase the fidelity of certain operations [47,48]. We consider implementing a flux echo based on the following observation: the relative dynamical phase in Eq. (51) depends on the SC phase difference as  $\theta^D \propto \sin(\phi/2)$ . Due to the  $4\pi$  periodicity, changing  $\phi \rightarrow \phi + 2\pi$ , the sign of  $\theta^D$  changes. In this way, the dynamical phase contributions from subsequent operations cancel out. Concretely, we propose to adjust the SC phase difference by tuning the magnetic flux  $\Phi_2$  and set its value to  $\phi$  when performing the first two charge-transfer processes in Fig. 2. Ideally,  $\phi/(2\pi)$  is integer, but presumably it is difficult to assess its value in experiment and it may drift. Then, for the last operation, the SC phase difference is tuned  $\phi \rightarrow \phi + 2\pi$ . Optimally, this cancels the dynamical phase in the two  $U$  operations in sequences A and B. This is contrasted by trivial states whose  $2\pi$ -periodic spectrum will not see the effect of the flux echo.

An advantage of this flux echo is that the required change in the SC phase difference is independent of the (unknown) value of  $\phi$ . This is in contrast to proposals such as  $\phi \rightarrow -\phi$  which also flips the sign of the relative dynamical phase [48]. A byproduct of the change  $\phi \rightarrow \phi + 2\pi$  is that the sign of the relative geometric phase also changes, see Eq. (5). We therefore define primed charge-transfer operators  $U'$  which are equal to the original operators introduced in Eq. (8), replacing  $\phi$  by  $\phi + 2\pi$ , which leads to a sign flip of  $\theta^G$  and  $\theta^D$  with respect to  $U$ . Including the flux echo as described in sequence A and B gives the following.

Sequence A',

$$U' U \gamma_2 |0\rangle_{M12} |\psi\rangle_{M34} = i \cos \theta^G |1\rangle_{M12} |\psi\rangle_{M34} + \sin \theta^G |0\rangle_{M12} |\psi'\rangle_{M34}. \quad (11)$$

Sequence B',

$$U' \gamma_2 U |0\rangle_{M12} |\psi\rangle_{M34} = i |1\rangle_{M12} |\psi\rangle_{M34}. \quad (12)$$

Because of the  $4\pi$  periodicity of the spectrum, we can design a flux echo, equivalent to flipping the system parity. It increases

the regime with maximal visibility due to the cancellation of the dynamical phase. Also, the outcome becomes insensitive to the operation timescale. In sequences  $A'$  and  $B'$ , the final state is  $|0\rangle_{M12}$  with probability  $\sin^2\theta^G$  and 0 respectively. Maximal visibility thus occurs for  $\theta^G = \pi/2$ .

To make a measure of the discernibility of the outcome of the two sequences, we introduce the sequence visibility  $\Lambda$ . We define  $\Lambda$  as the difference in probability of measuring the state  $|0\rangle_{M12}$  after the two sequences where unit visibility corresponds to the ideal situation. Thus the sequence visibility for sequences  $A$  and  $B$  is

$$\Lambda = \sin^2(\theta^G + \theta^D) - \sin^2(\theta^D). \quad (13)$$

For sequences  $A'$  and  $B'$ , the visibility would simply be

$$\Lambda' = \sin^2(\theta^G), \quad (14)$$

due to the cancellation of dynamical phase. The sequence visibility quantifies the degree to which the orders of operations can be distinguished to show the MBS non-Abelian properties.

In a realistic experiment, tuning the additional SC phase contribution for the flux echo is presumably simpler than tuning  $\phi$  to the degeneracy point, integer  $\phi/(2\pi)$ . However, inaccuracies and phase fluctuations can play a role, leading to a nonzero dynamical phase. An additional complication is that the relative dynamical phase is dependent on the exact dynamics of the adiabatic transport. In the next section, we approach the problem of minimizing the dynamical phase contribution using APT to study fast adiabatic processes.

### C. Deriving adiabatic perturbation theory

The adiabatic theorem predicts that a system initialized in an eigenstate  $|n(t=0)\rangle$  of the initial Hamiltonian  $H(t=0)$  will follow the instantaneous eigenstate  $|n(t)\rangle$  of the slowly varying time-dependent Hamiltonian  $H(t)$ . The instantaneous eigenstates fulfill the instantaneous Schrödinger equation,

$$H(t)|n(t)\rangle = E_n(t)|n(t)\rangle. \quad (15)$$

Typically, the adiabatic approximation is valid for

$$\frac{|\langle m(t) | \frac{dH(t)}{dt} | n(t) \rangle|}{|E_m(t) - E_n(t)|} = \frac{|\langle m(t) | \frac{dH(t)}{dt} | n(t) \rangle|}{(E_m(t) - E_n(t))^2} \ll 1, \quad n \neq m. \quad (16)$$

However, this is not always a sufficient condition to ensure adiabaticity [49]. Adiabatic perturbation theory (APT) [28] attempts to determine the validity of the adiabatic approximation, describing nonadiabatic corrections. APT has previously been used in a variety of situations, including quench dynamics through a quantum critical point [50], quasiadiabatic Monte Carlo algorithm [51], as well as corrections to non-Abelian processes involving Majorana exchange [33]. Additionally, APT has also inspired Floquet adiabatic perturbation theory [52–54].

APT is based on a perturbative expansion in the small parameter  $1/T$  where  $T$  is the relevant timescale of the system [28]. In our case,  $T$  is the time of a single charge-transfer operation. The APT expansion parameter  $1/T$  is not dimensionless as required by perturbation theories and should be compared to a relevant energy scale. In our system, we have two energy

scales  $\varepsilon_0$  and  $w$  whose ratio  $x_0 = \varepsilon_0/(2w)$  we take to be large. It is therefore not obvious how to a priori choose the proper dimensionless expansion parameter.

In our study of APT, we simultaneously address this issue and find fast adiabatic energy sweeps of the dot energy to perform efficient charge-transfer operations. While our results are specific to the charge-transfer processes, the framework we use is completely general and may be applied to any nondegenerate quantum system. Further work can presumably extend the framework to degenerate systems as well [55]. We begin our treatment by giving a brief overview of APT as presented in Ref. [28]. Then, we apply it to the charge-transfer process, addressing the issues due to the dimensionful expansion parameter  $1/T$ , and studying fast adiabatic paths.

For a nondegenerate  $N$ -level quantum system, APT is based on the following ansatz for the time-evolved state [28]:

$$|\Psi(s)\rangle = \sum_p \frac{1}{T^p} \sum_{n,m=0}^{N-1} e^{-iT\omega_m(s)} e^{i\xi_m(s)} b_{nm}^{(p)}(s) |n(s)\rangle, \quad (17)$$

which is given in terms of the dimensionless time  $s = t/T$ . The quantities  $\omega_m(s)$  and  $\xi_m(s)$  are the dynamical and geometric phases of the instantaneous state  $|m(s)\rangle$ ,

$$\omega_m(s) = \int_0^s E_m(s') ds', \quad (18)$$

$$\xi_m(s) = i \int_0^s \langle m(s') | \frac{dm(s')}{ds'} ds'. \quad (19)$$

The expansion in Eq. (17) introduces complex, time-dependent coefficients  $b_{nm}^{(p)}(s)$  to be determined. Due to the dimensionful expansion parameter  $1/T$ , the coefficients also carry dimensions such that  $b_{nm}^{(p)}(s)/T^p$  is dimensionless. The ansatz in Eq. (17) recasts the problem of solving the time-dependent Schrödinger equation,

$$i \frac{d}{ds} |\Psi(s)\rangle = H(s) |\Psi(s)\rangle, \quad (20)$$

into computing the coefficients  $b_{nm}^{(p)}(s)$  from linear, recursive equations. The initial conditions for the coefficients are determined by the initial state. In the expansion, the zeroth-order terms correspond to the adiabatic approximation at all times,

$$b_{nm}^{(0)}(s) = 0, \quad n \neq m. \quad (21)$$

It further implies that the initial state is described by the adiabatic approximation, giving the initial constraint on the  $p \geq 1$  order coefficients:

$$\sum_m b_{nm}^{(p)}(0) = 0, \quad p \geq 1. \quad (22)$$

By inserting the ansatz in Eq. (17) into the time-dependent Schrödinger equation (20) and taking the inner product with  $\langle m(s) |$ , we get

$$i\Delta_{nm}(s)b_{nm}^{(p+1)}(s) + \dot{b}_{nm}^{(p)}(s) + W_{nm}(s)b_{nm}^{(p)}(s) + \sum_{k \neq n} M_{nk}(s)b_{km}^{(p)}(s) = 0. \quad (23)$$



The following quantities have been defined,

$$\Delta_{nm}(s) = E_n(s) - E_m(s), \quad (24)$$

$$M_{nm}(s) = \langle n(s) | \dot{H}(s) | m(s) \rangle, \quad (25)$$

$$W_{nm}(s) = M_{nn}(s) - M_{mm}(s), \quad (26)$$

where the dot denotes time differentiation,  $d/ds$ . Equation (23) is the main result of Ref. [28] from which the coefficients of order  $p + 1$  can be recursively computed from the  $p$ -order coefficients.

For illustration purposes, we compute the first-order correction in a two-level system initialized in the ground state. Using the initial condition  $b_{00}^{(0)}(0) = 1$ , the first-order coefficients are

$$b_{01}^{(1)}(s) = 0, \quad (27)$$

$$b_{10}^{(1)}(s) = \frac{iM_{10}(s)}{\Delta_{10}(s)}, \quad (28)$$

$$b_{00}^{(1)}(s) = i \int_0^s \frac{|M_{10}(s')|^2}{\Delta_{10}(s')} ds', \quad (29)$$

$$b_{11}^{(1)}(s) = -\frac{iM_{10}(0)}{\Delta_{10}(0)}. \quad (30)$$

These first-order coefficients will be the starting point of the next section where we apply APT to the charge-transfer process. We find the optimal adiabatic path and investigate what conditions must be satisfied to be consistent with the adiabatic approximation.

#### D. Applying adiabatic perturbation theory

We continue our study by applying APT to the two-level system given in Eq. (2), which describes two MBSs coupled to a quantum dot. We use Eqs. (24)–(26) to compute the relevant quantities in the expansion  $\Delta_{10}(s) = -\Delta_{01}(s)$ ,  $M_{10}(s) = -(M_{01}(s))^*$ ,  $W_{10}(s) = -W_{01}(s)$ . At the degeneracy point  $\sin(2\theta) \sin(\phi/2) \ll 1$ , we find

$$\Delta_{10}(s) = 2w\sqrt{x(s)^2 + 1}, \quad (31)$$

$$M_{10}(s) = \frac{\dot{x}(s)}{2(x(s)^2 + 1)}, \quad (32)$$

$$W_{10}(s) = 0. \quad (33)$$

We have expressed the above quantities in terms of the dimensionless level energy  $x(s) = \varepsilon_2(s)/(2w)$ . Notice that  $M_{10}(s)$  is dimensionless and  $\Delta_{10}(s)$  has dimension of energy.

To find fast adiabatic paths, we minimize the first-order coefficient  $b_{00}^{(1)}(s)$ , describing the leading correction to the adiabatic evolution. That is, we minimize the integral

$$I(s) = \frac{1}{T} \int_0^s \frac{|M_{10}(s')|^2}{\Delta_{10}(s')} ds', \quad (34)$$

$$= \frac{1}{8Tw} \int_0^s \frac{\dot{x}(s')^2}{(x(s')^2 + 1)^{5/2}} ds'. \quad (35)$$

We choose to minimize this coefficient as it describes the nonadiabatic corrections accumulated during the operation. We could also have considered  $b_{10}^{(1)}(s)$  or  $b_{11}^{(1)}(s)$  which depend

on the instantaneous configuration. Before APT, a condition corresponding to  $b_{10}^{(1)}(s)$  and Eq. (16) was heuristically chosen to find the so-called local adiabatic evolution [29–31]. By minimizing Eq. (35), we find the optimal adiabatic energy sweep  $x_{\text{opt}}(s)$ . Later, we check whether the found adiabatic path is consistent with APT, i.e., the magnitude of the coefficients decrease with the order  $p$  and do not grow with  $x_0 \gg 1$ .

The integral in Eq. (35) is straightforward to minimize by standard methods. Using the Beltrami identity, we find that the optimal path fulfills

$$\dot{x}_{\text{opt}}(s) = \pm \Omega_\eta [x_{\text{opt}}(s)^2 + 1]^{\eta/2} \propto [\Delta_{10}(s)]^\eta, \quad (36)$$

where the  $\pm$  sign in front corresponds to emptying or filling the dot and  $\Omega_\eta > 0$  is a constant dependent on the initial conditions. The minimization of Eq. (35) leads to  $\eta = 5/2$  as the ideal adiabatic path. The further analysis below, however, shows that  $\eta = 5/2$  is not optimal as higher-order coefficients are significant for this  $\eta$  value. In the following of the section, we find the optimal  $\eta$  value in Eq. (36) consistent with APT constraints. Eq. (36) is the simplest parametrization which can be physically motivated: the speed of the dot level sweep is proportional to the energy gap between the ground and excited state raised to a power. The energy sweep and the energy gap for  $\eta = 0, 1, 2$  is displayed in the right panel of Fig. 3. The case  $\eta = 0$  corresponds to a linear energy sweep of the quantum dot, independent from the gap to the excited state.  $\eta > 0$  describes an increasing energy speed of the dot with the gap between the ground and the excited states. APT also allows to describe more general ansatzes than the one in Eq. (36).

The solution to Eq. (36) can be given in terms of the Gaussian hypergeometric function  ${}_2F_1(a, b; c; z)$ , see Appendix B. This enables us to compute the scaling of  $\Omega_\eta$  to leading order in  $1/x_0$  for  $x_0 \gg 1$ ,

$$\Omega_\eta \approx \begin{cases} \frac{\sqrt{\pi} \Gamma(\frac{\eta+1}{2})}{\Gamma(\frac{\eta}{2})} & \text{for } \eta > 1, \\ 2 \sinh[-1](x_0) & \text{for } \eta = 1, \\ \frac{2}{1-\eta} x_0^{1-\eta} & \text{for } \eta < 1. \end{cases} \quad (37)$$

We provide the complete analytic expressions in Appendix B. Importantly,  $\Omega_\eta$  scales with  $x_0$  for  $\eta \leq 1$ . It can be problematic for APT when evaluating Eq. (35) at  $s = 1$  in the limit  $x_0 \gg 1$ . Using  $x_{\text{opt}}(s)$  from Eq. (36),

$$I(1) = \frac{\Omega_\eta}{8Tw} \frac{\sqrt{\pi} \Gamma(\frac{4-\eta}{2})}{\Gamma(\frac{5-\eta}{2})}, \quad \text{for } \eta < 4. \quad (38)$$

A necessary (but insufficient) condition for APT to hold is  $I(1) \ll 1$ , or equivalently,  $Tw \gg \Omega_\eta$ . It means that for  $\eta < 1$ ,  $Tw \gg x_0^{1-\eta}$ , which thus requires very slow processes to achieve adiabaticity. For  $\eta = 1$ ,  $\Omega_\eta$  scales logarithmically with  $x_0$ . For  $\eta > 4$ , Eq. (35) scales as  $x_0^{\eta-4}$ . This analysis tells us that for  $1 < \eta < 4$ , we need  $Tw \gg 1$  to satisfy  $I(1) \ll 1$ . Outside this range,  $T$  scales with  $x_0$ , meaning that the total time for to complete the operation is sensitive to the large energy  $\varepsilon_0$ . We may also check that the other first-order corrections are small,

$$\frac{M_{10}(s)}{T \Delta_{10}(s)} = \frac{\Omega_\eta}{4Tw} (x_{\text{opt}}(s)^2 + 1)^{\frac{\eta-3}{2}} \ll 1, \quad (39)$$

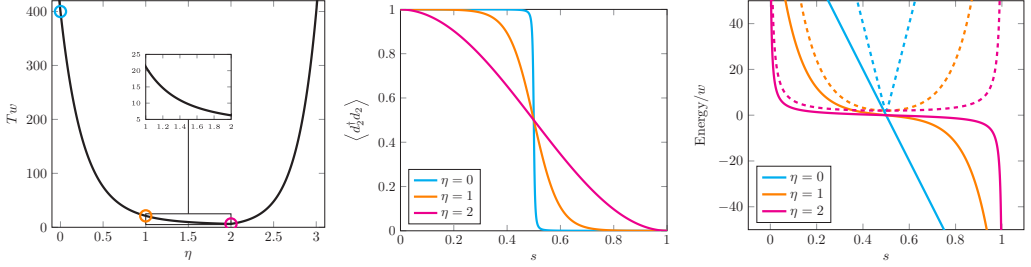


FIG. 3. Characteristics of a single charge-transfer process at the degeneracy point (integer  $\phi/(2\pi)$ ) for different values of  $\eta$  and  $x_0 = 100$ . (Left) Operation timescale  $T$  (relative to  $w$ ) as a function of  $\eta$  for fixed dimensionless expansion parameter  $\Sigma_{\eta}/(Tw) = 0.5$ , see Eqs. (49) and (B4). The panel shows an optimal region for  $1 < \eta \leq 2$  with an optimal point  $\eta = 2$ , where the adiabatic timescale is the minimal. Colored markers at  $\eta = 0, 1, 2$  are reference for the middle and right panels. (Middle) Dot occupation  $\langle d_2^{\dagger} d_2 \rangle = \partial E_{-}/\partial \varepsilon_2$  as a function of dimensionless time  $s = t/T$ . For the optimal path ( $\eta = 2$ ), charge is smoothly transferred during the entire process. For the linear sweep ( $\eta = 0$ ), charge is transferred only near the half-way point of the process ( $s \approx 1/2$ ), necessitating a longer operation time to ensure adiabatic charge-transfer. (Right) Energy sweeps  $\varepsilon_2(s)$  (solid lines) and excitation energies  $\Delta_{10}(s)$  (dashed lines). For the optimal path ( $\eta = 2$ ), most of the operation time is spent where the gap is smallest to avoid nonadiabatic errors. For the linear sweep ( $\eta = 0$ ), most of the operation time is spent where the gap is large, leading to a large timescale of the process.

which decreases with  $x_0$  for  $\eta < 3$  and grows as  $x_0^{\eta-3}$  for  $\eta > 3$ , introducing a further restriction to APT validity:  $\eta < 3$ . In summary, this preliminary analysis suggests that the first-order corrections are small for  $Tw \gg 1$  when  $1 < \eta < 3$ . If  $\eta$  is chosen outside this range,  $T$  grows with  $x_0 \gg 1$ . In the following, we show that it is insufficient to demand that the first-order corrections are small for APT to be applicable. This was not mentioned in Ref. [28], but the sufficient conditions are nevertheless contained in APT. Like in the above analysis, we find that  $Tw \gg 1$  is sufficient but only in the range  $1 < \eta \leq 2$ . Outside of this range, large  $x_0$  values can make higher-order contributions more significant than the lowest ones in the expansion in Eq. (17). As exemplified in Eqs. (38) and (39), this is due to the  $w$  and  $\varepsilon_0$  dependence of the dimensionful coefficients resulting from the dimensionful expansion coefficient. To resolve this, we express the coefficients in (17) of order  $p+1$  in terms of  $p$ -order coefficients,

$$b_{nm}^{(p+1)}(s) = \frac{i}{\Delta_{nm}(s)} \frac{d}{ds} b_{nm}^{(p)}(s) \quad (n \neq m) + \sum_{k \neq n} \frac{iM_{nk}(s)}{\Delta_{nm}(s)} b_{km}^{(p)}(s), \quad (40)$$

$$b_{nm}^{(p+1)}(s) = \sum_{k \neq n} \int_0^s \frac{iM_{nk}(s')}{\Delta_{nk}(s')} \frac{d}{ds'} b_{kn}^{(p)}(s') ds' \quad (n = m) + \sum_{\substack{k \neq n \\ l \neq k}} \int_0^s \frac{iM_{nk}(s')M_{kl}(s')}{\Delta_{nk}(s')} b_{ln}^{(p)}(s') ds' - \sum_{k \neq n} b_{nk}^{(p+1)}(0). \quad (41)$$

We demand that the sum of the magnitude of the coefficients of order  $p+1$  should be smaller than the corresponding sum

of order  $p$ ,

$$\sum_n \sum_m \frac{|b_{nm}^{(p+1)}(s)|}{T^{p+1}} \ll \sum_n \sum_m \frac{|b_{nm}^{(p)}(s)|}{T^p}. \quad (42)$$

In Appendix C, we insert Eqs. (40) and (41) into Eq. (42) and get the following adiabatic convergence criteria:

$$\frac{\Omega_{\eta}(x_{\text{opt}}(s)^2 + 1)^{\frac{\eta-1}{2}}}{T \Delta_{10}(s)} \ll 1, \quad (43)$$

$$\frac{|M_{10}(s)|}{T \Delta_{10}(s)} \ll 1, \quad (44)$$

$$\int_0^s \Omega_{\eta}(x_{\text{opt}}(s')^2 + 1)^{\frac{\eta-1}{2}} \frac{|M_{10}(s')|}{T \Delta_{10}(s')} ds' \ll 1, \quad (45)$$

$$\int_0^s \frac{|M_{10}(s')|^2}{T \Delta_{10}(s')} ds' \ll 1. \quad (46)$$

Notice that Eq. (44) is identical to the usual adiabatic condition in Eq. (16). Furthermore, Eqs. (44) and (46) correspond to the conditions found in the first-order coefficients in Eqs. (38) and (39). Our extended analysis in Appendix C have thus provided two additional conditions to satisfy adiabaticity, Eqs. (43) and (45). The additional conditions come from terms in Eqs. (40) and (41) which do not appear when computing the first-order coefficients but become relevant in higher-order ones.

In the regime  $|x_{\text{opt}}(s)| \sim 1$ , the conditions (43)–(46) result in  $\Omega_{\eta}/(Tw) \ll 1$ , which gives the lower bound  $\eta > 1$  as discussed above. For large  $|x_{\text{opt}}(s)|$ , the convergence of the integral in Eq. (45) gives the upper bound  $\eta < 3$  which was the same as in the conditions (39) and (44). Importantly, the first condition (43) gives a further restriction for large  $|x_{\text{opt}}(s)|$ ,

$$\frac{\Omega_{\eta}}{Tw} x_0^{\eta-2} \ll 1. \quad (47)$$

This is the final restriction on  $\eta$  and gets us the bound for optimal operation time  $Tw \gg 1$ ,

$$1 < \eta \leq 2. \quad (48)$$

We note that both the linear energy sweep ( $\eta = 0$ ) and the best adiabatic path ( $\eta = 5/2$ ) predicted by the first-order correction in Eq. (35) lie outside the optimal range.

To make an unified statement about the proper dimensionless expansion parameter, we define a quantity closely related to  $\Omega_\eta$ , including the scaling for  $\eta > 2$ ,

$$\Sigma_\eta = \begin{cases} \Omega_\eta x_0^{\eta-2} & \text{for } \eta > 2, \\ \Omega_\eta & \text{for } \eta \leq 2. \end{cases} \quad (49)$$

We thus propose  $\Sigma_\eta/(Tw)$  as the proper dimensionless expansion parameter, fulfilling  $\Sigma_\eta/(Tw) \ll 1$  for APT to hold. This expansion parameter depends in a nontrivial way on  $w$  and  $\varepsilon_0$  and the chosen path parametrized by  $\eta$ .

APT predicts that the fastest adiabatic path is the solution to Eq. (36) for  $\eta = 2$ , which minimizes the dimensionless expansion parameter  $\Sigma_{\eta=2}/(Tw) = \pi/(Tw)$ , see left panel of Fig. 3. For  $\eta = 2$ , the solution to Eq. (36) has a particularly simple expression given by

$$x_{\text{opt}}(s) = \pm \tan[\arctan(x_0)(2s - 1)]. \quad (50)$$

This result realizes the so-called local adiabatic evolution of the system [29–31]. In Fig. 3, the optimal sweep ( $\eta = 2$ ) is compared to a linear sweep ( $\eta = 0$ ). The ratio  $\Sigma_{\eta=0}/\Sigma_{\eta=2} \approx 2x_0/\pi$  quantifies how much faster the optimal sweep of  $x_{\text{opt}}(s)$  can be with respect to a linear one. This means that, for the same parameters, the ideal sweep is  $\approx 64$  times faster than the linear one for  $x_0 = 100$ . The intuition is that the charge is exchanged at a nearly constant rate for  $\eta = 2$ , see middle panel of Fig. 3. However, the system spends most of the time in a region where no charge is transferred for  $\eta = 0$ . Finally, using Eq. (36), we compute the relative dynamical phase considered in Sec. II A to first order in  $\sin(2\theta)\sin(\phi/2)$  and in the limit  $x_0 \gg 1$ ,

$$\begin{aligned} \theta^D &= -T \int_0^1 (E_-^+(s) - E_-^-(s)) ds, \\ &= -\sin(2\theta)\sin(\phi/2) \frac{\sqrt{\pi}\Gamma(\frac{\eta}{2}) Tw}{\Gamma(\frac{\eta+1}{2}) \Omega_\eta}. \end{aligned} \quad (51)$$

This equation describes a decreasing undesired dynamical phase when  $\eta$  increases. This further motivates the choice  $\eta = 2$  for the charge-transfer process.

We conclude this section by outlining the presented framework for finding fast adiabatic paths while checking adiabatic conditions. The method can be broken down into the following five steps:

- (1) Write down the first-order corrections using APT, Eqs. (27)–(30).
- (2) From the first-order coefficients, choose a relevant functional, Eqs. (34) and (35), and minimize it.
- (3) Extend the family of considered paths by parametrizing the minimizing differential equation, Eq. (36).
- (4) Check the adiabatic conditions, constraining the parameters, Eqs. (37) and (40)–(48).
- (5) Choose the set of parameters that minimizes the proper dimensionless expansion parameter, Eq. (49). The path obtained through this procedure, Eq. (50), is the optimal adiabatic one for the family considered in step 3.

This procedure thus provides an optimal adiabatic path, taking into account nonadiabatic corrections. The framework is general and may be used to find fast adiabatic paths in other systems. Future efforts may also expand the framework to include degenerate quantum systems [55].

In general, higher time-derivatives of the Hamiltonian at  $s = 0$  and  $s = 1$  can lead to additional nonadiabatic contributions not captured by APT. We have not considered these effects as they appear to play a minor role due to the large initial and final energy gaps between the ground and excited states. In the case where these gaps are comparable to other energy scales in the system, the contributions from the higher time derivatives of the Hamiltonian can have some influence in the result. In this case, boundary cancellation techniques can be used to reduce such contributions [56]. Finally, we would like to mention the existence of methods exploiting symmetry to improve the error scaling [44,57]. It may further reduce the timescale of the charge-transfer process.

### III. NUMERICAL RESULTS

In this section, we test the predictions of APT numerically. We show that the dimensionless expansion parameter  $\Sigma_\eta/(Tw)$  describes the adiabatic condition. We pick an optimal path based on the APT prediction, which minimizes the operation timescale and the nonadiabatic errors. We simulate numerically the protocol with and without the flux echo. We find that the echo protocol substantially extends the parameter space where MBS non-Abelian properties can be shown using charge-transfer operations.

In the left panel of Fig. 4, we display the probability of transitioning to the excited state,  $\Pi$ , as a function of  $\eta$  and the inverse operation time,  $(Tw)^{-1}$ . We show results after a single charge-transfer operation in the case where the even and odd parity sectors are degenerate. As expected, the transition probability to the excited state decreases when the operation time increases. The white line is a contour of the dimensionless expansion parameter,  $\Sigma_\eta/(Tw) = 2$ . As suggested from APT, the dimensionless expansion parameter separates well the adiabatic (suppressed  $\Pi$  region below the line) and the nonadiabatic regimes (larger  $\Pi$  region above the line). APT agrees quantitatively with the numerical calculations for  $\eta \leq 2$ . For  $\eta > 2$ , the contour avoids the regions of nonzero transition probability in the lower right corner. In this region outside of the APT regime, the system behavior is nonmonotonic, as shown by the local  $\Pi$  maxima as a function of the operation time. In Appendix C, we further discuss the APT prediction at  $\eta > 2$ .

The solid cyan line, given by  $\Sigma_\eta/(Tw) = 0.5$ , lies in the adiabatic region, where charge-transfer operations can be done with high accuracy. In the right panel of Fig. 4, we show the relative phase between the even and odd ground states after a single charge transfer operation following the cyan line in the left panel for  $\phi = 0.05\pi$ . For charge-transfer operations, small deviations from the ideal conditions can lead to a significant relative dynamical phase as illustrated by the difference between the dashed (ideal result) and the solid lines. The agreement between the numerical result and APT is good, except close to  $\eta = 0$ . This is due to the approximation  $x_0 \rightarrow \infty$  when computing  $\theta^D$  in Eq. (51).

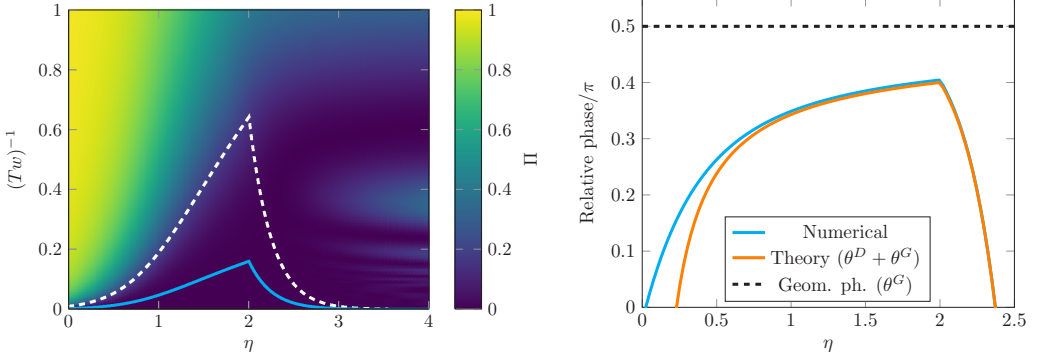


FIG. 4. Numerical results for a charge-transfer process with  $\theta = \pi/4$  and  $x_0 = 100$ . (Left) Color map of the transition probability after a single charge-transfer operation at the degeneracy point ( $\phi = 0$ ) as a function of  $\eta$  and the inverse time  $(Tw)^{-1}$ . The two lines represent the prediction from APT for  $\Sigma_\eta/(Tw) = 2$  (dashed white) and  $\Sigma_\eta/(Tw) = 0.5$  (solid cyan). For  $\eta \leq 2$ , the dashed white line separates the adiabatic region (dark blue) from the nonadiabatic region (green and yellow). The solid cyan line lies well in the adiabatic region and is used for reference to the right panel. (Right) Plot of the relative phase for a slight detuning  $\phi = 0.05\pi$  from the ideal phase ( $\phi = 0$ ) following the cut at the solid cyan line in the left panel ( $\Sigma_\eta/(Tw) = 0.5$ ). We display the numerical result (cyan), theoretical prediction (orange) and the geometric phase (dashed) for reference to the ideal situation.

Combining the results obtained by the numerically simulated charge-transfer operations, we conclude that  $\Sigma_\eta/(Tw) \simeq 0.5$  and  $\eta = 2$  are the best values, as suggested by APT. As for realistic parameters, we assume that the induced superconducting gap is  $\Delta_{SC} = 0.1$  meV. To avoid transitioning to the continuum of states, we take  $\varepsilon_0 = 0.5 \Delta_{SC} = 50 \mu\text{eV}$ . Using a value of  $x_0 = \varepsilon_0/(2w) = 100$ , we get  $w = 0.25 \mu\text{eV}$  and  $T \approx 17$  ns. It is thus possible to perform fast adiabatic charge-transfer operations on the  $\sim 10$  ns scale. The transition probability for these parameters is  $\Pi < 10^{-5}$ . Using the same parameters, but with a linear sweep ( $\eta = 0$ ), the corresponding timescale is approximately  $1 \mu\text{s}$  with similar transition probability. Previous experiments have shown that parity lifetime in trivial superconducting islands are  $\sim 1 \mu\text{s}$  [58], illustrating that it might not be possible to perform accurate operations using a linear sweep.

Using the optimal path found,  $\Sigma_\eta/(Tw) = 0.5$  and  $\eta = 2$ , we simulate the protocols described in Sec. II B to demonstrate MBS non-Abelian properties. The results are shown in Fig. 5. Here we make color maps of the sequence visibility  $\Lambda$  as a function of  $\phi$  and the coupling asymmetry  $\cos^2\theta$ . As explained around Eq. (13),  $\Lambda$  measures how well the sequences in Eqs. (9)–(12) can be distinguished by the measured parity of the M12 fermion. It thus quantifies the confidence of demonstrating non-Abelian properties. Here,  $\Lambda = \pm 1$  means that the parity of M12 fermion can distinguish between the two sets of operations, while the protocol fails for  $\Lambda = 0$ .

In the top left panel of Fig. 5, we display numerical results for the visibility for the protocol without the echo. Note that the optimal parameter values  $\theta = \pi/4$  and  $\phi = 0$  lie at the central yellow sliver with maximal visibility. The narrow width ( $\approx 0.1\pi$ ) of this high-visibility region is due to the contribution of the dynamical phase and illustrates the importance of accurately tuning  $\phi$ . It appears less important to tune the coupling asymmetry  $\theta$ . In Appendix D, we display the sequence visibility for different  $T$  values to show that the width

of the high-visibility regions decreases as  $T$  is increased. The top left panel should be compared to the numerical results for the echo protocol displayed in the top right panel. Here the central yellow region is significantly extended due to the cancellation of the dynamical phase, making the experiment rather insensitive to  $\phi$ . The outcome is also insensitive to  $T$ , as shown in Appendix D. The echo protocol, however, depends on tuning  $\phi \rightarrow \phi + \delta\phi$  with  $\delta\phi = 2\pi$  ideally and is thus robust to drifts in  $\phi$ . In Appendix E, we offset the parameter  $\delta\phi$  and find that the echo protocol is robust up to deviation of  $\sim 0.2\pi$  in  $\delta\phi$ . For completeness, we show the probability to end up in the state  $|0\rangle_{M12}$  after each sequence in Appendix F.

In the bottom panels of Fig. 5, we display the visibility obtained from APT, in good agreement with the numerical results shown in the top row panels. However, there is a discrepancy in the region  $\sin(2\theta)\sin(\phi/2) \sim 1$ . The disagreement between theory and the numerical results is due to the closing of the gap between the ground and the excited states as  $w\sqrt{1-\rho}\sin(2\theta)\sin(\phi/2)$ , Eq. (3). This results in transitions and large nonadiabatic errors to the phase in that region.

#### IV. CONCLUSIONS AND DISCUSSIONS

In this work, we have proposed a minimal experiment for demonstrating Majorana non-Abelian properties. The experiment requires three Majorana bound states (MBSs), the minimal number to measure non-Abelian signatures. Our proposal is based on charge-transfer operations between a quantum dot and two MBSs. Another quantum dot is used for the initialization and readout. We also devise a minimal protocol relying on two sequences of three adiabatic charge-transfer operations. The final result depends on the order of operations due to Majorana non-Abelian properties.

We study the robustness of the protocol as a function of the model parameters, taking into account nonadiabatic effects.

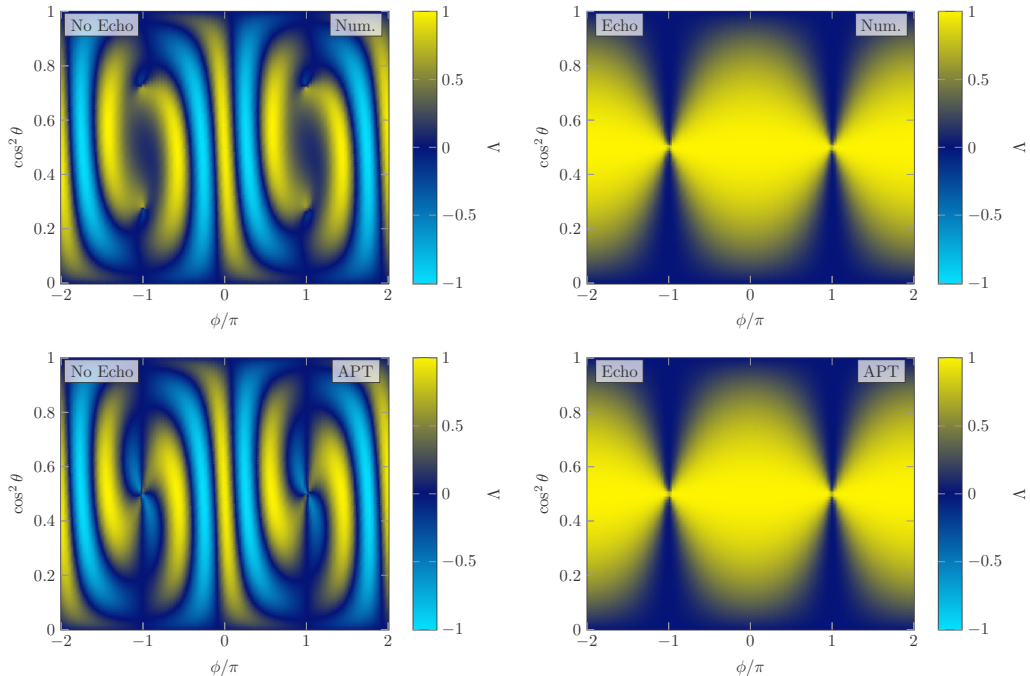


FIG. 5. Sequence visibility, Eq. (13), as a function of the initial detuning  $\phi$  and the coupling strength asymmetry  $\cos^2\theta$ . We compare numerical simulations of the protocol proposed in Sec. II B (top panels) and APT predictions (bottom panels). We show results with (right panels) and without the flux echo protocol (left panels).

To this end, we develop a framework based on adiabatic perturbation theory (APT) for finding fast adiabatic paths in nondegenerate quantum systems. This framework describes the optimal adiabatic energy sweep for the charge-transfer operation. We find that the experiment is sensitive to the SC phase difference,  $\phi$ . Small deviations,  $\sim 0.05\pi$  from the degeneracy point ( $\phi = 0$ ) lead to a substantial dynamical phase that can dominate over the non-Abelian signal. To solve this issue, we propose a flux echo protocol that significantly reduces the sensitivity on  $\phi$ . The flux echo relies on increasing the superconducting phase difference by  $2\pi$  between subsequent operations, exploiting the  $4\pi$  periodicity of the topological state. The tolerance on the additional phase is  $\sim 0.2\pi$ , while the outcome of the protocol is insensitive to the operation time and robust to drifts in  $\phi$ .

Since our proposal relies on parameter space operations rather than real space braiding, it is relevant to discuss the uniqueness of the MBS signature in the proposed experiment. A system hosting trivial subgap states may also acquire geometric and dynamical phases during charge-transfer operations. As a result, charge-transfer operations might not commute, leading to potentially large  $\Lambda$  values for some parameters. However, the flux echo, exploiting MBSs  $4\pi$ -periodicity, leads to a robust non-Abelian signal over a wide

range of parameters. This is in contrast to trivial bound states, which are  $2\pi$ -periodic, where large  $\Lambda$  values only appear at fine-tuned situations due to the dynamical phase. Other than trivial states, the experiment might also suffer from various sources of error that can lead to a reduction of the non-Abelian signal. First, fluctuations in the superconducting phase difference will introduce a random phase. However, the flux echo protocol reduces their effect if the operations are faster than the timescale of phase fluctuation. Second, the coupling between MBSs will split the ground state degeneracy introducing a constraint on the upper limit for the charge-transfer operations. However, as shown in Ref. [12], this effect is likely not a limiting factor. Additionally, quasiparticle poisoning is detrimental to the experiment and its timescale should therefore be longer than that of the experiment. Finally, nonzero temperature and electric fluctuations in the gates will reduce the non-Abelian signal. In these cases, the tunnel coupling strength should be larger than the temperature and electric variations. Also, the optimal path found, minimizing the operation timescale reduces their impact.

#### ACKNOWLEDGMENTS

This research was supported by the Danish National Research Foundation, the Danish Council for Independent



Research | Natural Sciences. This project has received funding from the European Research Council (ERC) under the European Union’s Horizon 2020 research and innovation programme under Grant Agreement No. 856526. We acknowledge support from the Deutsche Forschungsgemeinschaft (DFG)—project grant 277101999—within the CRC network TR 183 (subproject C03). R.S.S. acknowledges funding from QuantERA project “2D hybrid materials as a platform for topological quantum computing” and from NanoLund.

#### APPENDIX A: THE GEOMETRIC PHASE

There is a technical subtlety when computing the relative geometric phase in Eq. (5): a single charge-transfer process does not constitute a loop in parameter space. It makes difficult to determine the acquired geometrical phase. We instead compare the geometric phases collected by the even and odd ground states during a charge-transfer process. However, the even and odd parity ground states live in different Hilbert spaces. Since there is a clear one-to-one mapping between these two spaces, we treat the ground state vectors as living in the same Hilbert space.

The gauge choice in Eq. (4) is such that for each parity, there is no mathematical contribution to the geometric phase when changing  $\varepsilon_2 : \varepsilon_0 \rightarrow -\varepsilon_0$  in time  $T$ ,

$$i \int_0^T dt (\psi_-^\rho)^\dagger \frac{d\psi_-^\rho}{dt} = 0. \quad (\text{A1})$$

This is easy to see as the ground states have the form  $(\psi_-^\rho)^\dagger = (e^{i\varepsilon} \cos(\lambda(t)), \sin(\lambda(t)))$ . The gauge choice in Eq. (4), however, is different for the two parity sectors and this gives a relative geometric phase between the even and odd parity ground states. To compute this relative geometric phase contribution, we evaluate the phase difference between the ground states using  $\arctan[\frac{\Im(\psi_-^\rho)^\dagger \cdot \psi_-^\rho}{\Re(\psi_-^\rho)^\dagger \cdot \psi_-^\rho}]$  and compare the results at initial and final values of the level energy. This calculation leads to the result in Eq. (5).

The relative geometric phase can also be understood as a proper loop in parameter space by noticing that the even and odd parity Hamiltonian and eigenvectors can be transformed into each other by  $\theta \rightarrow -\theta$ . We can thus compute the relative geometric phase by considering the loop  $\varepsilon_0 \rightarrow -\varepsilon_0, \theta \rightarrow -\theta, -\varepsilon_0 \rightarrow \varepsilon_0, -\theta \rightarrow \theta$ . This can be understood as performing a charge-transfer operation in the even parity state, inverting  $\theta$  to transform it to the odd parity state. We then perform another operation and invert again the sign of  $\theta$  to return to the even subspace. The geometric phase due to this loop corresponds to the relative geometric phase acquired between the even and odd parity ground states due to a single charge-transfer process. There is no contribution to the geometric phase for large negative level energies as the ground states become  $(\psi_-^\rho)^\dagger = (0, -1)$  in this limit. At the other side of the loop, where the level energy has a large positive value, the ground states are  $(\psi_-^\rho)^\dagger = (w^\rho/w^\rho, 0)$ . Using the gauge in Eq. (4) no geometrical phase is acquired by the system when varying  $\varepsilon_2$ . The relative geometric phase is given by

$$\theta^G = i \int_{-\theta}^{\theta} d\theta' (\psi_-^\rho)^\dagger \frac{d\psi_-^\rho}{d\theta'}, \quad (\text{A2})$$

in the limit of large positive level energies. This approach provides an alternative picture of how to calculate the geometric phase, but mathematically it is tedious to carry out. Performing the integration in Eq. (A2) and evoking the identity

$$2 \arctan(\tan(x) \cos(y)) = \arctan\left(\frac{\tan x}{\cos y} - \frac{\tan y}{\cos x}\right) + \arctan\left(\frac{\tan x}{\cos y} + \frac{\tan y}{\cos x}\right), \quad (\text{A3})$$

we arrive at Eq. (5).

#### APPENDIX B: SOLUTION IN TERMS OF THE GAUSSIAN HYPERGEOMETRIC FUNCTION

For a symmetric charge-transfer following:

$$\dot{x}_{\text{opt}}(s) = \pm \Omega_\eta [x_{\text{opt}}(s)^2 + 1]^{n/2}, \quad (\text{B1})$$

the solution is

$$\pm \Omega_\eta (s - 1/2) = x_{\text{opt}}(s) {}_2F_1\left(\frac{1}{2}, \frac{\eta}{2}; \frac{3}{2}; -x_{\text{opt}}(s)^2\right), \quad (\text{B2})$$

where the Gaussian hypergeometric function is defined by

$${}_2F_1(a, b; c; z) = \frac{\Gamma(c)}{\Gamma(a)\Gamma(b)} \sum_n \frac{\Gamma(a+n)\Gamma(b+n)}{\Gamma(c+n)!} z^n, \quad |z| < 1. \quad (\text{B3})$$

The initial and final conditions determine  $\Omega_\eta$ ,

$$\Omega_\eta = 2x_0 {}_2F_1\left(\frac{1}{2}, \frac{\eta}{2}; \frac{3}{2}; -x_0^2\right). \quad (\text{B4})$$

To get the approximation for large  $x_0$  in Eq. (37), we use the transformation rule

$${}_2F_1(a, b; c; z) \quad (\text{B5})$$

$$= \frac{\Gamma(c)\Gamma(b-a)}{\Gamma(b)\Gamma(c-a)} (-z)^{-a} {}_2F_1(a, a-c+1; a-b+1; 1/z) \quad (\text{B6})$$

$$+ (a \leftrightarrow b), \quad \text{for } |\arg(-z)| < \pi. \quad (\text{B7})$$

#### APPENDIX C: DERIVING ADIABATIC CONDITIONS

In this section, we derive the adiabatic conditions, Eqs. (43)–(46) in the main text, starting from Eqs. (40)–(42). We omit in the following the time variable for simplicity.

In Eq. (42), we split the left-hand side term into contributions from  $n = m$  and  $n \neq m$ ,

$$\sum_n \sum_m \frac{|b_{nm}^{(p+1)}|}{T^{p+1}} = \sum_n \left( \sum_{m \neq n} \frac{|b_{nm}^{(p+1)}|}{T^{p+1}} + \frac{|b_{nn}^{(p+1)}|}{T^{p+1}} \right). \quad (\text{C1})$$

The condition (42) is satisfied if each term is individually smaller than its right-hand side,

$$\sum_n \sum_{m \neq n} \frac{|b_{nm}^{(p+1)}|}{T^{p+1}} \ll \sum_n \sum_m \frac{|b_{nm}^{(p)}|}{T^p}, \quad (\text{C2})$$

$$\sum_n \frac{|b_{nn}^{(p+1)}|}{T^{p+1}} \ll \sum_n \sum_m \frac{|b_{nm}^{(p)}|}{T^p}. \quad (\text{C3})$$

We study these two cases separately. We begin with the  $n \neq m$  case, substituting Eq. (40) in Eq. (C2)

$$\begin{aligned} & \sum_n \sum_{m \neq n} \frac{|b_{nm}^{(p+1)}|}{T^{p+1}} \\ &= \sum_n \sum_{m \neq n} \left| \frac{i}{T \Delta_{nm}} \frac{d}{ds} \frac{b_{nm}^{(p)}}{T^p} + \sum_{k \neq n} \frac{i M_{nk}}{T \Delta_{nm}} \frac{b_{km}^{(p)}}{T^p} \right| \quad (\text{C4}) \\ &\leq \sum_n \sum_{m \neq n} \left( \frac{1}{T |\Delta_{nm}|} \left| \frac{d}{ds} \frac{b_{nm}^{(p)}}{T^p} \right| + \sum_{k \neq n} \frac{|M_{nk}|}{T |\Delta_{nm}|} \frac{|b_{km}^{(p)}|}{T^p} \right). \quad (\text{C5}) \end{aligned}$$

Again, the condition (42) is satisfied if each term fulfills

$$\sum_n \sum_{m \neq n} \frac{1}{T |\Delta_{nm}|} \left| \frac{d}{ds} \frac{b_{nm}^{(p)}}{T^p} \right| \ll \sum_n \sum_m \frac{|b_{nm}^{(p)}|}{T^p}, \quad (\text{C6})$$

$$\sum_n \sum_m \left( \sum_{k \neq n, m} \frac{|M_{nk}|}{T |\Delta_{mk}|} \right) \frac{|b_{nm}^{(p)}|}{T^p} \ll \sum_n \sum_m \frac{|b_{nm}^{(p)}|}{T^p}, \quad (\text{C7})$$

where we have relabelled the sums. Similarly, by substituting Eq. (41) to the left-hand side of Eq. (C3) and considering each term separately, we get

$$\sum_n \sum_{m \neq n} \int_0^s \frac{|M_{nm}|}{T |\Delta_{nm}|} \left| \frac{d}{ds'} \frac{b_{nm}^{(p)}}{T^p} \right| ds' \ll \sum_n \sum_m \frac{|b_{nm}^{(p)}|}{T^p}, \quad (\text{C8})$$

$$\sum_n \sum_m \int_0^s \left| \sum_{k \neq n, m} \frac{M_{mk} M_{kn}}{T \Delta_{mk}} \right| \frac{|b_{nm}^{(p)}|}{T^p} ds' \ll \sum_n \sum_m \frac{|b_{nm}^{(p)}|}{T^p}, \quad (\text{C9})$$

$$\sum_n \sum_{m \neq n} \frac{|b_{nm}^{(p+1)}(0)|}{T^{p+1}} \ll \sum_n \sum_m \frac{|b_{nm}^{(p)}|}{T^p}. \quad (\text{C10})$$

Note that the last of these conditions is included in Eq. (C2).

We first focus on Eqs. (C7) and (C9), which are the simplest inequalities. They are satisfied for

$$\sum_{k \neq n, m} \frac{|M_{nk}|}{T |\Delta_{mk}|} \ll 1, \quad (\text{C11})$$

$$\int_0^s \left| \sum_{k \neq n, m} \frac{M_{mk} M_{kn}}{T \Delta_{mk}} \right| ds' \ll 1. \quad (\text{C12})$$

For a two level system as the one considered in Sec. IID, Eqs. (C11) and (C12) results in the conditions in Eqs. (44) and (46).

To continue with Eqs. (C6) and (C8), we need to understand how  $db_{nm}^{(p)}/ds$  relates to  $b_{nm}^{(p)}$  for  $n \neq m$ . For that, we restrict ourselves to the example of a two level system, Eq. (2). In the following, we make an argument based on induction for the approximation

$$\left| \frac{d}{ds} b_{nm}^{(p)} \right| \sim \Omega_\eta (x^2 + 1)^{\frac{\eta-1}{2}} |b_{nm}^{(p)}| \quad n \neq m. \quad (\text{C13})$$

The argument relies on the basic observation that all operators  $\Delta_{10}$ ,  $M_{10}$  and  $d/ds = \dot{x}(\partial\sqrt{x^2+1}/\partial x) \partial/\partial\sqrt{x^2+1}$ , used to compute the coefficients  $b_{nm}^{(p)}$ , are polynomial in  $\sqrt{x^2+1}$  with

rational exponents, see Eqs. (31), (32), and (36). We begin the argument by checking that Eq. (C13) holds for the first-order coefficients found in Sec. IIC. Taking the derivative of the only  $n \neq m$ , nonconstant, first-order coefficient, we get

$$\left| \frac{d}{ds} b_{10}^{(1)} \right| = \Omega_\eta (x^2 + 1)^{\eta/2} \left| \frac{\partial\sqrt{x^2+1}}{\partial x} \right| \left| \frac{\partial(M_{10}/\Delta_{10})}{\partial\sqrt{x^2+1}} \right|. \quad (\text{C14})$$

Since  $\Delta_{10}$  and  $M_{10}$  are polynomials in  $\sqrt{x^2+1}$ , we make the assertion

$$\left| \frac{\partial(M_{10}/\Delta_{10})}{\partial\sqrt{x^2+1}} \right| = |3 - \eta| \frac{|M_{10}/\Delta_{10}|}{\sqrt{x^2+1}} \quad (\text{C15})$$

$$\sim \frac{|M_{10}/\Delta_{10}|}{\sqrt{x^2+1}} = \frac{|b_{10}^{(1)}|}{\sqrt{x^2+1}}. \quad (\text{C16})$$

Combining this with Eq. (C14) and dropping  $|\partial\sqrt{x^2+1}/\partial x|$  as it is unimportant, we conclude that  $b_{10}^{(1)}$  fulfills Eq. (C13). To complete the induction, we show that if the coefficients of order  $p$  fulfill Eq. (C13), then also the  $p+1$  order coefficients should fulfill Eq. (C13). We rewrite Eq. (40) using the hypothesis in Eq. (C13),

$$\begin{aligned} b_{nm}^{(p+1)} &\sim \frac{i\Omega_\eta (x^2 + 1)^{\frac{\eta-1}{2}}}{\Delta_{nm}} b_{nm}^{(p)}(s) \\ &+ \sum_{k \neq n, m} \frac{iM_{nk}(s)}{\Delta_{nm}(s)} b_{km}^{(p)} + \frac{iM_{nm}(s)}{\Delta_{nm}(s)} b_{nm}^{(p)}. \quad (\text{C17}) \end{aligned}$$

This equation consists of polynomials in  $\sqrt{x^2+1}$  and  $n \neq m$  coefficients of order  $p$ , which by the hypothesis fulfills Eq. (C13). Therefore also the coefficients of order  $p+1$  obeys Eq. (C13). The only exception in Eq. (C17) is the last term with the  $n = m$  coefficient. However, for large  $|x|$ , this coefficient is almost constant as the tails of the integrals are very close to zero and it is unimportant. For  $|x| \sim 1$ , all of the  $p$ -order coefficients are of the same magnitude,  $(\Omega_\eta/w)^p$ , and thus the coefficient of order  $p+1$  still fulfills Eq. (C13). This completes the argument.

A heuristic argument that leads to the same scaling behavior for large  $x$  is that whatever  $d/ds = \dot{x}d/dx$  acts on, gets multiplied by  $\dot{x}$  while a power of  $x$  gets subtracted from the differentiation  $d/dx$ .

We may now use Eq. (C13) to rewrite Eqs. (C6) and (C8) and extract the corresponding adiabatic conditions:

$$\frac{\Omega_\eta (x^2 + 1)^{\frac{\eta-1}{2}}}{T |\Delta_{nm}|} \ll 1 \quad n \neq m, \quad (\text{C18})$$

$$\int_0^s \Omega_\eta (x^2 + 1)^{\frac{\eta-1}{2}} \frac{|M_{nm}|}{T |\Delta_{nm}|} ds' \ll 1 \quad n \neq m. \quad (\text{C19})$$

That is, if Eqs. (C18) and (C19) are satisfied, then also Eqs. (C6) and (C8) are satisfied. By inserting  $\Delta_{10}$  and  $M_{10}$  we arrive at the conditions in Eqs. (43) and (45).

As a final remark, we discuss the APT prediction for  $\eta > 2$ . The conditions in Eqs. (43) and (C18), that gives the APT prediction for  $\eta > 2$ , rely on Eq. (C13) whose proof is somewhat heuristic. The APT prediction for  $\eta > 2$  is therefore approximated but still required to achieve adiabaticity as

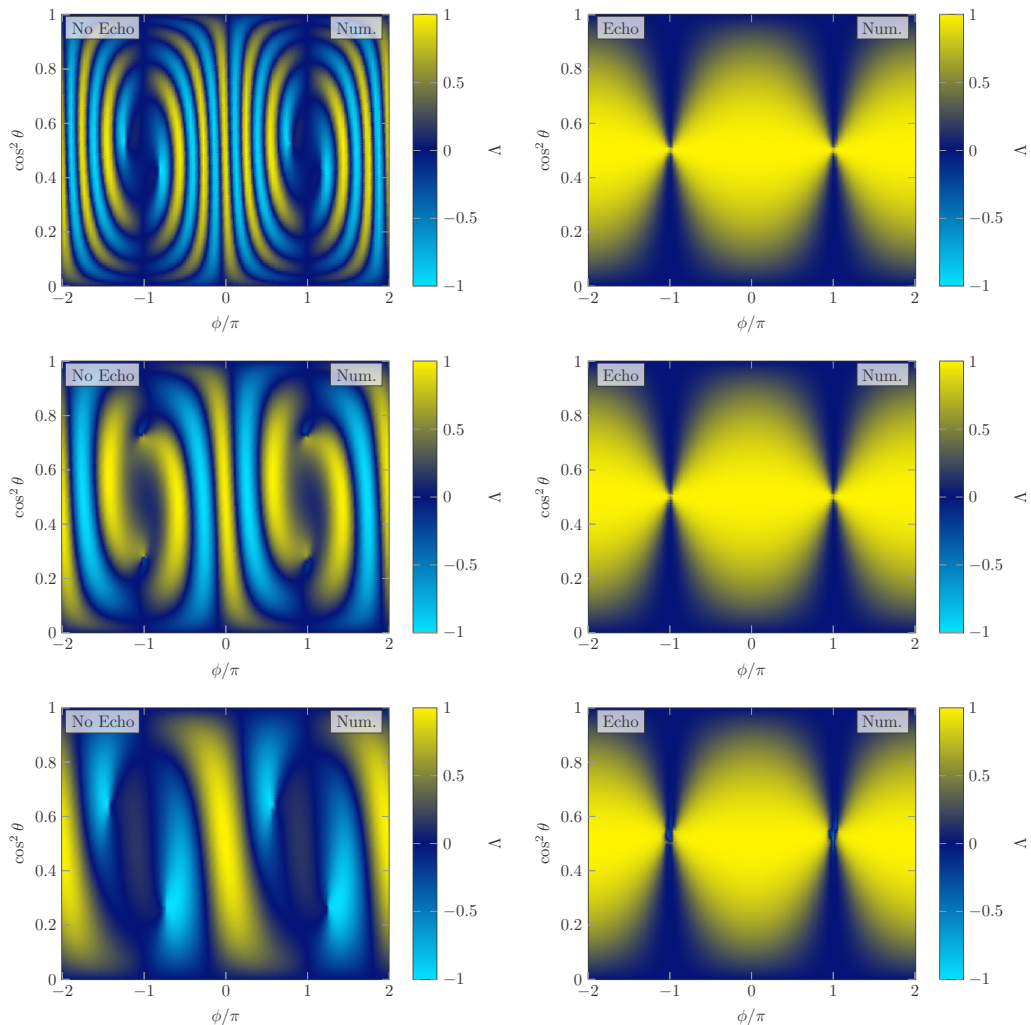


FIG. 6. Sequence visibility  $\Lambda$  obtained from numerical simulation with  $x_0 = 100$  and  $\eta = 2$ . The dimensionless expansion parameter is varied from top to bottom:  $\Sigma_\eta/(T\omega) = 0.25, 0.5,$  and  $1$ .

shown in Fig. 4. The conditions in Eqs. (43) and (C18) are important to ensure that higher-order contributions in the adiabatic expansion do not grow with the order. These conditions do not appear in the first-order coefficients. It may therefore be possible to relax the requirement in Eq. (42), replacing the  $\ll$  with  $<$ , while still requiring that the first-order coefficients are small. Convergence of the adiabatic expansion in Eq. (17) is then ensured by the geometric series. This would relax the condition for adiabaticity in the region  $2 < \eta \leq 3$  from  $\Omega_\eta/(T\omega) \ll x_0^{\eta-2}$  to  $\Omega_\eta/(T\omega) < x_0^{\eta-2}$ . The other conditions in Eqs. (44) and (46) would still be in effect.

#### APPENDIX D: SEQUENCE VISIBILITY AT DIFFERENT TIMESCALES

In Fig. 6, we display the sequence visibility from numerical simulation for different values of the dimensionless expansion parameter. We show results for decreasing  $T$  values from top to bottom. The panels in the left column show the protocol without the flux echo. Since this protocol is sensitive to the dynamical phase, we observe an increased number of fringes in the top left panel where the operation time is slower. In the bottom left panel, we see fewer fringes but also distortions due to nonadiabatic errors. In the right column,



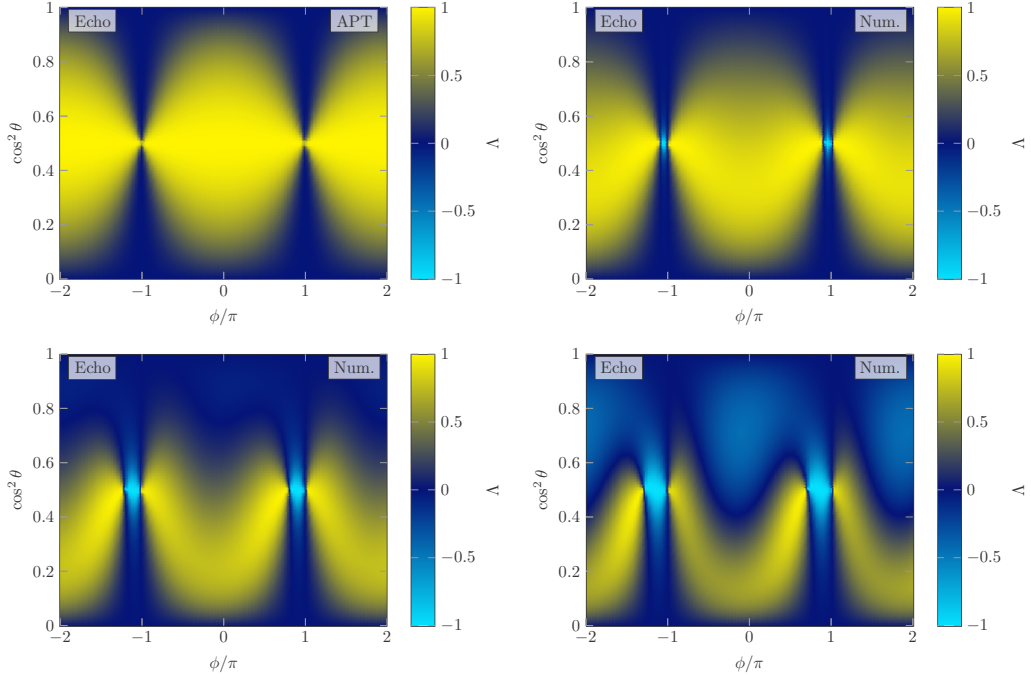


FIG. 7. Sequence visibility  $\Lambda$  obtained from numerical simulation with parameters  $x_0 = 100$ ,  $\Sigma_\eta/(Tw) = 0.5$ , and  $\eta = 2$  for the echo protocol. The additional phase  $\delta\phi$  used is varied from top left to bottom right with increasing offset from the ideal point:  $\delta\phi = 2\pi$ ,  $1.05 \times (2\pi)$ ,  $1.1 \times (2\pi)$ , and  $1.15 \times (2\pi)$ .

we show results for the flux echo protocol that cancels out the contribution from the dynamical phase. For this reason, we only see the contribution from the geometric phase which is insensitive to the time of operation as long as it is adiabatic.

The number of fringes  $\nu$  in the left column panels can be theoretically estimated. For symmetric couplings,  $\theta = \pi/4$ , the sequence visibility simply becomes

$$\Lambda = \cos(2\theta^D) \quad (\text{D1})$$

$$= \cos\left(\frac{2\sqrt{\pi}\Gamma(\frac{\eta}{2})}{\Gamma(\frac{\eta+1}{2})} \frac{Tw}{\Omega_\eta} \sin(\phi/2)\right). \quad (\text{D2})$$

The number of fringes can then be counted by the number of times  $\Lambda$  is  $\pm 1$ . In the region  $-\pi < \phi < \pi$ , the number of fringes is well-approximated by

$$\nu = 2 \left\lfloor \frac{2\Gamma(\frac{\eta}{2})}{\sqrt{\pi}\Gamma(\frac{\eta+1}{2})} \frac{Tw}{\Omega_\eta} \right\rfloor + 1, \quad (\text{D3})$$

for the optimal path found in this paper. Here,  $\lfloor \cdot \rfloor$  is the floor function. In agreement with the left column in Fig. 6, Eq. (D3) predicts 11, 5, and 3 fringes for the top, middle, and bottom panels.

#### APPENDIX E: ROBUSTNESS OF FLUX ECHO

In Fig. 7, we display the sequence visibility  $\Lambda$  for the echo protocol at different values of the additional SC phase  $\phi \rightarrow \phi + \delta\phi$ . In the top left panel, we show the ideal situation of  $\delta\phi = 2\pi$ . In top right and bottom panels, we tune slightly away from the optimal point ( $\delta\phi = 2\pi$ ) by 5%, 10%, and 15%. A 5% offset, as shown in the top right panel, still results in a large region in parameter space with good visibility. At a 10% offset, as shown in the bottom left panel, the region size and visibility is slightly reduced and shifted to nonzero coupling asymmetry. However, even for 10% error in  $\delta\phi$ , a high visibility can be reached by tuning  $\theta$ , which gives the ratio between  $w_3$  and  $w_4$ . At 15% offset, as shown in the bottom right panel, the dynamical phase plays a significant role and reduces the visibility.

#### APPENDIX F: MEASUREMENT SIGNATURE FOR EACH SEQUENCE

In Fig. 8, we resolve the sequence visibility into the specific probabilities after each sequence. We display the probability  $\kappa$  to end up in the  $|0\rangle_{M12}$  state. In the top panels, we show  $\kappa$  for sequences A and B. Besides weak nonadiabatic corrections, sequence A only gets contributions from the dynamical phase

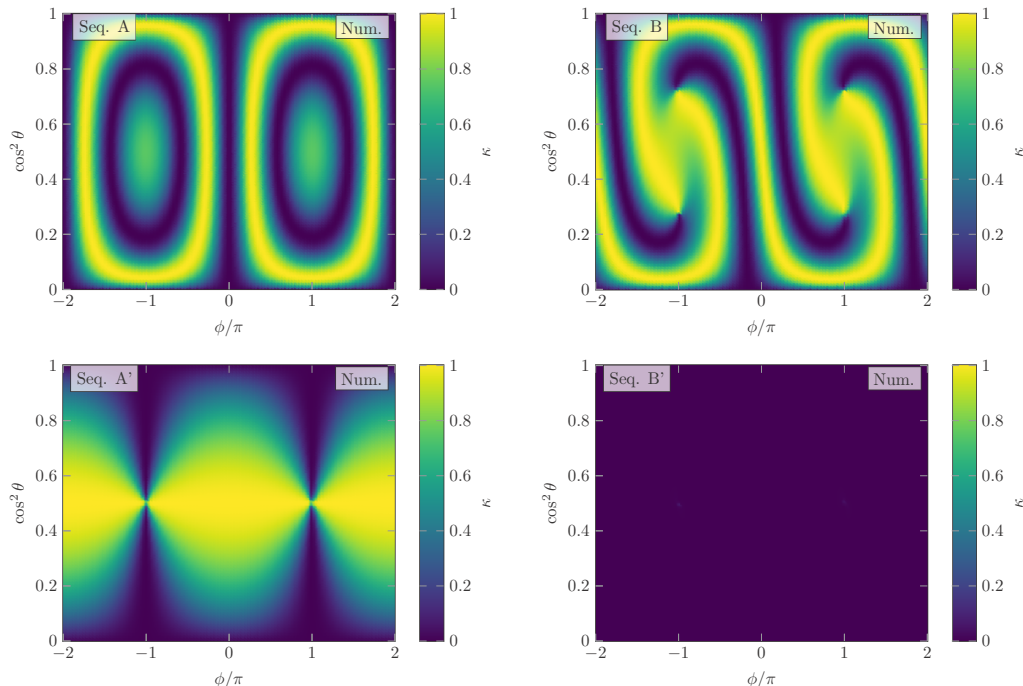


FIG. 8. The probability of finding the state  $|0\rangle_{M12}$  after each sequence. Numerical results with parameters  $\eta = 2$ ,  $\Sigma_\eta/(T w) = 0.5$ , and  $x_0 = 100$ .

and sequence B gets contributions from both geometric and dynamical phases. For sequences A' and B', where the flux echo is in effect, there is no contribution from the dynamical

phase. In this case, only sequence A' gets a contribution from the geometric phase, this is the reason why  $\kappa$  remains zero after sequence B'.

- [1] C. Nayak, S. H. Simon, A. Stern, M. Freedman, and S. Das Sarma, *Rev. Mod. Phys.* **80**, 1083 (2008).
- [2] M. Leijnse and K. Flensberg, *Semicond. Sci. Technol.* **27**, 124003 (2012).
- [3] R. Aguado, *La Rivista del Nuovo Cimento* **40**, 523 (2017).
- [4] R. M. Lutchyn, E. P. A. M. Bakkers, L. P. Kouwenhoven, P. Krogstrup, C. M. Marcus, and Y. Oreg, *Nat. Rev. Mater.* **3**, 52 (2018).
- [5] C. W. J. Beenakker, *SciPost Phys. Lect. Notes*, **15** (2020), doi: 10.21468/SciPostPhysLectNotes.15.
- [6] D. A. Ivanov, *Phys. Rev. Lett.* **86**, 268 (2001).
- [7] J. Alicea, Y. Oreg, G. Refael, F. von Oppen, and M. P. A. Fisher, *Nat. Phys.* **7**, 412 (2011).
- [8] L. Fu and C. L. Kane, *Phys. Rev. Lett.* **100**, 096407 (2008).
- [9] R. M. Lutchyn, J. D. Sau, and S. Das Sarma, *Phys. Rev. Lett.* **105**, 077001 (2010).
- [10] Y. Oreg, G. Refael, and F. von Oppen, *Phys. Rev. Lett.* **105**, 177002 (2010).
- [11] K. Flensberg, *Phys. Rev. Lett.* **106**, 090503 (2011).
- [12] R. Seoane Souto, K. Flensberg, and M. Leijnse, *Phys. Rev. B* **101**, 081407(R) (2020).
- [13] K. Flensberg, F. von Oppen, and A. Stern, *Nat. Rev. Materials* **6**, 944 (2021).
- [14] V. Mourik, K. Zuo, S. M. Frolov, S. R. Plissard, E. P. A. M. Bakkers, and L. P. Kouwenhoven, *Science* **336**, 1003 (2012).
- [15] M. T. Deng, S. Vaitiek, E. B. Hansen, J. Danon, M. Leijnse, K. Flensberg, P. Krogstrup, and C. M. Marcus, *Science* **354**, 1557 (2016).
- [16] F. Nichele, A. C. C. Drachmann, A. M. Whiticar, E. C. T. O'Farrell, H. J. Suominen, A. Fornieri, T. Wang, G. C. Gardner, C. Thomas, A. T. Hatke, P. Krogstrup, M. J. Manfra, K. Flensberg, and C. M. Marcus, *Phys. Rev. Lett.* **119**, 136803 (2017).
- [17] A. Whiticar, A. Fornieri, E. O'Farrell, A. Drachmann, T. Wang, C. Thomas, S. Gronin, R. Kallaher, G. Gardner, M. Manfra, C. Marcus, and F. Nichele, *Nat. Commun.* **11**, 3212 (2020).
- [18] S. M. Albrecht, A. P. Higginbotham, M. Madsen, F. Kuemmeth, T. S. Jespersen, J. Nygård, P. Krogstrup, and C. M. Marcus, *Nature (London)* **531**, 206 (2016).

- [19] S. Vaitiekėnas, G. W. Winkler, B. van Heck, T. Karzig, M. T. Deng, K. Flensberg, L. I. Glazman, C. Nayak, P. Krogstrup, R. M. Lutchyn, and C. M. Marcus, *Science* **367**, 1442 (2020).
- [20] M. T. Deng, S. Vaitiekėnas, E. Prada, P. San-Jose, J. Nygård, P. Krogstrup, R. Aguado, and C. M. Marcus, *Phys. Rev. B* **98**, 085125 (2018).
- [21] F. Harper, A. Pushp, and R. Roy, *Phys. Rev. Res.* **1**, 033207 (2019).
- [22] M. I. K. Munk, J. Schulenburg, R. Egger, and K. Flensberg, *Phys. Rev. Res.* **2**, 033254 (2020).
- [23] J. F. Steiner and F. von Oppen, *Phys. Rev. Res.* **2**, 033255 (2020).
- [24] T. B. Smith, M. C. Cassidy, D. J. Reilly, S. D. Bartlett, and A. L. Grimsmo, *PRX Quantum* **1**, 020313 (2020).
- [25] G. Széchenyi and A. Pályi, *Phys. Rev. B* **101**, 235441 (2020).
- [26] A. Khindanov, D. Pikulin, and T. Karzig, *SciPost Phys.* **10**, 127 (2021).
- [27] J. Schulenburg, M. Burrello, M. Leijnse, and K. Flensberg, *Phys. Rev. B* **103**, 245407 (2021).
- [28] G. Rigolin, G. Ortiz, and V. H. Ponce, *Phys. Rev. A* **78**, 052508 (2008).
- [29] J. Roland and N. J. Cerf, *Phys. Rev. A* **65**, 042308 (2002).
- [30] G. Schaller, S. Mostame, and R. Schützhold, *Phys. Rev. A* **73**, 062307 (2006).
- [31] A. T. Rezakhani, W.-J. Kuo, A. Hamma, D. A. Lidar, and P. Zanardi, *Phys. Rev. Lett.* **103**, 080502 (2009).
- [32] J. M. Martinis and M. R. Geller, *Phys. Rev. A* **90**, 022307 (2014).
- [33] M. Cheng, V. Galitski, and S. Das Sarma, *Phys. Rev. B* **84**, 104529 (2011).
- [34] M. S. Scheurer and A. Shnirman, *Phys. Rev. B* **88**, 064515 (2013).
- [35] T. Karzig, G. Refael, and F. von Oppen, *Phys. Rev. X* **3**, 041017 (2013).
- [36] T. Karzig, A. Rahmani, F. von Oppen, and G. Refael, *Phys. Rev. B* **91**, 201404(R) (2015).
- [37] T. Karzig, F. Pientka, G. Refael, and F. von Oppen, *Phys. Rev. B* **91**, 201102(R) (2015).
- [38] C. Knapp, M. Zaletel, D. E. Liu, M. Cheng, P. Bonderson, and C. Nayak, *Phys. Rev. X* **6**, 041003 (2016).
- [39] A. Rahmani, B. Seradjeh, and M. Franz, *Phys. Rev. B* **96**, 075158 (2017).
- [40] M. Sekania, S. Plugge, M. Greiter, R. Thomale, and P. Schmitteckert, *Phys. Rev. B* **96**, 094307 (2017).
- [41] K. Ritland and A. Rahmani, *New J. Phys.* **20**, 065005 (2018).
- [42] A. Nag and J. D. Sau, *Phys. Rev. B* **100**, 014511 (2019).
- [43] Z.-T. Zhang, F. Mei, X.-G. Meng, B.-L. Liang, and Z.-S. Yang, *Phys. Rev. A* **100**, 012324 (2019).
- [44] T. Posske, C.-K. Chiu, and M. Thorwart, *Phys. Rev. Res.* **2**, 023205 (2020).
- [45] N. Breckwoldt, T. Posske, and M. Thorwart, *New J. Phys.* (2022), doi: 10.1088/1367-2630/ac46e2.
- [46] J. A. Jones, V. Vedral, A. Ekert, and G. Castagnoli, *Nature (London)* **403**, 869 (2000).
- [47] T. Karzig, Y. Oreg, G. Refael, and M. H. Freedman, *Phys. Rev. X* **6**, 031019 (2016).
- [48] J. Liu, W. Chen, M. Gong, Y. Wu, and X. C. Xie, *Sci. China Phys. Mech. Astron.* **64**, 117811 (2021).
- [49] K.-P. Marzlin and B. C. Sanders, *Phys. Rev. Lett.* **93**, 160408 (2004).
- [50] C. De Grandi, V. Gritsev, and A. Polkovnikov, *Phys. Rev. B* **81**, 012303 (2010).
- [51] C.-W. Liu, A. Polkovnikov, and A. W. Sandvik, *Phys. Rev. B* **87**, 174302 (2013).
- [52] P. Weinberg, M. Bukov, L. D'Alessio, A. Polkovnikov, S. Vajna, and M. Kolodrubetz, *Phys. Rep.* **688**, 1 (2017).
- [53] M. Rodríguez-Vega, M. Vogl, and G. A. Fiete, *Ann. Phys.* **435**, 168434 (2021).
- [54] C. Deng, F. Shen, S. Ashhab, and A. Lupascu, *Phys. Rev. A* **94**, 032323 (2016).
- [55] G. Rigolin and G. Ortiz, *Phys. Rev. Lett.* **104**, 170406 (2010).
- [56] M. Passos, M. Taddei, and R. de Matos Filho, *Ann. Phys.* **418**, 168172 (2020).
- [57] N. Wiebe and N. S. Babcock, *New J. Phys.* **14**, 013024 (2012).
- [58] S. M. Albrecht, E. B. Hansen, A. P. Higginbotham, F. Kuemmeth, T. S. Jespersen, J. Nygård, P. Krogstrup, J. Danon, K. Flensberg, and C. M. Marcus, *Phys. Rev. Lett.* **118**, 137701 (2017).



---

Fast universal control of a flux qubit via exponentially tunable wave-function overlap

## Fast universal control of a flux qubit via exponentially tunable wave-function overlap

Svend Krøjer,<sup>1</sup> Anders Enevold Dahl,<sup>1</sup> Kasper Sangild Christensen,<sup>1,2</sup> Morten Kjaergaard,<sup>1</sup> and Karsten Flensberg<sup>1</sup>

<sup>1</sup>*Center for Quantum Devices, Niels Bohr Institute,  
University of Copenhagen, DK-2100 Copenhagen, Denmark*

<sup>2</sup>*Department of Physics and Astronomy, Aarhus University, Ny Munkegade 120, 8000 Aarhus C, Denmark*

(Dated: November 29, 2023)

Fast, high fidelity control and readout of protected superconducting qubits are fundamentally challenging due to their inherent insensitivity. We propose a flux qubit variation which enjoys a tunable level of protection against relaxation to resolve this outstanding issue. Our qubit design, the double-shunted flux qubit (DSFQ), realizes a generic double-well potential through its three junction ring geometry. One of the junctions is tunable, making it possible to control the barrier height and thus the level of protection. We analyze single- and two-qubit gate operations that rely on lowering the barrier. We show that this is a viable method that results in high fidelity gates as the non-computational states are not occupied during operations. Further, we show how the effective coupling to a readout resonator can be controlled by adjusting the externally applied flux while the DSFQ is protected from decaying into the readout resonator. Finally, we also study a double-loop gradiometric version of the DSFQ which is exponentially insensitive to variations in the global magnetic field, even when the loop areas are non-identical.

### I. INTRODUCTION

Qubits based on superconducting junctions form a promising platform for quantum computation (QC) architectures [1–3]. In order to scale up fault-tolerant QC, it is crucial that gate and readout infidelities must be lower than the threshold for quantum error correction (QEC), which for the surface code is about 1% [4, 5]. A number of experiments using transmon-based multi-qubit chips have demonstrated surface code QEC close to the threshold [6–8].

To go beyond the capabilities of contemporary transmon-based architectures, a number of  $T_1$ -protected qubit designs have appeared [2, 9–12]. The general idea of a  $T_1$ -protected superconducting qubit is that the computational states are localized in different quantum wells, leading to exponentially suppressed noise-induced transitions, enhancing the relaxation time significantly [2]. Additionally, the double-well potential realizes low-frequency qubits resulting in less sensitivity to dielectric loss and Ohmic noise channels [13, 14].

In the flux qubit modality, this kind of double-well protection can be reached by biasing the superconducting loop with an external flux close to half a flux quantum [15, 16]. Here, the low-energy computational states corresponds to supercurrent flowing in opposite directions in the loop. At a bias of half a flux quantum, the fluxon states are degenerate up to the exponentially small splitting due to overlap of the evanescent part of the wave functions across the barrier separating the two wells. Below we refer to this small splitting as the wave-function overlap. The fluxon states are sensitive to the external magnetic flux as it picks out a preferred current direction and determines the energy splitting. The strong flux dependence leads to a linear sensitivity of the qubit frequency to flux noise, causing dephasing of the qubit and limiting coherence [10, 17].

Despite the enhanced relaxation time of low-frequency

qubits (e.g. heavy fluxonium [10, 18],  $0 - \pi$  qubit [9, 19], etc.), a general disadvantage is that gate times typically also increase due to the vanishing wave-function overlap of the computational states. One way of circumventing this limitation is to use higher lying non-computational states [2, 10, 19]. In this manner, single and two qubit gates can be activated through multi-tone driving [20]. The downside of such an approach, however, is that the momentary occupancy of the non-computational states leads to increased decoherence, limiting gate fidelities [21]. Another possibility is to rely on diabatic single qubit control [18].

In this paper, we explore an alternative approach to perform gates on  $T_1$ -protected qubits that rely on adiabatically adjusting the level of protection by lowering the barrier between the two wells. We propose a qubit design, the double-shunted flux qubit (DSFQ), which aims to be a relatively simple modification of a flux qubit with exponentially tunable wave-function overlap. The DSFQ is related to the persistent current flux qubit (PCFQ) [15, 17] and the capacitively shunted flux qubit (CSFQ) [22] as they all share the same circuit layout of three Josephson junctions (JJs) connected in a loop, see Fig. 1. While the PCFQ realizes a large  $E_J/E_C$  via three large junctions, the CSFQ uses smaller junctions with one large capacitive shunt such that one mode is heavy (large  $E_J/E_C$ ) and one mode is light (smaller  $E_J/E_C$ ). The DSFQ finds the middle ground between these designs by using small junctions and two large capacitive shunts such that both modes are heavy, similar to the PCFQ. Since both modes are heavy, the lowest energy wave functions are localized in separate wells, protecting the qubit from relaxation. Other designs, namely the super-semi  $\cos(2\phi)$  qubit and the bifluxon, have successfully shown an order-of-magnitude improvement of the relaxation time in the protected regime [11, 12]. However, both qubits are challenging to fabricate and tune to the ideal regime and two-qubit gates have not yet been

arXiv:2303.01102v2 [quant-ph] 28 Nov 2023

realized [2]. The DSFQ offers a comparatively simple platform for studying universal gate sets for qubits with variable wave-function overlap. In addition to the universal gate scheme, we also propose a noise-insensitive readout method for the DSFQ.

We imagine tuning the barrier height by a tunable junction, implemented either in a SQUID-loop as in previous PCFQ experiments [23–26] or in a hybrid version where the tunable junction is a superconductor-semiconductor-superconductor junction. This type of junction has been demonstrated earlier to be stable and having coherence times longer than the anticipated gate times [11, 27–30]. However, we note that the coherence times for the semiconductor-based junctions are still shorter than the more standard insulator-barrier junctions. The physics of this is still not understood and the coherence times could improve with future devices [31].

We calculate the coherence properties of the DSFQ and discuss the flux-noise sensitivity. In order to reduce the flux dephasing, we propose a double-loop gradiometric version of the DSFQ which gives exponential protection against global flux noise. Gradiometric qubit designs have been proposed previously but rely on identical areas in the two loops [23, 26, 32]. We show that small area variations can be compensated for by adjusting the tunable junction without introducing sensitivity to the junction control line. The main focus of our study is a set of one- and two-qubit gates where the idea is to tune the qubit out of the protected regime by adiabatically lowering the barrier between the two wells and thereby hybridize the computational states. Two-qubit gates can be performed by simultaneously lowering the barriers for two capacitively coupled DSFQ's while single qubit gates require a fast single-tone microwave pulse in the intermediate regime. Advantages of variable-protection gates are that fast-decaying non-computational states do not participate in gate operations and that two-qubit interactions can be turned off with exponential on/off ratio while maintaining the ability to perform one-qubit gates. Finally, we show how the effective coupling to a readout resonator can be adjusted with a simple flux control of the qubit, leading to an order-of-magnitude on/off ratio while decay to the readout resonator is suppressed.

## II. THE DOUBLE-SHUNTED FLUX QUBIT

We consider a system of three Josephson junctions connected in a ring. The circuit is illustrated in Fig. 1(a) where the Josephson energy of the tunable junction is denoted by  $\alpha E_J$ . The two other junctions have Josephson energy  $E_J$ , but they do not have to be identical for our proposal to work. In the phase variables  $\phi = (\phi_1 - \phi_2)/2$  and  $\theta = (\phi_1 + \phi_2)/2$ , the potential energy of the qubit is thus given by

$$H_J = -2E_J \cos(\phi) \cos(\theta) - \alpha E_J \cos(2\phi + \phi_{\text{ext}}), \quad (1)$$

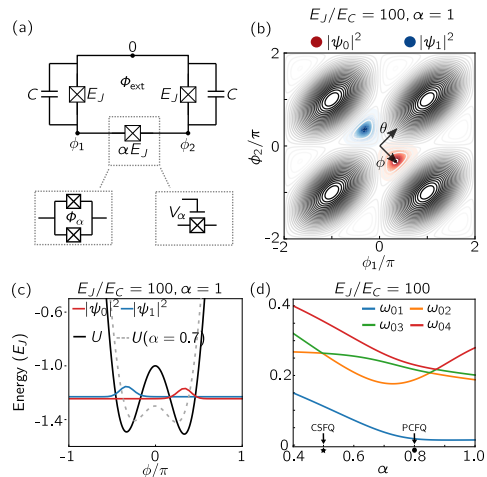


FIG. 1. (a) Circuit layout for the DSFQ with a variable junction by either a SQUID or gate voltage tunable nanowire junction. (b) Potential landscape of the DSFQ with the two lowest energy eigenstates shown in red and blue with  $E_J/E_C = 100$ ,  $\alpha = 1$  and  $\phi_{\text{ext}} = 0.997\pi$ . (c) One dimensional cut of (b) along  $\phi = (\phi_1 - \phi_2)/2$  with wave functions showing their exponential separation at  $\alpha = 1$ . The potential at  $\alpha = 0.7$  is shown in gray dashed. (d) Energy splitting of the qubit as a function of the barrier height controlled by  $\alpha$ . The value of  $\alpha$  corresponding to the CSFQ/PCFQ is indicated with a star/bullet ( $\alpha = 0.5/0.8$ ). Energies are in units of the Josephson energy,  $E_J$ .

where  $\phi_{\text{ext}} = 2\pi\Phi/\Phi_0$  and  $\Phi$  is the flux through the loop, controlled by an external magnetic field whose value is typically set to  $\phi_{\text{ext}} = 0.997\pi$  unless other stated. At  $\alpha = 0.5$ , the barrier is completely lowered, making the potential along the  $\phi$ -direction approximately quartic as for the CSFQ [22]. At a value of  $\alpha = 0.8$ , the barrier is significant and the potential of the PCFQ [15, 17] is recovered. Controlling the barrier height of the DSFQ through  $\alpha$  thus interpolates between the PCFQ and the CSFQ. Note that in the flux-tunable PCFQ, the barrier height can be controlled via an external flux in a slightly different geometry [23, 25, 26].

The charging energy is determined by the capacitances  $C$  shown in Fig. 1(a) and gives rise to the kinetic energy [33]

$$H_C = 2E_C (-i\partial_\phi - n_{g\phi})^2 + 2E_C (-i\partial_\theta - n_{g\theta})^2. \quad (2)$$

Here we have included offset charges  $n_{g\phi}$  and  $n_{g\theta}$  (the  $4E_C$  typically found as the prefactor is reduced due to the change of variables  $n_{\theta/\phi} = n_1 \pm n_2$ ). The qubit will be operated in the regime of small  $E_C = e^2/2C$  (i.e., both  $\phi$  and  $\theta$  being heavy modes). Realistically, the Josephson capacitances are about two orders of magnitude smaller

than the large shunting capacitances and thus merely renormalizes  $E_C$  without affecting the results presented in this work.

The potential landscape and the ground-state wave functions are shown in Fig. 1(b) in the heavy-modes regime ( $E_J/E_C = 100$ ). The external flux is tuned to a value close to half a flux quantum. The two wave function shown in red and blue ( $\psi_0$  and  $\psi_1$ ) are clearly well separated and localized in the two wells. They represent the qubit states  $|0\rangle$  and  $|1\rangle$ . The state separation is most easily seen in Fig. 1(c) which is a cut along the  $\phi$ -direction. Due to their separation, the tunneling between the two wells is suppressed. It results in a small qubit splitting near  $\alpha = 1$  determined by the external flux and also a large anharmonicity, see Fig. 1(d). Lowering the barrier by reducing  $\alpha$ , increases the qubit frequency and decreases the anharmonicity  $\alpha_{\text{an}} = (\omega_{02} - \omega_{01}) - \omega_{01}$ , as the states hybridize and change significantly. This fact is used below to perform fast gates by lowering the value of  $\alpha$  to  $\alpha \approx 0.7$  where the logical states partially overlap.

### A. Gradiometric DSFQ

The qubit discussed above is designed to have a large relaxation time due to the exponential suppression of inter-well coupling. However, it is likely to have a poor dephasing coherence time because of the sensitivity of the energy difference of the two wells to flux noise. To improve the dephasing time, we propose a double-loop variation as in Fig. 2(e) which is designed to cancel out any fluctuations in the global flux. In the double-loop design, we picture the variable junctions as tunable nanowire junctions. Alternatively, these could be SQUIDS controlled by individual flux lines without defeating the purpose of the gradiometric setup. However, the additional flux loops will complicate the control of the qubit because there will be flux lines to each SQUID and one to control the global flux. The tunable Josephson junctions give an advantage with fewer flux control lines compared to using SQUIDS at the potential expense of reduced coherence due to semiconducting junctions. To understand the double-loop cancellation better, we consider the situation where half a flux quantum threads through each loop. This gives rise to two lowest-energy combinations of current flowing in the circuit;  $|\uparrow\downarrow\rangle, |\downarrow\uparrow\rangle$ , where an arrow indicates the direction of the current in each loop. Thus, the two lowest energy states correspond to the situation where current flows in opposite directions, making them indifferent to variations in the external flux. Said differently, the magnetic dipole moment vanishes and the computational states are only affected by magnetic field gradients through the magnetic quadrupole moment as verified in Refs. [26, 32, 34]. In Fig. 2(b,f), we show the dependence of the qubit splitting on the global flux for both single- and double-loop DSFQs.

For a symmetric situation where the areas of the two loops and the Josephson energies of two outer junctions

are identical, the dependence of the global flux  $\Phi_G$  (proportional to a global magnetic field) has zero slope when  $\Phi_G$  is at half flux quantum (see Fig. 2(f), blue solid line). In an experimental situation, the loop areas will be slightly different, leading to a sensitivity to the global magnetic field (blue dash-dotted line). However, by appropriately choosing the ratio of the tunable junctions, the dispersion with  $\Phi_G$  can become exponentially flat again at the expense of splitting the degeneracy (blue dashed line). If the flux through the two non-identical loops is controlled by a single global field, and the tunable junctions can be tuned to be asymmetric,  $\alpha_2 = (1 + \delta)\alpha_1$ , then the sweet-spot simply shifts to

$$\delta = -1 + \frac{1+r}{1-r} \cos\left(\frac{2\pi r}{1-r}\right) \approx 2r, \quad r = \frac{A_1 - A_2}{A_1 + A_2}. \quad (3)$$

where  $r$  is a measure of the loop area asymmetry and assumed small, see also Appendix A where the condition on  $\delta$  is derived. Here, it is also shown that the fluctuations in  $\delta$  has very little effect on the energies near half a flux quantum as can also be seen by comparing the dashed ( $\delta = 2r$ ) and dash-dotted blue line ( $\delta = 0$ ). Fig. 2(f) summaries how the sensitivity to the external global magnetic field and how choosing the value of the Josephson energy of the second junction can make the spectrum practically insensitive to the global field. As detailed in Appendix A, the slope and height of the curve is set by the area and junction asymmetry. While being insensitive to variations in the global magnetic field, the qubit frequency is still linearly sensitive to the local fluxes in the individual loops, see Fig. 2(h) and discussion below.

### B. Decoherence times

The decoherence of the DSFQ is estimated by calculating relaxation and dephasing rates for different noise sources. The relaxation time  $T_1 = (\sum_\lambda \Gamma_1^\lambda)^{-1}$  is computed through the relaxation rates which are given by Fermi's Golden rule [13, 14, 35]

$$\begin{aligned} \Gamma_1^\lambda &= \frac{1}{\hbar^2} |\langle 1 | \partial_\lambda H | 0 \rangle|^2 S_\lambda(\omega), \\ \Gamma_1^{\text{diel}} &= \hbar |\langle 1 | \phi | 0 \rangle|^2 S^{\text{diel}}(\omega) \end{aligned} \quad (4)$$

where  $\lambda$  is an external noise source and  $S_\lambda(\omega)$  is the power spectral function for a given noise source. We consider  $1/f$  and ohmic noise which were the limiting noise channels for flux and charge noise respectively for the CSFQ [22] in addition to dielectric loss, the limiting factor for fluxonium relaxation time [14, 36]. The associated spectral functions are

$$\begin{aligned} S_\lambda^{\frac{1}{f}}(\omega) &= \frac{2\pi A_\lambda^2 \text{Hz}}{|\omega|}, \quad S_\lambda^\Omega(\omega) = \frac{B_\lambda^2 \omega}{2\pi \times 1\text{GHz}}, \\ S^{\text{diel}}(\omega) &= \frac{\omega^2 \tan \delta^{\text{diel}}}{4E_C} \left[ \coth\left(\frac{\omega}{k_B T}\right) + 1 \right], \end{aligned}$$



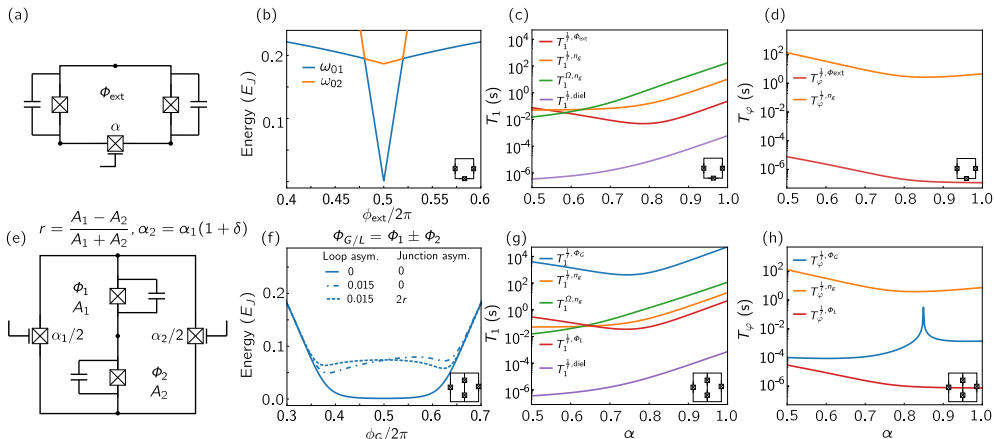


FIG. 2. (a) Circuit layout of the single-loop DSFQ. (b) Dispersion of the qubit frequency with respect to the reduced external flux through the loop, showing the linear dependence in the region  $\phi_{\text{ext}}/2\pi = 0.47 - 0.53$ . (c-d) Relation between the relaxation/dephasing time ( $T_1/T_c$ ) and the barrier height controlled by  $\alpha$  for the single loop DSFQ. (e) Circuit layout of the gradiometric DSFQ with two tunable junctions. The inconvenient placement of large capacitors in the loops can be worked around by using cross-over junctions. (f) Dispersion of the qubit frequency with respect to the reduced external global flux,  $\phi_G = \frac{2\pi\Phi_G}{\Phi_0}$ . We display the cases where the loop areas are identical (solid line), non-identical (dot-dashed line) and non-identical with compensating asymmetric junctions (dashed line). (g-h) Relation between the relaxation/dephasing time ( $T_1/T_c$ ) and the barrier height controlled by  $\alpha$  for the gradiometric DSFQ. Note the insensitivity to noise in the global magnetic field and sensitivity to local magnetic field noise. The noise amplitudes in all figures are  $A_\Phi = 10^{-6}\Phi_0/\sqrt{\text{Hz}}$ ,  $A_{n_g} = 10^{-4}e/\sqrt{\text{Hz}}$  [13],  $B_{n_g} = 5.2 \times 10^{-9}e/\sqrt{\text{Hz}}$  [22] and  $\tan\delta_{\text{diel}} = 2 \times 10^{-7}$  [14]. The Josephson energy is  $E_J = 10 h \text{GHz}$  and external flux is  $\phi_{\text{ext}} = 0.997\pi$  where relevant.

where  $A_\lambda$  and  $B_\lambda$  are noise amplitudes for  $1/f$  and ohmic noise respectively,  $\tan\delta_{\text{diel}} = 2 \times 10^{-7}$  is the loss tangent and  $T = 20\text{mK}$  is the temperature [14]. We use typical noise amplitudes  $A_\Phi = 10^{-6}\Phi_0/\sqrt{\text{Hz}}$  [13],  $A_{n_g} = 10^{-4}e/\sqrt{\text{Hz}}$  [13] and  $B_{n_g} = 5.2 \times 10^{-9}e/\sqrt{\text{Hz}}$  [22].

In Fig. 2(c, g), we display the computed relaxation times for the single loop and double loop (gradiometric) versions of the DSFQ. Both panels show exponentially enhanced  $T_1$  in the protected regime ( $\alpha = 1$ ) with  $T_1 = 603 \mu\text{s}$  in the single loop and  $T_1 = 733 \mu\text{s}$  in the gradiometric setup, the limiting factor being dielectric loss. In the unprotected regime ( $\alpha = 0.5$ ), the relaxation time is reduced to  $T_1 = 0.35 \mu\text{s}$  in the single loop and  $T_1 = 0.35 \mu\text{s}$  in the gradiometric equivalent to 3 orders of magnitude.

We can compare the relaxation times to the dephasing times shown in Fig. 2(d, h). The first order dephasing rates for  $1/f$  noise are computed through [13],

$$\Gamma_\varphi^{\dagger,\lambda} = \sqrt{2A_\lambda(\partial_\lambda\omega_q)^2 \ln|\omega_{\text{ir}}t|},$$

where we have introduced an infrared cutoff and a characteristic time with the product  $\omega_{\text{ir}}t = 2\pi \times 10^{-6}$  as in Ref. [13]. The dephasing times shown in Fig. 2(d, h) are

limiting the coherence time  $\frac{1}{T_2} = \frac{1}{2T_1} + \frac{1}{T_\varphi}$  compared to the relaxation time due to the linear sensitivity to (local) flux noise in the  $T_1$ -protected regime. Conversely, in the unprotected regime, the coherence is limited by relaxation through dielectric loss, illustrating the trade-off between  $T_1$ -protection and dephasing due to flux noise is general to flux qubits. Note that the sensitivity to global flux noise in Fig. 2(g, h) is reduced due to the gradiometric construction of the device. In the  $T_1$  protected regime ( $\alpha = 1$ ) the dephasing time is  $T_\varphi = 0.12 \mu\text{s}$  in the single loop and  $T_\varphi = 0.74 \mu\text{s}$  in the gradiometric setup. In the unprotected regime ( $\alpha = 0.5$ ) the dephasing time is enhanced to  $T_\varphi = 7.6 \mu\text{s}$  in the single loop and  $T_\varphi = 98 \mu\text{s}$  in the gradiometric setup. The CSFQ has relaxations times reported in the range  $T_1 = 20 - 60 \mu\text{s}$  [22]. State of the art transmon qubit report relaxations times up to  $T_1 = 0.5 \text{ms}$  [37].

In total, the DSFQ does not exceed the relaxation time of state of the art transmon qubits but offers a platform with adjustable and strong noise bias and a tunable degree of  $T_1$ -protection, which can be used to study optimum strategies for gate operations on protected qubits. While the noise bias, in principle, opens up paths towards efficient noise biased error correcting codes, the linear sensitivity to (local) flux noise is a limiting factor.

This could be suppressed by choosing a larger qubit splitting, creating a wider sweet spot at half flux quantum. However, we have chosen to focus on the  $T_1$  protected regime here. We note that such compromise is relevant for other qubit proposals such as the heavy fluxonium and the bifluxon [10, 12, 18].

### III. QUBIT CONTROL

To control the DSFQ, we leave the protected regime ( $\alpha = 1$ ) and lower the barrier between the two wells ( $\alpha \simeq 0.5 - 0.7$ ). When the barrier is lowered, traditional techniques in microwave control such as DRAG and IQ-mixing can be used for the DSFQ [38, 39]. As detailed in the sections below, the height of the barrier at the operating point and the rate at which it is lowered depends on whether single or two-qubit gates are performed. We continue in the following section by implementing an  $\sigma_x$  gate numerically to illustrate how single qubit gates can be performed on qubits with variable-protection using single-tone driving.

#### A. Variable-protection single qubit gates

Our proof-of-concept  $\sigma_x$ -gate has three steps as illustrated in Fig. 3:

- I. Lower the barrier adiabatically,  $\alpha = 1 \rightarrow 0.7$ .
- II. Apply an appropriate microwave pulse to the qubit.
- III. Raise the barrier adiabatically,  $\alpha = 0.7 \rightarrow 1$ .

This control sequence is illustrated in Fig. 3 where the lowering and raising of the barrier takes 7 ns and the microwave drive takes 11 ns (including 1.5 ns ramp up/down), totalling a gate time of 25 ns. The microwave drive line is coupled to one of the nodes of the qubit through a small capacitance  $C_d \ll C$ , giving rise to the Hamiltonian term  $H_d = \frac{C_d}{C+C_d} V_d(t) n_1$  [39]. As the barrier is lowered, the quantum states changes significantly and a small subspace of states is insufficient to describe the evolution due to  $H(t) = H_C + H_J(t)$ . We therefore perform simulation in a relatively large Hilbert space with 625 states (in the charge basis with cutoff  $n_{\text{cutoff}} = 12$  for both the  $\phi$ - and  $\theta$ -mode) and numerically evaluate  $\exp(-i\Delta t H(t))$  at each time step to perform the time-evolution (857 timesteps/nanosecond). When the drive is turned on at fixed  $\alpha$ , we instead numerically integrate the time-dependent Schrödinger equation using the same Hilbert space dimension. At each time-step, we numerically diagonalize the Hamiltonian and compute the overlap with the instantaneous qubit states to produce Fig. 6(c).

In our single qubit gate scheme, we choose to lower the barrier only partially ( $\alpha = 0.7$ ) to limit the time spent adiabatically adjusting  $\alpha$  and to avoid small, unwanted interactions with neighboring qubits which arise

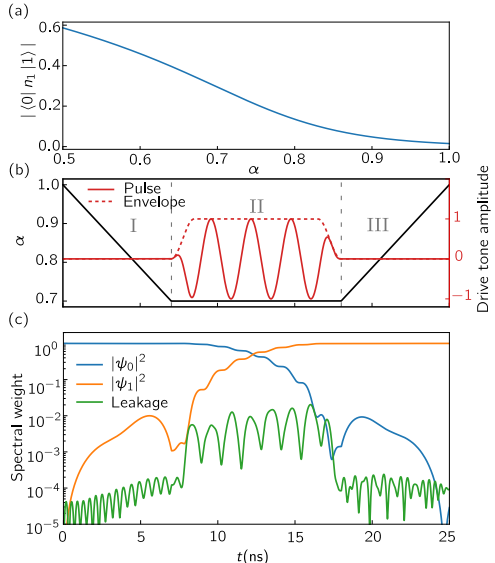


FIG. 3. (a) The coupling of computational states through the charge operator as a function of  $\alpha$ , showing when transitions can be stimulated through a capacitively coupled drive-line. (b) The pulse profile for the  $\sigma_x$  gate displaying the low-frequency  $\alpha$  drive (black) and the high-frequency microwave drive (red). The envelope of the microwave pulse is 11 ns long with a 1.5 ns cosine ramp up/down. The drive frequency is slightly detuned from the qubit frequency  $\omega_d = 0.979 \omega_q$ . (c) Numerical data from non-dissipative simulations showing the time history of the spectral weights during the low-leakage, high fidelity  $\sigma_x$  gate. In all panels, the scale of the Josephson energy is  $E_J = 10 h$  GHz and  $E_J/E_C = 100$  with the flux bias set to  $\phi_{\text{ext}} = 0.995\pi$ .

when the barrier is completely lowered, see also Appendix C. The qubit frequency is changed from  $\omega_q(\alpha = 1) = 0.25 h$  GHz to  $\omega_q(\alpha = 0.7) = 0.39 h$  GHz, where the Josephson energy is  $E_J = 10 h$  GHz and  $E_J/E_C = 100$  with the flux bias set to  $\phi_{\text{ext}} = 0.995\pi$ . At the operating point ( $\alpha = 0.7$ ) the relaxation time is reduced to 1.6 ps. The speed at which the barrier is lowered is adiabatic with respect to the energy gap between the computational states and the non-computational states such that the adiabatic time is set by the desired leakage bound. The 7 ns lowering time results in a very small ( $\sim 10^{-4}$ ) leakage but does admit for a small ( $\sim 10^{-3}$ ) probability to transition from one logical state to the other. This small effect makes it necessary to slightly adapt the microwave pulse to achieve high fidelity. One possibility is to marginally reduce the drive amplitude, but the qubit frequency is also shifted due to the AC-Stark effect. We therefore instead adapt the pulse by a minor frequency

shift of the drive,  $\omega_d = 0.979\omega_q$ , to account for both of these contributions. The limit to the fidelity imposed by coherent errors (leakage) during the  $\sigma_x$  gate is 99.98% while the gate time is  $T_g = 25$  ns. The single qubit gate fidelity is limited by decay from the shorter relaxation time at the operating point. We estimate the  $T_1$  limited fidelity via  $F \approx \exp\left[-\int_0^{T_g} dt \Gamma_1(t)\right]$ , where  $\Gamma_1(t)$  is the sum of (instantaneous) decay rates. The resulting  $T_1$ -limited fidelity is 99.1% for the single qubit X-gate. While the gate is limited by decay in this device, the coherence limited gate fidelity is comparable to state-of-the-art single qubit gates on unprotected qubits such as the transmon [7] and potentially faster than alternative gates on  $T_1$ -protected qubits [20]. The latter makes use of non-computational states, multi-tone driving and an optimal control algorithm to optimize gate performance. The comparatively simple variable-protection gate shows the benefits of tuning in and out of protection, and that the access to fast, single tone pulse control outweigh the additional overhead from the adiabatic control of the level of protection. In Appendix B, we exemplify using standard IQ-mixing how also  $\sigma_y$  and  $(\sigma_x - \sigma_y)/\sqrt{2}$  gates can be implemented with similar fidelity as the  $\sigma_x$  gate. Combined with virtual  $\sigma_z$  gates, we have thus demonstrated a compelling scheme for realizing universal single-qubit control. It is natural to improve upon this proof-of-principle design using more advanced  $\alpha$ -profiles combined with microwave pulse shaping techniques such as DRAG [38] in order to reduce the time spent at low coherence for smaller  $\alpha$ . Alternatively, sudden gates or gates where the flux bias is also controlled may be explored with inspiration from Ref. [18]. Ref. [18] also shows how multi-tone driving can initialize low-frequency qubits where the qubit frequency is subthermal. Alternatively, our flexible design also allows for thermal initialization in the unprotected regime.

### B. Variable-protection two-qubit gates

An advantage of qubits with variable protection is that they can act as their own tunable couplers with exponential on/off ratio. In the protected idling regime, the qubit-qubit coupling vanishes due to the exponentially small wave-function overlap, see also Appendix C. As a result of the exponentially suppressed coupling between the computational states in the idling regime, a capacitive qubit-qubit coupling,

$$H_{Q-Q} = 4EC \frac{C_g}{C + C_g} n_1 n_3, \quad (5)$$

may be relatively strong  $C_g \simeq 0.3C$  compared to e.g. transmon qubits, see Appendix C for a derivation of Eq. 5. We can thus implement two-qubit gates that rely solely on the simultaneous lowering of both barriers of two capacitively coupled DSFQs.

Our implementation of two-qubit gates has three steps:

I. Lower both barriers simultaneously in a time  $T_a/2$ ,  
 $\alpha_1 = \alpha_2 = 1 \rightarrow \alpha_{\min}$ .

II. Wait for a time  $T_w$ .

III. Raise the barriers simultaneously in a time  $T_a/2$ ,  
 $\alpha_1 = \alpha_2 = \alpha_{\min} \rightarrow 1$ .

The total gate time thus becomes the sum of the waiting time and the adiabatic control time,  $T_{2Q} = T_a + T_w$ .

When the barriers are lowered, the qubits can exchange excitations through the capacitive coupling element resulting in an effective  $\sigma_x^{(1)}\sigma_x^{(2)} + \sigma_y^{(1)}\sigma_y^{(2)}$  interaction. Crucially, the adiabatic control time can be adjusted such that there occurs a transition between the states  $|01\rangle$  and  $|10\rangle$  due to their small energy difference and not between other computational states whose energy difference is large compared to the adiabatic time. As shown in Fig. 4(b), an avoided crossing occurs near  $\alpha = 0.75$ . On the other side of this avoided crossing, when  $\alpha$  is further decreased, the coupling dramatically increases. See also Fig. 7, where the  $\sigma_z^{(1)}\sigma_z^{(2)}$ -interaction strength is shown. The avoided crossing shown in Fig. 4(b) is a generic feature of the coupled spectrum as long as the qubit frequencies of the two interacting qubits are similar at  $\alpha = 1$ .

To exclude transitions between the other computational states and transitions out of the computational subspace, the speed at which  $\alpha$  is lowered should be slower compared to the single qubit gate. As a concrete example, we consider lowering the barriers with a constant speed, meaning that the adiabatic time is proportional to the minimum value  $\alpha_{\min} = 1 - \frac{T_a/2}{2 \cdot 35 \text{ ns}}$ . Thus, the barrier can be completely lowered in 35 ns which is three times slower than for the lowering rate used for the single qubit gate. Adiabatic lowering/raising times  $T_a/2$  less than 35 ns results in only partly lowering the barrier due to the constant lowering/raising speed, see also Fig. 4(c).

In addition to the  $\sigma_x^{(1)}\sigma_x^{(2)} + \sigma_y^{(1)}\sigma_y^{(2)}$  interaction, the energies of the coupled system shifts relative to the bare energies due to an effective  $\sigma_z^{(1)}\sigma_z^{(2)}$  interaction, see also Appendix C. Below we simulate the two-qubit gate shown in Fig. 4 and discuss the types of gates achieved. The two-qubit unitaries can be modelled by a two-qubit interacting system of the following form

$$H_{\text{eff}} = -\frac{\omega_1}{2}\sigma_z^{(1)} - \frac{\omega_2}{2}\sigma_z^{(2)} \quad (6)$$

$$+ \frac{g_{xy}}{2} \left( \sigma_x^{(1)}\sigma_x^{(2)} + \sigma_y^{(1)}\sigma_y^{(2)} \right) + \frac{g_z}{2}\sigma_z^{(1)}\sigma_z^{(2)},$$

where the  $\sigma_{x,y,z}^{(i)}$ 's are Pauli matrices acting in the logical subspace of qubit  $i$ ,  $\omega_i$  describe the qubit frequencies, and the swap coupling  $g_{xy}$  and  $\sigma_z^{(1)}\sigma_z^{(2)}$  coupling  $g_z$  are all  $\alpha$ -dependent. This model Hamiltonian gives rise to the so-called fSim-gates which interpolate between the

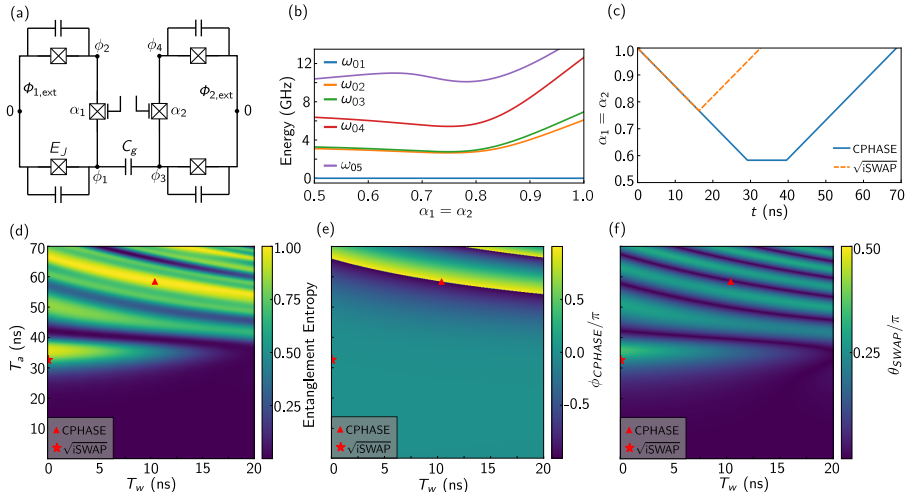


FIG. 4. Two qubit setup and gate characteristics from non-dissipative simulations. (a) Schematic of two capacitively coupled DSFQs with substantial coupling capacitance  $C_g = 0.3C$ . (b) The five lowest energy states shown as the two barriers are lowered simultaneously by decreasing  $\alpha_1 = \alpha_2$ . (c) The  $\alpha_1 = \alpha_2$  profile as a function of time for the CPHASE gate. (d) The entanglement entropy of the final two-qubit gate as a function of the waiting time  $T_w$  and the total adiabatic control time  $T_a$ . The red markers in this and subsequent panels show the optimal  $\sqrt{i}$ SWAP (star) and CPHASE (triangle) gates which have respective fidelities limited by coherent gate errors and gate times of  $\mathcal{F}_{\sqrt{i}\text{SWAP}} = 99.96\%$ ,  $T_{\sqrt{i}\text{SWAP}} = 32.66$  ns and  $\mathcal{F}_{\text{CPHASE}} = 99.95\%$ ,  $T_{\text{CPHASE}} = 68.76$  ns. The estimated  $T_1$ -limited fidelities are  $F_{\sqrt{i}\text{SWAP}} = 99.7\%$  and  $F_{\text{CPHASE}} = 91.4\%$ . (e-f) The resulting phase and swap parameters  $\phi_{\text{CPHASE}}$  and  $\theta_{\text{SWAP}}$  of the final two-qubit gate as a function of the waiting time  $T_w$  and the total adiabatic control time  $T_a$ . The flux bias is set to  $\phi_{\text{ext}} = 0.99\pi$ .

iSWAP- and CPHASE-gate [39, 40],

$$U_{\text{fSim}} = \begin{pmatrix} 1 & 0 & 0 & 0 \\ 0 & \cos(\theta_{\text{SWAP}}) & -i \sin(\theta_{\text{SWAP}}) & 0 \\ 0 & -i \sin(\theta_{\text{SWAP}}) & \cos(\theta_{\text{SWAP}}) & 0 \\ 0 & 0 & 0 & e^{-i\phi_{\text{CPHASE}}} \end{pmatrix} \quad (7)$$

which is precisely what we see in the simulation of the full model. By timing the adiabatic control time and the waiting time to match  $|01\rangle \leftrightarrow |10\rangle$  swap oscillations and the rotating  $\sigma_z^{(1)}\sigma_z^{(2)}$ -phase, different gates in the fSim-space can be targeted as shown in Fig. 4(d-f). Here, we sweep over the adiabatic and waiting times,  $T_a$  and  $T_w$ , and in panel (d), we display the entanglement entropy which is normalized to unity for maximally entangling gates [41]. The only maximally entangling gates in the fSim-space are CPHASE and iSWAP. In panels (e) and (f), we decompose the resulting unitary into the fSim-parameters; the phase angle  $\phi_{\text{CPHASE}}$  and the swap angle  $\theta_{\text{SWAP}}$ . The red markers show two example gates in the fSim-space; the CPHASE and  $\sqrt{i}$ SWAP gates. The fidelity limited by coherent errors (leakage) is well beyond 99.9% (up to single qubit  $\sigma_z$ -gates) and can be performed in about 69 ns and 33 ns respectively. Again, the two-qubit gates are limited by decay, with

estimated  $T_1$ -limited fidelities of  $F_{\sqrt{i}\text{SWAP}} = 99.7\%$  and  $F_{\text{CPHASE}} = 91.4\%$ . The fidelity of the CPHASE gate is severely impacted by the low qubit coherence near  $\alpha = 0.6$  where  $T_1 = 0.6\mu\text{s}$  but the  $\sqrt{i}$ SWAP gate is a promising high fidelity alternative. The iSWAP gate cannot be implemented to high fidelity as it requires both fine-tuning of energies to achieve a full swap of excitations and zero (mod  $2\pi$ )  $\sigma_z^{(1)}\sigma_z^{(2)}$ -phase. The combined requirement is challenging to tune with our parameters, so we instead propose to simply apply two  $\sqrt{i}$ SWAP gates successively. The  $\sqrt{i}$ SWAP gate is comparatively easy to perform as a partial swap of excitations happens before any significant  $\sigma_z^{(1)}\sigma_z^{(2)}$  phase is accrued. Finally, The CPHASE gate depends to an intermediate degree on the Hamiltonian parameters as it does not require a transfer of excitations. Our testing finds that appropriate times  $T_a$  and  $T_w$  can be chosen for a range of parameters to yield a CPHASE gate.

As mentioned, the wave functions change substantially as the barriers are lowered and complicates the simulation of the qubit interactions. In order to faithfully simulate the time-evolution, we numerically diagonalize the charge-basis Hamiltonian ( $n_{\text{cutoff}} = 9$ ) at each  $\alpha$  and keep the 24 lowest states. Since the diagonalizing unitary,  $V : V^\dagger H V = \text{diag}(E_1, E_2, \dots)$ , is time-dependent,

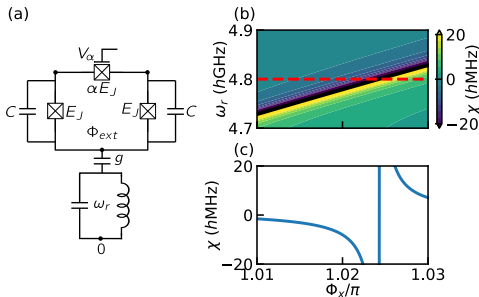


FIG. 5. (a) The qubit coupled to a readout resonator. The qubit induces a state-dependent shift of the frequency of the resonator, which can be measured using standard techniques. (b) Dispersive shift as a function of external flux. By adjusting the flux away from half flux bias, a resonance between one of the computational states become and a higher energy states comes close to the frequency of the readout resonator. The resonator shift is increased resulting in a stronger readout signal. A smaller shift is preferable in the context of error suppression where it reduces the sensitivity to photon-shot noise.

the Schrödinger equation acquires an additional term,  $-iV^\dagger\partial_t V$ . Finally, using the combined Hamiltonian  $H = H_1 + H_2 + H_{Q-Q}$  (Eqs. (1), (2) and (5)), the time-evolution operator of the lowest 24 states is evolved by  $\exp[-i(V^\dagger H V - iV^\dagger\partial_t V)\Delta t]$  at each timestep  $\Delta t$  (286 timesteps/nanosecond).

Despite relying only on adiabatic control, the two-qubit gates presented here are competitive compared to state-of-the-art two-qubit gates for both single- and double-well qubits [18, 19, 21]. Further advantages include the exponential on/off coupling ratio, that only the computational states are used and the possibility of being able to produce different gates in the fSim-space. Further developments, for example controlling  $\alpha_1$  and  $\alpha_2$  individually as well as the fluxes, will likely provide more control over what fSim-gates can be reached and reduce the overall gate time or increase fidelities using optimized strategies. Additionally, recent work suggests to also use the DSFQ as a transmon-transmon coupler (called the “double transmon coupler”), which illustrates the exciting flexibility of the device [42].

### C. Readout

Readout of the DSFQ device can be performed using conventional dispersive readout techniques [39]. However, rather than reading out via the  $\phi$ -mode, similar to fluxonium qubits, we instead propose to readout via the  $\theta$ -mode. By coupling the qubit capacitively to a readout resonator through the  $\theta$  degree of freedom, as shown in Fig. 5(a), we can achieve substantial dispersive shifts

while remaining in the protected qubit regime to suppress (Purcell enhanced) relaxation. As we detail below, the plasmon frequency of the  $\theta$ -mode depends on which well the  $\phi$ -mode is localized in. Further, the difference in plasma frequencies for the two wells are tuned by the external magnetic flux. In this way, we can use the external flux to control the state dependent shift of the readout resonator as shown in Fig. 5(b-c).

We start by considering the Hamiltonian of the combined system which can be written as [39]

$$H = H_{\text{sys}} + g(a + a^\dagger)n_\theta + \omega_r a^\dagger a, \quad (8)$$

where  $H_{\text{sys}}$  is the qubit Hamiltonian,  $a(a^\dagger)$  is the resonator annihilation(creation) operator,  $\omega_r$  is the bare resonator frequency and  $g$  is the coupling strength between resonator and qubit. In the dispersive regime, the resonator frequency is effectively shifted by the state of the qubit. This can be seen by performing a Schrieffer-Wolff transformation [43, 44] to second order,

$$H_{\text{eff}} = H_{\text{sys}} + \omega_r a^\dagger a - \left(\frac{\chi}{2} a^\dagger a + \delta\right) \sigma_z, \quad (9)$$

where  $\chi$  is the qubit state dependent resonator shift,  $\delta$  is a small shift of the qubit frequency and  $\sigma_z = |0\rangle\langle 0| - |1\rangle\langle 1|$  is the qubit Pauli Z operator. To correctly estimate the dispersive resonator shift it is important to account for higher levels outside of the computational subspace. Carrying out the perturbation calculation, we find the dispersive shift as  $\chi = \sum_j \chi_{1j} - \chi_{0j}$ , where

$$\chi_{ij} = g^2 |\langle i|n_\theta|j\rangle|^2 \left( \frac{1}{E_i - E_j - \omega_r} + \frac{1}{E_i - E_j + \omega_r} \right). \quad (10)$$

Figure 5(b, c) shows the resonator shift as a function of the externally applied magnetic flux. For these simulations, we have used a bare resonator frequency of  $\omega_r = 4.8 h$  GHz and coupling strength of  $g = 25 h$  MHz.

To explain the working principle of the readout, we briefly adopt a simple, minimal model of the DSFQ. In this model, we assume that we are away from the sweet-spot at exactly half flux quantum and write an effective potential for the  $\theta$ -degree of freedom by freezing the  $\phi$ -degree of freedom to one of the two minima at  $\phi_\pm = (\pm\pi - \delta\phi_{\text{ext}})/3$  for  $\alpha = 1$  and thus momentarily neglect tunneling between the two wells,

$$V_\pm = \mp E_J \frac{\delta\phi_{\text{ext}}}{2\sqrt{3}} - E_J \left( 1 \pm \frac{\delta\phi_{\text{ext}}}{\sqrt{3}} \right) \cos(\theta), \quad (11)$$

where  $\phi_{\text{ext}} = \pi + \delta\phi$  and  $\delta\phi \ll 1$ . In this picture, each minima corresponds to one of the computational states. Close to half flux bias ( $\delta\phi_{\text{ext}} \approx 0$ ),  $V_\pm$  are nearly identical and the readout resonator cannot discriminate between the computational states as the matrix elements  $|\langle \pm|n_\theta|j\rangle|$  are approximately the same for the two qubit states  $|\pm\rangle$ . By increasing the offset from the flux frustration point, the two terms in Eq. (11) lead to differences between the two wells that can result in a large dispersive

shift if the readout resonator is close in frequency to the plasma frequency of the  $\theta$ -mode in one of the wells. The first term in Eq. (11) contains the simple energy splitting between the two wells due to the external flux which does not change the plasmon frequency. The second term in Eq. (11) shows that the plasmon frequency of the  $\theta$ -mode in each well  $\omega_{\theta}^{\pm} = \sqrt{8\tilde{E}_C\tilde{E}_J^{\pm}}$ , where  $\tilde{E}_C$  and  $\tilde{E}_J^{\pm}$  are the effective charging and Josephson energies of the  $\theta$ -mode [39], also depends on the offset from half flux bias. In this way, we may tune the plasmon frequency in one of the wells close to the readout resonator frequency and thereby achieve a large dispersive shift, see Fig. 5(b-c). We may now consider what happens at exactly half flux quantum where the small tunneling between the wells results in wave functions that are even/odd in  $\phi$ . In this situation, different selection rules for the even/odd computational states dictate what matrix elements can be nonzero and will generally result in a nonzero dispersive shift. However, as the resonator frequency can be far off the frequency of the contributing transitions, the dispersive shift remains small.

There are several advantages to performing readout in the proposed scheme: Suppression of the dispersive shift controlled by the external flux grants us insensitivity to dephasing through photon shot noise [39]. By coupling the readout resonator to the  $\theta$ -mode of the qubit, we also obtain protection against Purcell decay: The matrix element  $\langle 0|n_{\theta}|1\rangle$  (or in the notation surrounding Eq. (11)),  $\langle +|n_{\theta}|-\rangle$  is zero since the computational states are both in the even  $\theta$ -mode ground state in their respective wells. Via this mechanism, the qubit is protected from the Purcell effect due to the symmetries of the wave functions. There are no additional Purcell effect due to  $n_{\phi}$  as the readout resonator remains decoupled from this mode. In total, the dominant source of error during readout is the direct tunneling between the qubit states. The  $T_1$ -times computed in Sec. II depends weakly on the external flux and for readout at  $\phi_{\text{ext}} = 1.023\pi$  we find  $T_1 = 519 \mu\text{s}$ . For a readout integration time around  $1 \mu\text{s}$ , the  $T_1$ -limited readout fidelity is  $F = 99.8\%$ .

#### IV. CONCLUSIONS AND DISCUSSIONS

In this paper, we have shown how gates and readout can be performed on a new flux qubit variation with a variable level of  $T_1$ -protection, the DSFQ. By adiabatically reducing the height of the barrier, the otherwise insensitive qubit can be made sensitive to a microwave drive. Our implementation of this variable-protection gate scheme shows that fast, high fidelity single qubits gates can be performed without involving lossy non-computational states. We achieve single qubit gates with coherence limited fidelities at 99.98% in 25 ns, making it competitive with established gate schemes for both protected and unprotected qubits. However, non-optimized gates suffer from  $T_1$  decay during the lowering of the

barrier and results in a  $T_1$ -limited gate fidelity of 99.1%. Likewise, we show that by lowering the barriers of two capacitively coupled DSFQs, that high fidelity two qubit gates in the fSim-space can be performed. Specifically, we find CPHASE and  $\sqrt{\text{ISWAP}}$  gates with a coherence limited fidelity above 99.9% in 69 ns and 33 ns respectively without residual ZZ-interactions. Again, the two-qubit gates are limited by relaxation and the  $T_1$ -limited fidelities are  $F_{\text{CPHASE}} = 91.4\%$  and  $F_{\sqrt{\text{ISWAP}}} = 99.7\%$  respectively. The fidelities and gate times can be further improved by using optimized protocols.

We have further shown that readout can be performed efficiently in the  $T_1$ -protected regime by adjusting the external flux bias away from the flux frustration point. Near half a flux bias, the dispersive shift is not only reduced due to the qubit-resonator detuning, but also due to the approximate symmetry between the two wells. With the order-of-magnitude variations in dispersive shift and separated double-wells, the DSFQ is robust against noise channels arising from the coupling to the resonator.

In addition to the  $T_1$ -protection, we have also proposed a gradiometric double-loop variation of the DSFQ which is exponentially insensitive to global flux noise while remaining linearly sensitive to local flux noise. We show that area variability of the loops can be compensated for by making the tunable junction slightly asymmetric without being sensitive to the noise in the tunable junctions.

In total, the DSFQ presents an experimentally available platform for studying qubits with a variable level of  $T_1$ -protection, where gates can be performed without involving non-computational states. This contribution may help pave the way for achieving fast, high fidelity gates on protected qubits using this novel gate implementation.

#### V. ACKNOWLEDGMENTS

We acknowledge helpful discussions from András Gyenis and Jonas Vinther and are grateful to Terry P. Orlando for comments on the manuscript. This research was supported by the Danish National Research Foundation, the Danish Council for Independent Research | Natural Sciences. This project has received funding from the European Research Council (ERC) under the European Union's Horizon 2020 research and innovation programme under Grant Agreement No. 856526. We acknowledge support from the Deutsche Forschungsgemeinschaft (DFG) – project grant 277101999 – within the CRC network TR 183 (subproject C03). MK gratefully acknowledges support for this research in part by the U.S. Army Research Office Grant No. W911NF-22-1-0042 and in part by the Villum Foundation (grant 37467) through a Villum Young Investigator grant.

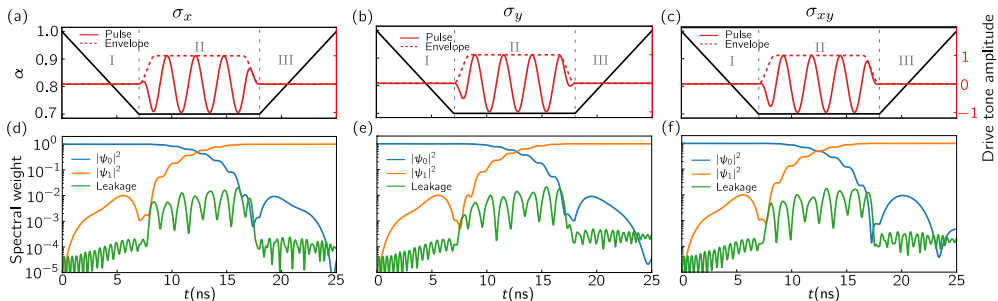


FIG. 6. (a)-(c) Pulse sequence for the  $\sigma_x$ ,  $\sigma_y$  and  $\sigma_{xy} = (\sigma_x - \sigma_y)/\sqrt{2}$ . Parameters for the pulse envelope and the  $\alpha$ -profile is identical to those in Fig. 3. The phase offset and drive frequency are in the three cases: (a)  $\phi_{\text{offset}} = 0\pi$ ,  $\omega_d = 0.979\omega_q$ , (b)  $\phi_{\text{offset}} = 0.5\pi$ ,  $\omega_d = 0.979\omega_q$  and (c)  $\phi_{\text{offset}} = 0.26\pi$ ,  $\omega_d = 0.977\omega_q$ . (d)-(f) Corresponding evolution of the states during the gate operation. The fidelities in the three panels are (d)  $F_x = 99.98\%$ , (e)  $F_y = 99.98\%$  and (f)  $F_{xy} = 99.93\%$ .

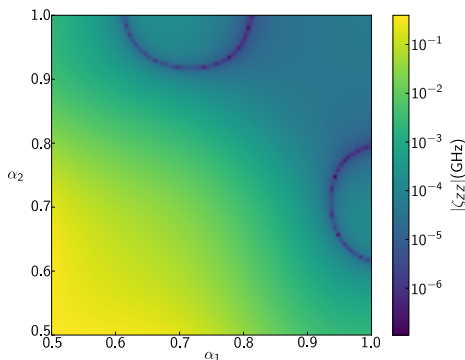


FIG. 7. Plot of the ZZ-interaction strength due to the capacitive coupling. When one or none of the barriers are lowered, the interaction strength is suppressed to the 10 kHz level.

### Appendix A: Gradiometric DSFQ

To better understand the dependence on the global flux, we look at the potential energy for the double-loop qubit

$$H_J = -E_J \cos(\phi_1) - E_J \cos(\phi_2) + H_{J\alpha},$$

$$H_{J\alpha} = -\frac{E_J}{2} [\alpha_1 \cos(\phi_{\text{ext},1} + 2\phi) + \alpha_2 \cos(\phi_{\text{ext},2} + 2\phi)]. \quad (\text{A1})$$

Here the flux-induced phases are given by

$$\phi_{\text{ext},1,2} = \frac{\pm 2\pi A_{1,2} B_{1,2}}{\Phi_0}, \quad (\text{A2})$$

where  $A_{1,2}$  are the areas of the two loops and  $B_{1,2} = (B \pm b)/2$  are the field through them.

In the symmetric case when  $A_1 B_1 = A_2 B_2$ ,  $\alpha_1 = \alpha_2$  the flux-dependent term becomes

$$H_{J\alpha} = -\frac{E_J}{2} \alpha_1 \cos(2\phi) \cos(\phi_{\text{ext},1}), \quad (\text{A3})$$

and we see that the potential maintains the symmetry with two degenerate minima for all values of the global field  $B$ . However, it is not realistic to assume that the two areas can be fabricated to be identical. Therefore, we consider the situation where they differ by some (small) amount. To study this case, we write  $H_{J\alpha}$  as

$$H_{J\alpha} = -\frac{E_J}{2} [V_c \cos(2\phi) - V_s \sin(2\phi)], \quad (\text{A4})$$

where

$$V_c = \alpha_1 \cos(\phi_{\text{ext},1}) + \alpha_2 \cos(\phi_{\text{ext},2}), \quad (\text{A5a})$$

$$V_s = \alpha_1 \sin(\phi_{\text{ext},1}) + \alpha_2 \sin(\phi_{\text{ext},2}). \quad (\text{A5b})$$

The splitting of the degeneracy of the minima of  $V_c$  is controlled by the second term  $V_s$ . One could, in principle, choose a set parameters  $(\alpha_1, \alpha_2, B_1, B_2)$  such that  $V_s = 0$  and regain the degenerate double-well potential. However, the degeneracy is lifted linearly in both the global external field  $B$  and the tuning of the Josephson junctions, and the situation is therefore worse than before. Instead, we search for a point where the qubit is split by the different well depths, but with at least quadratic protection against deviations from the mentioned set of parameters. If both junctions in the outer SQUID-loop are tunable junctions, we have to minimize with respect to both which gives the condition  $\sin(\phi_{\text{ext},1}) = \sin(\phi_{\text{ext},2})$  at the operating point. Consequently, the condition for the junctions when minimizing with respect to the global field  $B$  is

$$A_1 \alpha_1 = A_2 \alpha_2. \quad (\text{A6})$$

If the tunable junctions are parameterized as  $\alpha_2 = (1 + \delta)\alpha_1$ , the condition obtaining the sweet spot where the splitting is quadratic or better in  $\delta$  and  $B$  is

$$\frac{\partial V_s}{\partial \delta} = 0 \rightarrow \sin(\phi_{\text{ext},2}) = 0, \quad (\text{A7a})$$

$$\frac{\partial V_s}{\partial B} = 0 \rightarrow \cos(\phi_{\text{ext},1}) = \frac{(1 + \delta)A_2}{A_1} \cos(\phi_{\text{ext},2}). \quad (\text{A7b})$$

Note that the condition in Eq. (A7a) results in a  $V_s$  which is insensitive to  $\delta$  for all  $\delta$ . If the flux through the two loops is controlled by a single global field (i.e.,  $b = 0$ ), the two equations above can be combined to give the following condition on  $\delta$ ,

$$\delta = -1 + \frac{1+r}{1-r} \cos\left(\frac{2\pi r}{1-r}\right) \approx 2r, \quad r = \frac{A_1 - A_2}{A_1 + A_2}, \quad (\text{A8})$$

for small  $r$ .

### Appendix B: IQ-mixing

We show that our single qubit gate scheme is compatible with IQ-mixing in Fig. 6. The pulses are parameterized by  $\varepsilon(t) \cos(\omega_d t + \phi_{\text{offset}})$ , where  $\varepsilon(t)$  is the envelope with cosine ramp up/down and  $\phi_{\text{offset}}$  is the phase offset that determines the  $I$  and  $Q$  components. We display three flip gates  $\sigma_x$  (also found in Fig. 3),  $\sigma_y$  and  $\sigma_{xy} = (\sigma_x - \sigma_y)/\sqrt{2}$  with similar fidelities  $> 99.9\%$  and a 25 ns gate time. The pulse parameters can be found in the caption of Fig. 6.

### Appendix C: Q-Q coupling

Two coupled DSFQs are shown in Fig. 4(a). The Lagrangian for the total circuit is

$$\begin{aligned} \mathcal{L} = & \frac{C}{2} \dot{\phi}_1^2 + \frac{C}{2} \dot{\phi}_2^2 + \frac{C}{2} \dot{\phi}_3^2 + \frac{C}{2} \dot{\phi}_4^2 \\ & + \frac{C_g}{2} (\dot{\phi}_1 - \dot{\phi}_3)^2 \\ & + E_J \cos \phi_1 + E_J \cos \phi_2 + \alpha_1 E_J \cos(\phi_1 - \phi_2 + \phi_{\text{ext},1}) \\ & + E_J \cos \phi_3 + E_J \cos \phi_4 + \alpha_2 E_J \cos(\phi_3 - \phi_4 + \phi_{\text{ext},2}). \end{aligned} \quad (\text{C1})$$

By performing a Legendre transformation, we arrive at the result

$$\begin{aligned} H_{1(2)} = & 4E_C \left( \frac{C + C_g}{C + 2C_g} \right) n_{1(3)}^2 + 4E_C n_{2(4)}^2 \\ & - E_J \cos \phi_{1(3)} + E_J \cos \phi_{2(4)} \\ & + \alpha_{1(2)} E_J \cos(\phi_{1(3)} - \phi_{2(4)} + \phi_{\text{ext}_{1(2)}}), \\ H_{\text{Q-Q}} = & 4E_C \left( \frac{C_g}{C + C_g} \right) n_1 n_3, \end{aligned} \quad (\text{C2})$$

where 1(2) refers to qubit 1(2) with charge and phase operators  $n_{1(3)}, n_{2(4)}, \phi_{1(3)}, \phi_{2(4)}$ . The full Hamiltonian is a sum the two qubit Hamiltonians and the interaction term,  $H = H_1 + H_2 + H_{\text{Q-Q}}$ . The qubit Hamiltonians have been renormalized due to the coupling capacitance between the two circuits. In Fig. 7, we show the  $\sigma_z^{(1)} \sigma_z^{(2)}$  coupling due to the capacitive coupling defined by  $\zeta_{ZZ} = \omega_{00} - \omega_{01} - \omega_{10} + \omega_{11}$ . In Fig. 7, it is apparent that the  $\sigma_z^{(1)} \sigma_z^{(2)}$  coupling is suppressed unless both barriers are lowered. Thus, single qubit gates where only one barrier is lowered do not give rise to unwanted  $\sigma_z^{(1)} \sigma_z^{(2)}$  interactions. However, we are limited to only half-grid single qubit gates if we neglect the next nearest neighbor stray capacitances. As a final remark, we would like to point to the half-circular suppression of  $\zeta_{<<}$  in Fig. 7. This interesting feature appears when the sign of the  $\sigma_z^{(1)} \sigma_z^{(2)}$  interaction changes. In colloquial terms, the  $\sigma_z^{(1)} \sigma_z^{(2)}$  interaction is exactly cancelled when the “push” or “pull” on the  $|11\rangle$  state from states below it is exactly compensated for by the push/pull from states above it.

- 
- [1] M. Kjaergaard, M. E. Schwartz, J. Braumüller, P. Krantz, J. I.-J. Wang, S. Gustavsson, and W. D. Oliver, Superconducting Qubits: Current State of Play, *Annual Review of Condensed Matter Physics* **11**, 369 (2020).
- [2] A. Gyenis, A. Di Paolo, J. Koch, A. Blais, A. A. Houck, and D. I. Schuster, Moving beyond the Trans-

mon: Noise-Protected Superconducting Quantum Circuits, *PRX Quantum* **2**, 030101 (2021).

- [3] I. Siddiqi, Engineering high-coherence superconducting qubits, *Nature Reviews Materials* **6**, 875 (2021).
- [4] E. Dennis, A. Kitaev, A. Landahl, and J. Preskill, Topological quantum memory, *Journal of Mathematical Physics* **43**, 4452 (2002).



- 
- [5] A. G. Fowler, M. Mariantoni, J. M. Martinis, and A. N. Cleland, Surface codes: Towards practical large-scale quantum computation, *Phys. Rev. A* **86**, 032324 (2012).
- [6] Y. Zhao *et al.*, Realization of an Error-Correcting Surface Code with Superconducting Qubits, *Physical Review Letters* **129**, 030501 (2022).
- [7] S. Krimmer *et al.*, Realizing repeated quantum error correction in a distance-three surface code, *Nature* **605**, 669 (2022).
- [8] R. Acharya *et al.*, Suppressing quantum errors by scaling a surface code logical qubit, *Nature* **614**, 676 (2023).
- [9] P. Brooks, A. Kitaev, and J. Preskill, Protected gates for superconducting qubits, *Physical Review A* **87**, 052306 (2013).
- [10] N. Earnest *et al.*, Realization of a  $\Lambda$  system with metastable states of a capacitively shunted fluxonium, *Phys. Rev. Lett.* **120**, 150504 (2018).
- [11] T. W. Larsen, M. E. Gershenson, L. Casparis, A. Kringhøj, N. J. Pearson, R. P. G. McNeil, F. Kuemmeth, P. Krogstrup, K. D. Petersson, and C. M. Marcus, Parity-Protected Superconductor-Semiconductor Qubit, *Physical Review Letters* **125**, 056801 (2020).
- [12] K. Kalashnikov, W. T. Hsieh, W. Zhang, W.-S. Lu, P. Kamenov, A. Di Paolo, A. Blais, M. E. Gershenson, and M. Bell, Bifluxon: Fluxon-Parity-Protected Superconducting Qubit, *PRX Quantum* **1**, 010307 (2020).
- [13] P. Groszkowski, A. D. Paolo, A. L. Grimsmo, A. Blais, D. I. Schuster, A. A. Houck, and J. Koch, Coherence properties of the  $0-\pi$  qubit, *New Journal of Physics* **20**, 043053 (2018).
- [14] L. B. Nguyen *et al.*, Blueprint for a high-performance fluxonium quantum processor, *PRX Quantum* **3**, 037001 (2022).
- [15] T. P. Orlando, J. E. Mooij, L. Tian, C. H. van der Wal, L. S. Levitov, S. Lloyd, and J. J. Mazo, Superconducting persistent-current qubit, *Physical Review B* **60**, 15398 (1999).
- [16] V. E. Manucharyan, J. Koch, L. I. Glazman, and M. H. Devoret, Fluxonium: Single Cooper-Pair Circuit Free of Charge Offsets, *Science* **326**, 113 (2009).
- [17] J. E. Mooij, T. P. Orlando, L. Levitov, L. Tian, C. H. van der Wal, and S. Lloyd, Josephson Persistent-Current Qubit, *Science* **285**, 1036 (1999).
- [18] H. Zhang, S. Chakram, T. Roy, N. Earnest, Y. Lu, Z. Huang, D. K. Weiss, J. Koch, and D. I. Schuster, Universal Fast-Flux Control of a Coherent, Low-Frequency Qubit, *Physical Review X* **11**, 011010 (2021).
- [19] A. Gyenis, P. S. Mundada, A. Di Paolo, T. M. Hazard, X. You, D. I. Schuster, J. Koch, A. Blais, and A. A. Houck, Experimental Realization of a Protected Superconducting Circuit Derived from the  $0-\pi$  Qubit, *PRX Quantum* **2**, 010339 (2021).
- [20] M. Abdelhafez, B. Baker, A. Gyenis, P. Mundada, A. A. Houck, D. Schuster, and J. Koch, Universal gates for protected superconducting qubits using optimal control, *Physical Review A* **101**, 022321 (2020).
- [21] Q. Ficheux, L. B. Nguyen, A. Somoroff, H. Xiong, K. N. Nesterov, M. G. Vavilov, and V. E. Manucharyan, Fast Logic with Slow Qubits: Microwave-Activated Controlled-Z Gate on Low-Frequency Fluxoniums, *Physical Review X* **11**, 021026 (2021).
- [22] F. Yan *et al.*, The flux qubit revisited to enhance coherence and reproducibility, *Nature Communications* **7**, 12964 (2016).
- [23] F. G. Paauw, A. Fedorov, C. J. P. M. Harmans, and J. E. Mooij, Tuning the Gap of a Superconducting Flux Qubit, *Physical Review Letters* **102**, 090501 (2009).
- [24] X. Zhu, A. Kemp, S. Saito, and K. Semba, Coherent operation of a gap-tunable flux qubit, *Applied Physics Letters* **97**, 102503 (2010).
- [25] S. Gustavsson, J. Bylander, F. Yan, W. D. Oliver, F. Yoshihara, and Y. Nakamura, Noise correlations in a flux qubit with tunable tunnel coupling, *Phys. Rev. B* **84**, 014525 (2011).
- [26] M. J. Schwarz, J. Goetz, Z. Jiang, T. Niemczyk, F. Deppe, A. Marx, and R. Gross, Gradiometric flux qubits with a tunable gap, *New Journal of Physics* **15**, 045001 (2013).
- [27] T. W. Larsen, K. D. Petersson, F. Kuemmeth, T. S. Jespersen, P. Krogstrup, J. Nygård, and C. M. Marcus, Semiconductor-Nanowire-Based Superconducting Qubit, *Physical Review Letters* **115**, 127001 (2015).
- [28] L. Casparis, T. W. Larsen, M. S. Olsen, F. Kuemmeth, P. Krogstrup, J. Nygård, K. D. Petersson, and C. M. Marcus, Gatemon benchmarking and two-qubit operations, *Phys. Rev. Lett.* **116**, 150505 (2016).
- [29] L. Casparis *et al.*, Superconducting gatemon qubit based on a proximitized two-dimensional electron gas, *Nature Nanotechnology* **13**, 915 (2018).
- [30] A. Hertel *et al.*, Gate-tunable transmon using selective-area-grown superconductor-semiconductor hybrid structures on silicon, *Phys. Rev. Appl.* **18**, 034042 (2022).
- [31] R. Aguado, A perspective on semiconductor-based superconducting qubits, *Applied Physics Letters* **117**, 240501 (2020).
- [32] D. Gusenkova *et al.*, Operating in a deep underground facility improves the locking of gradiometric fluxonium qubits at the sweet spots, *Applied Physics Letters* **120**, 054001 (2022).
- [33] S. E. Rasmussen, K. S. Christensen, S. P. Pedersen, L. B. Kristensen, T. Bækkegaard, N. J. S. Loft, and N. T. Zinner, Superconducting Circuit Companion—An Introduction with Worked Examples, *PRX Quantum* **2**, 040204 (2021).
- [34] A. Kou, W. C. Smith, U. Vool, R. T. Brierley, H. Meier, L. Frunzio, S. M. Girvin, L. I. Glazman, and M. H. Devoret, Fluxonium-Based Artificial Molecule with a Tunable Magnetic Moment, *Physical Review X* **7**, 031037 (2017).
- [35] G. Ithier, E. Collin, P. Joyez, P. J. Meeson, D. Vion, D. Esteve, F. Chiarello, A. Shnirman, Y. Makhlin, J. Schrieffer, and G. Schön, Decoherence in a superconducting quantum bit circuit, *Physical Review B* **72**, 134519 (2005).
- [36] L. B. Nguyen, Y.-H. Lin, A. Somoroff, R. Mencia, N. Grabon, and V. E. Manucharyan, High-Coherence Fluxonium Qubit, *Physical Review X* **9**, 041041 (2019).
- [37] C. Wang, X. Li, H. Xu, Z. Li, J. Wang, Z. Yang, Z. Mi, X. Liang, T. Su, C. Yang, G. Wang, W. Wang, Y. Li, M. Chen, C. Li, K. Linghu, J. Han, Y. Zhang, Y. Feng, Y. Song, T. Ma, J. Zhang, R. Wang, P. Zhao, W. Liu, G. Xue, Y. Jin, and H. Yu, Towards practical quantum computers: transmon qubit with a lifetime approaching 0.5 milliseconds, *npj Quantum Information* **8**, 1 (2022), number: 1 Publisher: Nature Publishing Group.
- [38] F. Motzoi, J. M. Gambetta, P. Rebentrost, and F. K. Wilhelm, Simple pulses for elimination of leakage in weakly nonlinear qubits, *Phys. Rev. Lett.* **103**, 110501 (2009).

- (2009).
- [39] P. Krantz, M. Kjaergaard, F. Yan, T. P. Orlando, S. Gustavsson, and W. D. Oliver, A Quantum Engineer's Guide to Superconducting Qubits, *Applied Physics Reviews* **6**, 021318 (2019).
- [40] B. Foxen *et al.*, Demonstrating a Continuous Set of Two-Qubit Gates for Near-Term Quantum Algorithms, *Physical Review Letters* **125**, 120504 (2020).
- [41] P. Zanardi, C. Zalka, and L. Faoro, Entangling power of quantum evolutions, *Phys. Rev. A* **62**, 030301(R) (2000).
- [42] H. Goto, Double-transmon coupler: Fast two-qubit gate with no residual coupling for highly detuned superconducting qubits, *Phys. Rev. Appl.* **18**, 034038 (2022).
- [43] A. Blais, A. L. Grimsmo, S. M. Girvin, and A. Wallraff, Circuit quantum electrodynamics, *Reviews of Modern Physics* **93**, 025005 (2021).
- [44] G. Zhu, D. G. Ferguson, V. E. Manucharyan, and J. Koch, Circuit QED with fluxonium qubits: Theory of the dispersive regime, *Physical Review B* **87**, 024510 (2013), publisher: American Physical Society.

---

Towards deep protection of qubits using realistic quarton  
array superinductors

## Towards deep protection of qubits using realistic quarton array superinductors

Svend Krøjer,<sup>1,2</sup> Alexandre Blais,<sup>3,4</sup> Morten Kjaergaard,<sup>1,2</sup> and Karsten Flensberg<sup>1,2</sup>

<sup>1</sup>*Center for Quantum Devices, Niels Bohr Institute,*

*University of Copenhagen, DK-2100 Copenhagen, Denmark*

<sup>2</sup>*NNF Quantum Computing Programme, Niels Bohr Institute,*

*University of Copenhagen, 2100 Copenhagen, Denmark*

<sup>3</sup>*Institut quantique & Département de Physique, Université de Sherbrooke, Sherbrooke J1K2R1, Quebec, Canada*

<sup>4</sup>*Canadian Institute for Advanced Research, Toronto, M5G1M1 Ontario, Canada*

(Dated: November 28, 2023)

Large superinductors allow engineering of qubits that are protected against noise-induced decoherence. Often, superinductors are based on arrays of hundreds of Josephson junctions in series, where the inductance is the sum of Josephson inductances. Less conventionally, it is possible to boost the inductance of the array by canceling the harmonic part of the Josephson inductances and thereby realizing a nonlinear superinductor. Common to both designs are parasitic capacitances to ground which sets a practical limit to the magnitude of the impedance. In this work, we perform a detailed analysis of a nonlinear superinductor comprised of an array of quarton elements and discuss effects of component variations and optimal design parameters. We study dephasing of the three common flux noise protected qubits, the  $0 - \pi$  qubit, the bifluxon, and the Blochonium, implemented with nonlinear superinductors. We show that fluctuations of the fluxes in the quarton array are generally a limiting noise channel. Further, in the  $0 - \pi$  qubit, the nonlinear inductance, resulting from the use of quartons, gives rise to an always-on coupling to the spurious  $\zeta$  mode, leading to shot-noise dephasing. We find that shot-noise is limiting the coherence time unless the  $\zeta$  mode is actively cooled. Despite the noise channel that they introduce, the use of quartons array in superconductors significantly reduce the experimental requirement for realizing deep qubit protection.

### I. INTRODUCTION

Through clever design, protected qubits enjoy exponentially suppressed sensitivity to some or all noise sources at the hardware level [1–12]. By this virtue, protected qubits are expected to be useful components of heterogeneous quantum computers, for example as quantum memory [1].

Qubits can be protected from relaxation, dephasing or enjoy full protection from both mechanisms of decoherence [1]. Exponential enhancement of relaxation time  $T_1$  can be accomplished by engineering qubits with disjoint support of their logical wavefunctions [2–10]. The exponential suppression of dephasing due to charge noise can be attained in the transmon limit of large ratio of Josephson to charging energy [13] or by shunting the qubit with a superinductor [14, 15].

Realizing protection against dephasing due to flux noise at the hardware level, however, sets demanding requirements for the circuit components. While protection against dephasing due to charge noise is obtained in the transmon, it is a fundamental challenge to suppress flux noise in analogous fashion [1, 4, 5, 14, 15]. In principle, protection against flux noise dephasing can be achieved using an ultra-high inductance element such that the circuit impedance is much larger than the resistance quantum  $Z \gg R_Q = h/(2e)^2 \approx 6.45 \text{ k}\Omega$ . This limit defines  $Z \gg R_Q$  the “deep” regime of protection and results in large phase fluctuations  $\langle \phi^2 \rangle \propto Z/R_Q$  [2, 4, 5, 14]. In practice, however, the self-impedance of a simple wire loop is limited by the vacuum impedance  $Z_{\text{vac}} = 8\alpha R_Q \approx 377 \Omega$ , which is small compared to the resistance quan-

tum owing to the smallness of the fine-structure constant  $\alpha \approx 1/137$  [14–16]. The limit set by the impedance of free space can be circumvented in a number of ways to realize superinductors with a self-impedance  $Z_{\text{self}} > R_Q$ , however, self-capacitance or parasitic capacitance to ground always limits the maximal impedance [12, 14–26]. In broad terms, superinductance can result from large geometric or kinetic inductance [12, 14–26]. In a geometric superinductor, a superconducting wire is coiled in a planar spiral to overcome the vacuum impedance limit through increased self-inductance [12, 17]. Kinetic superinductors either leverage the large kinetic inductance inherent to disordered superconductors [18–26] or result from an ordered array of hundreds of Josephson junctions whose combined inductance is given by the sum of the (kinetic) Josephson inductances [14, 15]. The latter approach is widely used in, for example, fluxonium qubits [9, 10, 15, 27–32].

Three qubit designs with superinductor-based flux noise protection have been realized experimentally: the  $0 - \pi$  qubit [6], the bifluxon [7] and the Blochonium [11, 12]. These experiments show promising features of general noise protection, such as beyond millisecond  $T_1$  in the  $0 - \pi$  qubit [6], and suppression of relaxation and charge noise dephasing in the bifluxon tuned to its protected regime [7]. Common to all attempts of realizing protected qubits is, that their deep protected regime is not reached due to the superinductor self-impedance limit.

In this work, we explore how replacing Josephson junctions by quartons in superinductors can facilitate the realization of protected qubits in the deep protected regime. The quarton is a SQUID-like device where one of

the junctions is replaced by a small subarray of junctions. By balancing the ratios of Josephson energies and biasing the quarton with half a flux quantum, interference effects cancel the energy contribution quadratic in phase and result in an approximately quartic element [33, 34]. Stringing together quartons in an array results in a nonlinear superinductor with quartic phase dependence on the energy, and has been studied in the context of the “quartic” Blochonium [35]. Superinductors with tunable nonlinearity has been experimentally realized in the initial study found in Ref. [36].

Compared to state-of-the-art conventional junction arrays, we estimate that an equivalent quarton array superinductor (QASI) can achieve an order of magnitude improvement in inductance while reducing the number of junctions by a factor of three. If the capacitance to ground is further reduced, the self-impedance limit gets significantly increased, leading to continued improvements in the QASI over the conventional array. We also study array nonidealities and, however, find that the QASI shows increased sensitivity to variations in Josephson energies, leading to imperfect cancellation of the harmonic contribution. Requiring the junction variation to be below 1% ensures that the phase dependence is approximately quartic. Additionally, variations in loop areas are found to contribute to an energy term linear in the superconducting phase, something that can be mitigated by alternating the quarton loop orientations. To test the coherence properties of protected qubits based on QASIs, we numerically evaluate the dephasing time due to flux noise of the  $0 - \pi$ , bifluxon and Blochonium qubits. For the QASI-based  $0 - \pi$  qubit, we also evaluate the dephasing from photon shot-noise in the spurious  $\zeta$  mode, a known limiting noise channel [1, 4–6]. Based on our results, we argue that flux noise protection in the  $0 - \pi$  and Blochonium qubits can be achieved with reduced experimental requirements using the quarton array superinductor.

Finally, we note that there are several other applications of junction array superinductors that can potentially benefit from QASIs. These include models of 1D quantum systems [37], traveling wave parametric amplifiers [38–40] and Bloch oscillations for a quantum-metrology current standard [14, 41–46].

## II. JUNCTION ARRAY SUPERINDUCTORS

We begin by reviewing conventional junction array superinductors following Refs. [14, 15] before turning to the quarton array superinductor (QASI). The description of the QASI follows closely that of the conventional array which also serves as a natural comparison.

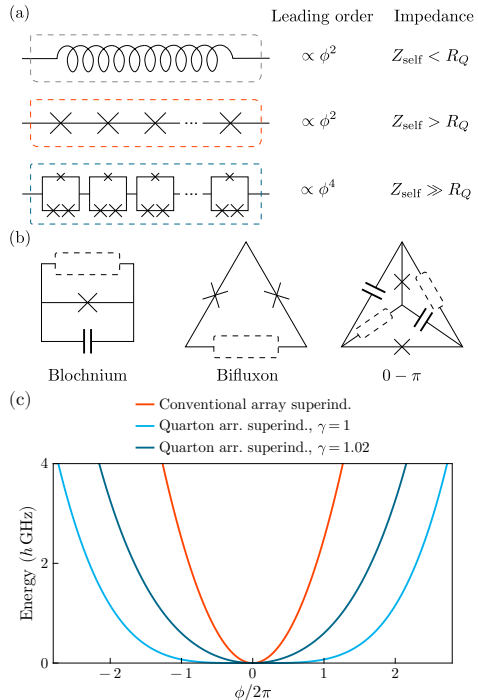


FIG. 1. (a) Comparison between geometric, conventional junction array and quarton array superinductors. (b) Circuit diagrams of Blochonium, bifluxon and  $0 - \pi$  qubits. The dashed boxes should contain large superinductors as shown in (a) to protect the qubits from flux noise. (c) The effective potentials of the conventional array (red line) and the quarton array with full/partial suppression of  $E_L$  (lightblue/darkblue lines). The quarton array superinductor can achieve larger inductances than the conventional array and also be tailored via the  $E_L$  suppression parameter  $\gamma - 1 \in [0, 1]$  to interpolate between  $\phi^4$ - and  $\phi^2$ -dominated potentials. The parameters are  $E_{JA} = 40 h$  GHz,  $E_{CA} = 0.25 h$  GHz and  $C_{gr}/C_{JA} = 10^{-5}$ .

### A. Conventional array superinductors

The conventional junction array superinductor consists of a series of  $N_J$  Josephson junctions with nominally identical Josephson energies  $E_{JA}$  and identical charging energies  $E_{CA} = e^2/2C_{JA}$ , see Fig. 1(a). In order for the array to effectively operate as a classical inductive element, the junctions are required to behave semi-classically. In other words, quantum phase slips should be suppressed and quantum excitations in the array should have a large energy cost. Avoiding quantum phase slips is straightforwardly satisfied by ex-

ponentially suppressing tunneling by making the ratio  $E_{JA}/E_{CA}$  large. Furthermore, the large  $E_{JA}/E_{CA}$  ratio results in a protection against random charge fluctuations [13]. The second requirement assures that the low-energy physics of the device is not dominated by the low-energy excitations of the array. This can be satisfied by taking  $\hbar\omega_{JA} = \sqrt{8E_{CA}E_{JA}} \gtrsim 10h\text{GHz}$  [16].

Using a large  $E_J/E_C$  ratio allows for two useful approximations to be made in the description of the device. We refer to the first approximation as the “distributed phase approximation” (DPA) which replaces the phase drop across the  $i$ th junction  $\phi_i$  with  $\phi/N_J$ , distributing the total phase drop across the array evenly among the identical junctions. Secondly, we may perform the standard expansion and truncation  $E_{JA}[1 - \cos(\phi/N_J)] = E_{JA}[(\phi/N_J)^2/2 - (\phi/N_J)^4/4! + \dots]$ . Summing up the contributions for all  $N_J$  junctions in these approximations results in an effective potential for the junction array,

$$V = \frac{1}{2}E_L\phi^2 + \frac{1}{2}E_{NL}\phi^4 + \dots, \quad (1)$$

where

$$E_L = \frac{E_{JA}}{N_J}, \quad (2)$$

$$E_{NL} = \frac{E_{JA}}{12N_J^3}. \quad (3)$$

The inductive energy is inversely proportional to the inductance  $E_L = (\Phi_0/2\pi)^2/L$  and thus the inductance scales with the number of junctions in the array,  $L \propto N_J$ . For large arrays,  $N_J \gg 1$ , the quartic and higher order terms are further reduced by higher powers of  $N_J^{-1}$  and can safely be neglected.

The inductance, however, is in practice limited by parasitic capacitances to ground [15, 16], see Fig. 2. As for the excitations in the individual junctions, the plasma oscillating frequency between the inductive array and ground should be larger than the low-frequency modes of the device. With each superconducting island in the array having a capacitance  $C_{gr}$  to ground, the aggregate capacitance of the array is approximately  $C_{self} = N_J C_{gr}$ , resulting in an excitation energy  $\hbar\omega_{self} = \sqrt{8E_L E_C^{self}}$  and self-impedance  $Z_{self} = \frac{\sqrt{2}}{\pi} R_Q \sqrt{E_C^{self}/E_L}$  where  $E_C^{self} = e^2/2C_{self}$ . Demanding the array plasma frequency to be larger than the junction frequency,  $\omega_{self} \gtrsim \omega_{JA}$ , results in a limit to the number of junctions  $N_J \lesssim (C_{gr}/C_{JA})^{-1/2}$  [16]. In turn, setting a limit to how small (large) the inductive energy (inductance) can be

$$E_L \gtrsim E_{JA} \sqrt{\frac{C_{gr}}{C_{JA}}}. \quad (4)$$

Thus, the magnitude of the inductance and self-impedance is primarily set by the smallness of  $C_{gr}$ , and less so by  $E_{JA}$  and  $C_{JA}$  which are constrained by the “no

quantum phase slips” and “no low-energy excitations” requirements. In Fig. 1(c), we show the array energy versus phase (red line) for typical parameters (see caption) and assuming the capacitance to ground to be of the order of one attofarad. The conventional array is characterized by  $N_J \approx 300$ ,  $\omega_{gr}/2\pi = \omega_{JA}/2\pi = 8.9\text{GHz}$ ,  $E_L = 0.13h\text{GHz}$ ,  $L = 1.3\mu\text{H}$  and  $Z_{self} = 11R_Q$ , similar to Ref. [10].

As a final remark, we mention relative insensitivity to variations in  $E_{JA}$ . If  $\delta_J$  is the relative deviation in the Josephson energies, the relative deviation in the inductive energy is smaller by a factor of  $N_J^{-1/2}$ :  $\delta_L = \delta_J/\sqrt{N_J}$ . In practice, the junction variation is around  $\delta_J = 10\%$ , leading to expected variations in inductive energy of  $\delta_L \approx 0.5\%$ .

## B. Ideal quarton array superinductors

The goal for the quarton array superinductor is to suppress the leading order quadratic contribution in Eq. (1) to significantly increase the associated inductance. The cancelation of the quadratic term can be accomplished in more advanced junction arrays via interference effects [35, 36]. We exemplify the cancelation mechanism by considering an array of  $N_q$  quartons. The quarton consists of a subarray of  $N_s > 1$  identical junctions shunted by a single junction with Josephson energy  $E_{JA}$  [33, 34], see Fig. 2(a) for a diagram with  $N_s = 2$ . Each junction in the subarray has a Josephson energy  $\gamma N_s E_{JA}$ , where  $\gamma$  is the parameter controlling the suppression of  $E_L$ . When  $\gamma = 1$  and the quarton loop is biased by exactly half a flux quantum, the interference between the subarray and the single junction exactly cancels the quadratic term in Eq. (1) (up to small renormalization corrections derived in Appendix C and similar to the renormalization discussed in Refs. [36, 37]). As detailed in Appendix A, the ideal quarton array results in an effective potential of the same form as Eq. (1) where

$$E_L = (\gamma - 1) \frac{E_{JA}}{N_q}, \quad (5)$$

$$E_{NL} = \frac{1}{12} \left(1 - \frac{\gamma}{N_s^2}\right) \frac{E_{JA}}{N_q^3}. \quad (6)$$

When  $E_L \approx 0$  and the leading contribution is quartic, the inductive element is sometimes referred to as a nonlinear superinductor. Similarly, we refer to  $E_{NL}$  as the nonlinear inductive energy. In the case where  $\gamma = 2$ , the quarton array mimics a conventional array with  $N_q$  junctions and inductive energy  $E_L = E_{JA}/N_q$ . For this reason, we interpret  $\gamma - 1 \in [0, 1]$  as the  $E_L$  suppression parameter that interpolates between a purely quartic and a quadratic potential. Values  $\gamma - 1 < 0$  formally result in two minima, but the distributed phase approximation fails in this regime. In Fig. 1(c), we compare effective potentials for the conventional array (red line), the fully  $E_L$  suppressed ( $\gamma = 1$ ) quarton array (light blue) and the

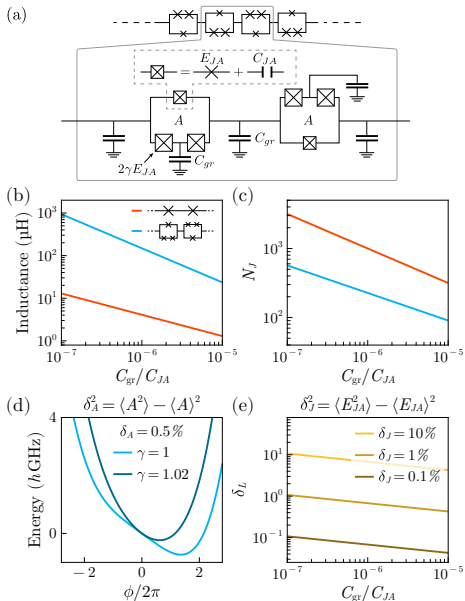


FIG. 2. (a) A closer look of the qurton array, showing capacitance to ground and qurton loop areas. (b) Largest achievable inductance for the conventional (red line) and qurton (blue line) array superinductors when limited by capacitance to ground. (c) Same as (b) for the optimal number of junctions in the array. (b) and (c) together shows increased inductance and improved scaling with  $C_{gr}$  for the qurton array. (d) Effective potentials of the qurton superinductor when subject to unmitigated area variations  $\delta_A = 0.5\%$ . An array with partial suppression of  $E_L$  (darkblue) is less sensitive to area variations than an array with full suppression (lighblue). (e) The relative variations in inductance  $\delta_L$  for different levels of variations in Josephson energy  $\delta_J$ . The sensitivity to junction variations require precise fabrication  $\delta_J < 1\%$ . We use the value  $E_{JA} = 40$  hGHz throughout the paper.

partially  $E_L$  suppressed ( $\gamma = 1.02$ ) qurton array (dark blue).

There is not a unique way of relating the nonlinear inductive energy  $E_{NL}$  to the standard inductive energy  $E_L$ . One option is to compare an oscillator, consisting of a QASI shunted by a capacitor, to an  $LC$ -oscillator. To establish an equivalence between the two oscillators, we can consider the  $|0\rangle \rightarrow |1\rangle$  excitation energy of the QASI-oscillator and equate it with the frequency of the  $LC$ -oscillator  $\omega_{LC} = 1/\sqrt{LC}$ . The equivalent inductive energy can then be defined as the inductive energy of the same-frequency  $LC$ -oscillator. In Appendix B, we discuss further ways of defining an equivalent inductive

energy an arrive at the following approximate result,

$$E_{eq} = (4E_C E_{NL}^2)^{1/3}. \quad (7)$$

Importantly, the equivalent inductive energy depends on the oscillator charging energy  $E_C$  since harmonic and anharmonic oscillator frequencies depend differently on this quantity. The present case is complicated by the relevance of two charging energy scales that result in two different equivalent inductive energies. The charging energy due to capacitance to ground  $E_C^{\text{self}}$  determines the array plasma frequency  $\omega_{\text{self}}$  which corresponds to an equivalent inductive energy  $E_{\text{eq}}^{\text{self}}$ . When the QASI is implemented in a qubit, the charging energy  $E_C$  of the qubit determines the qubit excitation energies which result in a different equivalent inductive energy  $E_{\text{eq}}$ . The equivalent inductive energy defined in Eq. (7) shows that the equivalent inductive energies  $E_{\text{eq}}^{\text{self}}$  and  $E_{\text{eq}}$  are related by the ratio  $E_{\text{eq}}^{\text{self}}/E_{\text{eq}} = (E_C^{\text{self}}/E_C)^{1/3}$ .

Using the equivalent inductive energy determined by  $E_C^{\text{self}}$ , we may now consider the inductance limit set by parasitic capacitance to ground, see Fig. 2 for a circuit diagram. The aggregate capacitance to ground for the qurton array is approximately  $C_{\text{self}} = N_s N_q C_{gr}$  and results in  $\hbar\omega_{\text{self}} \approx \sqrt{8E_{\text{eq}}^{\text{self}} E_C^{\text{self}}}$  and self-impedance  $Z_{\text{self}} \approx \frac{\sqrt{2}}{\pi} R_Q \sqrt{E_C^{\text{self}}/E_{\text{eq}}^{\text{self}}}$ . Requiring that  $\omega_{\text{self}} \gtrsim \omega_{JA}$  yields an analogous condition on the equivalent inductive energy relevant to the self-impedance,

$$E_{\text{eq}}^{\text{self}} \gtrsim E_{JA} N_s N_q \frac{C_{gr}}{C_{JA}}. \quad (8)$$

We note that  $E_L$  should replace  $E_{\text{eq}}^{\text{self}}$  if the suppression of  $E_L$  is only partial such that  $E_L > E_{\text{eq}}^{\text{self}}$ . Since the total capacitance to ground scales with the number of junctions in the qurton subarray  $N_s > 1$ , Eq. (8) shows that arrays with subarray size  $N_s = 2$  achieves the largest self-impedance. For this reason, we focus on  $N_s = 2$  for the remainder of the paper. Enforcing equality in Eq. (8), assuming  $\gamma - 1 \ll 1$  while using  $E_{\text{eq}}^{\text{self}}/E_{\text{eq}} = (E_C^{\text{self}}/E_C)^{1/3}$ , we find the maximal number of qurtons and minimal equivalent inductive energy  $E_{\text{eq}}$  relevant to the qubit when limited by capacitance to ground,

$$N_q = \frac{1}{2} \left( \frac{E_{CA}}{E_{JA}} \right)^{1/10} \left( \frac{C_{gr}}{C_{JA}} \right)^{-2/5}, \quad (9)$$

$$E_{\text{eq}} = E_{JA} \left( \frac{E_{CA}}{E_{JA}} \right)^{2/15} \left( \frac{E_C}{E_{CA}} \right)^{1/3} \left( \frac{C_{gr}}{C_{JA}} \right)^{4/5}. \quad (10)$$

Compared to the conventional array, the QASI enjoys improved scaling relations with  $C_{gr}$  for both the array size and inductive energy. Using the values also used for the conventional array  $E_{JA} = 40$  hGHz,  $E_{CA} = 0.25$  hGHz and  $C_{gr}/C_{JA} = 10^{-5}$  and assuming the QASI to be in a circuit with charging energy  $E_C = 10$  hGHz, results in  $N_J = 3N_q = 90$ ,  $\omega_{gr}/2\pi = \omega_{JA}/2\pi = 8.9$  GHz,  $E_{\text{eq}} = 6.9$  hMHz,  $L_{\text{eq}} = 24$   $\mu$ H and  $Z_{\text{self}} = 59R_Q$ . Thus at 3

times fewer junctions, the QASI achieves more than an order of magnitude increase in (equivalent) inductance compared to the conventional array. These results are shown in Fig. 1(c) and Fig. 2(b, c) and summarized in Table I. Our results show that the QASI can be a useful tool in the engineering of ultra-large impedance circuits such as those displayed in Fig. 1(b).

### C. Nonideal quarton array superinductors

The downside of the above approach to obtain large inductance is that the array becomes relatively sensitive to variations in junctions and geometry. If the Josephson energies vary, the offset amount can give rise to significant contributions to the (standard) inductive energy  $E_L$ . Likewise, in the presence of a global external  $B$ -field, variations in the quarton loop areas away from the nominal value  $A_0$  give rise to offset terms in the potential energy that are proportional to the phase  $\phi$ . As illustrated in Fig. 2(d), even small terms linear in  $\phi$  can severely modify the QASI effective potential.

To better quantify these effects, we present a detailed analysis of the nonideal quarton array in Appendix C. The dominant offset terms are

$$\Delta V = \Delta\varphi_A \frac{E_{JA}}{\sqrt{N_q}} \phi + \frac{1}{2} \Delta E_L \phi^2, \quad (11)$$

where  $\Delta\varphi_A$  is defined in Eq. (13). The second term results from relative variations in Josephson energies  $\delta_J$  and  $\Delta E_L$  is given by

$$\Delta E_L = \sqrt{\frac{3}{2}} \delta_J \frac{E_{JA}}{N_q^{3/2}}. \quad (12)$$

As shown in Fig. 2(e), when assuming full nominal cancellation  $\gamma = 1$ , the offset contribution  $\Delta E_L$  can be significant compared to the quartic term as measured by  $\delta_L = \Delta E_L / E_{\text{eq}}$ . Ensuring that the inductance of the array is not limited by variations in junctions therefore requires  $\delta_J \sim 1\%$ . This is beyond what is currently achievable with state-of-the-art fabrication [47, 48]. Until fabrication improves below  $\delta_J = 1\%$ , we propose to only partially suppress  $E_L$  to accommodate for large variations  $\Delta E_L$ . The optimal degree of suppression and the corresponding value of  $\gamma$  depends on the experimentally realized variation in junctions.

The first term in Eq. (11) is related to the relative variation in loop areas  $\delta_A = \Delta A / A$  and locally fluctuating fields  $\Delta B_f$  with,

$$\Delta\varphi_A = \pi \left( \frac{N_+ - N_-}{\sqrt{N_+ + N_-}} \frac{\Delta B_g}{B_0} + \delta_A + \frac{\Delta B_f}{B_0} \right). \quad (13)$$

Here, the total applied field is given by  $B = B_0 + \Delta B_g$  such that the nominal values of loop area and  $B$ -field satisfy the half flux-quantum condition,  $A_0 B_0 = \Phi_0 / 2$ . The

	Conv.	Qarton
Leading Term	Quadratic	Quartic
$Z_{\text{self}}$ scales with	$C_{\text{gr}}^{-1/2}$	$C_{\text{gr}}^{-7/10}$
$L$ scales with	$C_{\text{gr}}^{-1/2}$	$C_{\text{gr}}^{-4/5}$
$N_J$ scales with	$C_{\text{gr}}^{-1/2}$	$C_{\text{gr}}^{-2/5}$
$\delta_L$ scales with	$C_{\text{gr}}^{1/4}$	$C_{\text{gr}}^{-1/5}$
Sensitive to JJ variation	No	Yes
Sensitive to flux	No	Yes

TABLE I. Comparison between conventional and quarton array superinductors.

total number of quartons  $N_q = N_+ + N_-$  is distributed between  $N_{\pm}$  quartons with orientation  $\pm$  as discussed below. We account for the small offset magnetic field  $\Delta B_g$  because the array can be sensitive to fluctuations and offsets in the global field and because careful adjustments in the global field away from  $B_0$  can compensate for the offset due to area variations  $\delta_A$ . Since the effects of area variations drastically change the effective QASI potential, it is crucial to mitigate this issue. As detailed below, we propose to do this by adjusting the global field  $\Delta B_g$ , which is straightforward in experiment.

Important to the array's response to the external field is the orientation of the quarton loops. The quarton loops can all be oriented in the same direction as shown in Fig. 1 or in alternating directions shown in Fig. 2. The loop orientation determines the sign of the external flux relative to the phase drop across the single junctions. In Eq. (13), we assume the general case where  $N_{\pm}$  quartons are oriented to yield a  $\pm$  sign on the flux. As seen in Eq. (13), the sensitivity to the offset global field  $\Delta B_g$  is determined by the quarton loop orientation through the prefactor  $K = (N_+ - N_-) / \sqrt{N_+ + N_-}$ . A desired value of  $K$  can be realized by picking the quarton orientation according to

$$N_{\pm} = \frac{1}{2} \left( N_q \pm K \sqrt{N_q} \right). \quad (14)$$

The parameter  $K$  can be interpreted as the lever arm in the quarton array's response to the global offset field  $\Delta B_g$ . Using this gradiometric lever arm, the offset due to loop area variation can be exactly canceled by adjusting the global field by an amount  $\Delta B_g = -\delta_A B_0 / K$ . When choosing a value for  $K$ , it is important to also consider the random fluctuations in  $\Delta B_g$ . Experiments show that the amplitude of flux noise in flux bias lines is more than two orders of magnitude less than the locally fluctuating fields often associated with randomly flipping spins in the surface oxide [49–51]. For  $K \sim 1$ , the global field fluctuations will thus not be a dominant noise source compared to random local fields  $\Delta B_f$  and the contribution from  $\delta_A$  can be canceled by a small field offset  $\Delta B_g \sim \delta_A B_0$  without additional effects. As a consequence, we can assume



that  $\Delta B_f$  approximately cancels the  $\delta_A$  contribution and only take the locally fluctuating fields as a noise source such that Eq. (13) becomes

$$\Delta\varphi_A \approx \frac{\pi\Delta B_f}{B_0}. \quad (15)$$

Fluctuations in  $\Delta B_f$  is likely a significant dephasing channel for QASI-based devices. To address this potential issue, we again propose to only partially suppress  $E_L$ . When the effective potential is approximately quadratic, the addition of a term linear in  $\phi$  merely leads to a shift of the harmonic potential, which does not affect transition energies. The impact of unmitigated loop area variations at a realistic value of  $\delta_A = 0.5\%$  [49, 51] is displayed in Fig. 2(d), where the effective potential of the quartic ( $\gamma = 1$ , light blue) and approximately quadratic ( $\gamma = 1.02$ , dark blue) QASI is compared.

Considering the impact of component variation, it is not obvious how to best choose  $\gamma$  and the corresponding degree of  $E_L$  suppression. When implementing the QASI in protected qubit design, competing factors are at play: A fully  $E_L$  suppressed QASI is more sensitive to variations, but it also achieves a higher (equivalent) inductance that can protect the qubit against noise. Conversely, a partially  $E_L$  suppressed QASI is more robust against variations but results in lower inductance and qubits that are more sensitive to noise. In the subsequent sections, we therefore study dephasing due to  $1/f$  flux noise in protected qubits: the  $0 - \pi$ , bifluxon and Blochium qubits. By sweeping the degree of  $E_L$  suppression through  $\gamma - 1$ , we obtain optimal design recipes for the QASI for all three protected qubit designs and discuss the feasibility of reaching their respective protected regimes. Since the quartic potential also introduces a coupling to the spurious  $\zeta$  mode in the  $0 - \pi$  qubit, we also analyze the dephasing time due to photon shot-noise in this qubit.

### III. THE QASI $0 - \pi$ QUBIT

In this section, we consider the consequences of using QASIs in the realization of the  $0 - \pi$  qubit. We study its coherence properties and discuss the possibility of realizing the deep protected regime.

The  $0 - \pi$  circuit consists of pairs of identical capacitances, Josephson junctions and inductors arranged in a nontrivial circuit layout [2], see Fig. 3(a). The four nodes in the  $0 - \pi$  circuit give rise to three independent modes which are typically collected in qubit modes  $\phi, \theta$  and the spurious  $\zeta$  mode. The phase drop across circuit components are conveniently expressed by the  $\phi, \theta, \zeta$  modes,

$$\text{Junctions : } \phi \pm \theta, \quad (16)$$

$$\text{Capacitors : } \theta \pm \zeta, \quad (17)$$

$$\text{Inductors : } \phi \pm \zeta, \quad (18)$$

where  $\pm$  refers to the two elements in the circuit. These modes also diagonalize the capacitance matrix of the circuit and leads to a succinct formulation of the  $0 - \pi$  Hamiltonian [3–5, 52].

In the QASI  $0 - \pi$  qubit, the inductive elements are replaced by qarton array superinductors, see Fig. 3(a). By using the  $\phi, \theta, \zeta$  modes, we find the Hamiltonian describing the QASI  $0 - \pi$  qubit,  $H = H_C + H_J + H_L$ , which differs from the conventional  $0 - \pi$  qubit [3–5, 52] only in the inductive term  $H_L$ ,

$$H_C = 4E_C^\phi n_\phi^2 + 4E_C^\theta (n_\theta - n_g)^2 + 4E_C^\zeta n_\zeta^2, \quad (19)$$

$$H_J = -2E_J \cos(\phi + \varphi_{\text{ext}}/2) \cos(\theta), \quad (20)$$

$$H_L = \sqrt{2}\Delta\varphi_A \frac{E_{JA}}{\sqrt{N_q}} \phi + E_L (\phi^2 + \zeta^2) + E_{NL} (\phi^4 + \zeta^4 + 6\phi^2\zeta^2). \quad (21)$$

The charging energies are given by their usual expressions  $E_C^\phi = e^2/4C_J$ ,  $E_C^\theta = e^2/4(C + C_J)$  and  $E_C^\zeta = e^2/4C$  where  $C$  and  $C_J$  are the large circuit and small junction capacitances respectively. The Josephson energy of the junctions are  $E_J$  and the external flux in the qubit loop formed by the junctions and inductors enters via  $\varphi_{\text{ext}} = 2\pi\Phi_{\text{ext}}/\Phi_0$ .

The inductive part of the Hamiltonian in Eq. (21) is found from  $V + \Delta V$  in Eqs. (1) and (11) where the phase drop is replaced by  $\phi \pm \zeta$  for the two QASIs. We highlight the origin of the important coupling term in Eq. (21) which appears as a cross-term in the quartic potential,  $E_{NL}(\phi + \zeta)^4/2 + E_{NL}(\phi - \zeta)^4/2 = E_{NL}(\phi^4 + \zeta^4 + 6\phi^2\zeta^2)$ . Just as for the conventional  $0 - \pi$  qubit, asymmetry in the device components can also lead to coupling between the  $\phi$  and  $\zeta$  modes. It is believed that this coupling is limiting the coherence of the conventional  $0 - \pi$  qubit via shot-noise dephasing [1, 4–6]: The thermal population of the low-energy  $\zeta$  mode leads to dephasing in the qubit through a dispersive interaction. The analysis of component asymmetry will not be reiterated here and we refer to Refs. [4, 5] for a thorough treatment. Instead, we focus on the shot-noise dephasing derived from the new  $\phi^2\zeta^2$ -coupling in Sec. III B and Appendix D.

The linear term in Eq. (21) is due to locally fluctuating fluxes in the qarton array as discussed in the context of Eq. (15). This flux noise dephasing channel is expected to be significant and we study it in Sec. III A. The corresponding linear term in  $\zeta$  is left out since random flux fluctuations are small and leads to decoherence of the  $\zeta$  mode, which is not a direct decoherence channel of the qubit. We account for dephasing of the qubit modes induced by relaxation of the  $\zeta$  mode when considering shot-noise dephasing.

The quartic contribution  $E_{NL}\phi^4$  slightly alters the QASI  $0 - \pi$  qubit states. However, they remain very similar to the conventional  $0 - \pi$  qubit states, see Fig. 3(c); the QASI  $0 - \pi$  states show the characteristic localization to the  $\theta = 0$  and  $\theta = \pi$  valleys while the  $\phi$  mode

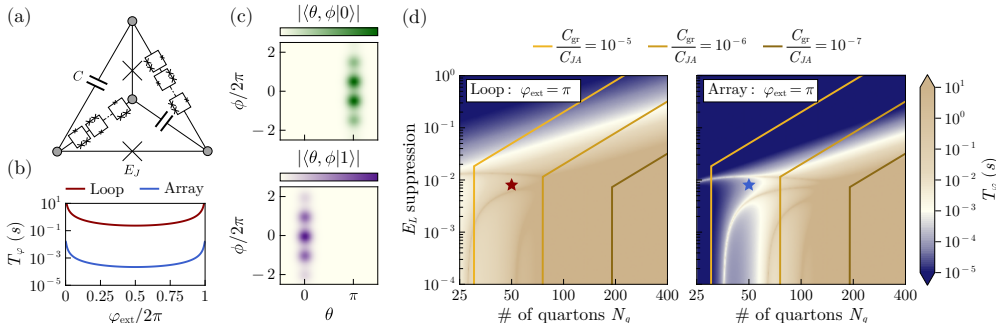


FIG. 3. Flux dephasing in the  $0 - \pi$  qubit with quarton array nonlinear superinductors. (a) The  $0 - \pi$  circuit diagram with QASIs. (b) Dephasing due to  $1/f$  loop (red line) and array (blue line) flux noise as a function of external flux in the qubit loop,  $\varphi_{\text{ext}} = \Phi_{\text{ext}}/2\pi\Phi_0$ , showing sweet-spots at integer flux quanta. The parameters used are  $(N_q, \gamma - 1) = (50, 8 \cdot 10^{-3})$  as indicated by the stars in (d). (c) Qubit state wave functions of the  $0 - \pi$  qubit for the same parameters and evaluated at  $\varphi_{\text{ext}} = 0$ . (d) Dephasing due to  $1/f$  loop flux noise (left) and array flux noise (right) as a function of the number of quartons  $N_q$  and the  $E_L$  suppression parameter  $\gamma - 1$ . The yellow lines indicate the maximal number of quartons allowed by the parasitic capacitance to ground for a given level of  $E_L$  suppression, see Eq. (7). The  $0 - \pi$  qubit is sensitive to the array fluxes but becomes protected for large enough arrays ( $C_{\text{gr}}/C_{JA} \lesssim 10^{-7}$ ). The dephasing times are computed following Ref. [4] using the same noise parameter  $A_\Phi = 1 \mu\Phi_0$  and the same infrared and ultraviolet cutoffs for the  $1/f$  noise. The circuit parameters used here and in Fig. 4 are also taken from Ref. [4]:  $E_J = 10$  h GHz,  $E_C = 10$  h GHz,  $E_C^\zeta = 0.01$  h GHz with  $E_C^\zeta = (1/E_C^\phi + 1/E_C^\zeta)^{-1}$ .

is spread across several troughs of the cosine potential of Eq. (20). As discussed, both of these properties are important for realizing the deep protected  $0 - \pi$  regime [1–5]. We also remark that the  $\zeta$  mode remains approximately harmonic despite the quartic term  $E_{NL}\zeta^4$ : the large shunting capacitors  $C$  localizes the  $\zeta$  mode near zero where the quartic contribution is small compared to the quadratic contribution, see Fig. 4(c) where the  $\zeta$  mode potential and energies are displayed. We discuss the  $\zeta$  mode further in Appendix D and quantify when the  $\zeta$  mode is harmonic to a good approximation.

### A. Flux noise dephasing

To study dephasing due to flux noise, we start by simplifying the Hamiltonian in Eqs. (19)–(21). Since the qubit states are localized in the  $0$  and  $\pi$  valleys, we freeze that mode to  $\theta = 0, \pi$ . Moreover, as argued in Appendix D, we replace  $\zeta^2$  by its mean value  $\bar{\zeta}^2$  such that the coupling to the  $\zeta$  mode results in a renormalizing term,  $6E_{NL}\bar{\zeta}^2\phi^2$ . The resulting effective Hamiltonian describing the  $\phi$  mode is given by

$$H_\phi = 4E_C^\phi n_\phi^2 \mp 2E_J \cos(\phi + \varphi_{\text{ext}}/2) + \sqrt{2}\Delta\varphi_A \frac{E_{JA}}{\sqrt{N_q}} \phi + (E_L + 6E_{NL}\bar{\zeta}^2) \phi^2 + E_{NL}\phi^4, \quad (22)$$

where  $\mp$  refers to the  $0$  and  $\pi$  valleys. The dephasing time  $T_\phi$  due to  $1/f$  flux noise can be numerically evaluated from  $H_\phi$  to second order in flux fluctuations following Ref. [4]. We use realistic noise parameters and

Hamiltonian parameters identical to those used to study the protected  $0 - \pi$  regime in Ref. [4], see the caption of Fig. 3 for details.

Figure 3(b,d) shows the dephasing time due to  $1/f$  noise in the qubit loop (red) and quarton array (blue). In panel (b), we show the dephasing times as a function of external flux in the qubit loop  $\varphi_{\text{ext}}$  for QASIs with 50 quartons and  $E_L$  suppression  $\gamma - 1 = 8 \cdot 10^{-3}$ . For this realization, we also display the qubit states in panel (c). As expected, the QASI  $0 - \pi$  qubit is very sensitive to fluctuations in the local fluxes entering the quarton array  $\Delta\varphi_A$  (blue line) compared to the qubit loop flux  $\varphi_{\text{ext}}$  (red line), see Fig. 3(b). These dephasing times also show sweet-spots at integer flux quanta in the qubit loop. However, many competing noise channels might not make these flux sweet-spots the optimal operating point, see for example Fig. 4(b) and Ref. [4]. For this reason, we evaluate the loop flux and array flux dephasing times at half-integer flux quantum and sweep the number of quartons  $N_q$  and the  $E_L$  suppression  $\gamma - 1$  in panel (d). The red and blue stars correspond to the parameters used in panels (b) and (c). The left (loop flux) and right (array flux) panels in (d) share the same qualitative features: no protection and low coherence at a small number of quartons or low level of  $E_L$  suppression (larger  $\gamma - 1$ ) and exponentially high coherence at a large number of quartons and high degree of  $E_L$  suppression (small  $\gamma - 1$ ). The high-coherence lines arching out from the protected regime correspond to parameters where the  $\theta = 0$  and  $\theta = \pi$  ground states become degenerate. Near these lines the  $\theta = 0$  and  $\theta = \pi$  states

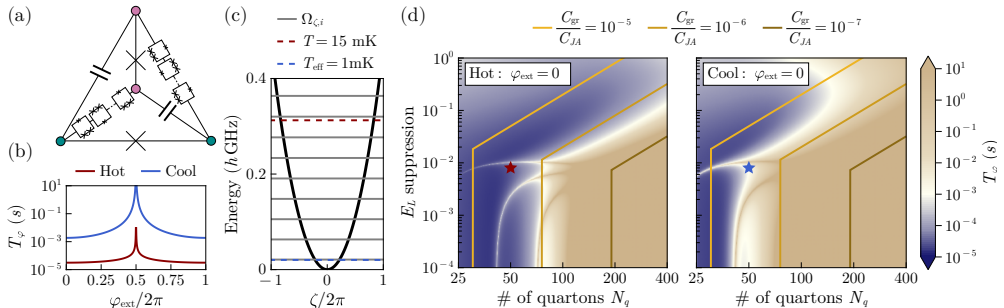


FIG. 4. Shot-noise dephasing in the qurton array based  $0 - \pi$  qubit via the always-on coupling to the spurious  $\zeta$  mode in Eq. (25). (a) The  $0 - \pi$  circuit diagram showing the spurious  $\zeta$  mode as the phase difference between pink and teal nodes. (b) Shot-noise dephasing due to the “hot” (red line) and cooled (blue line)  $\zeta$  mode as a function of external flux in the qubit loop, showing sweet-spots at half-flux frustration. Parameters are identical to Fig. 3 and indicated by the stars in (d). (c) Bare potential and energies of the  $\zeta$  mode showing its approximately harmonic potential even at a large suppression of  $E_L$  (small  $\gamma - 1$ ). The hot (red line) and cooled (blue line) temperatures are also indicated on the energy axis and correspond to  $n_{\text{th}}^{\text{hot}} = 7.0$  and  $n_{\text{th}}^{\text{cool}} = 0.14$ . (d) Dephasing due to  $1/f$  loop flux noise (left) and array flux noise (right) as a function of the number of qurtons  $N_q$  and the  $E_L$  suppression parameter  $\gamma - 1$ . The yellow lines indicate the maximal number of qurtons allowed by the parasitic capacitance to ground for a given level of  $E_L$  suppression, see Eq. (7). The cooling of the  $\zeta$  mode decreases its effective temperature and increases coherence significantly near the protected regime ( $C_{\text{gr}}/C_{\text{JA}} < 10^{-6}$ ). The dephasing time is evaluated away from sweet-spots at  $\varphi_{\text{ext}} = 0$ . The shot-noise dephasing and  $\zeta$  mode cooling is computed following Refs. [4, 5] using similar parameters:  $T = 15$  mK  $= 0.3125 h k_B^{-1}$  GHz,  $T_\zeta = \kappa_\zeta^{-1} = 0.1$  ms,  $T_b = \kappa_b^{-1} = 80$  ns,  $\omega_b/2\pi = 5$  GHz,  $\epsilon/2\pi = 400$  MHz,  $\bar{g} = 10$  h MHz, such that the lossy resonator has a  $Q$ -factor around 1250. See Appendix E for further details on the cooling scheme.

exchange role as ground and excited states. The change of qubit ground/excited states is a curious feature of the quartic potential and is also seen in panel (c) where one would expect the  $\theta = 0$  state to be the ground state in the conventional  $0 - \pi$  qubit [1–6]. On top of the dephasing time colormaps, we show yellow to brown lines that indicate the limit set by capacitance to ground, see Eq. (8). For a given value of capacitance to ground, the colormap is divided into an experimentally accessible regime (left of the line) and an inaccessible regime (right of the line). Looking at the array flux dephasing with these guiding lines, we conclude that above millisecond coherence can be achieved when the capacitance to ground is around  $C_{\text{gr}} \sim 10^{-6} \times C_{\text{JA}}$  and the  $E_L$  suppression is around  $\gamma - 1 \sim 10^{-2}$  or less. If the capacitance to ground approaches  $C_{\text{gr}} \sim 10^{-7} \times C_{\text{JA}}$ , the coherence time increases exponentially and quickly grows beyond one second. However, the current estimate of the parasitic capacitance to ground is  $C_{\text{gr}} \sim 10^{-5} \times C_{\text{JA}}$  [10]. Attaining one to two orders of magnitude decrease in capacitance to ground is a significant experimental challenge. In context, the previous decade have seen a decrease in capacitance to ground by about one order of magnitude [14–16]. An advanced fabrication procedures where the junction array is lifted off the substrate, shows that it is possible to further decrease the capacitance to ground [11]. However, this technique is likely not compatible with the QASI as the qurton array requires precise flux

bias.

## B. Shot-noise dephasing

Photon shot-noise dephasing via the  $\zeta$  mode is another candidate for a limiting noise channel in the QASI  $0 - \pi$  qubit. To estimate the shot-noise dephasing, we simplify the Hamiltonian in Eqs. (19)–(21) by performing steps similar to those leading to Eq. (22), see Appendix D. The resulting effective Hamiltonian contains a dispersive coupling at first order in  $E_{NL}$  from the diagonal part of  $\phi^2 \zeta^2$ ,

$$H_{\text{disp}} = -\frac{\omega_q}{2} \sigma_z + \Omega_\zeta a^\dagger a + \chi \sigma_z (a^\dagger a - n_{\text{th}}), \quad (23)$$

where

$$\chi = \frac{24 E_{NL} E_C^\zeta}{\hbar \Omega_\zeta} [\langle \phi^2 \rangle_0 - \langle \phi^2 \rangle_\pi]. \quad (24)$$

We have labeled the qubit states  $|0\rangle, |\pi\rangle$  according to the  $\theta = 0, \pi$  valleys and introduced the qubit Pauli Z operator  $\sigma_z = |0\rangle\langle 0| - |\pi\rangle\langle \pi|$  along with  $\langle \phi \rangle_i = \langle i | \phi^2 | i \rangle$ . The dispersive shift  $\chi$  can be numerically evaluated from the renormalized  $\phi$  mode Hamiltonian in Eq. (22) at  $\Delta\varphi_A = 0$ . The raising operator of the  $\zeta$  mode is  $a^\dagger$  and  $\Omega_\zeta = 4\sqrt{E_C^\zeta (E_L + 6E_{NL}\bar{\phi}^2)}$  is its renormalized energy.

The  $\zeta$  mode is indicated in Fig. 4(a) as the difference between pink and teal nodes. Using the  $\zeta$  mode potential  $V_\zeta = (E_L + 6E_{NL}\phi^2)\zeta^2 + E_{NL}\zeta^4$ , we numerically evaluate the  $\zeta$  mode energy  $\Omega_{\zeta,i}$  of the  $i$ th state. The  $\zeta$  mode potential and energies are displayed in Fig. 4(c), showing the approximately harmonic  $\zeta$  mode. The ladder of energies can be compared to the  $\zeta$  mode temperature  $T$  which sets the photon number  $n_{\text{th}} = 1/[\exp(\hbar\Omega_\zeta/k_B T) - 1]$ .

When the  $\zeta$  mode photon number fluctuates, the dispersive interaction in Eq. (23) leads to dephasing of the QASI  $0 - \pi$  qubit with rate [4, 5, 53–55]

$$\Gamma_\phi^{\text{SN}} = \frac{\kappa_\zeta}{2} \text{Re} \left[ \sqrt{\left(1 + \frac{2i\chi}{\kappa_\zeta}\right)^2 + \frac{8i\chi n_{\text{th}}}{\kappa_\zeta}} - 1 \right], \quad (25)$$

where  $\kappa_\zeta$  is the decay rate of the  $\zeta$  mode. The Hamiltonian of Eq. (23) is similar to the one studied in Refs. [4, 5] where a coupling  $\propto \phi\zeta$  results in a dispersive interaction at second order. There, the authors find that the conventional  $0 - \pi$  qubit is protected against shot-noise dephasing in the weak dispersive limit,  $\chi n_{\text{th}} \ll \kappa_\zeta$ . Further, Ref. [5] proposes to actively cool the  $\zeta$  mode by coupling it to a lossy resonator while modulating the resonators inductance harmonically. This procedure cools the  $\zeta$  mode to an effective temperature  $T_{\text{eff}}$  and can increase the shot-noise dephasing time substantially. The cooled  $\zeta$  mode effective temperature is shown in Fig. 4(c) and we discuss further  $\zeta$  mode cooling in Appendix E.

We present photon shot-noise dephasing via the  $\zeta$  mode in Fig. 4 as obtained from Eq. (25). In panel (b), the shot-noise dephasing times are shown against the qubit loop flux  $\varphi_{\text{ext}}$  using the same parameters as in Fig. 3 and indicated by stars in panel (d). We denote the cooled  $\zeta$  mode by “cool” (blue line) and the  $\zeta$  mode without cooling by “hot” (red line), using the cryostat base temperature  $T = 15$  mK as in Refs. [4, 5]. As also found in Ref. [5], panel (b) shows that  $\zeta$  mode cooling can increase the shot-noise dephasing time by a few orders of magnitude; in this particular instance, by two orders of magnitude. Moreover, panel (b) also shows that the flux sweet spot for dephasing due to photon shot-noise is at  $\phi_{\text{ext}}/2\pi = 1/2$ . This is to be contrasted to flux noise where the sweet spot is at  $\phi_{\text{ext}}/2\pi = (0, 1)$ , see Fig. 3(b).

In addition to the bare  $\zeta$  mode potential and energies, panel (c) displays the  $\zeta$  mode (effective) temperature using the same parameters as in panel (b). For these parameters, the  $\zeta$  mode is cooled from the 15 mK cryostat base temperature to about  $T_{\text{eff}} = 1$  mK, corresponding to reducing the photon number from  $n_{\text{th}}^{\text{hot}} = 7.0$  to  $n_{\text{th}}^{\text{cool}} = 0.14$ .

Panel (d) is similar to Fig. 3(d), here showing the “hot” (left colormap) and “cool” (right colormap) shot-noise dephasing times evaluated at  $\varphi_{\text{ext}} = 0$ . The arching high-coherence lines in panel (d) are different from those in Fig. 3 and are present when quantum fluctuations in  $\phi$  for  $\theta = 0$  and  $\theta = \pi$  are identical such that  $\chi = 0$  in Eq. (24). Shot-noise dephasing due to the hot  $\zeta$  mode (left colormap) is similar to the array flux noise dephasing

in Fig. 3(d) and these are simultaneously limiting the QASI qubit coherence. However, when the  $\zeta$  mode is cooled (right colormap), the shot-noise dephasing is no longer limiting the qubit coherence. In this case, the QASI  $0 - \pi$  qubit can be operated at the flux noise sweet-spot which is at integer flux quanta in the qubit loop. Consequently, we estimate that the deep  $0 - \pi$  regime can be reached when the capacitance to ground is  $C_{\text{gr}} = 10^{-6} \times C_{JA}$  or smaller. On the other hand, if the  $\zeta$  mode is not cooled, the estimates given in Sec. III A pertain.

In addition to the shot-noise dephasing studied here, component asymmetry also leads to a shot-noise dephasing channel studied in Refs. [4, 5]. In general, we expect this noise channel to be less significant as it is due to a second order process but it ultimately depends on the precision with which each component of the device can be fabricated.

#### IV. THE QASI BIFLUXON

In this section, we study the bifluxon qubit implemented with a quarton array superinductor. Similar to Sec. III A, we evaluate the dephasing time limited by flux noise and compare it to the  $0 - \pi$  qubit.

The conventional bifluxon qubit consists of two identical junctions ( $E_J$ ) and an inductor ( $E_L$ ) connected in a loop [7], see Fig. 5(a) for a diagram where the inductive element is the QASI. As derived in Refs. [1, 7] and briefly discussed in Appendix F, the bifluxon can be described by an effective Hamiltonian akin to the effective  $0 - \pi$  qubit Hamiltonian. Replacing the device’s inductance with a QASI, this effective Hamiltonian takes the form,

$$H_{\text{bi}} = 4E_C n_\phi^2 \mp E_J \cos\left(\frac{\phi}{2} + \frac{\varphi_{\text{ext}}}{2}\right) + \Delta\varphi_A \frac{E_{JA}}{\sqrt{N_q}} \phi + \frac{E_L}{2} \phi^2 + \frac{E_{NL}}{2} \phi^4, \quad (26)$$

where  $E_C$  is the charging energy of the  $\phi$  mode, which is the phase difference across the inductive element. The  $\mp$  sign in Eq. (26) correspond to the even/odd configurations of zero and one Cooper pairs on the middle island in Fig. 5, see Appendix F for further details. The resulting ground states  $|\psi_\pm\rangle$  of the effective bifluxon Hamiltonian are the computational states [7]. These are shown in Fig. 5(c) and are similar to cuts at  $\theta = 0, \pi$  of the QASI  $0 - \pi$  qubit states in Fig. 3.

We compute the dephasing time due to  $1/f$  flux noise in the bifluxon qubit loop and the quarton array in the same manner as for the QASI  $0 - \pi$  qubit. Fig. 5(b, d) shows the dephasing times which are qualitatively similar compared to Fig. 3. We find identical sweet-spots at integer flux quanta in panel (b) and the same high-coherence features in panel (d). Most importantly, we find that the QASI bifluxon coherence time is much reduced compared to the QASI  $0 - \pi$  qubit. In agreement

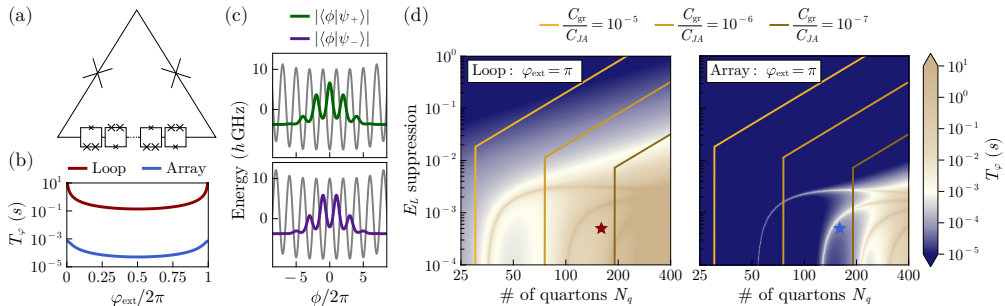


FIG. 5. Flux dephasing in the bifluxon qubit with a quarton array nonlinear superinductor. (a) The QASI bifluxon circuit diagram. (b) Dephasing due to  $1/f$  loop (red line) and array (blue line) flux noise as a function of external flux in the qubit loop,  $\varphi_{\text{ext}} = \Phi_{\text{ext}}/2\pi\Phi_0$ , showing sweet-spots at integer flux quanta. The parameters used are  $(N_q, \gamma - 1) = (160, 5 \cdot 10^{-4})$  as indicated by the stars in (d). (c) Qubit state wave functions in the effective bifluxon potentials for the same parameters and evaluated at  $\varphi_{\text{ext}} = 0$ . (d) Dephasing due to  $1/f$  loop flux noise (left) and array flux noise (right) as a function of the number of quartons  $N_q$  and the  $E_L$  suppression parameter  $\gamma - 1$ . The yellow lines indicate the maximal number of quartons allowed by the parasitic capacitance to ground for a given level of  $E_L$  suppression, see Eq. (7). The bifluxon's response to flux noise is qualitative the same as that shown by the  $0 - \pi$  qubit in Fig. 3. Albeit, the bifluxon requires much larger array sizes as explained Appendix F. The dephasing time is evaluated away from sweet-spots at  $\varphi_{\text{ext}} = \pi$ . The parameters and approach are identical to Fig. 3 with  $E_J = E_C = 10$  hGHz.

with the result of Appendix F, we find that the protected regime has receded in the  $(N_q, \gamma - 1)$ -parameter space.

Despite the bifluxon's advantages compared to the  $0 - \pi$  qubit; simpler design and no spurious  $\zeta$  mode, from Fig. 5(d) it appears exceedingly challenging to satisfy the component requirements that lead to its protected regime,  $C_{\text{gr}} < 10^{-7} \times C_{JA}$ . Meeting these requirements demands substantial improvements in fabrication techniques beyond what can be expected in the near-term.

## V. THE QASI BLOCHNIUM

We now turn to the Blochonium qubit whose circuit is identical to the fluxonium circuit [11, 15], see Fig. 6(a) for a diagram of the QASI-based Blochonium. The ideal parameter regime for the Blochonium qubit, however, differs from the fluxonium parameter regime by requiring smaller  $E_J/E_C$  and  $E_L/E_C$  [11, 12]. Ref. [11] realizes a Blochonium qubit with  $E_J < E_C$  and  $E_L/E_C \sim 1/100$ . There, the authors lift the qubit off the substrate to decrease the parasitic capacitance to ground and thereby decrease  $E_L$  significantly.

This Blochonium qubit distinguishes itself from the  $0 - \pi$  and bifluxon qubits by being a single mode circuit [11]. The computational states of the Blochonium qubit is the ground and first excited states, see Fig. 6(c) [1, 11], as opposed to the valley-degenerate states of the  $0 - \pi$  and bifluxon qubits. As we elaborate later in this section, it turns out that valley-degenerate states and ground/excited states of a single mode responds qualitatively different to flux noise in the quarton array. Addi-

tionally, the Blochonium qubit is also susceptible to relaxation as its computational states are not disjointly supported in phase space [1].

The Hamiltonian describing the QASI Blochonium qubit in Fig. 6(a) is given by

$$H_{\text{Bloch}} = 4E_C n_\phi^2 - E_J \cos(\phi + \varphi_{\text{ext}}) + \Delta\varphi_A \frac{E_{JA}}{\sqrt{N_q}} \phi + \frac{E_L}{2} \phi^2 + \frac{E_{NL}}{2} \phi^4, \quad (27)$$

where  $E_C$  and  $E_J$  are the charging and Josephson energy of the capacitor and junction in Fig. 6(a) and  $\varphi_{\text{ext}}$  is the flux in the qubit loop. Using Eq. (27), it is straightforward to compute the dephasing time due to flux noise in the same way as in Secs. III A and IV.

We show the numerically evaluated dephasing times due to  $1/f$  flux noise in the qubit loop (red) and the quarton array (blue) in Fig. 6(b, d). In panel (b), we see the large difference in sensitivity to flux in the qubit loop and the quarton array which is common to all three qubit designs. Additionally, we identify sweet-spots at half-integer flux quanta. In the left of panel (d), we find the same qualitative response to flux noise in the qubit loop as found in Figs. 3 and 5. Compared to the QASI  $0 - \pi$  and bifluxon qubits, protection against qubit loop flux noise is more easily attained for the Blochonium qubit. The (slight) enhancement of the Blochonium's protection to this noise channel is simply due to the factor of  $1/2$  in the inductive terms in Eq. (27), compare to Eq. (22) and the discussion in Appendix F. In the right of panel (d), the response to flux noise in the quarton array shows very different features compared to the QASI

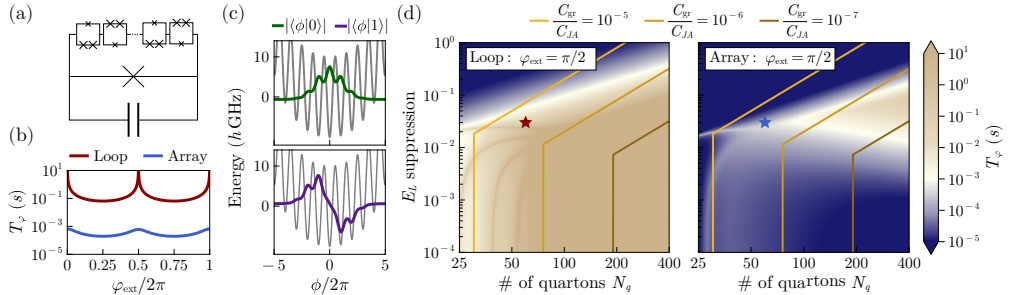


FIG. 6. Flux dephasing in the Blochonium qubit with a quarton array nonlinear superinductor. (a) The QASI Blochonium circuit diagram. (b) Dephasing due to  $1/f$  loop (red line) and array (blue line) flux noise as a function of external flux in the qubit loop,  $\varphi_{\text{ext}} = \Phi_{\text{ext}}/2\pi\Phi_0$ , showing sweet-spots at half-integer flux quanta. The parameters used are  $(N_q, \gamma - 1) = (60, 3 \cdot 10^{-2})$  as indicated by the stars in (d). (c) Qubit state wave functions in the Blochonium potential for the same parameters and evaluated at  $\varphi_{\text{ext}} = 0$ . (d) Dephasing due to  $1/f$  loop flux noise (left) and array flux noise (right) as a function of the number of quartons  $N_q$  and the  $E_L$  suppression parameter  $\gamma - 1$ . The yellow lines indicate the maximal number of quartons allowed by the parasitic capacitance to ground for a given level of  $E_L$  suppression, see Eq. (7). The Blochonium’s response to loop flux noise is qualitative the same as that shown by the  $0 - \pi$  and bifluxon qubits in Figs. 3 and 5. However, due to the non-degeneracy of the qubit states, the Blochonium qubit is not protected from array flux noise in the  $\phi^4$ -dominated regime at large  $E_L$  suppression (small  $\gamma - 1$ ). Instead, the Blochonium qubit requires an approximately harmonic potential to become insensitive to array flux noise. The dephasing time is evaluated away from sweet-spots at  $\varphi_{\text{ext}} = \pi/2$ . The parameters and approach are identical to Figs. 3 and 5 with  $E_J = E_C = 10$  h GHz.

$0 - \pi$  and bifluxon qubits. Protection against this noise channel vanishes for large suppression of  $E_L$  (small values of  $\gamma - 1$ ), showing that the Blochonium qubit requires an approximately quadratic inductive potential. The spread of the first excited state in the qubit’s potential can be substantially larger than the ground state, resulting in greater sensitivity to the linear term  $\Delta\varphi_A E_{JA} \phi / \sqrt{N_q}$ . This displacement generally shifts the energies unless the inductive potential is quadratic as discussed in Sec. II C. Thus, we find that the protected Blochonium regime can be realized starting at around  $C_{\text{gr}} = 10^{-6} \times C_{JA}$  at a relatively low level of  $E_L$  suppression,  $\gamma - 1 \approx 3 \cdot 10^{-2}$ .

## VI. CONCLUSION

We have studied a quarton array superinductor whose energy as a function of phase can be either quadratic, quartic or interpolate between these two limiting cases. We consider the self-impedance of the QASI which is limited by parasitic capacitances to ground. By comparing the QASI to state-of-the-art conventional junction array superinductors, we find that more than an order of magnitude increase in (equivalent) inductance can be achieved. This gain does not compromise the size of the array. Contrary, the QASI utilizes about a factor of three fewer junctions than the conventional array in this example. Further, the quantities of interest in the QASI (inductance, self-impedance, number of junctions, etc.) scale significantly better with capacitance to ground relative to the conventional junction array.

The promising results, however, are at a cost. The QASI shows increased sensitivity to variations due to fabrication. Variations in quarton loop area can be highly detrimental but it is possible to mitigate this issue by alternating the quarton orientation. Worse are relative variations in Josephson energies of the junctions which should be below 1% and, ideally, smaller still to be able to control the exact ratios between quadratic and quartic contributions to the energy. We speculate that it might be possible to design other junction array superinductors where the requirements on junction variations are less but likely at the cost of additional junctions that increase the total capacitance to ground.

High-impedance superinductors are useful components in the design of protected superconducting qubits as it allows for exponentially suppressed sensitivity to flux-noise. We have explored using the QASI in the  $0 - \pi$ , bifluxon and Blochonium qubits. Numerical evaluation of the dephasing time due to  $1/f$  flux noise in the qubit loop and array loops show 2-3 orders of magnitude increase in the sensitivity to flux noise in the quarton array compared to the qubit loop. Despite this limiting noise channel introduced by the QASI, the significantly higher inductance makes up for this deficit as the deep protected regimes of these qubits can be more easily reached. Additionally, the QASI introduces a significant coupling to the  $\zeta$  mode in the  $0 - \pi$  qubit leading to shot-noise dephasing on the same level as the dephasing due to flux noise in the quarton array.

We estimate that if the parasitic capacitance to ground is reduced by about one order of magnitude beyond cur-

rent state-of-the-art, the deep protected regime of the  $0 - \pi$  qubit and Blochonium can be reached while the conditions set by the bifluxon qubit remain hard to meet. An additional requirement is an order of magnitude or more improvement in the precision of fabricated Josephson energies to go below the 1% threshold. These predictions should be seen in the light of the more than 2-3 orders of magnitude decrease in capacitance to ground necessary to reach a similar level of protection using conventional junction array superinductors.

### ACKNOWLEDGMENT

We acknowledge support from the Danish National Research Foundation, the Danish Council for Independent Research — Natural Sciences, the European Research Council (Grant Agreement No. 856526) and the Novo Nordisk Foundation, Grant number NNF22SA0081175, NNF Quantum Computing Programme.

### Appendix A: Ideal quarton array

In this appendix, we derive the effective potential of the ideal quarton array superinductor. We start by considering a single quarton, consisting of a subarray of  $N_s$  junctions shunted by a single junction as explained in Sec. II and Ref. [14, 15]. When the phase drop across the single quarton is  $\phi_i$ , the distributed phase approximation can be invoked for the subarray itself, leading to a term of the form

$$V_{\text{sub},i} = N_s^2 \gamma E_{JA} (1 - \cos(\phi_i/N_s)). \quad (\text{A1})$$

In the ideal scenario, exactly half a flux quantum threads the quarton loop. We allocate the external flux  $\phi_{\text{ext},i} = 2\pi\Phi/\Phi_0 = \pi$  in the single junction, changing the sign of the cosine,

$$V_{\text{single},i} = E_{JA} (1 + \cos(\phi_i)). \quad (\text{A2})$$

Summing up the contributions from all  $N_q$  quarton elements while using the DPA across the entire array,  $\phi_i \rightarrow \phi/N_q$ , we get

$$V = N_q E_{JA} [\cos(\phi/N_q) - N_s^2 \gamma \cos(\phi/N_s N_q)] + \text{const.} \quad (\text{A3})$$

Finally, we may expand the effective potential in  $\phi$ ,

$$V = \frac{1}{2}(\gamma-1) \frac{E_{JA}}{N_q} \phi^2 + \frac{1}{24} \left(1 - \frac{\gamma}{N_s^2}\right) \frac{E_{JA}}{N_q^3} \phi^4 + \dots, \quad (\text{A4})$$

giving the results quoted in Sec. II.

### Appendix B: Equivalent Inductive Energy

The task of comparing the nonlinear inductive energy  $E_{NL}$  to a linear inductive energy  $E_L$  is not unique and

depends on the relevant physics. For example, for a (non-linear)  $LC$ -resonator, the relevant quantity may be the ground to excited state energy  $\omega_{01}$ . For the  $0 - \pi$ , bifluxon and Blochonium qubits, it is instead more important to know the spread of the ground state wavefunctions  $\sqrt{\langle 0 | \phi^2 | 0 \rangle}$  to assess the degree of protection against flux induced dephasing. We note that defining the inductance from the energy separation is similar to [36] and the wavefunction spread is considered in [35]. For a quartic oscillator  $H = 4E_C n^2 + \frac{1}{2} E_{NL} \phi^4$ , the energy  $\omega_{01}$  can be straightforwardly computed in the WKB approximation and the wavefunction spread can be approximated by the classical turning points of the ground state,

$$\omega_{01}^{\text{WKB}} \approx 5.77 \dots \times E_C^{2/3} E_{NL}^{1/3}, \quad (\text{B1})$$

$$\sqrt{\langle 0 | \phi^2 | 0 \rangle} \approx \phi_{\text{cl}}^{\text{WKB}} = 1.36 \dots \times \frac{E_C}{E_{NL}}^{1/6}. \quad (\text{B2})$$

The WKB approximation is notoriously inaccurate for the lowest energy levels, but in the present situation, we are only interested in approximate scaling relations. The results in Eqs. (B1) and (B2) can be compared to the equivalent results from a harmonic oscillator  $H = 4E_C n^2 + \frac{1}{2} E_L \phi^2$ ,

$$\omega_{01}^{\text{HO}} = \sqrt{8E_C E_L}, \quad (\text{B3})$$

$$\sqrt{\langle 0 | \phi^2 | 0 \rangle} \approx \phi_{\text{cl}}^{\text{HO}} = \left(\frac{8E_C}{E_L}\right)^{1/4}. \quad (\text{B4})$$

By equating  $\omega_{01}^{\text{WKB}} = \omega_{01}^{\text{HO}}$  and  $\phi_{\text{cl}}^{\text{WKB}} = \phi_{\text{cl}}^{\text{HO}}$ , we get two expressions for an equivalent inductive energy  $E_L$ ,

$$E_L^\omega \approx 0.89 \dots \times E_C^{1/3} E_{NL}^{2/3}, \quad (\text{B5})$$

$$E_L^\phi \approx 2.31 \dots \times E_C^{1/3} E_{NL}^{2/3}. \quad (\text{B6})$$

These approximate results have the same scaling in the Hamiltonian parameters but different numerical prefactors. For simplicity, we define a single equivalent inductive energy similar to Eqs. (B5) and (B6),

$$E_{\text{eq}} = (4E_C E_{NL}^2)^{1/3}. \quad (\text{B7})$$

The prefactor  $4^{1/3} \approx 1.59 \dots$  is chosen to be a compromise between Eqs. (B5) and (B6) and simplifies the equations presented in the main text.

### Appendix C: Nonideal quarton array

In this Appendix, we derive the effective potential for the disordered QASI and assume variations in Josephson energies and quarton loop areas.

We begin by considering a single quarton at position  $i$  in the array, this time specializing to  $N_s = 2$  from the beginning. We label the single junction  $j = 0$  and label the two junctions in the subarray  $j = 1, 2$ . The Josephson energy of the single junction and subarray junctions are

given by  $E_{JA} + dE_{JA}^{(i,0)}$  and  $2\gamma(E_{JA} + dE_{JA}^{(i,j)})$  respectively. The independent random variations in Josephson energy  $dE_{JA}^{(i,j)}$  are assumed to be distributed with zero mean and standard deviation  $\sigma_J = \delta_J E_{JA}$ . The junction capacitances are assumed to take their nominal values,  $C_{j=0} = C_{JA}$  and  $C_{j=1,2} = \gamma N_s C_{JA}$ , as variations in the capacitances does not directly influence the quarton array potential. The total phase drop across quarton  $i$  is distributed across the two junctions in the subarray  $\phi_i = \phi_{i,1} + \phi_{i,2}$ . The external flux threading the  $i$ th quarton  $2\pi\Phi_i/\Phi_0 = \varphi_A^{(i)}$  is allocated to the single junction whose phase drop becomes  $\phi_i + \rho_i \varphi_A^{(i)}$ . The orientation of the quarton loop relative to the externally applied field is encoded in the sign  $\rho_i = \pm 1$ . Finally, we rotate to the basis  $\phi_i = \phi_{i,1} + \phi_{i,2}$ ,  $\theta_i = \phi_{i,1} - \phi_{i,2}$  to obtain the general single quarton Hamiltonian  $H_i = T_i + V_i$ ,

$$T_i = 4 \frac{E_{CA}}{1+\gamma} n_{\phi,i}^2 + 4 \frac{E_{CA}}{\gamma} n_{\theta,i}^2, \quad (C1)$$

$$V_i = (E_{JA} + dE_{JA}^{(i,0)}) \cos(\phi_i + \rho_i d\varphi_A^{(i)}) \quad (C2)$$

$$- 4\gamma (E_{JA} + dE_{JA}^{(i,+)}) \cos(\phi_i/2) \cos(\theta_i/2)$$

$$+ 4\gamma dE_{JA}^{(i,-)} \sin(\phi_i/2) \sin(\theta_i/2),$$

where  $dE_{JA}^{(i,\pm)} = (dE_{JA}^{(i,1)} \pm dE_{JA}^{(i,2)})/2$ . Nominally, the flux in the quarton loop is  $\Phi_i = A_0 B_0 = \Phi_0/2$ , however, deviations in the loop areas  $dA_i$  and magnetic field  $dB_i$  results in deviations  $d\varphi_A^{(i)} = \varphi_A^{(i)} - \pi = \frac{2\pi}{\Phi_0} (dA_i B_0 + A_0 dB_i)$ . The area variation  $dA_i$  is assumed to be drawn independently from a distribution with zero mean and deviation  $\sigma_A = \delta_A A_0$ .

As a first step, we integrate out the internal  $\theta$  degree of freedom. We assume that it remains in its ground state since  $E_{JA}/E_{CA} \gg 1$  and replace  $\theta_i$  with its expectation value

$$\langle \theta_i \rangle = - \frac{2dE_{JA}^{(i,-)} \sin(\phi_i/2)}{E_{JA} \cos(\phi_i/2)}, \quad (C3)$$

Next, we approximate the  $\theta$  mode to be a harmonic oscillator whose ground state energy is

$$\frac{\hbar\omega_\theta}{2} = E_{JA} \sqrt{\frac{2E_{CA}}{E_{JA}}} \sqrt{\cos(\phi_i/2)}. \quad (C4)$$

In this approximation, the effective potential for the  $\phi_i$  mode becomes

$$V_i = (E_{JA} + dE_{JA}^{(i,0)}) \cos(\phi_i + \rho_i d\varphi_A^{(i)}) \quad (C5)$$

$$- 4\gamma (E_{JA} + dE_{JA}^{(i,+)}) \cos(\phi_i/2)$$

$$- 8\gamma E_{JA} \left( \frac{dE_{JA}^{(i,-)}}{E_{JA}} \right)^2 \frac{\sin^2(\phi_i/2)}{\cos(\phi_i/2)}$$

$$+ E_{JA} \sqrt{\frac{2E_{CA}}{E_{JA}}} \sqrt{\cos(\phi_i/2)}.$$

We expand the potential and keep significant terms  $\{\phi_i^2, \phi_i^4, \sqrt{\frac{E_{CA}}{E_{JA}}} \phi_i^2, dX_i \phi_i, dX_i \phi_i^2, dX_i^2 \phi_i^2\}$  while disregarding higher order terms  $\{\sqrt{\frac{E_{CA}}{E_{JA}}} dX_i, dX_i dY_i, dX_i \phi_i^3, dX_i \phi_i^4, \sqrt{\frac{E_{CA}}{E_{JA}}} \phi_i^4\}$  and beyond. The result is  $V_i = V_{0,i} + dV_i$  where

$$V_{0,i} = \frac{1}{2} E_{JA} \left( \gamma - 1 - \sqrt{\frac{E_{CA}}{32E_{JA}}} \right) \phi_i^2 \quad (C6)$$

$$+ \frac{1}{2} \frac{E_{JA}}{12} \left( 1 - \frac{\gamma}{4} \right) \phi_i^4,$$

$$dV_i = - E_{JA} \rho_i d\varphi_A^{(i)} \phi_i \quad (C7)$$

$$+ \left( \frac{(d\varphi_A^{(i)})^2}{2} + \frac{dE_{JA}^{(i,\Sigma)}}{E_{JA}} - 4\gamma \left( \frac{dE_{JA}^{(i,-)}}{E_{JA}} \right)^2 \right) \frac{E_{JA} \phi_i^2}{2},$$

where  $dE_{JA}^{(i,\Sigma)} = \gamma dE_{JA^{+,i}} - dE_{JA}^{(i,0)}$ . The value of  $\gamma$ , where the quadratic contribution is canceled, gets slightly perturbed by the internal  $\theta$  mode;  $\gamma^* = 1 + \sqrt{E_{CA}/32E_{JA}}$ . The renormalization of  $\gamma$  does not change the results in the main text as the  $E_L$  suppression parameter can simply be interpreted as  $\gamma - \gamma^*$  rather than  $\gamma - 1$ . For this reason, we neglect the small renormalization of  $\gamma$  due to the internal quarton mode.

Assuming that variations are small, we invoke the distributed phase approximation across the entire quarton array  $\phi_i = \phi/N_q$  and sum all quarton potentials. The resulting potential of the quarton array  $V = V_0 + \Delta V$ , as quoted in the main text, becomes

$$V_0 = \sum_i V_{0,i} = \frac{1}{2} E_L \phi^2 + \frac{1}{2} E_{NL} \phi^4, \quad (C8)$$

$$\Delta V = \sum_i dV_i = E_{JA} \frac{\Delta\varphi_A}{\sqrt{N_q}} \phi + \frac{1}{2} \Delta E_L \phi^2, \quad (C9)$$

where we define

$$E_L = (\gamma - 1) \frac{E_{JA}}{N_q}, \quad (C10)$$

$$E_{NL} = \frac{1}{12} \left( 1 - \frac{\gamma}{4} \right) \frac{E_{JA}}{N_q^3}, \quad (C11)$$

$$\Delta E_L = \left( \frac{\Delta\varphi_A^2}{2} + \sqrt{\frac{3}{2N_q}} \delta_J - 2\delta_J^2 \right) \frac{E_{JA}}{N_q}. \quad (C12)$$

For realistic parameters, the middle term in Eq. (C12) is dominant since  $1/N_q$  is generally larger than  $\delta_J^2$  and area variations are generally smaller than variations in junctions.

While every realization of the QASI is unique, the result in Eq. (C9) is obtained by replacing  $\sum_i dX_i \rightarrow \sqrt{N_q} \sigma_X$ . We make this general simplification due to the following reasoning: If the  $dX_i$ 's are identical and independently distributed with zero mean and standard deviation  $\sigma_X$ , then the sum is distributed with zero mean and



standard deviation  $\sqrt{N_q}\sigma_X$ . We thus assume the statistically likely outcome that a particular realization of the array lies one standard deviation from the mean. In a similar line of reasoning, we replace  $\sum_i dX_i^2$  by its non-zero mean  $N_q\sigma_X^2$ . In this approach, other combinations like  $dX_i dY_i$  and  $dX_i^3$  are higher order and are not included. As an example, we compute  $\Delta\varphi_A$  and  $\Delta\varphi_A^2$  (note that in this notation  $(\Delta\varphi_A)^2 \neq \Delta\varphi_A^2$ ). The phase offset  $d\phi_A^{(i)}$  contain contributions from both the globally applied field and locally fluctuating field  $dB_i = \Delta B_g + dB_f^{(i)}$  as well as the area variations,

$$d\varphi_A^{(i)} = \frac{2\pi}{\Phi_0}(dA_i B_0 + A_0 \delta B_g + A_0 dB_f^{(i)}). \quad (\text{C13})$$

The qartons orientation encoded in the sign  $\rho_i$  can be absorbed in the random variables  $dB_f^{(i)}$  and  $dA_i$  if we assume they come from even distributions. Summing up the contributions for all qartan elements, we get

$$\Delta\varphi_A = \frac{1}{\sqrt{N_q}} \sum_i \rho_i d\phi_A^{(i)} \quad (\text{C14})$$

$$= \frac{1}{\sqrt{N_q}} \frac{2\pi}{\Phi_0} \sum_i \rho_i dA_i B_0 + A_0 \Delta B_g + A_0 dB_f^{(i)}$$

$$= \pi \left( \delta_A + \frac{N_+ - N_-}{\sqrt{N_+ + N_-}} \frac{\Delta B_g}{B_0} + \frac{\Delta B_f}{B_0} \right),$$

$$\Delta\varphi_A^2 = \frac{1}{N_q} \sum_i \left( \rho_i d\phi_A^{(i)} \right)^2 \quad (\text{C15})$$

$$= \frac{1}{N_q} \frac{4\pi^2}{\Phi_0^2} \sum_i \rho_i^2 \left( dA_i B_0 + A_0 \Delta B_g + A_0 dB_f^{(i)} \right)^2$$

$$= \pi^2 \left[ \left( \delta_A^2 + \frac{\Delta B_g}{B_0} \right)^2 + \left( \frac{\Delta B_f}{B_0} \right)^2 \right. \\ \left. + \frac{2\Delta B_g}{\sqrt{N_q} B_0} \left( \delta_A + \frac{\Delta B_f}{B_0} \right) \right].$$

Here, the the cumulative locally fluctuating field  $\Delta B_f = \sum_i dB_f^{(i)}/\sqrt{N_q}$  shares the same noise amplitude  $A_{\Phi_0}$  as the individual fields  $dB_f^{(i)}$ . Immediately, we see that  $\Delta\varphi_A^2$  only gives rise to higher order contributions. On the other hand, the contributions from  $\Delta\varphi_A$  play an important role as discussed in the main text. While the argument in Sec. II, regarding the cancellation of the offset due to area variations, assumes a realization of loop areas  $\sum_i dA_i = \sqrt{N_q}\delta_A A_0$ , we wish to emphasize that the external magnetic field may always be adjusted to cancel this term regardless of the realization of loop areas.

#### Appendix D: Coupling to the $\zeta$ mode

In this Appendix, we discuss the coupling to the  $\zeta$  mode in the QASI  $0 - \pi$  qubit and derive the effective

Hamiltonians used in Sec. III. The coupling term in Eq. 21 can be rewritten by adding and subtracting mean values which denote by a bar,

$$H_{\text{coup}} = 6E_{NL}\bar{\phi}^2\zeta^2 + 6E_{NL}\bar{\zeta}^2\phi^2 + 6E_{NL}(\phi^2 - \bar{\phi}^2)(\zeta^2 - \bar{\zeta}^2) \quad (\text{D1})$$

The last term contains the fluctuations away from the mean and we find appropriate expressions for  $\bar{\phi}^2$  and  $\bar{\zeta}^2$  when we later treat this term. The first two terms in Eq. (D1) renormalizes bare  $\phi$ - and  $\zeta$  modes in Eq. (21) and presents us with a ‘‘chicken or the egg’’ situation; the mean  $\bar{\phi}^2$  cannot be found without  $\bar{\zeta}^2$  and vice versa. Since the ratio  $\langle\phi^2\rangle/\langle\zeta^2\rangle$  is large, the heavy  $\zeta$  mode will be influenced more by the renormalization than the light  $\phi$  mode. We argue that the  $\phi$  mode can be used to find the bare mean  $\bar{\phi}_{\text{bare}}^2$  which renormalizes the  $\zeta$  mode Hamiltonian to good approximation. Then, the renormalized energy  $\Omega_\zeta = 4\sqrt{(E_L + 6E_{NL}\bar{\phi}_{\text{bare}}^2)E_C^\zeta}$  and mean  $\bar{\zeta}_{\text{reno}}^2$  can be computed and used to renormalize the  $\phi$ -potential,  $6E_{NL}\bar{\zeta}_{\text{reno}}^2\phi^2$ . This approach is somewhat reminiscent of the Born-Oppenheimer approximation and is an alternative to solving for the expectations values self-consistently.

We may now consider the last term in Eq. (D1). We start by considering the part that is diagonal in the (renormalized) qubit eigenstates  $|i\rangle$ ,

$$H_{\text{diag}} = 6E_{NL} \left[ \frac{4E_C^\zeta}{\hbar\Omega_\zeta} (a^\dagger + a)^2 - \bar{\zeta}^2 \cdot \mathbf{1} \right] \\ \times \sum_i |i\rangle \langle i| (\langle\phi^2\rangle_i - \bar{\phi}^2), \quad (\text{D2})$$

where  $a^\dagger$  and  $a$  are the raising and lowering operators for the harmonic  $\zeta$  mode and  $\mathbf{1}$  is the identity in this space. We also shorten the notation  $\langle\phi^2\rangle_i = \langle i|\phi^2|i\rangle$ . The off-diagonal part of the operator  $(a^\dagger + a)^2$  is  $(a^\dagger)^2 + a^2$  and can be treated, for example, via a Schrieffer-Wolff transformation [56, 57]. We will not attempt to perform this perturbative calculation, but instead argue that the terms acquired from such a calculation will be subleading compared to the diagonal part  $\propto 2a^\dagger a + 1$ . The Schrieffer-Wolff transformation is useful in the dispersive regime defined by

$$\frac{E_{NL}E_C^\zeta n_{\text{th}}}{(\hbar\Omega_\zeta)^2} (\langle\phi^2\rangle_i - \bar{\phi}^2) \ll 1. \quad (\text{D3})$$

For the qubit states  $i = 0, \pi$ , this perturbative parameter is small when  $\bar{\phi}^2$  is chosen appropriately,

$$\bar{\phi}^2 = \frac{\langle\phi^2\rangle_0 + \langle\phi^2\rangle_\pi}{2}. \quad (\text{D4})$$

For parameters where the qubit is unprotected, the  $\zeta$  mode has a large energy and low photon number  $n_{\text{th}}$  such that Eq. (D3) is satisfied. On the other hand, when

the qubit is protected, the qubit states becomes indistinguishable and  $\langle \phi^2 \rangle_{i=0,\pi} - \bar{\phi}^2$  tends towards zero, again satisfying Eq. (D3). We therefore dismiss the off-diagonal part of Eq. (D2) and focus only on the computational qubit states,

$$H_{\text{diag}} \approx \chi \sigma_z (a^\dagger a - n_{\text{th}}), \quad (\text{D5})$$

$$\chi = \frac{24E_{NL}E_C^\zeta}{\hbar\Omega_\zeta} [\langle \phi^2 \rangle_0 - \langle \phi^2 \rangle_\pi], \quad (\text{D6})$$

where  $\sigma_z = |0\rangle\langle 0| - |\pi\rangle\langle \pi|$  is the qubit Pauli Z operator and  $\bar{\zeta}^2 = \frac{4E_C^\zeta}{\hbar\Omega_\zeta} (2n_{\text{th}} + 1)$ . The dispersive interaction in Eq. (D5) becomes relevant when the  $\zeta$  mode number operator  $n = a^\dagger a$  fluctuates relative to its thermal average  $n_{\text{th}}$ . The time-scale of these fluctuations are much longer than the device dynamics and we therefore only include this term when we study photon shot-noise dephasing in Sec. III B.

We are still left to tackle the terms in Eq. (D1) that are off-diagonal in the qubit states,

$$H_{\text{offdiag}} = 6E_{NL} \left[ \frac{4E_C^\zeta}{\hbar\Omega_\zeta} (a^\dagger + a)^2 - \bar{\zeta}^2 \cdot \mathbf{1} \right] \times \sum_{i,j} |i\rangle\langle j| \langle \phi^2 \rangle_{ij}. \quad (\text{D7})$$

The matrix element  $\langle \phi^2 \rangle_{ij} = \langle i | \phi^2 | j \rangle$  predominantly couples the computational qubit states to states which are excited twice in the  $\phi$ -direction due to even/odd selection rules. These states are significantly higher in energy and will only give a small dispersive correction to the diagonal part in Eq. (D5), as could be computed from a Schrieffer-Wolff transformation as mentioned. We therefore also dismiss these contributions and arrive at the coupling term

$$H_{\text{comp}} \approx 6E_{NL}\bar{\phi}^2\zeta^2 + 6E_{NL}\bar{\zeta}^2\phi^2 + \chi\sigma_z(a^\dagger a - n_{\text{th}}), \quad (\text{D8})$$

where the two first terms renormalizes the bare  $\phi$ - and  $\zeta$  modes and is used throughout Sec. III. The latter term is only relevant when computing the shot-noise dephasing in Sec. III B.

Finally, we may consider when the  $\zeta$  mode is approximately harmonic by comparing the quadratic prefactors  $2E_L$  and  $12E_{NL}\bar{\phi}^2$  to the equivalent inductive energy relevant to the  $\zeta$  mode,  $E_{\text{eq}}^\zeta = n_{\text{th}}(4E_C^\zeta(2E_{NL}^2))^{1/3}$ . We include  $n_{\text{th}} \approx k_B T / \hbar\Omega_\zeta$  to make sure that the quadratic contribution at least dominates up to  $k_B T$ . The resulting

conditions are

$$E_L : \sqrt{N_q(\gamma-1)^3} \gtrsim \frac{1}{8} \left( \frac{E_C^\zeta}{4E_{JA}} \right)^{1/3} \frac{k_B T}{\sqrt{E_C^\zeta E_{JA}}} \approx 0.002, \quad (\text{D9})$$

$$\bar{\phi}^2 : \sqrt{\frac{(\bar{\phi}^2)^3}{N_q^5}} \gtrsim \sqrt{\frac{2}{3}} \left( \frac{E_C^\zeta}{4E_{JA}} \right)^{1/3} \frac{k_B T}{\sqrt{E_C^\zeta E_{JA}}} \approx 0.015, \quad (\text{D10})$$

Since  $\bar{\phi}^2 \propto N_q$ , see for example Eq. (B2), the second condition is fulfilled when  $N_q \lesssim 100$ . For larger  $N_q$ , the first condition takes over and is satisfied when  $\gamma-1 \gtrsim 3 \cdot 10^{-3} \times (100/N_q)^{1/3}$ . In the situation where both  $N_q$  is large and  $\gamma-1$  is small, two considerations can be made: In this case, the photon number  $n_{\text{th}}$  is large such that the anharmonicity between relevant states around  $k_B T$  is small. Additionally, the qubit will be deep into the protected regime and is thus insensitive to the  $\zeta$  mode regardless of its anharmonicity. Alternatively, the cooling scheme studied in Sec. III B also cools the  $\zeta$  mode sufficiently to satisfy Eqs. (D9)-(D10).

### Appendix E: Cooling the $\zeta$ mode

This appendix briefly reviews the  $\zeta$  mode cooling scheme envisioned by Ref. [5] and used in Sec. III B.

Ref. [5] proposes to capacitively couple the  $\zeta$  mode to a lossy resonator,

$$H_{\text{cool}} = \hbar\Omega_\zeta a^\dagger a + \hbar\omega_b(t) - \hbar g(t)(a^\dagger - a)(b^\dagger - b). \quad (\text{E1})$$

The lossy resonator is described by raising and lowering operators  $b^\dagger$ ,  $b$  and by its frequency  $\omega_b(t) = \bar{\omega}_b + \epsilon \cos(\omega_m t)$ . The time-dependence enters via a small harmonic modulation of the resonator inductance, resulting in a frequency modulation with amplitude  $\epsilon$  away from the mean  $\bar{\omega}_b$ . Similarly, the mean of the coupling  $g(t)$  is  $\bar{g}$ . By choosing the modulation frequency to be  $\omega_m = \bar{\omega}_b - \Omega_\zeta$ , excitations in the  $\zeta$  mode can be swapped to the lossy resonator where they are lost at an increased rate  $\kappa_b$ .

When the coupling is small  $\bar{g} \ll \bar{\omega}_b, \Omega_\zeta$ , the system described by Eq. (E1) can be treated in a master equation formalism to reveal the effective  $\zeta$  mode up and down rates  $\Gamma_{\uparrow/\downarrow}$  and the effective coupling  $g'$ ,

$$\Gamma_{\uparrow} = \kappa_b \left( \frac{2g'}{\kappa_b} \right)^2 \left/ \left[ \left( \frac{4\Omega_\zeta}{\kappa_b} \right)^2 + 1 \right] \right., \quad (\text{E2})$$

$$\Gamma_{\downarrow} = \kappa_b \left( \frac{2g'}{\kappa_b} \right)^2, \quad (\text{E3})$$

$$g' \approx \bar{g} \frac{\epsilon}{4\bar{\omega}_b}. \quad (\text{E4})$$

To avoid saturating the lossy resonator, the loss-rate is required to be larger than the effective coupling,  $\kappa_b \gg g'$ . In this case, the effective  $\zeta$  mode cooling rate becomes

$$\gamma_{\text{cool}} = \kappa_{\zeta} + \Gamma_{\downarrow} - \Gamma_{\uparrow}, \quad (\text{E5})$$

and its equilibrium photon number is

$$n_{\text{th}}^{\text{cool}} = \frac{\kappa_{\zeta}}{\gamma_{\text{cool}}} n_{\text{th}} + \frac{\Gamma_{\uparrow}}{\gamma_{\text{cool}}}. \quad (\text{E6})$$

By this prescription, we cool the  $\zeta$  mode in Sec. III B using parameters that are in agreement with the stated requirements for the derivation.

### Appendix F: The bifluxon qubit

In this appendix, we briefly introduce the conventional bifluxon qubit and compare its flux noise response to the  $0 - \pi$  qubit.

The bifluxon qubit consists of two modes; a Cooper pair box mode and a light  $\phi$  mode [7]. The middle island between the Josephson junctions forms a Cooper pair box whose offset charge  $2en_g$  can be controlled by external circuitry. When the offset charge is exactly  $n_g = 1/2$ , the lowest energy Cooper pair box states are formed by the even and odd combinations of zero and one Cooper pairs on the island,  $|\pm\rangle = (|0\rangle \pm |1\rangle)/\sqrt{2}$ . In this case, the effective Hamiltonian describing the dynamics of the phase difference across the inductor is given by [1, 7]

$$H_{\text{bi}} = 4E_C n_{\phi}^2 \mp \frac{2E_J}{k} \cos\left(\frac{\phi}{k} + \frac{\varphi_{\text{ext}}}{2}\right) + kE_L \left(\frac{\phi}{k}\right)^2, \quad (\text{F1})$$

where  $E_C$  is the charging energy of the light  $\phi$  mode and  $\varphi_{\text{ext}}$  is the flux in the qubit loop. The label  $k$  relates the  $0 - \pi$  ( $k = 1$ ) and bifluxon ( $k = 2$ ) effective Hamiltonians. Given the similar descriptions, we expect the flux noise response to also be similar. However, the bifluxon's  $4\pi$ -periodicity in the cosine term necessitates larger inductance to achieve protection against flux noise. Exponential suppression of flux noise is present when the ground state wave function spreads across several troughs of the cosine [1, 2]. We can estimate the spread of the ground state wave function by dropping the cosine term in Eq. (F1),  $w = \sqrt{\langle \phi^2 \rangle} \approx (kE_C/E_L)^{1/4}$ , and compare it to the wavelength of the cosine-potential,  $\lambda = 2\pi k$ :

$$w/\lambda = \frac{1}{2\pi} \left(\frac{E_C}{k^3 E_L}\right)^{1/4}. \quad (\text{F2})$$

Thus, the inductive element in a bifluxon qubit ( $k = 2$ ) should be  $2^3 = 8$  times larger than the inductors in a  $0 - \pi$  qubit ( $k = 1$ ) in order to achieve the same level of flux noise protection. Realizing this factor of 8 would require almost two orders of magnitude decrease in the capacitance to ground, see Eq. (4), as verified by comparing panel (d) in Figs. 3 and 5.

The  $T_1$ -protection of the bifluxon qubit, however, requires the computational states to be separated in phase space [1, 7]. Disjoint support of the computational states is achieved when  $E_C < E_J$  such that the wave functions localize in the cosine wells. Demanding smaller  $E_C$  further increases the requirement on the inductance to reach flux noise protection in Eq. (F2) and this is a trade-off inherent to the bifluxon. Despite these considerations, we do not change the charging energy of the QASI bifluxon qubit relative to the QASI  $0 - \pi$  qubit,  $E_C = E_C^{\phi} = 10 h \text{ GHz}$ , to make comparison to the QASI  $0 - \pi$  qubit straightforward.

- 
- [1] A. Gyenis, A. Di Paolo, J. Koch, A. Blais, A. A. Houck, and D. I. Schuster, PRX Quantum **2**, 030101 (2021).
  - [2] P. Brooks, A. Kitaev, and J. Preskill, Physical Review A **87**, 052306 (2013), arXiv: 1302.4122.
  - [3] J. Dempster, B. Fu, D. G. Ferguson, D. I. Schuster, and J. Koch, Physical Review B **90**, 094518 (2014), arXiv: 1402.7310.
  - [4] P. Groszkowski, A. D. Paolo, A. L. Grimsmo, A. Blais, D. I. Schuster, A. A. Houck, and J. Koch, New Journal of Physics **20**, 043053 (2018).
  - [5] A. D. Paolo, A. L. Grimsmo, P. Groszkowski, J. Koch, and A. Blais, New Journal of Physics **21**, 043002 (2019).
  - [6] A. Gyenis, P. S. Mundada, A. Di Paolo, T. M. Hazard, X. You, D. I. Schuster, J. Koch, A. Blais, and A. A. Houck, PRX Quantum **2**, 010339 (2021).
  - [7] K. Kalashnikov, W. T. Hsieh, W. Zhang, W.-S. Lu, P. Kamenov, A. Di Paolo, A. Blais, M. E. Gershenson, and M. Bell, PRX Quantum **1**, 010307 (2020).
  - [8] T. W. Larsen, M. E. Gershenson, L. Casparis, A. Kringhøj, N. J. Pearson, R. P. G. McNeil, F. Kuemmeth, P. Krogstrup, K. D. Petersson, and C. M. Marcus, Physical Review Letters **125**, 056801 (2020), publisher: American Physical Society.
  - [9] N. Earnest, S. Chakram, Y. Lu, N. Irons, R. K. Naik, N. Leung, L. Ocola, D. A. Czaplewski, B. Baker, J. Lawrence, J. Koch, and D. I. Schuster, Phys. Rev. Lett. **120**, 150504 (2018).
  - [10] H. Zhang, S. Chakram, T. Roy, N. Earnest, Y. Lu, Z. Huang, D. K. Weiss, J. Koch, and D. I. Schuster, Physical Review X **11**, 011010 (2021), publisher: American Physical Society.
  - [11] I. V. Pechenezhskiy, R. A. Mencia, L. B. Nguyen, Y.-H. Lin, and V. E. Manucharyan, Nature **585**, 368 (2020).
  - [12] M. Peruzzo, F. Hassani, G. Szep, A. Trioni, E. Redchenko, M. Zemlička, and J. M. Fink, PRX Quantum **2**, 040341 (2021).
  - [13] J. Koch, T. M. Yu, J. Gambetta, A. A. Houck, D. I. Schuster, J. Majer, A. Blais, M. H. Devoret, S. M. Girvin, and R. J. Schoelkopf, Physical Review A **76**, 042319 (2007).

- [14] V. E. Manucharyan, *Superinductance*, Ph.D. thesis, Yale University (2012).
- [15] V. E. Manucharyan, J. Koch, L. I. Glazman, and M. H. Devoret, *Science* **326**, 113 (2009).
- [16] N. A. Masluk, I. M. Pop, A. Kamal, Z. K. Mineev, and M. H. Devoret, *Phys. Rev. Lett.* **109**, 137002 (2012).
- [17] M. Peruzzo, A. Trioni, F. Hassani, M. Zemlicka, and J. M. Fink, *Phys. Rev. Appl.* **14**, 044055 (2020).
- [18] N. Maleeva, L. Grünhaupt, T. Klein, F. Levy-Bertrand, O. Dupre, M. Calvo, F. Valenti, P. Winkel, F. Friedrich, W. Wernsdorfer, A. V. Ustinov, H. Rotzinger, A. Monfardini, M. V. Fistul, and I. M. Pop, *Nature Communications* **9**, 3889 (2018).
- [19] L. Grünhaupt, M. Spiecker, D. Gusenkova, N. Maleeva, S. T. Skacel, I. Takmakov, F. Valenti, P. Winkel, H. Rotzinger, W. Wernsdorfer, A. V. Ustinov, and I. M. Pop, *Nature Materials* **18**, 816 (2019).
- [20] P. Kamenov, W.-S. Lu, K. Kalashnikov, T. DiNapoli, M. T. Bell, and M. E. Gershenson, *Phys. Rev. Appl.* **13**, 054051 (2020).
- [21] W. Zhang, K. Kalashnikov, W.-S. Lu, P. Kamenov, T. DiNapoli, and M. E. Gershenson, *Phys. Rev. Appl.* **11**, 011003 (2019).
- [22] S. E. de Graaf, S. T. Skacel, T. Hönl-Deccrinis, R. Shaikhaidarov, H. Rotzinger, S. Linzen, M. Ziegler, U. Hübner, H.-G. Meyer, V. Antonov, E. Il'ichev, A. V. Ustinov, A. Y. Tzalenchuk, and O. V. Astafiev, *Nature Physics* **14**, 590 (2018).
- [23] D. Niepce, J. Burnett, and J. Bylander, *Phys. Rev. Appl.* **11**, 044014 (2019).
- [24] T. M. Hazard, A. Gyenis, A. Di Paolo, A. T. Asfaw, S. A. Lyon, A. Blais, and A. A. Houck, *Phys. Rev. Lett.* **122**, 010504 (2019).
- [25] K. R. Amin, C. Ladner, G. Jourdan, S. Hentz, N. Roch, and J. Renard, *Applied Physics Letters* **120**, 164001 (2022).
- [26] O. Dupré, A. Benoît, M. Calvo, A. Catalano, J. Goupy, C. Hoarau, T. Klein, K. L. Calvez, B. Sacépé, A. Monfardini, and F. Levy-Bertrand, *Superconductor Science and Technology* **30**, 045007 (2017).
- [27] L. B. Nguyen, Y.-H. Lin, A. Somoroff, R. Mencia, N. Grabon, and V. E. Manucharyan, *Phys. Rev. X* **9**, 041041 (2019).
- [28] Q. Ficheux, L. B. Nguyen, A. Somoroff, H. Xiong, K. N. Nesterov, M. G. Vavilov, and V. E. Manucharyan, *Physical Review X* **11**, 021026 (2021).
- [29] L. B. Nguyen, G. Koolstra, Y. Kim, A. Morvan, T. Chistolini, S. Singh, K. N. Nesterov, C. Jünger, L. Chen, Z. Pedramrazi, B. K. Mitchell, J. M. Kreikebaum, S. Puri, D. I. Santiago, and I. Siddiqi, *PRX Quantum* **3**, 037001 (2022).
- [30] A. Somoroff, Q. Ficheux, R. A. Mencia, H. Xiong, R. Kuzmin, and V. E. Manucharyan, *Phys. Rev. Lett.* **130**, 267001 (2023).
- [31] I. N. Moskalenko, I. A. Simakov, N. N. Abramov, A. A. Grigorev, D. O. Moskalev, A. A. Pishchimova, N. S. Smirnov, E. V. Zikiy, I. A. Rodionov, and I. S. Besedin, *npj Quantum Information* **8**, 130 (2022).
- [32] L. Ding, M. Hays, Y. Sung, B. Kannan, J. An, A. Di Paolo, A. H. Karamlou, T. M. Hazard, K. Azar, D. K. Kim, B. M. Niedzielski, A. Melville, M. E. Schwartz, J. L. Yoder, T. P. Orlando, S. Gustavsson, J. A. Grover, K. Serniak, and W. D. Oliver, *Phys. Rev. X* **13**, 031035 (2023).
- [33] F. Yan, S. Gustavsson, A. Kamal, J. Birenbaum, A. P. Sears, D. Hover, T. J. Gudmundsen, D. Rosenberg, G. Samach, S. Weber, J. L. Yoder, T. P. Orlando, J. Clarke, A. J. Kerman, and W. D. Oliver, *Nature Communications* **7**, 12964 (2016).
- [34] F. Yan, Y. Sung, P. Krantz, A. Kamal, D. K. Kim, J. L. Yoder, T. P. Orlando, S. Gustavsson, and W. D. Oliver, arXiv:2006.04130 [quant-ph] (2020), arXiv: 2006.04130.
- [35] L. Chirolli, M. Carrega, and F. Giazotto, The quartic blochium: an anharmonic quasicharge superconducting qubit (2023), arXiv:2304.10401 [cond-mat.mes-hall].
- [36] M. T. Bell, I. A. Sadovskyy, L. B. Ioffe, A. Y. Kitaev, and M. E. Gershenson, *Phys. Rev. Lett.* **109**, 137003 (2012).
- [37] M. T. Bell, B. Douçot, M. E. Gershenson, L. B. Ioffe, and A. Petković, *Comptes Rendus Physique* **19**, 484 (2018), quantum simulation / Simulation quantique.
- [38] M. T. Bell and A. Samolov, *Phys. Rev. Appl.* **4**, 024014 (2015).
- [39] M. Esposito, A. Ranadive, L. Planat, S. Leger, D. Fraudet, V. Jouanny, O. Buisson, W. Guichard, C. Naud, J. Aumentado, F. Lecocq, and N. Roch, *Phys. Rev. Lett.* **128**, 153603 (2022).
- [40] A. Ranadive, M. Esposito, L. Planat, E. Bonet, C. Naud, O. Buisson, W. Guichard, and N. Roch, *Nature Communications* **13**, 1737 (2022).
- [41] D. V. Averin, A. B. Zorin, and K. K. Likharev, *Sov. Phys. JETP* **61**, 407 (1985).
- [42] K. K. Likharev and A. B. Zorin, *Journal of Low Temperature Physics* **59**, 347 (1985).
- [43] F. Piquemal and G. Genevès, *Metrologia* **37**, 207 (2000).
- [44] J. Flowers, *Science* **306**, 1324 (2004), <https://www.science.org/doi/pdf/10.1126/science.11102156>.
- [45] F. Nguyen, N. Boulant, G. Ithier, P. Bertet, H. Pothier, D. Vion, and D. Esteve, *Phys. Rev. Lett.* **99**, 187005 (2007).
- [46] A. Di Marco, F. W. J. Hekking, and G. Rastelli, *Phys. Rev. B* **91**, 184512 (2015).
- [47] L. J. Zeng, S. Nik, T. Greibe, P. Krantz, C. M. Wilson, P. Delsing, and E. Olsson, *Journal of Physics D: Applied Physics* **48**, 395308 (2015).
- [48] D. Willsch, D. Rieger, P. Winkel, M. Willsch, C. Dickel, J. Krause, Y. Ando, R. Lescanne, Z. Leghtas, N. T. Bronn, P. Deb, O. Lanes, Z. K. Mineev, B. Dennig, S. Geisert, S. Günzler, S. Ihssen, P. Paluch, T. Reisinger, R. Hanna, J. H. Bae, P. Schüffelgen, D. Grützmacher, L. Buimaga-Iarinca, C. Morari, W. Wernsdorfer, D. P. DiVincenzo, K. Michielsen, G. Catelani, and I. M. Pop, Observation of josephson harmonics in tunnel junctions (2023), arXiv:2302.09192 [quant-ph].
- [49] A. Kou, W. C. Smith, U. Vool, R. T. Brierley, H. Meier, L. Frunzio, S. M. Girvin, L. I. Glazman, and M. H. Devoret, *Physical Review X* **7**, 031037 (2017).
- [50] J. Braumüller, L. Ding, A. P. Vepsäläinen, Y. Sung, M. Kjaergaard, T. Menke, R. Winik, D. Kim, B. M. Niedzielski, A. Melville, J. L. Yoder, C. F. Hirjibehedin, T. P. Orlando, S. Gustavsson, and W. D. Oliver, *Physical Review Applied* **13**, 054079 (2020).
- [51] D. Gusenkova, F. Valenti, M. Spiecker, S. Günzler, P. Paluch, D. Rieger, L.-M. Pioras-Timbolmas, L. P. Zárbo, N. Casali, I. Colantoni, A. Cruciani, S. Pirro, L. Cardani, A. Petrescu, W. Wernsdorfer, P. Winkel, and I. M. Pop, *Applied Physics Letters* **120**, 054001 (2022).
- [52] S. Rasmussen, K. Christensen, S. Pedersen, L. Kristensen, T. Bækkegaard, N. Loft, and N. Zimmer, *PRX*

- 
- Quantum **2**, 040204 (2021).
- [53] P. Bertet, I. Chiorescu, G. Burkard, K. Semba, C. J. P. M. Harmans, D. P. DiVincenzo, and J. E. Mooij, Phys. Rev. Lett. **95**, 257002 (2005).
- [54] A. A. Clerk and D. W. Utami, Phys. Rev. A **75**, 042302 (2007).
- [55] A. P. Sears, A. Petrenko, G. Catelani, L. Sun, H. Paik, G. Kirchmair, L. Frunzio, L. I. Glazman, S. M. Girvin, and R. J. Schoelkopf, Phys. Rev. B **86**, 180504 (2012).
- [56] G. Zhu, D. G. Ferguson, V. E. Manucharyan, and J. Koch, Phys. Rev. B **87**, 024510 (2013).
- [57] A. Blais, A. L. Grimsmo, S. M. Girvin, and A. Wallraff, Reviews of Modern Physics **93**, 025005 (2021).



---

## Colophon

This document was typeset using  $\text{\LaTeX}$ , a high-quality typesetting system. The template uses various packages to enhance the typographic quality and ease of use, providing a consistent and visually appealing result.

This thesis was typeset using the *Fantastic PhD Thesis Template*. It is licensed under the Creative Commons Attribution-Non Commercial 4.0 International License (CC-BY-NC 4.0). The source code for this template, along with the full documentation, can be found on GitHub at [https://github.com/maiani/fantastic\\_template](https://github.com/maiani/fantastic_template).